Receptance-Based Control and Uncertainty Quantification of Aeroservoelastic Systems

Thesis submitted in accordance with the requirements of the University of Liverpool for the degree of Doctor in Philosophy by

Liam Jon Adamson

June 2021

Abstract

Receptance-Based Control and Uncertainty Quantification of Aeroservoelastic Systems

by

Liam Jon Adamson

The desire for more efficient human flight has given impetus to the research and development of novel aerostructures that are both lightweight and flexible. Although delivering benefits such as greater fuel economy and aerodynamic efficiency, these new designs frequently suffer from poor aeroelastic performance. In particular, an unstable, self-excited oscillation, known as flutter, can arise within the desired flight envelope and compromise an aircraft's safety through mechanisms such as damage, degradation, and structural failure.

Historically, flutter has been avoided by making passive modifications to the structure. However, a new approach based on the principles of active control has been developed in recent years. This new approach, known as active flutter suppression (AFS), uses a series of actuators located at several points on the structure to actively modify the natural frequencies and damping of the system such that the conditions at which flutter arises are pushed outside of the desired flight envelope. Although the fundamental principles are now well-established, there are still few documented implementations of AFS systems in real-world aircraft. This is partly due to its reliance on highly accurate numerical models of the structure, aerodynamic and their interaction, which are all seldom available.

This thesis explores the use of receptance methods to facilitate an experiment-based approach to AFS. In this way, there is no requirement to model the system numerically and hence issues associated with modelling errors are mitigated entirely. The Receptance Method is extended to aeroservoelastic systems and some of its practical limitations, which previously inhibited its use on real-world aerostructures, are addressed. First, a method to measure receptance data at or above the flutter speed is developed and a procedure for optimum eigenstructure assignment is described. It is shown that both techniques can significantly improve the performance of the AFS solution and that the flutter speed can be pushed much higher using these approaches. The issue of robustness in receptance-based techniques is also addressed. Procedures to minimise the impact of uncertainty arising from misfitting of receptance data or physical variability between nominal systems are developed. Results show that proper eigenstructure assignment can reduce the propagation of uncertainty to the system's poles and hence reduce variability in the system's dynamics. Finally, an experiment-based approach to uncertainty quantification in aeroelastic systems is developed. The probability of flutter at a given

airspeed is calculated using only measured frequency response function data, which is available through standard modal testing techniques. The method is shown to accurately determine the probability of flutter and may be used as an alternative risk assessment method that could replace arbitrary, deterministic safety regulations that are currently used in industry.

The methods developed in this work are verified numerically on a reference aeroservoelastic model. They are also applied to a wind-tunnel model, which is housed in the University of Liverpool's subsonic wind-tunnel facility. The overarching aim of this thesis is to progress the use of receptance-based techniques in aeroservoelastic systems and to aid with their implementation on real-world aircraft.

Keywords: *receptance, control, uncertainty quantification, aeroelasticity, aeroservoelasticity, flutter, active flutter suppression, robust, probabilistic*

Acknowledgements

First and foremost, I express my deepest gratitude to my supervisors, Dr Sebastiano Fichera and Prof John Mottershead. Both have encouraged, supported, and guided me along every step of this project. I very much hope to continue working with them in future endeavours, whatever and wherever that may be.

I also wish to thank the numerous friends and colleagues with whom I have had the pleasure to work with. They include: Irma Isnardi, Bilal Mokrani, Cristiano Martinelli, Otto Braun, Francesco Palazzo, and Nicolò D'Amico. Your promises of places to stay in Italy, The Netherlands, and Germany have certainly not been forgotten! A special mention also goes to Raymond Edun, who has always been happy to provide a helping hand with experimental activities.

I must also acknowledge the support from my friends back in Cheshire; their daily chats and semi-regular zooms have kept me just about sane in the final months of writing.

Of course, I must thank several family members. Firstly, Ross and Summer, for their encouragement and use of their sofa for regular, pre-Covid weekend escapes. Secondly, to my grandparents, who have both taken a keen interest in my work and have unknowingly spurred me on by asking when I expect to finish. Finally, my parents, Claire and Ian, who give me endless support and encouragement.

This work has been funded by the Engineering and Physical Sciences Council's Doctoral Training Partnership.

This page is intentionally left blank.

Contents

This page is intentionally left blank.

List of Figures

List of Tables

This page is intentionally left blank.

List of Symbols

$\mathbf{A}$	State matrix
$\mathrm{Adj}(\cdot)$	Adjugate matrix
a_i	Weighting constants of the PC expansion
$\mathbf{B}_{CS\rightarrow F}$	Control surface to force input mapping
$\mathbf{B}_{CS}$	Control surface input matrix
$\mathbf{B}_F$	Force input matrix
$\mathbf{B}_a$	Aerodynamic force distribution matrix
b	Semi-chord length
C_{l_α}	Coefficient of lift due to pitch
C_{l_β}	Coefficient of lift due to the trailing-edge
C_{l_γ}	Coefficient of lift due to the leading-edge
$C_{m_{\alpha-eff}}$	Effective moment coefficient in α
$C_{m_{\beta-eff}}$	Effective moment coefficient in β
$C_{m_{\gamma-eff}}$	Effective moment coefficient in γ
$\mathbb{C}$	Complex number
$\mathbf{C}$	Damping matrix
$\mathbf{C}$	Output matrix
$\mathbf{C}_a$	Aerodynamic damping matrix
$\mathbf{C}_s$	Structural damping matrix
$\mathbf{C}_t$	Total damping matrix
$\mathrm{Cov}[\cdot]$	Covariance operator
c_α	Pitch damping coefficient
c_h	Plunge damping coefficient
c_{max}	Maximum gain norm
$\mathbf{d}$	Generalised displacement vector
$\mathcal{D}$	Dissipation term
$\mathrm{Det}(\cdot)$	Determinant operator
$d(s)$	Characteristic polynomial
$\mathbf{e}$	Vector with unit entries
$\mathrm{E}[\cdot]$	Expectation operator
$\mathbf{F}$	FRF matrix
$\mathbf{F}$	Multiple-input velocity feedback matrix
$\mathbf{f}$	Single-input velocity feedback vector
$\mathbf{f}^{(a)}$	Aerodynamic force vector
$\mathbf{f}^{(e)}$	Vector of external forces

f_α	Generalised force in the α degree-of-freedom
f_h	Generalised force in the h degree-of-freedom
$\mathbf{G}$	General transfer function
$\mathbf{G}$	Multiple-input displacement feedback matrix
$\mathbf{g}$	Single-input displacement feedback vector
$\breve{\mathbf{H}}_m$	Effective, measured receptance matrix
$\mathbf{H}$	Receptance matrix
$\mathbf{H}_m$	Measured receptance matrix
h	Plunge displacement
I_α	Second moment of inertia of the aerofoil
$\mathbf{I}$	Identity matrix
$\mathrm{Im}(\cdot)$	Imaginary part
i	Imaginary unit
J_i	Local robustness metric
K_{ij}	Number of zeros in the ij element of the numerator matrix
$\mathbf{K}$	Stiffness matrix
$\mathbf{K}_a$	Aerodynamic stiffness matrix
$\mathbf{K}_s$	Structural stiffness matrix
$\mathbf{K}_t$	Total stiffness matrix
k_α	Pitch stiffness
k_d	Derivative gain in the PID
k_h	Plunge stiffness
k_i	Integral gain in the PID
k_p	Proportional gain in the PID
L	Random characteristic equation
$\mathcal{L}[\cdot]$	Laplace operator
$\overline{L}$	Projected limit state function
l	Number of poles
M	Mass of the aerofoil
$\mathbf{M}$	Mass matrix
$\mathbf{M}_s$	Structural mass matrix
$\max(\cdot)$	Maximum operator
$\min(\cdot)$	Minimum operator
m	Number of inputs
m_1	Number of control inputs
m_2	Number of external force inputs
$\mathbf{N}(s)$	Numerator matrix
n	Number of states
$\mathbb{P}_Z$	Random parameter interval containing zero
$\mathbb{P}_i$	Random parameter interval
$\mathbf{q}$	Generalised degrees-of-freedom vector
R	Euclidean distance from the origin to a point on the limit state function
R^*	Euclidean distance from the origin to the most-probable point
$\hat{\mathbf{R}}$	Equivalent closed-loop input-output transfer function matrix
$\mathbb{R}$	Real number
$\mathbf{R}$	Input-output transfer function matrix
$\mathbf{R}_m$	Measured input-output transfer function matrix

$\mathrm{Re}(\cdot)$	Real part
$\mathrm{rank}(\cdot)$	Matrix rank operator
r	Number of outputs
$r(x)$	Generalised displacement
$S_{\alpha h}$	First moment of inertia of the aerofoil
$\mathbf{S}$	Sensitivity matrix
s_p	Aerofoil span
s	Complex Laplace variable
T	Kinetic energy
T_T	Total robustness metric
$\mathbf{T}$	Combined gain matrix
t	Time
$\mathbf{u}$	Input vector
$\mathbf{u}_i$	Unit vector corresponding to the modification location
V	Potential energy
$\mathbf{v}_{L,i}$	Open-loop left eigenvector
$\mathbf{v}_{R,i}$	Open-loop right eigenvector
$\mathbf{v}_j$	Unit vector corresponding to the modification location
$\mathrm{Var}[\cdot]$	Variance operator
v^*	Flutter speed
v_{ref}	Reference freestream speed
v_{it}	Iteration velocity
v_{lim}	Boundary between measurable and immeasurable regions
v	Freestream speed
$\mathbf{w}_{L,i}$	Closed-loop left eigenvector
$\mathbf{w}_{R,i}$	Closed-loop right eigenvector
w	Velocity feedback adjustment factor
w_{CL}	Closed-loop uncertain flutter speed function
w_{OL}	Open-loop uncertain flutter speed function
$\mathbf{x}$	State vector
$\mathbf{y}$	Output vector
$\mathbf{y}$	Vector of response variables
$\overline{\mathbf{y}}$	Upper bound of the vector of response variables
$\underline{\mathbf{y}}$	Lower bound of the vector of response variables
y_1	Displacement corresponding to the leading-edge LDS
y_2	Displacement corresponding to the trailing-edge LDS
$\mathbf{y}_0$	Nominal vector of response variables
$\check{\mathbf{Z}}$	Effective dynamic stiffness matrix
$\Delta\mathbf{Z}_r$	Structural modification matrix
$\mathbf{Z}$	Dynamic stiffness matrix
$\mathbf{Z}_n$	Nominal dynamic stiffness matrix
$z_{ij,k}$	k zero belonging to the ij element of the numerator matrix
z_r	Scalar modification term
α	Pitch angle
$\boldsymbol{\alpha}$	Weighting vector
β	Trailing-edge control surface deflection
β_d	Desired trailing-edge control surface deflection

β_i	Weighting term in the local robustness metric
Γ	Multivariate, orthogonal function
γ	Leading-edge control surface deflection
γ_i	Weighting term in the local robustness metric
ζ	Damping ratio
ζ^*	Damping adjustment factor
ζ_{pi}	Pitch damping ratio
ζ_{pl}	Plunge damping ratio
η_{ij}	scaling parameter belonging to the ij element of the numerator matrix
$\Delta\boldsymbol{\theta}$	Interval of the vector of random variables
$\boldsymbol{\theta}$	Vector of random variables
$\boldsymbol{\theta}_0$	Nominal vector of random variables
$\hat{\boldsymbol{\theta}}$	Sample of the random vector
$\hat{\theta}$	Standardised random variable
$\hat{\theta}_i^*$	Random parameter at most-probable point
$\overline{\boldsymbol{\theta}}$	Upper bound of the vector of random variables
θ^*	Random parameter boundary solutions
$\tilde{\boldsymbol{\theta}}$	Auxiliary random vector
$\underline{\boldsymbol{\theta}}$	Lower bound of the vector of random variables
κ	Reduced frequency
$\boldsymbol{\Lambda}$	Gain adjustment matrix
$\boldsymbol{\lambda}$	Set of open-loop poles
λ	Open-loop pole
$\boldsymbol{\mu}$	Set of closed-loop poles
μ	Closed-loop pole
ρ	Density
ρ	Objective function
$\rho(x)$	Mass per unit chord length
ρ_i	Weighting term in the total robustness metric
Φ	Cumulative distribution function of the unit Gaussian
Φ^{-1}	Inverse cumulative distribution function of the unit Gaussian
Ψ	Multivariate, orthogonal polynomial
ω	Frequency of oscillation
ω^*	Flutter frequency
ω_n	Natural frequency
ω_{pi}	Pitch natural frequency
ω_{pl}	Plunge natural frequency

List of Acronyms

ABS Acrylonitrile Butadiene Styrene.

AFS Active Flutter Suppression.

CAE Computational Aeroelasticity.

CFD Computational Fluid Dynamics.

CFRP Carbon Fibre Reinforced Plastic.

DC Direct Current.

FAA Federal Aviation Administration.

FEA Finite Element Analysis.

FORM First-Order Reliability Method.

FRF Frequency Response Function.

IATA International Air Transport Association.

ICAO International Civil Aviation Organisation.

ILAF Identically Located Accelerometers and Feedback.

LCC Low-Cost Carrier.

LCO Limit Cycle Oscillation.

LDS Laser Displacement Sensor.

LHS Latin Hypercube Sampling.

LQR Linear-Quadratic-Regulator.

LTI Linear Time-Invariant.

MCS Monte Carlo Simulation.

MIMO Multiple-Input Multiple-Output.

MPP Most-Probable Point.

NASA National Aeronautics and Space Administration.

PC Polynomial Chaos.

PDE Partial Differential Equation.

PDF Probability Density Function.

PID Proportional-Integral-Derivative.

QRA Quantitative Risk Assessment.

RBDO Reliability-Based Design Optimisation.

RDO Robust Design Optimisation.

RTF Rational Transfer Function.

SORM Second-Order Reliability Method.

TAE Traditional Aeroelasticity.

TF Transfer Function.

UQ Uncertainty Quantification.

Chapter 1

Introduction

1.1 Background

Today's world is more reliant on the aviation industry than ever. Increased globalisation, e-commerce, and the emergence of new markets have been driving factors for the rapid growth of both cargo and passenger air transport movements. Between 2009 and 2018, worldwide annual passenger numbers on scheduled, commercial flights grew from 2.5 billion to 4.3 billion [1]. Likewise, total worldwide freight movement, measured in tonne-km, grew from 156 billion to 231 billion in the same period [1]. Despite its expeditious growth over just a single decade, it is widely believed that the aviation industry will continue to grow well into the future. Indeed, in a recent estimate by the International Civil Aviation Organisation (ICAO), annual passenger numbers are expected to increase to 10 billion by 2040 [2][1]. It is also thought likely that air cargo will observe a similar upward trend.

To accommodate for the growing demand in the aviation industry, large numbers of new aircraft must be manufactured. This is both to increase the total worldwide fleet and to replace outdated aircraft that are no longer economical to operate. Despite this, however, significant challenges to the long-term sustainability of the aviation industry remain. As the world becomes increasingly aware of the potentially irreversible effects of climate change, pressure is mounting on the industry to produce a new generation of aircraft that have less of a detrimental impact on the environment. For instance, the International Air Transport Association (IATA) has set ambitious targets of reducing CO_2 emissions from aircraft by 50%, relative to 2005 levels, by 2050 [3].

Improving sustainability in the aviation industry is not a straightforward task. Firstly, step changes in the research and development of new technologies are required across multiple engineering fields. This, of course, is both costly and resource intensive. Secondly, even if new technologies are found, strict legislation can impede their rapid deployment to real-world aircraft. This causes a significant lag between the state-of-the-art and current industrial practice. Finally, improvements must be economically beneficial to aircraft operators. The growing trend of low-cost carrier (LCC) models in the aviation sector means that airlines increasingly rely upon maximising operational efficiency and minimising costs [4].

Whilst research in novel technologies, such as alternative propulsion devices, continues, it is important in the meantime to improve existing designs. One of the main ways to do this is by increasing fuel efficiency. Indeed, this is one of the primary targets identified by IATA [3].

[1] This prediction was made before the Covid pandemic.

Fuel efficiency is typically increased in one of three ways: (i) by improving the efficiency of the engines, (ii) by reducing the total weight of the aircraft, or (iii) by reducing aerodynamic drag. Historically, efforts have been concentrated mainly on the first of these three points. However, developments in material science and manufacturing technology have allowed the final two points to be considered more extensively in recent years.

Today, high-strength, low-density composite materials are used in new aircraft and serve to replace the conventional aerospace grade aluminium that was previously relied upon. Such materials yield significant weight savings and allow more flexible structures to be manufactured. The Boeing 787 Dreamliner, for instance, uses carbon fibre reinforced plastic (CFRP) in its structure and delivers a 20% weight reduction compared to traditional aluminium designs [5]. CFRP is also used in the new Airbus A350 XWB, which claims to have the largest aircraft part ever made entirely from carbon fibre [6]. These aircraft are both shown in Fig. 1.1.

(a) 787 Dreamliner *(Photo by John McArthur on Unsplash)*

(b) Airbus A350 *(Photo by Ramapasha Laksono on Unsplash)*

Figure 1.1: Commercial aircraft utilising high specific strength composites.

Both the Boeing 787 and Airbus A350 XWB may be considered early forerunners in the growing trend of super-lightweight, flexible aircraft structures. Indeed, these designs have helped to fuel a growing push for the creation of even lighter aircraft that could potentially replace older designs that are not as efficient. Although the manufacturing technology for such designs is nearly at a sufficient level of maturity, there remains several challenges that impede their deployment in both commercial and military settings. One such challenge relates to the stability of these structures at high speeds.

Aerostructures are designed to withstand a variety of different loads. In addition to static loads, such as aerodynamic loads due to manoeuvres etc., aerostructures must be able to resist loads that are dynamic. These dynamic loads are a combination of elastic, inertial and aerodynamic forces. Generally speaking, dynamic loads are much more difficult to predict and accommodate for in the design of aircraft structures. This is due to their mutual interaction; the dynamic forces are coupled and affect one another. The study of this interaction forms a major area of study known as aeroelasticity and is today a crucial part of the aircraft design process.

A well-known result from the field of aeroelasticity is the prediction of a phenomenon known as flutter. Flutter is a self-excited, unstable oscillation that arises when the structure extracts energy from the airflow at a rate faster than it can dissipate. The lowest airspeed at which this phenomenon appears is known as the flutter speed and is a limit that prevents aircraft from travelling faster. If this limit is inadvertently broken, serious damage can be done to the structure; it can lead to large deformations that result in fatigue, damage, or even catastrophic structural failure. For this reason, strict aviation regulations require a substantial margin between the maximum speed at which an aircraft can legally operate and the flutter speed.

The Federal Aviation Administration (FAA), for example, requires a fifteen percent factor of safety, across all flight conditions [7].

With the development of lightweight, flexible aircraft, the avoidance of flutter is much more difficult. Reduced inertial and elastic forces mean that aerodynamic forces tend to dominate and hence flutter is more likely to arise at lower speeds. This limits the maximum operating speed associated with such designs and hence methods are required to drive the flutter speed higher.

Flutter can be avoided by making modifications to the structure during the early stages of design. Typically, the mass or stiffness distribution is altered so that the instability is suppressed and the flutter speed increases. Despite the method historically used, this approach to flutter suppression has some restrictive limitations. Firstly, designing to avoid flutter during the early stages of design requires accurate modelling of the structure, the aerodynamics, and their coupled interaction. In practice, this is not always possible. Numerical models will always contain some degree of inaccuracy, caused by restrictive physical assumptions, limitations in computational effort and time, and poorly estimated parameters in both the structural and aerodynamic models. In fact, as discussed by Pettit [8], there is a general mistrust in using numerical models to predict the flutter characteristics and therefore exclusively using this method to avoid flutter is widely considered inappropriate. Secondly, the modifications are not easily changed post manufacture as they are static. If after flight testing an aeroelastic instability is identified, it is necessary to re-evaluate the design and make modifications. This can incur significant cost and time delays to the project. Finally, such modifications can invoke additional weight and are typically counter to the most optimum design, in terms of efficiency. This means that the weight saving achieved by use of composite materials or other technologies can be offset by flutter suppression modifications.

Spurred on by the limitations of conventional, passive methods, an alternative solution to flutter suppression has come to fruition in recent years. Instead of making modifications to the structure itself, actuators located at one or more locations on the structure can be used to suppress flutter actively. Typically, feedback controllers are used, where displacement, velocity or acceleration data measured at several locations are used to determine the input to the actuators. In this way, the damping or natural frequency of the system can be changed so that the flutter speed is pushed higher. Such an approach is known as active flutter suppression (AFS).

Despite their benefits over traditional, passive solutions, industry has been slow to adopt active flutter suppression techniques. Indeed, there are very few applications in both commercial and military settings. One of the main reasons for this is the risk imposed by such methods. Should the controller fail, there must be multiple redundancy systems that prevent flutter from arising. Another reason is that AFS techniques rely on accurate numerical models. Normally, the controller is designed by first creating a numerical model of the system and then choosing a desired control objective that modifies the dynamics in some suitable manner. As discussed previously, numerical models invariably contain errors and hence the controller that is designed may not be suited to the real-world system. Moreover, a controller based on a single, deterministic model is not suitable in practice due to variability between different aircraft, which arises from manufacturing tolerances, damage, degradation, and other such sources.

Clearly, the standard approach to designing AFS systems inhibits their mainstream use in an industrial setting. One could try to improve the performance of the controller by using more accurate numerical models of both the structure and the aerodynamic. However, this is not always possible. Firstly, sophisticated aerodynamic models can require significant computational

power that is either not available or is too costly. Secondly, some uncertainties in the system are irreducible and hence cannot be avoided. Clearly, so long as conventional methods are used, one must always be prepared to accept some degree of uncertainty invoked by such methods.

In recent years, an alternative approach to AFS has been developed. Instead of creating numerical models of the structure and aerodynamics, data collected experimentally from the aeroservoelastic system can be used directly to design the controller. In this way, there is no need to construct a model of the structure or of the aerodynamics. Furthermore, it is not necessary to estimate key structural or aerodynamic parameters and a purely experimental approach is facilitated.

One particular experimental method that has received considerable attention in recent years is that of receptance-based control. Receptance-based control methods use receptance data, collected by means of standard modal analysis tests, to design an AFS controller. Receptance-based active flutter suppression techniques have been successfully applied to several aeroservoelastic systems. However, these applications have been reserved only to numerical systems and small wind-tunnel models. If these techniques are to be used in real-world, large-scale aircraft, further developments are needed to address challenges in both the theory and practicality of such techniques. One challenge in receptance-based AFS relates to restrictions in the current theory. As discussed previously, such techniques rely upon receptance data, which are collected through modal testing. In practice, experimental data can only be collected from the system when it is stable. This means that only data collected below the flutter speed can be used. This restriction limits the design of the controller and often leads to a sub-optimal AFS solution. Another challenge in receptance-based AFS concerns the robustness of such methods. Since experimental data is used, errors in noise, data fitting and other such sources play a significant role in the performance of the controller. Consequently, the dynamics of the system become uncertain and the flutter speed becomes non-deterministic. If the effects of these uncertainties can be quantified, it may be possible to predict the variability of the flutter speed and hence support a risk-based approach to control. Furthermore, this information could be used to influence the design of the controller and choose appropriate control strategies that balance maximising both the flutter speed and its robustness.

1.2 Aim & Objectives

The aim of this thesis is to explore, develop, and extend the use of experiment-based methods in the design and analysis of aeroservoelastic systems. Receptance-based techniques are considered and some of the current limitations that impede their use on large-scale aircraft are addressed. A focus is also given to the problem of uncertainty and its impact on the final AFS solution.

There are two primary objectives in this thesis. The first is to extend the theory of receptance-based control methods so that it is better tailored to aeroservoelastic systems. This includes the development of new strategies to overcome some of the limitations discussed earlier. The second objective is to consider how uncertainty quantification in aeroelastic systems can be achieved using receptance data. Various techniques, including both probabilistic and non-probabilistic approaches, will be used and their relative merits will be discussed. It is hoped that these techniques will yield new approaches to uncertainty quantification in aeroelastic systems and may provide an alternative, less-conservative approach to aircraft certification. It is important to note that these two objectives are not mutually exclusive; at several points this work considers the combination of both UQ and receptance-based control methodologies, and assesses its impact on the design of active flutter suppression systems.

1.3 Thesis Outline

This thesis is structured as follows:

- **Chapter 2** reviews key literature from the fields of aeroelasticity and active flutter suppression, uncertainty quantification in aeroelasticity, and receptance-based control. It provides a concise summary of the work completed to date in these areas, highlights the current limitations, and identifies areas of future research.

- **Chapter 3** presents a brief overview of some mathematical preliminaries that are used in the main matter of the thesis. It presents a formal definition of what is meant by the poles, mode shapes and important aeroelastic quantities, such as the flutter speed. This chapter is intended to be used as a reference for the work presented in later chapters.

- **Chapter 4** describes two aeroservoelastic models that are used throughout the thesis as systems on which to test the developed methods. The first model is numerical and is one that is widely used in the aeroelastic research community. The second is an experimental model that is housed in the University of Liverpool's subsonic wind tunnel facility. This chapter also describes the experimental setup for both receptance data collection and the implementation of a high-level, receptance-based controller.

- **Chapter 5** considers the development of receptance-based active flutter suppression techniques. Using the Receptance Method, an experiment-only approach to flutter suppression is presented and two new methodologies are developed, which address some of the practical limitations that impede real-world applications. Firstly, an optimisation method is developed, which allows the eigenvalues to be assigned in a way that, in theory, maximises the flutter speed. Secondly, an iterative control technique is developed, which enables receptance data to be collected at speeds at or above the open-loop flutter speed. In this way, the controller is no longer designed about reference points well away from the onset of flutter in the closed-loop system.

- **Chapter 6** considers the effect of uncertainty on the Receptance Method. Errors arising from poor rational transfer function fitting of measured frequency response function data are modelled and the effects that they have on the eigenstructure assignment are quantified by means of local sensitivity analysis. A global optimisation method is then used to minimise the effect of the uncertainty by reducing the spread of the poles of the system, either in terms of their real part, imaginary part, or a combination thereof.

- **Chapter 7** continues on the work of Chapter 6 to consider the uncertainty that arises from differences between nominal systems. Uncertainties in mass, stiffness and damping properties are modelled as stochastic structural modifications to a set of measured receptance data. The spread of the poles is then determined using a series of polynomial chaos (PC) expansions. This enables a probabilistic approach, whereby the mean and variance of the real and imaginary part of the poles can be obtained. Again, an optimisation method is used to minimise the effect of uncertainty and render the system more robust, according to a user-defined objective function.

- **Chapter 8** expands on the work developed in Chapters 6 and 7 to consider uncertainty in the flutter speed itself, rather than the real and imaginary parts of the poles. An experiment-based uncertainty quantification method is developed, which estimates the

probability of flutter arising at a given airspeed. This is done by projecting the characteristic equation of the uncertain system into the space corresponding to the random parameters. The resulting bisection of the parameter space is then integrated with respect to the probability density function of the random parameters to obtain the probability of flutter. To improve computation speed, a first order reliability method (FORM) is incorporated into the method and is the first known application of such a technique in receptance-based methods.

- Finally, **Chapter 9** presents the main conclusions of the thesis and highlights areas of future research.

1.4 Research Contributions & Publications

1.4.1 Research Contributions

The main contributions of this thesis are summarised below:

- The development of both a gain iteration technique and an optimisation strategy to extend the Receptance Method so that it is better suited for active flutter suppression.
- The development of a new approach to quantify the uncertainty that arises in the Receptance Method from erroneous rational transfer function fitting of frequency response function data.
- The implementation of polynomial chaos (PC) expansion theory in receptance-based techniques to facilitate a probabilistic-based, experimental approach to uncertainty quantification.
- The development of a stochastic structural modification method to model uncertainty arising between nominal systems.
- The formalisation of procedures to perform optimum eigenstructure assignment in the presence of uncertainty, using global optimisation techniques.
- The development of a new technique to identify the likelihood of flutter at a given airspeed, using only experimental frequency response function data.

1.4.2 Publications

Some of the work presented in this thesis has been published in the form of journal articles and conference papers. These are listed below:

Journal articles:

- L. J. Adamson, S. Fichera, B. Mokrani, and J. E. Mottershead, "Pole placement in uncertain dynamic systems by variance minimisation", *Mech. Syst. Signal Pr.*, vol. 127, pp. 290-305. 2019
- B. Mokrani, A. Batou, S. Fichera, L. Adamson, D. Alaluf, J. E. Mottershead, "The minimum norm multi-input multi-output Receptance Method for partial pole placement", *Mech. Syst. Signal Pr.*, vol. 129, pp. 437-448. 2019

- L. J. Adamson, S. Fichera, J. E. Mottershead, "Receptance-based robust eigenstructure assignment", *Mech. Syst. Signal Pr.*, vol. 140, 106697. 2020
- L. J. Adamson, S. Fichera, J. E. Mottershead, "Aeroelastic stability analysis using stochastic structural modifications", *J. Sound Vib.*, vol. 477, 115333. 2020

Conference papers:

- L. J. Adamson, S. Fichera, and J. E. Mottershead, "Minimisation of the Effect of Aleatory Uncertainties on Dynamic Systems by Active Control using the Method of Receptances," presented at ISMA 2018 International Conference of Noise and Vibration Engineering, Leuven, Belgium, Sep. 17-19, 2018.
- B. Mokrani, F. Palazzo, S. Fichera, L. J. Adamson, and J. E. Mottershead, "Multi-Input Multi-Output Aeroelastic Control using the Receptance Method," presented at ISMA 2018 International Conference of Noise and Vibration Engineering, Leuven, Belgium, Sep. 17-19, 2018.
- L. J. Adamson, S. Fichera, and J. E. Mottershead, "Probabilistic Control Optimization of Aeroservoelastic Systems with Uncertainty," presented at AIAA Scitech 2019 Forum, Jan. 7-11, 2019.
- L. J. Adamson, O. Braun, S. Fichera, and J. E. Mottershead, "Gain scheduling in receptance-based control of aeroelastic systems," presented at ISMA 2020 International Conference of Noise and Vibration Engineering, Sep. 7-9, 2020.

This page is intentionally left blank.

Chapter 2

Literature Review

This chapter reviews some of the key literature that is pertinent to the work presented in later chapters of this thesis. It is divided into three topics: (i) aeroelasticity and active flutter suppression (§2.1), (ii) uncertainty quantification in aeroelasticity (§2.2), and (iii) receptance-based control (§2.3). The subsequent sections provide a summary of each topic's foundations and state of the art.

2.1 Aeroelasticity & Active Flutter Suppression

This first section reviews literature from the fields of aeroelasticity and active flutter suppression (AFS). The main discussion points include: the historical origins of aeroelasticity, aeroservoelasticity, and flutter suppression; the principles and design of AFS systems; and the testing and implementation of AFS in real-world systems.

2.1.1 Aeroelasticity & Flutter

The First World War was a major driving factor in the design and development of powered flight. During this period, considerable research effort was devoted to the creation of new flight technologies, with the aim of creating faster, more agile aircraft. Early efforts saw great progress made in terms of aerodynamic efficiency and propulsion [9]. However, issues surrounding structural stability inhibited their further development.

Engineers were aware of stability issues in aircraft structures even before the First World War. Brewer, in the now classic paper "The Collapse of Monoplane Wings" [10], highlighted an instability mechanism arising due to the interaction of the structure and the airflow. A few years later, F. W. Lancaster described an unstable, self-excited oscillation arising in the tail of the Handley Page O/400 bomber and attributed this to the coupling of aerodynamic and elastic forces [11]. It is even thought that the Wright Brothers were aware of structural and aerodynamic force coupling effects in their fabled Wright Flyer [11].

In light of these early observations, and spurred on by the limitations observed during the war, research blossomed in the 1920s throughout both Europe and the United States as researchers tried to understand and predict these instabilities [12]. This early work is now contained in a field of science known formally as 'aeroelasticity'. Today, aeroelasticity is a wide-ranging field, with applications in aerospace [13], mechanical [14] and civil systems [15]. However, Dowell [16] gives a broad description of aeroelasticity as the study of "the mutual

interaction among inertial, elastic, and aerodynamic forces".

Aeroelasticity itself is commonly divided into two branches: (i) *static* aeroelasticity, and (ii) *dynamic* aeroelasticity. Static aeroelasticity considers the coupling of aerodynamic and elastic forces, and predicts phenomena such as divergence and control reversal. Dynamic aeroelasticity, on the other hand, also considers the effect of coupling from inertial forces, as well the aerodynamic and elastic forces, and predicts phenomena such as flutter and limit cycle oscillations (LCOs). Figure 2.1 illustrates the branches of aeroelasticity pictorially in what is now commonly known as the 'Collar diagram' [17]. Some of the results predicted by aeroelastic the-

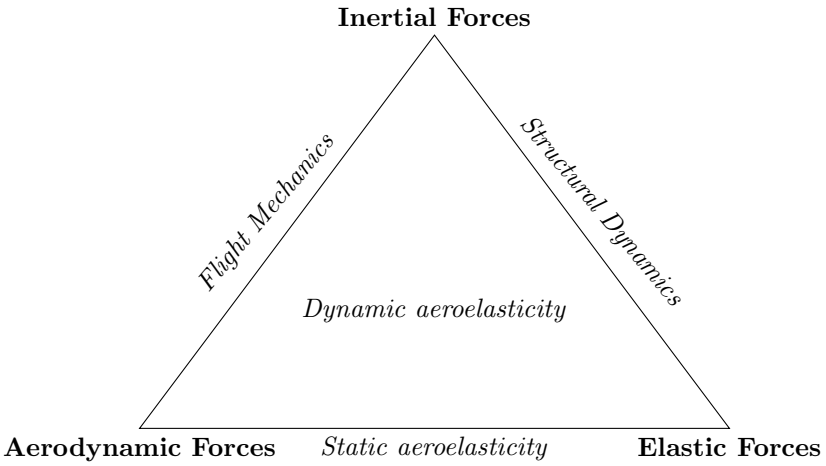

Figure 2.1: Collar's triangle of aeroelastic forces. *(Adapted from [17])*

ory can be used beneficially. For example, accurate predictions of wing load distributions can influence aircraft designs and improve their lift to drag ratio. However, aeroelastic theory also predicts detrimental phenomena that may arise within the desired flight envelope and hence forms an important aspect of the certification of modern aircraft.

One particularly dangerous aeroelastic phenomenon is known as flutter. Flutter is a self-excited, unstable oscillation that arises when the structure extracts more energy from the airflow than it can dissipate [18]. It is typically characterised by large structural deflections, which can cause damage, fatigue, or even complete catastrophic failure. Whether or not flutter arises depends on the external flow conditions. At low speeds, the aerodynamics have very little effect on the aircraft structure and thus the structural component of the dynamics tends to dominate. However, at high speeds, the influence of the aerodynamic force is comparable to that of the structure and thus can affect the dynamic greatly. In general, flutter is multi-parameter dependent and its presence can vary according to factors such as the Mach number, dynamic pressure, or Reynolds number. However, for subsonic aircraft it is common to describe the flutter characteristics by the so-called flutter speed. By definition, the flutter speed is the lowest freestream speed at which the system becomes dynamically unstable[1]. This will be defined more formally in Chapter 3.

Recent trends in aircraft design have seen the move towards lightweight, flexible aircraft structures and away from the more conventional rigid designs that were previously used. These new designs benefit from increased fuel and aerodynamic efficiency. However, they present a problem in terms of aeroelastic performance; they have lower inertial and elastic force contributions compared to their rigid counterparts and hence the aerodynamic forces tend to dominate more. For this reason, flutter can arise at relatively low speeds and can even exist inside the de-

[1]Note that this instability is associated with the structure, not the flight mechanics.

sired flight envelope. As a result, engineers must dedicate considerable effort designing solutions to avoid these instabilities. These solutions are collectively referred to as 'flutter suppression' methods.

2.1.2 Flutter Suppression Methods

There are two main approaches to flutter suppression: passive methods and active methods. These are both discussed here.

Passive Methods

Passive methods are based on the principle of using physical modifications to change the dynamic characteristics of the aerostructure. Passive methods typically involve: (i) changing the natural frequency of one or more modes, (ii) increasing the damping in the system, or (iii) a combination of both. Increasing the damping in the system is an obvious strategy for flutter suppression as it allows the structure to dissipate more kinetic energy per cycle of oscillation. Changing the natural frequencies, however, is a less obvious approach and is based on a feature frequently observed in aeroelastic systems. Prior to flutter itself, one or more modes in the system couple unfavourably. This manifests itself as a reduced frequency separation between successive modes, which decreases further as the freestream speed is increased. The idea behind passive frequency modification is to separate natural frequencies in the structural system so that the potential for coupling is reduced. In this way, the flutter speed is pushed higher.

Passive modifications are usually implemented in two ways. The first is by changing the stiffness parameters associated with one or more modes. This can involve modifying the materials used in the structure or the design of the structural members, such as beams or spars. The second approach is based on adjusting the mass distribution in the structure, also known as 'mass balancing'. This can also involve the alteration of structural components but can additionally require the removal or addition of new structural members, with the aim of shifting the mass distribution forwards or aft of a required point.

Historically, passive modification has been the most popular flutter suppression method used in practice. Indeed, this was the approach used by Lancaster to solve the issue of control surface flutter in the O/400 [11]. Even today, passive modification is used as a guiding principle for flutter avoidance. However, the application of mass balancing and stiffness modification is now usually more involved. These techniques were originally designed for systems with a small number of degrees-of-freedom [19]. Today, highly-flexible aircraft can exhibit a very large number of degrees-of-freedom and there is almost certainly coupling between more than just two modes. Thus, choosing which frequency modes to separate and the effect this has on the flutter speed is much more difficult.

Where previously used as a post manufacture fix, passive measures are now more commonly incorporated into the aircraft structure in the very early stages of design. This is done by constructing a model of the aeroelastic system and analysing areas where the design can be improved. Whilst avoiding costly post-manufacture fixes, this approach has two main drawbacks. The first stems from the use of numerical models. In practice, it is extremely difficult to obtain a reliable model of aeroelastic systems and thus one cannot be sure that the mass balancing and stiffness modification methods will work as anticipated. Secondly, these modifications frequently induce extra mass into the structure and hence can offset the performance gains made by the flexible structure in the first place.

Active Methods

In light of the restrictions imposed by passive measures, a new approach for flutter suppression has been developed in recent years. This new approach, known as active flutter suppression, is an application of active control technology and has seen a growth of interest in recent years.

The fundamental principle of active methods is to use a series of inputs, outputs, and a controller to modify the dynamics of the system. This is usually done by means of feedback control; however, other methods, such as feed-forward control, have also been used [20]. Unlike passive modifications, the relationship between the inputs and outputs can take any form and it is not restricted by physical relationships; indeed, it is determined by a theoretically arbitrary control law, which is discussed later.

The idea of using active control technology to modify the aeroelastic behaviour of a structure has been discussed since the early 1950s. In the fourteenth Wright Brother's lecture, Bollay [21] indicated that aeroelastic control could be used to enforce aircraft stability and for gust alleviation purposes. Since then, active control in aeroelastic applications has become a significant area of research, with applications in both experimental and real-world aircraft. This area is now known as active flutter suppression (AFS).

The main advantage of AFS is its adaptability. Although the actuators and sensors are generally fixed, it is usually straightforward to change the control law in the physical system and hence change the objective or performance of the AFS system. Moreover, AFS systems are capable of changing according to the environment in which they operate. For example, the controller may be programmed to use more 'effort' at higher speeds. Also, the controller may have different objectives at different flight conditions. Both of these examples form the principle of gain scheduling, which is discussed later.

2.1.3 AFS System Architecture

AFS systems are generally comprised of three main components: (i) the actuators, (ii) the sensors, and (iii) the controller. Figure 2.2 illustrates this pictorially.

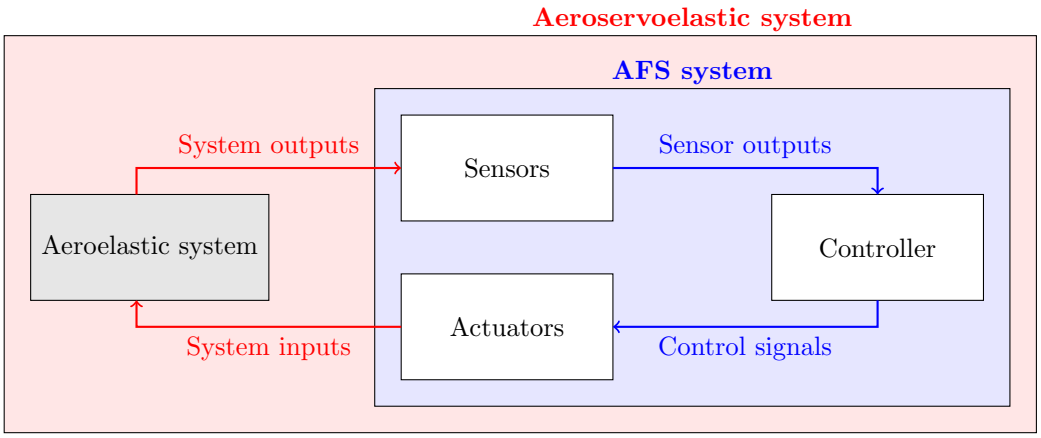

Figure 2.2: AFS system architecture.

It is common to describe the complete system, shown in red, as the complete '*aeroservoelastic* system'. This terminology is used hereinafter.

Actuators

The purpose of the actuators is to convert a control signal into a physical input to the aeroelastic system. Typically, the inputs to the system are forces that are purposely designed to modify the dynamics in some favourable manner. By far, the most common type of actuator used for AFS is the control surface. Control surfaces are panels on the structure that may be deflected, thus changing the shape of the lifting surface. This change in shape alters the aerodynamic configuration of the aircraft and invokes a net change in the aerodynamic force being applied. Figure 2.3 shows a typical example of control surfaces on a commercial aircraft wing.

Figure 2.3: Typical control surfaces on an aircraft wing. *(Photo by Khanh Duy Nguyen on Unsplash)*

Control surfaces come in a variety of different forms, including: ailerons, spoilers, flaps, flaperons, and trim devices. However, in AFS applications it is most common to use ailerons or flaperons. This is due to their high responsiveness and bandwidth. Generally speaking, the other devices are too large and have low response times that are not feasible to use for AFS.

The main advantage of using control surfaces for actuation is that they are readily available. Control surfaces are already used in aircraft wings for the purposes of flight control and thus little to no physical modifications need to be made to the structural design. Indeed, it is only necessary to change the control software associated with each control surface. It is even possible to overlay AFS systems with existing control systems so that they both operate simultaneously.

Control surfaces are the most common actuator used for AFS systems. However, other types of actuation equipment have been used too. These include: acoustic excitations [22], strain-based actuation [23], piezoelectric actuation [24], and flow control [25]. Another approach is based on morphing. This is where the structure is able to adapt its shape either across its chord or span. Such an approach has been demonstrated already in some simple experimental applications, such as that of Fichera et al. [26].

Regardless of the type used, it is important that the actuators are placed suitably to maximise their effectiveness. For instance, placing a control surface very close to the wing root is unlikely to have any significant control authority in either the bending or twisting modes of the structure. In general, the location of the actuators is usually a predetermined constant and is based on the location of the existing flight control devices. However, there are techniques to place the actuators optimally in the system [27]. Moreover, studies have considered approaches where the AFS system and actuator locations are integrated into the early stages of aircraft design [28].

Usually, the actuators are not controlled directly; instead, there is a low-level control system,

such as a PID, which is used to regulate the output from the actuator. This low-level controller takes into account the dynamics of the actuator itself and can mitigate its effect. This is considered in more detail later.

Sensors

The purpose of the sensing equipment is to measure one or more outputs from the system and to convert this data into signals that may be used by the control system. Most frequently, the outputs are either displacement or acceleration data. These data are measured at several points on the structure and are used in the control law to determine the input that feeds back to the system.

The device used to measure the outputs varies according to the specific application. In the case of acceleration data, accelerometers can be used and placed inside the wing section [29]. For displacement data, devices such as laser sensors may be used. Acceleration and displacement information appears to be the most widely used sensor data. However, other approaches, such as fibre optic strain sensors and stagnation point sensors have also been considered as potentially feasible approaches [30].

In many control laws, it is necessary to use displacement or velocity feedback. Therefore, if accelerometers are used, it is often required to perform real-time integration of the sensor signals. Whilst possible, such an approach is susceptible to noise amplification or integration drift. This is of course not an issue when using displacement data. However, displacement data will also have to be differentiated and thus smoothing filters are typically required to prevent spikes in the corresponding velocity and acceleration signals. Moreover, displacement data has the problem that it has to be measured relative to a fixed point, which is difficult to do on a moving aircraft.

As with the actuators, the placement of the sensors in an important aspect in the design of AFS systems. Inappropriate sensor locations can lead to sub-optimal controllers and can mean that more sensors are used than are really required. For example, if a sensor is placed in a location where the displacement is small, e.g. a vibration node point, little information will be obtained from that sensor and thus it is wasteful. Moreover, this information will likely be highly dominated by measurement noise.

Controller

The final element of an AFS system is the controller. The purpose of the controller is to determine the control outputs, which lead to the actuators, based on data measured by the sensors. The design of the controller is itself a major task and is thus considered separately in §2.1.5.

2.1.4 Aeroservoelastic Modelling

Before the AFS controller can be designed, it is usually necessary to construct a numerical model of the aeroservoelastic system. This is because the model is normally used to guide the choice of control law.

Aeroservoelastic systems are comprised of three main components: (i) the structure, (ii) the aerodynamics, and (iii) the actuators. This is shown diagrammatically in Fig. 2.4. These three components are usually modelled independently and then joined together under a single, unified system. This section briefly explores how each of these components is modelled and their limitations in the presence of uncertainty.

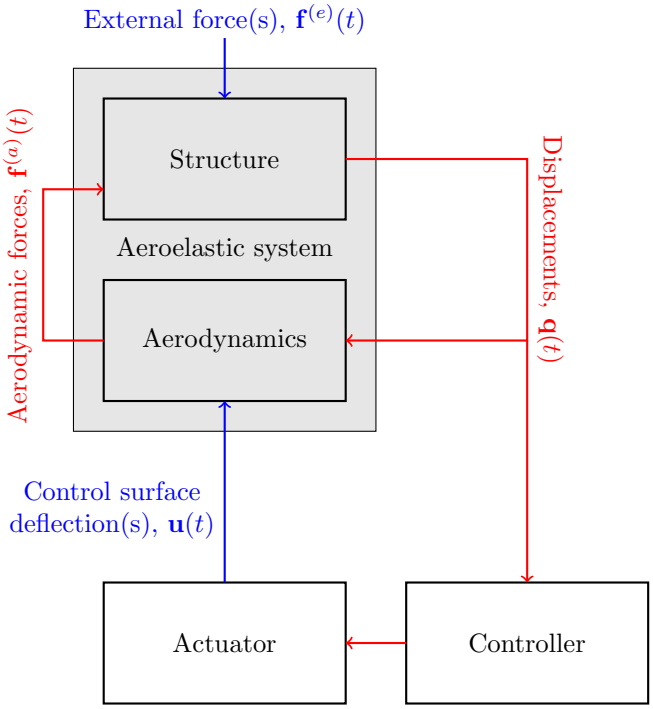

Figure 2.4: Architecture of an aeroservoelastic model.

Structural Modelling

The first subsystem that is modelled is usually the structure. The purpose of the structural model is to relate the displacement at one or more points on the structure to any external forces or moments that may be applied. In other words, to find a mathematical expression of the form

$$\mathbf{q} = g(\mathbf{f}), \tag{2.1}$$

where $\mathbf{q}$ is a vector of arbitrary displacements on the structure, and $\mathbf{f}$ is a vector of external forces or moments. In principle, this relationship can be found from first principles by separately modelling each of the components in the structure. This involves constructing a partial differential equation (PDE) for each component, such as a beam or plate, and then joining them all together under a single, coupled model. However, this approach is impractical due to the high degree of complexity involved. Instead, it is common to approximate the structural dynamics using discretisation techniques. These discretisation techniques work by reducing the system to a small number of masses, each of which are associated with a degree-of-freedom. These degrees-of-freedom are then each connected to one another through a series of spring and damping elements.

For linear systems, the general discretised structural model is of the form

$$\mathbf{M}\ddot{\mathbf{q}} + \mathbf{C}\dot{\mathbf{q}} + \mathbf{K}\mathbf{q} = \mathbf{f}, \tag{2.2}$$

where $\mathbf{M}, \mathbf{C}, \mathbf{K}$ are the mass, damping, and stiffness matrices receptively; $\mathbf{q}$ is the reduced degrees-of-freedom vector associated with the discrete masses; and $\mathbf{f}$ is the vector of generalised forces [2]. The key challenges of structural modelling are: (i) to determine the number of degrees of freedom that are necessary, and (ii) to find suitable mass, stiffness and damping matrices.

[2] At this point it is important to stress that the vector $\mathbf{f}$ in the structural model is left in a general form and does not consider how these forces arise in the first place.

The number of degrees-of-freedom that are selected is an intricate balance of model accuracy and computation time. In the early days of aeroelasticity, it was common to approximate aircraft wing structures using only two-degrees-of-freedom. These degrees-of-freedom were normally associated with the first bending and torsional modes[3]. Such models are now referred to as 'binary aeroelastic systems' and are used even today as simple systems on which to verify AFS controllers. Binary models are advantageous in that they lend themselves well to simple eigenvalue analyses due to the low order of the model. Moreover, they can be constructed simply by direct application of Newton's laws. However, they only work well if the wing has two modes in the frequency range of flutter. If this is not the case, the wing can posses additional modes that lie close to the frequency range of the mode associated with flutter. In such cases, it will most likely be necessary to increase the number of degrees-of-freedom and thus increase the complexity of the model.

For simple systems, the mass, stiffness and damping matrices can be obtained through direct methods, such as Lagrangian mechanics. However, given the complexity of modern aircraft structures, it is now far more common to use computational methods, such as finite element analysis (FEA). Indeed, this is the main approach that is used in industry. Regardless of the method used, it is often difficult to obtain highly accurate parameters in the mass, stiffness and damping matrices. This is because the parameters are often selected from historical information or manufacturing data sheets. This is further discussed in §2.2.

Aerodynamic Modelling

After the model of the structure has been created, it is then possible to model the aerodynamics. The aim of the aerodynamic model is to relate the forces on the structure to the instantaneous displacements, velocities, and accelerations at the reduced degrees-of-freedom. In other words, to find a function of the form

$$\mathbf{f} = h(\mathbf{q}, \dot{\mathbf{q}}, \ddot{\mathbf{q}}). \tag{2.3}$$

Doing this creates a coupled interaction between the aerodynamic and structural model. This may be visualised as a closed-loop feedback, as shown in Fig. 2.4.

There are a plethora of different aerodynamic models that may be used in aeroservoelastic applications; the main differences between them rests on the fundamental assumptions that are made about the flow. Arguably the simplest type of aerodynamic model is that of the steady flow model. In this model, the aerodynamic forces are assumed to be time-invariant. That is, the aerodynamic forces are a function of only the instantaneous positions in each degree-of-freedom. Although conceptually straightforward and easy to implement, this model is typically inadequate for dynamic aeroelasticity problems. This is due to the fact that unsteady aerodynamic effects are neglected and hence estimates of the aerodynamic forces and moments are erroneous.

An alternative aerodynamic model, which overcomes some of the limitations imposed by the steady flow assumption, is the quasi-steady model. As before, the aerodynamic forces are not written explicitly as a function of time. However, in contrast to the steady model, they are also a function of the instantaneous velocities. Indeed, it is assumed that the behaviour of the aerofoil at any instant of time is equivalent to the same aerofoil with the instantaneous displacements and velocities [31]. In other words, it is assumed that there are no frequency dependent effects [31]. In general, the quasi-steady model only works well when the relative degree of unsteadiness in the airflow is sufficiently low.

[3]However, other degrees-of-freedom, such as flapping modes [31], were also considered

One way in which to quantify the degree of unsteadiness in an aeroelastic system is the reduced frequency parameter. The reduced frequency parameter is a dimensionless quantity defined by

$$\kappa = \frac{\omega b}{v}, \tag{2.4}$$

where ω is the frequency of oscillation of the aerofoil, b is the semi-chord length, and v is the freestream speed. Agreed values of κ for which the quasi-steady model is acceptable vary by source and by the degree of error that one wishes to accept. However, in general, the larger the reduced frequency the less applicable the quasi-steady model is.

In cases where the degree of unsteadiness is high, it is inappropriate to use the steady or quasi-steady aerodynamic models. Instead, it is necessary to use models that encapsulate the full effect of the unsteadiness. One such popular model is known as the Theordorsen model of aerodynamic lift. This model, first developed in 1949 [32], uses a potential flow approach to model the unsteady aerodynamic forces acting on a thin, symmetric aerofoil. The original formulation of the Theodorsen method was developed for binary aeroelastic systems. However, its general principles have since been extended to consider more complex aeroelastic systems. One such extension is the doublet-lattice method [33], which works on the principle of dividing a general wing into multiple plate components and then calculating the aerodynamic forces and moments arising on each plate.

Even though it captures the unsteady effects of the aerodynamics, the Theodorsen method still relies on numerous restrictive assumptions. Firstly, it assumes that the flow is inviscid and thus boundary layer effects are negligible. Secondly, it imposes the restriction that the flow is irrotational, which is something that is known not to be true. Finally, it assumes that the flow is incompressible and thus density variations in the flow can be ignored. Some methods have been developed to overcome some of these limitations. For example, piston theory [34] is now a popular approach for modelling aeroelastic forces when compressibility effects are to be considered. However, even these models have fundamental limitations in their applicability.

As with the structure, modelling of the aerodynamics can now be done through computational methods, such as computational fluid dynamics (CFD). Usually, the aim of the computational methods is to extract the aerodynamic influence coefficients to determine the aerodynamic loading on the structure under any arbitrary deflection. Whilst these models accurately capture the physics of the model better, as they utilise the full Navier-Stokes equations, they come at the penalty of increase model complexity. This is especially problematic for the purposes of control and often model-reduction techniques are required. Moreover, construction of these models still relies on user-entered flow parameters, which are estimated and thus can introduce errors into the model.

Actuator Modelling

The final stage of creating the numerical model is to model the actuators. The purpose of an actuator model is to relate the dynamics between the desired control input and the observed control input. In other words, to adjust the control input to account for any dynamic behaviour that may be present between itself and the controller output.

Actuation systems are often comprised of multiple, cascaded electro-mechanical subsystems that each require complex modelling in order to accurately capture their dynamic behaviour. Control surfaces, for example, have dynamics associated with the hydraulics and mechanical connections. Moreover, the inertia of the control surfaces themselves means that the response is never instantaneous; there is always some lag between the desired and actual control surface

deflection angle.

Of course, each electro-mechanical device can be modelled independently and then joined together in the final numerical model. However, doing this can add a high degree of complexity that requires the addition of multiple state variables (see Chapter 4) associated with the dynamics of actuator. In turn, this increases the size of the eigenvalue problem to be solved. Another approach is to instead use an approximation model based on a second-order filter. For control surfaces, this means using a model of the form

$$\ddot{\beta} + 2\zeta\omega_n\dot{\beta} + \omega_n^2\beta = \omega_n^2\beta_d, \tag{2.5}$$

where β is the actual control surface deflection and β_d is the desired control surface deflection, i.e. the output from the control law. Whilst this model does not encapsulate the full dynamics of the actuators, it is often sufficient as it can capture dynamic effects such as phase lags and overshooting. This is the approach that has been used by numerous authors [35].

In some special circumstances, it may not be necessary to model the dynamics of the actuator at all. For example, if a low-level controller, such as a PID, is used between the desired and actual input, the lag between the desired input and output may be negligibly small. This, however, must be assessed on a case-by-case basis with each experimental model. An example of this is shown in Chapter 4.

Model Coupling

The final stage of numerical modelling is to join the aerodynamic, structural and actuator models together as a unified system. The most common way to do this is to cast each of these sub-models into a state-space form and then couple them together to create a single state-space model. This approach is discussed in Chapters 3 and 4.

2.1.5 Control System Design

Once a model of the aeroservoelastic system has been created, the controller itself can be designed. The main challenge at this point is to choose and implement a control law; that is, a mathematical expression relating the inputs to one or more of the measured outputs. There are numerous methods to do this, each with their own advantages and disadvantages. By convention, these methods are divided into two broad categories: (i) physics-based methods, and (ii) mathematical control methods. This is shown pictorially in Fig. 2.5. This section discusses control system design and provides a very brief overview of some important control laws that have been used in AFS applications.

Physics-Based Methods

The early days of AFS saw great interest in physics-based methods [36]. The fundamental principle of these methods is to design the controller based on physical insights obtained from the numerical model of the system. These physical insights can include key parameters from the structural dynamics, the aerodynamics, or both.

One popular physics-based method is known as ‘the concept of aerodynamic energy’. This method treats the problem of AFS from an energy point of view; the work done by the system on its surroundings per oscillation cycle is expressed as an eigenvalue problem [37]. The main aim of this technique is to design a control law so that all energy-based eigenvalues are positive, thereby ensuring positive work is done by the system to the surroundings. In doing so, stability

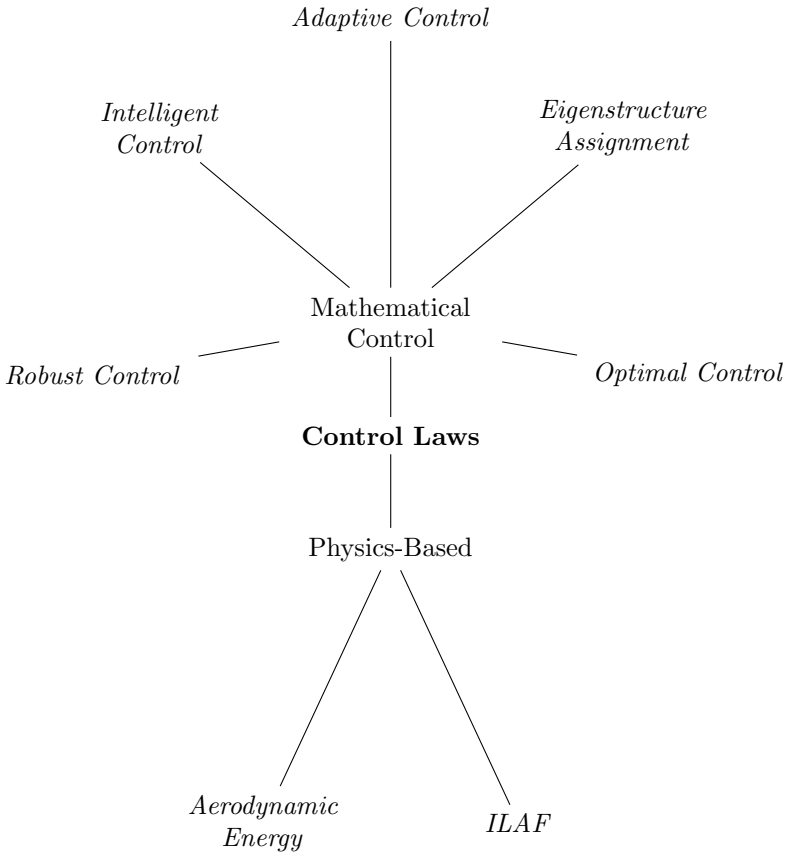

Figure 2.5: A selection of different control laws used for AFS.

is enforced and hence flutter is pushed to a higher speed. Aerodynamic energy methods appear to have been most popular during the 1980s due to the work of Nissim. However, they have regained some interest more recently [38], [39].

Another physics-based method that has gained some notoriety is known as 'identically located accelerometers and feedback' (ILAF). ILAF was first developed by NASA for the purposes of modal suppression in the XB-70 military aircraft [40]. The main principle of ILAF is to locate the sensing equipment, in this case accelerometers, and the force arising from the control system at the same physical point. A control law is then designed to enforce stability of the system [41]. The control law for ILAF uses real-time integration of the acceleration data to obtain the velocity at one or more points on the structure. This velocity information is then used to create a feedback loop, where the controller applies a proportional but opposite force to the velocity in a given mode. This invokes an active damping modification to the system.

Overall, physics-based methods are advantageous in that they offer meaningful insight into how the principle of active control works. Indeed, in the case of ILAF, one is able to make a direct analogy between the effect of the controller and traditional, passive damping measures. However, as noted by Livne [36], these methods appear to have waned in popularity over time; recent literature shows that mathematical-based methods prevail by a significant margin. One possible reason for this is the higher degree of generality that mathematical control methods afford. Although mathematical-based methods still rely upon numerical models of the aeroelastic system, they do not require deep understanding of the actual physical processes arising in the model and thus, in principle, allow the modelling and control of the aeroservoelastic system to be done separately.

Mathematical Control Methods

Leading on from the surge in popularity of modern control theory in the late 1960s and early 1970s, mathematical-based control methods have been applied extensively to aeroservoelastic systems in recent years. Indeed, these approaches have become the most widely used in AFS applications and there is a vast array of literature that demonstrate both numerical and experimental implementations [42].

The earliest work in mathematical-based AFS control laws considered static, model-based approaches. This is where the control law is designed about a single reference point, which is taken from a deterministic numerical model of the system. One example of a static model approach is linear-quadratic-regulator (LQR) [43] control. LQR is an optimal control approach where a feedback controller is designed to minimise a quadratic performance index, which is chosen according to a desired control objective. The performance index usually includes a weighted sum of the states, inputs, and their coupled effect. In aeroelastic applications, the purpose of the method is to find an optimum balance of ensuring overall stability whilst the inputs, such as control surface deflections, do not become too large. Lazarrus et al. [23] considered LQR control of a strain-actuated pitch-plunge numerical aeroelastic model. Niel et al. [44] considered LQR control applied for the purposes of stall flutter suppression, again on a numerical pitch-plunge model.

Another conventional mathematical-based control approach is based on eigenstructure assignment. Eigenstructure assignment is the principle of designing a control law to achieve an assigned set of closed-loop eigenvalues and eigenvectors. In aeroelastic systems, this typically involves pushing the eigenvalues further into the left hand side of the complex plane in order to ensure greater system stability. For multiple-input systems, the eigenvectors may be chosen so that either robustness, low control effort, or a combination thereof is achieved. There have been numerous applications of eigenstructure assignment in aeroelastic systems; however, these will be considered later in §2.3.

Conventional control design methods, such as LQR or eigenstructure assignment, are normally designed from a single reference numerical system. Whilst conceptually straightforward, using only one fixed numerical model is problematic in that errors in the numerical model are not considered. For this reason, there have been a number of studies that attempt to address uncertainty in the design of the control law. These methods are known as 'robust control' methods. The central idea of robust control is to incorporate a model for uncertainty into the nominal, reference aeroservoelastic system. Using this model, a controller that is robust across all possible conditions of the uncertainty model is then designed. Some robust control methods that have been applied to aeroservoelastic systems include: μ synthesis [45] and $\mathcal{H}_\infty$ control [46]. Robust control methods normally model the uncertainty in structural and aerodynamic parameters by means of intervals. However, some limited studies have considered probabilistic approaches, where the parameters are modelled as random variables [47].

Another approach to considering uncertainty in AFS is to incorporate adaptivity into the control law. These approaches, known generally as 'adaptive control', consider variation in the structural and aerodynamic parameters of the numerical model and adjust the control law accordingly so that the desired control objective is still achieved. Adaptive control is not only useful to account for uncertainty in the numerical model but also to consider real-world, physical changes. These physical changes may arise from things such as variable fuel loading, or detachable external stores, such as missiles. Literature in adaptive control of aeroelastic systems is vast; however, some key papers include: Xing and Singh [48] and Reddy et al. [49].

Whilst robust and adaptive control methods explicitly consider the effect of uncertainties in the design of the control law, they are still reliant on a numerical model. Moreover, there is no definitive guarantee that the uncertainty model will capture the behaviour of the true system. For this reason, there has been a recent growth of interest in alternative control methods, such as experiment-based AFS and intelligent control.

Experiment-based AFS techniques do away with numerical models entirely and instead design the control law using only data collected experimentally from the real-world system. Of course, this thesis is concerned with receptance-based approaches, which may be considered a subclass of experimental-based methods. Receptance-based methods are considered separately in §2.3.

So-called 'intelligent control' methods have also been used in AFS applications. Intelligent control methods rely upon techniques drawn from machine learning, and avoid the conventional approaches where numerical models of the aeroservoelastic system are constructed from first principles. One approach has been based on neural-based control, where neutral networks are used to either: (i) construct a model of the aeroelastic system, (ii) to control it, or (iii) both of the above [50], [51]. Other approaches include fuzzy logic control [52] and radial basis function methods [53].

Due to space limitations, it is impossible to review all of the different mathematical control methods in great detail. However, one may find a more comprehensive review in the papers by Livne [36], Ghiringhelli et al. [54], and Librescu and Marzocca [42].

2.1.6 AFS Testing and Implementation

Once the AFS system has been designed, it is crucial to perform testing to ensure that: (i) the control objective is achieved, and (ii) the system is sufficiently robust across all expected flight conditions. Today, there are two key ways to test AFS systems; wind-tunnel testing and real-world flight testing. These two types of tests form a crucial element of validation and verification of AFS systems and are thus part of modern certification requirements. This section gives a brief review of AFS wind-tunnel testing and the challenges associated with it. It also provides a brief overview of some real-world applications and the future of AFS technology.

Wind-Tunnel Testing

Once the numerical modelling has been completed, it is usual to perform wind-tunnel testing of the final AFS system. Wind-tunnel testing typically involves applying the AFS controller to a scaled model of the final system and then verifying the stability of both the system and the controller under various simulated flight conditions. Of course, due to physical limitations, the wind-tunnel is usually unable to reconstruct the exact conditions expected in the flight envelope of the final aircraft. However, a dynamically equivalent test can be performed by suitably scaling the wind-tunnel model and wind-tunnel conditions.

Wind-tunnel testing can be conducted in a number of different ways, depending on the type of information that is to be obtained. In AFS applications, testing usually consists of exciting the system with the controller active and observing some measurable output, such as readings from accelerometers or laser displacement sensors. The two most common ways of exciting the system during testing include shaker actuation and control surface actuation. Shaker activation is where an electro-mechanical or inertial shaker is used to impart a force of the structure. These shakers are placed at strategic locations so that a sufficient level of actuation is achieved in the structure. These shakers are usually equipped with transducers at the connection points so

that the imparted force can be measured in real-time. Control surface actuation, on the other hand, is where one or more control surfaces are used to change the aerodynamic configuration of the system and thus create an aerodynamic disturbance. Unlike the shakers, control surfaces are already built into the system and thus require less physical setup in the wind-tunnel.

Once the wind-tunnel testing has been completed, post-processing of the data can begin. For linear systems, one of the most common approaches is to consider the frequency domain information obtained by the measured sensor outputs. This allows the frequency response function data between the measured inputs and outputs to be extracted. In turn, the eigenvalues of the system at different flight conditions can be found too. These eigenvalues are then used to determine the margin of stability across the full range of aerodynamic variables.

Despite its necessity, wind-tunnel testing does have several restrictions. One of the main issues is how to *safely* determine the new flutter speed with the controller active. To determine the exact flutter speed experimentally requires demonstrating instability at a given airspeed. However, this is impractical as the test model or wind-tunnel may be destroyed in the process. This is especially true if the flutter mechanism itself is sharp, i.e. changes rapidly over a small range of airspeeds. To overcome this problem, methods that predict the flutter speed using sub-critical flight test data, i.e. below the flutter speed, have been developed. These include the work of Zimmerman and Weissenburger [55], Lind and Brenner [56], and Cooper et al. [57]. However, these methods are usually restrictive and impose restrictive assumptions on the nature of the experimental system. The question of how to accurately determine the flutter speed experimentally remains an open problem.

Real-World Implementations

The application of active flutter suppression to real-world aircraft has thus far been mainly limited to experimental and research settings. However, it has also been applied to a very limited number of civil and military aircraft too.

One military aircraft that is known to use AFS technology is the F-16. The F-16 uses accelerometer feedback to actuate flaperons, which are located on both wings. In the paper by Peloubet et al. [58], the operating principles of the F-16 AFS control law are given and experimental flight test data are shown. Furthermore, issues surrounding uncertainty and fail-safe systems are discussed; the authors discuss the use of the technology when of the control surface fails mid-operation.

As pointed out earlier, one of the main issues with designing AFS systems for military aircraft is that they must be highly adaptable. Military aircraft are designed to carry jettison-able loads, such as missiles, or other such weapons. Consequently, the AFS system must be able to respond appropriately to sudden changes in inertia and load distribution, without any compromise to the safety of the aircraft.

A commercial aircraft that is known to implement some type of AFS technology is the 747-8F. Due to confidentiality restrictions, little is known about the precise nature of the AFS system. However, it is suggested by Livne [36] that modal suppression is used to mitigate an instability that arises at the upper end of the flight envelope. Moreover, it has been speculated that the instability itself is restricted by an LCO and thus, even if the AFS system fails, the aircraft does not immediately suffer from catastrophic structural damage.

Despite the few details known about its implementation, the fact that the 747-8F has been permitted by regulation authorities to use AFS systems is an important milestone. Although restrictive, changes to existing aeroelastic safety regulations demonstrate some willingness in

industry and the wider aerospace community to adopt this technology [59]. With further progress and maturity in the field, AFS may become commonplace in the future.

2.2 Uncertainty Quantification in Aeroelasticity

Recent advances in computational speed allow sophisticated aeroelastic analyses to be performed on a wide range of systems. Even today, techniques to predict both linear and non-linear aeroelastic phenomena are available in popular finite element analysis (FEA) software, such as NASTRAN [60]. Despite this, however, there is still a general mistrust in industry in using numerical models to predict the exact conditions under which aeroelastic phenomena arise [8]. Indeed, aircraft manufacturers primarily use numerical aeroelastic analysis during the early stages of development to merely *estimate* key aeroelastic characteristics, such as the flutter speed. Moreover, validation and certification of aeroelastic performance does not usually rely on numerical analysis alone and instead usually relies on a mixture of wind-tunnel and real-world flight testing. One of the reasons for this is that it is difficult to construct highly accurate models of aeroelastic systems. This is because it is tricky to model the interactions between both the fluid and the structure. Furthermore, it is impractical to know exact values of key parameters in both the aerodynamic and structural models.

It is common in industry to predict aeroelastic phenomena using deterministic numerical models. These models yield static solutions to important aeroelastic quantities. The structural and aerodynamic parameters used in these deterministic models are fixed and usually must be selected from manufacturing data sheets or historical information. Conventionally, the most likely values of the parameters are selected so that the results of the deterministic analysis correspond to the most likely behaviour of the aeroelastic system. Whilst conceptually straightforward, the main problem with this approach, however, is that it ignores the variability in the response behaviour. Indeed, a high degree of uncertainty in the model parameters may lead to a high variance in the key aeroelastic quantities and hence a singular estimate is potentially dangerous to use. For this reason, it has been argued in recent years that non-deterministic methods should instead be used to predict aeroelastic behaviour. Non-deterministic methods do not attempt to give a single solution to key aeroelastic variables. Instead, they quantify a range of values, which accounts for the uncertainties that were previously discussed.

The science of the non-deterministic methods described above is commonly referred to as 'uncertainty quantification' (UQ) and the application of these methods to aeroelastic systems is a growing area of research known as 'uncertainty quantification (UQ) in aeroelasticity'. This section reviews key literature from UQ in aeroelasticity; it considers what uncertainty quantification is, its usefulness, and its applications.

2.2.1 The Principles of Uncertainty Quantification

This first section discusses what UQ is and its usefulness in aeroservoelastic applications.

What is Uncertainty Quantification?

Uncertainty quantification (UQ) can be thought of as "the coming together of probability theory and statistical practice with the real world" [61]. The primary aim of UQ is replace deterministic methods with approaches that explicitly considered variability in numerical models or experimental data. When applied to aeroelastic systems, UQ gives a metric to define likely and

unlikely behaviour, allows more uncertainty conscious design choices to be made, and permits qualitative risk assessment.

Uncertainty quantification is commonly divided into two main areas: (i) *forward* uncertainty propagation, and (ii) *inverse* uncertainty quantification. Forward uncertainty propagation concerns the prediction of the variability in one or more variables of interest, otherwise known as response variables, when they are functions of one or more uncertain parameters. This is done by propagating the uncertainty through the numerical system and observing the behaviour of the response variables. The precise nature of how the propagation is performed depends on the techniques that is chosen. However, figure 2.6 illustrates the general principles of forward uncertainty propagation. As shown, there is a black box system between the uncertain parameters and the response variable. The aim is to construct a model of the black box, i.e. the mapping from the inputs to the outputs, and to use this to predict the nominal value and variation of each response variable.

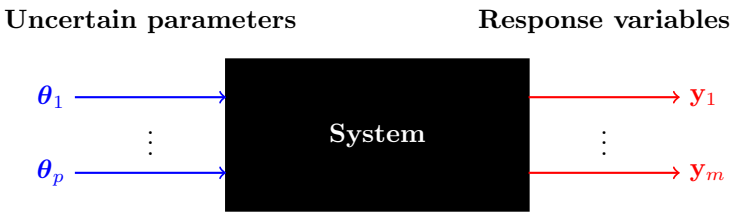

Figure 2.6: Forward uncertainty quantification.

The effect of the uncertain parameters on each response variable may be visualised graphically, as shown in Fig. 2.7. This type of graph is commonly referred to as the response surface and is used to predict the behaviour of the response variable. The response surface itself originates from the model of the system; indeed, it is just a visualisation of the mapping between the uncertain variables and the response variable. However, obtaining this response curve is often computationally expensive and instead it is frequently approximated through various techniques. One technique is known as surrogate modelling and will be considered later.

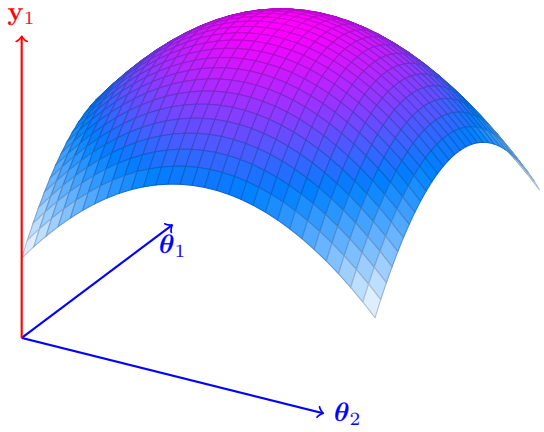

Figure 2.7: Typical response surface for two random parameters.

Throughout this thesis, the response variable is taken as the flutter speed. However, this does not have to be the case. Indeed, there are numerous works that consider other response variables, such as LCO amplitudes [62].

The other type of UQ, inverse uncertainty quantification, considers the opposite problem. Given a set of measured response variables, determine the random parameters (i.e. the inputs).

This problem bares a close resemblance to the field of stochastic model identification and updating. That is, improving the accuracy of a numerical model from a set of measured experimental data, which may contain errors or other undesired artefacts.

This thesis will consider only forward uncertainty propagation methods. Thus, the remainder of this review is focused on these techniques.

How is Uncertainty Quantification Useful?

The application of uncertainty quantification to aeroelasticity is thought to play a significant role in the development of future aircraft [63]. Some of its benefits include:

- **Enabling quantitative risk assessment (QRA)** – Uncertainty quantification supports a standardised language to be used across multiple sectors and therefore allows designers to use a common framework for assessing the robustness or reliability of their designs.
- **Supporting an alternative to deterministic safety criteria** – The safety regulations for air vehicles are currently based on deterministic criteria. For instance, the FAA mandates a 15% factor of safety between the conditions at which flutter arises and the maximum operating conditions of commercial aircraft [7]. As Pettit [63] discusses, these factors of safety are essentially empirical; there is no physical reasoning as to why 15% is used. It is well known that deterministic factors of safety are restrictive and can lead to overly conservative designs. Thus, there is a growing voice in the aerospace industry that would like to replace deterministic criteria with alternative methods from the field of uncertainty quantification.
- **Rerouting wasted computational effort** – With the rise of computational power, more "accurate" solutions to aeroelastic problems are achievable. However, as Pettit explains [8], such an approach is wasteful. In practice, the uncertainties present in aeroelastic systems make the solutions inherently uncertain. Thus, homing in on solutions with a high resolution is not representative of the true system and it is argued that this computational effort would be better used for UQ purposes to instead to predict the variability and all possible outcomes of aeroelastic phenomena.
- **Informing and influencing design decisions** – Uncertainty quantification techniques can also be used during the design phase. By considering the effects of uncertainty early on, engineers can modify designs so that the risk of aeroelastic phenomena arising during normal flight conditions is reduced. Moreover, optimisation techniques can be used so that the weight or drag of an aircraft can be reduced, without compromising safety [64]. This promotes better efficiency and reduces the environmental impact of aircraft.

2.2.2 Sources of Uncertainty and Their Classifications

Before reviewing some of the uncertainty quantification techniques that have been applied to aeroelastic systems, it is useful to first consider how uncertainty arises in the first place. It is also helpful to look at how these sources of uncertainty are classified and how this influences the type of UQ analysis that is performed.

At the most abstract level, uncertainties are usually sorted into the two categories described by Melchers [65]. These are 'aleatory uncertainties' and 'epistemic uncertainties'. Aleatory uncertainties, otherwise known as 'irreducible uncertainties', are those that are inherent and cannot be reduced further. In other words, further knowledge does not reduce their magnitude

nor impact. A typical example of an aleatory uncertainty is parameter variation. Epistemic uncertainties, on the other hand, arise from a lack of knowledge, such as poor modelling of a physical process.

Dai and Yang [66] describe how the sources of uncertainty may also be categorised in a hierarchical fashion, as shown in Fig. 2.8. The highest level is known as the 'system level' and describes the complete aeroelastic system. Below this is the subsystem level. This level is comprised of both the structural and aerodynamic model. At the lowest level is the physical level, which itemises the individual sources of uncertainty. Although not mentioned by the authors, there is also a further categorisation beneath the physical level, which considers the original source of the uncertainties. However, it is usually impractical to consider the individual sources separately; rather, their effects are treated holistically at the physical level.

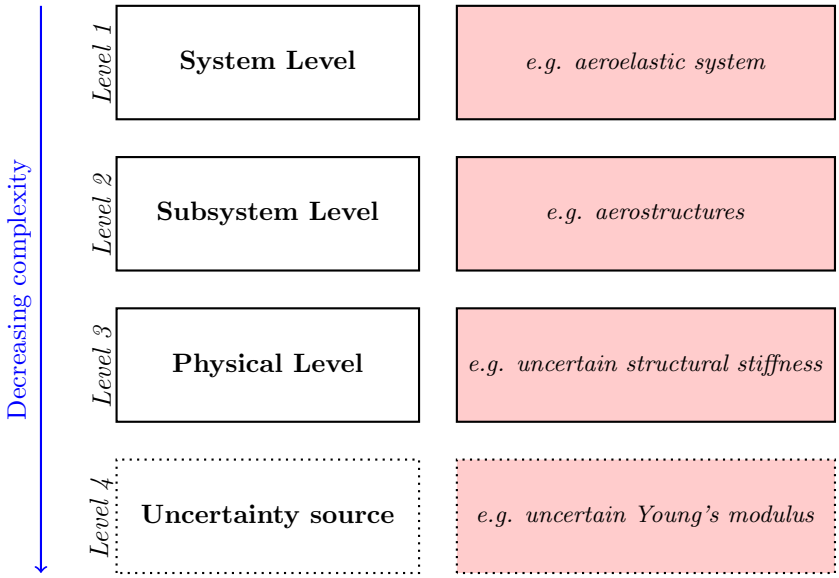

Figure 2.8: Hierarchical classification of uncertainties. *(Adapted from Dai and Yang [66])*

The literature in UQ in aeroelasticity is commonly separated into two branches: traditional aeroelasticity (TAE) and computational aeroelasticity (CAE) [64]. Traditional aeroelasticity typically uses simplified aeroelastic models, such as the classic pitch-plunge model that is studied by Theodorsen [32]. For this reason, attention is primarily given to structural sources of uncertainty. For example, variable mass, stiffness and damping parameters. However, approaches to model aerodynamic uncertainty have been used; this normally involves modelling the uncertainty through a single, global variable, such as the flow speed or air density. CAE, on the other hand, deals with uncertainty in the aerodynamics in greater detail by incorporating UQ methods into CFD methods. Since this thesis considers experiment-based approaches to aeroelasticity, the work here is a sub-branch of TAE and thus TAE is primarily considered in the discussion that follows. However, a detailed review of UQ in CAE may be found in the paper by Badcock et al. [67].

2.2.3 Uncertainty Quantification Techniques: Non-Probabilistic Methods

The following two subsections provide an overview of some uncertainty quantification techniques that have been applied to aeroelastic and aeroservoelastic systems. Following the convention in the literature, these techniques are divided into two categories: probabilistic and

non-probabilistic methods. This first subsection considers non-probabilistic methods.

1. Local Sensitivity Analysis

The first, and arguably simplest, uncertainty quantification technique is known as 'local sensitivity analysis'. Local sensitivity analysis aims to quantify the relationship between a set of uncertain parameters and one or more response variables. This is done through a perturbation approach, where small changes in the uncertain parameters are applied and the corresponding changes in the response variables are measured. Strictly speaking, the method only works when the changes in the uncertain parameters are infinitesimally small. However, it is normal to consider larger, physically realisable changes in the input parameters if one accepts some degree of truncation error.

A brief mathematical overview of the technique is as follows. Suppose that the uncertainty in a system is parameterised by a vector $\boldsymbol{\theta} \in \mathbb{R}^p$ of p variables. Let the vector of m response variables be denoted $\mathbf{y} \in \mathbb{R}^m$. The response variables are related to the vector of uncertain variables by the general relationship

$$y_i = f_i(\boldsymbol{\theta}), \quad i = 1, 2, \ldots, m, \tag{2.6}$$

where $f_i : \mathbb{R}^p \to \mathbb{R}$. For each response variable, the truncated Taylor series gives that

$$dy_i = \sum_{j=1}^{p} \frac{\partial f_i}{\partial \theta_j} d\theta_j, \quad i = 1, 2, \ldots, m, \tag{2.7}$$

and so

$$d\mathbf{y} = \mathbf{S} d\boldsymbol{\theta}, \tag{2.8}$$

where $\mathbf{S} \in \mathbb{R}^{m \times p}$ is termed the sensitivity matrix and has elements, or sensitivities, given by

$$s_{p,q} = \frac{\partial f_p}{\partial \theta_q}. \tag{2.9}$$

Extending the infinitesimal in Eq. 2.8 to small values gives that

$$\delta\mathbf{y} = \mathbf{S} \delta\boldsymbol{\theta}. \tag{2.10}$$

Thus, the variation in the response variables is expressed in terms the sensitivity matrix and the small change in the uncertain parameters.

It is important to note that Eq. 2.10 is only suitable to use when the local behaviour of each function f_i is well approximated as linear in the domain of the uncertain variables. If this is not true, the predicted change in the output variables may be highly erroneous and thus a poor estimate of the variability of the parameters of interest. This will be further considered later.

As shown above, the sensitivity matrix is constructed by the partial derivatives of each output with respect to each input. These partial derivatives may be computed numerically or through analytic formulae. In general, local sensitivity analysis is most powerful when one has access to analytic formulae for the partial derivatives. This is because the computational effort is significantly reduced compared to numerical approaches. In the review by Beran and Stanford [68], a detailed methodology is shown for how to obtain the sensitivity of the flutter speed to one or more parameters in the system. They show that the sensitivities may be obtained

analytically using the state matrices and the left and right eigenvectors that correspond to the nominal flutter condition (i.e. that without uncertainty). The solution shown by the authors had a significant benefit in terms of computational speed; they were able to demonstrate how the sensitivities across different parameters had very similar forms. This means that some elements of the sensitivities can be pre-calculated, regardless of the uncertain parameter considered. As a result, the authors suggested that this approach may be appropriate to use for systems with a very large number of uncertain variables.

2. Interval Analysis

Another type of non-probabilistic method that has been applied to numerous aeroelastic systems is that of 'interval analysis'. Interval analysis is a parametric uncertainty quantification technique in which one or more uncertain input parameters are modelled as intervals with upper and lower bounds. In other words, the uncertain vector $\boldsymbol{\theta}$ is expressed as $\boldsymbol{\theta} = [\underline{\boldsymbol{\theta}}, \overline{\boldsymbol{\theta}}]$, where $\underline{\boldsymbol{\theta}}$ and $\overline{\boldsymbol{\theta}}$ are the lower and upper bounds, respectively. The aim of the interval approach is either: (i) to determine whether some condition is satisfied for all possible outcomes of the interval variables, or (ii) to find the upper and lower bounds, and hence the interval, of the response parameter. The study of interval analysis is itself a field of mathematics that has been studied widely over the last century [69]. However, it is only recently that such approaches have been used more rigorously in engineering applications [70].

Interval analysis has been used for the purposes of flutter uncertainty quantification in two ways. Firstly, directly to the flutter speed; in other words, to determine the upper and lower limits of the flutter speed when subjected to interval uncertainties in the structural or aerodynamic properties. Secondly, to determine whether flutter arises within the flight envelope when uncertainties are present. Zheng and Qiu [71], [72] used an interval method to estimate the upper and lower bounds of the flutter speed in both an aerofoil model and a panel model. Chen et al. [73] incorporated an interval method into a CFD model to simulate the effect of aerodynamic uncertainty on the flutter characteristics of both a two-dimensional aerofoil and the AGARD 445.6 wing. Marques et al. [74] considered interval analysis to predict the variation in the eigenvalues in aeroelastic models with uncertain structural parameters.

Historically, interval analysis has been used to assess variability in systems described by linear, algebraic equations. Such systems lend themselves well to conventional interval arithmetic [75] or other straightforward approaches [70]. However, aeroelastic problems typically involve eigenvalue problems, which require more involved methods. These types of problems do not lend themselves well to interval arithmetic as they can severely overestimate the upper and lower bounds of the flutter speed due to the so-called 'dependency problem' [76].

The most common interval analysis method used in the aeroelastic community is known as the perturbation method. The perturbation method uses a sensitivity-based approach as follows. Suppose that the difference between the upper and lower bounds of the random parameters is given by

$$\Delta\boldsymbol{\theta} = \overline{\boldsymbol{\theta}} - \underline{\boldsymbol{\theta}}. \tag{2.11}$$

From Eq. 2.10, the upper and lower limit of the response variable is given respectively by

$$\overline{\mathbf{y}} = \mathbf{y}_0 + \mathbf{S}\frac{\Delta\boldsymbol{\theta}}{2}, \tag{2.12}$$

$$\underline{\mathbf{y}} = \mathbf{y}_0 - \mathbf{S}\frac{\Delta\boldsymbol{\theta}}{2}, \tag{2.13}$$

where $\mathbf{y}_0$ is the nominal value of $\mathbf{y}$. Of course, the perturbation method only works if the response surface is approximately linear. Otherwise, this approach may lead to erroneous upper and lower bound estimates of the response variable.

Other more involved methods do exist to calculate better predictions of the upper and lower bounds of the response variable. The paper by Zheng and Qiu [72], for example, is a surrogate modelling approach and uses Bernstein polynomials to capture some of the nonlinear effects of the response surface.

3. Other Non-Probabilistic Methods

The two methods presented above are the most popular non-probabilistic approaches for UQ in aeroelasticity and are those that are used in the latter chapters of this thesis. There are also some other non-probabilistic methods that have been used, such as fuzzy analysis [77] and approaches based on μ synthesis theory [78]. However, these methods are beyond the scope of the thesis.

2.2.4 Uncertainty Quantification Techniques: Probabilistic Methods

Non-probabilistic methods cannot estimate the likelihood of certain outcomes and hence give no indication of the behaviour that is to be expected or is highly unlikely. In practice, this likelihood information can inform better decisions during the design process and can be used as the basis on which to perform design optimisation, which is discussed later. For this reason, probabilistic methods have been used in numerous applications.

In the world of aeroelasticity, the main aim of probabilistic methods is to either: (i) determine the likelihood of certain aeroelastic phenomena arising, or (ii) obtain the probabilistic distribution of some aeroelastic response variable. The easiest way to obtain the probability distribution of the flutter speed is through direct sampling of the system. Direct sampling is where numerous outcomes of the random parameters are selected, obeying their probability distribution, and are fed into a numerical model of the aeroelastic system to obtain the corresponding sample outcomes. If the number of samples is sufficiently large, the Law of Large Numbers states that the statistics given by the sampled response variable should closely match the true statistics of the response variable. This is the basis of techniques such as Monte Carlo simulation (MCS) or more advanced sampling methods, such as Latin hypercube sampling (LHS).

Whilst straightforward, direct sampling is computationally demanding. Obtaining the flutter speed usually requires solving a potentially large eigenvalue problem. Consequently, this approach is usually impractical for real-world applications. To counter this, another approach has been used, where sampling is instead performed on a so-called surrogate model. The surrogate model attempts to approximate the response surface with a simpler model that does not rely on the fundamental physics of the problem. This surrogate model can then be sampled instead, rather than the true response surface, and hence the computational effort can be reduced.

There are numerous approaches for surrogate modelling. Here, attention is given to two approaches: (i) surrogate modelling via sensitivities, and (ii) surrogate modelling via spectral expansions.

1. Surrogate Modelling via Sensitivities

The sensitivity-based approach presented earlier can be extended to create a surrogate model that probabilistic information can be easily extracted from. Suppose that the response surface is linearised about some chosen, nominal point, as shown in Fig. 2.9. From Eq. 2.10

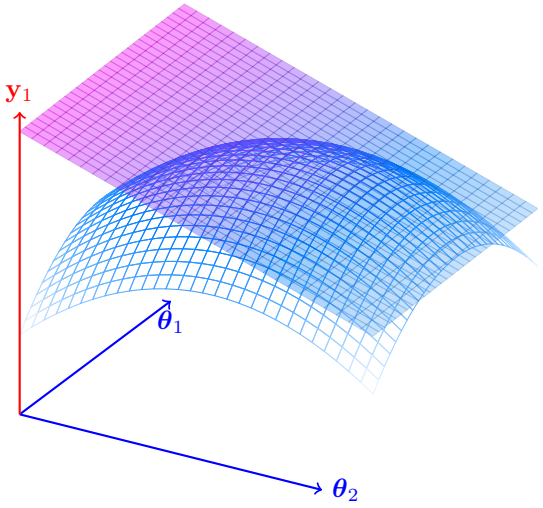

Figure 2.9: Linearisation of the response surface.

$$\int \delta \mathbf{y} = \int \mathbf{S} \delta \boldsymbol{\theta}, \tag{2.14}$$

and thus

$$\mathbf{y} = \mathbf{S}\boldsymbol{\theta} + \mathbf{c}, \tag{2.15}$$

where $\mathbf{c}$ is a vector constant. At the point of linearisation $\boldsymbol{\theta} = \boldsymbol{\theta}_0$, $\mathbf{y} = \mathbf{y}_0$ and so

$$\mathbf{c} = \mathbf{y}_0 - \mathbf{S}\boldsymbol{\theta}_0. \tag{2.16}$$

Substituting this into the above yields

$$\mathbf{y} = \mathbf{S}\left(\boldsymbol{\theta} - \boldsymbol{\theta}_0\right) + \mathbf{y}_0. \tag{2.17}$$

The main benefit of the linearisation is that the mean and variance can be obtained immediately from the sensitivities. By taking the expectation and covariance operator, it may be easily shown that

$$\mathrm{E}[\mathbf{y}] = \mathbf{S}\left(\mathrm{E}[\boldsymbol{\theta}] - \boldsymbol{\theta}_0\right) + \mathbf{y}_0, \tag{2.18}$$

$$\mathrm{Cov}[\mathbf{y}] = \mathbf{S}\mathrm{Cov}[\boldsymbol{\theta}]\mathbf{S}^T. \tag{2.19}$$

Therefore, based on simple analytic formulae, one can evaluate the expectation and covariance of the response vector, if the sensitivities and statistics of the input variables are known.

2. Surrogate Modelling via Spectral Expansions/Polynomial Chaos (PC) Expansions

A major issue with surrogate modelling via sensitivities is that there is little justification for assuming that the response surface is linear. Indeed, it is often the case that the response

surface will exhibit nonlinear behaviour, even close to the origin or point of linearisation. Consequently, the sensitivity approach can sometimes yield large errors in its estimate of the mean and variance. To address this issue, another approach has been developed and is based on the principles of spectral expansions.

Spectral expansions, in essence, are function series that aim to replicate the response characteristics of a stochastic process. One of the most widely used types of spectral expansion is known as the polynomial chaos (PC) expansion, which was first proposed by Wiener [79] and further popularised in engineering applications by Ghanem and Spanos [80]. The PC expansion uses a series of orthogonal polynomials to reconstruct the response surface across the entire domain of the uncertain variables. This is in contrast to sensitivity-based methods, which only consider the local domain of the random parameters about some nominal points. Mathematically, the expansion is written as

$$y_j = \sum_i a_i \Psi_i(\boldsymbol{\theta}), \tag{2.20}$$

where Ψ_i is a multi-variate polynomial, and y_j is the j^{th} response variable. In the literature, the exact polynomials that are selected are based on the probabilistic distribution of the random variables. If the random variables are all independent Gaussian with unit variance, the polynomials are taken as the multidimensional Hermite polynomials. In practice, however, it may be the case that the random variables do not follow a Gaussian distribution. Moreover, two or more of the random variables may be correlated with each other. In these circumstances, the formulation presented above cannot be directly used. Instead, the random variables must be transformed. One well-known transformation is known as the Rosenblatt transformation [81]. This technique allows correlated, non-Gaussian variables to be converted to a form that is compatible with the PC expansion using the Hermite polynomials.

The coefficients in Eq. 2.20 can be found through two distinct methods: (i) intrusive methods, and (ii) non-intrusive methods. Intrusive methods aim to directly construct a stochastic model of the system from first principles. This is typically done by 'projecting' the physical model of the system into the uncertain space using techniques such as Galerkin methods. Non-intrusive methods, on the other hand, aim to construct the PC expansion through sampling of a deterministic model. In other words, to treat the physical system as a black box and to construct a parametric model of it, in terms of the random parameters. Some ways to do this include Monte-Carlo simulation (MCS), Latin hypercube sampling (LHS) and other such methods.

Once the coefficients of the expansion have been found, it is straightforward to obtain the mean and variance of the response variable. From Eq. 2.20, it may be shown that

$$\mathrm{E}[y_j] = a_0, \tag{2.21}$$

$$\mathrm{Var}[y_j] = \sum_{i=1}^{N} a_i^2 \mathrm{E}[\Psi_i^2(\boldsymbol{\theta})]. \tag{2.22}$$

These relationships come from the principle of orthogonality, which is explained in greater detail in [80]. Of course, one of the limiting factors in the accuracy of the mean and variance is the number of polynomials N used in the expansion. If this is too small, the accuracy of the mean and variance may not be sufficient. However, if N is too large, it is possible that there is severe overfitting of the model or the expansion itself may not be computationally realisable.

One of the benefits of polynomial chaos expansions is that they allow an alternative,

probabilistic-based sensitivity analysis to be performed. As shown above, the net variance of the response variable is found by summing over the contribution of each multidimensional polynomial. These multidimensional polynomials are each associated with a combination of one or more of the uncertain variables. Thus, the contributing factor of each combination of the uncertain variables to the total variance of the response factor can be found. This type of analysis is known as global sensitivity analysis and has been applied to several aeroelastic systems. Kumar et al. [82] used the PC expansion to perform global sensitivity analysis [83], [84] on aeroelastic wind turbine models. Sobol indices were constructed using sparse PC expansions and applied to the NM80 model. Suryawanshi and Ghosh [85] followed a similar approach, but in the context of design optimisation, which is discussed later.

Despite its clear advantage over conventional sensitivity methods, that are several restrictions in the use of PC expansions. One of the main restrictions is related to the number of uncertain parameters in the model. Using more uncertain parameters requires more terms in the expansion and hence a large number of samples are needed to find the coefficients accurately. For this reason, PC expansions are typically used in aeroelastic settings when the number of uncertain parameters is less than four or five. The problem of dealing with more parameters in a computationally efficient manner is known as the "problem of dimensionality", which is an open challenge that remains in the field of UQ.

Further details on the formulation of the PC expansion can be found in Chapter 7 or in the paper by Eldred [86].

2.2.5 Design Optimisation

The aim of uncertainty quantification is to determine the degree of variability in key response characterises, such as the flutter speed. This alone is useful as it identifies the bounds of likely and unlikely behaviour, hence satisfying the first three benefits that were outlined in §2.2.1. However, UQ is arguably most rewarding when incorporated into the design process. UQ has the power to identify areas of vulnerability or areas that are overly conservative in the design. This information can then be used to improve the design so that better performance or robustness is achieved. The process of doing this is known as design optimisation and is usually approached in two ways: (i) reliability-based design optimisation (RBDO), and (ii) robust design optimisation (RDO).

RBDO and RDO are methods that aim to reduce a defined 'cost' by optimising one or more design variables [87]. In aeroelasticity literature, the cost is usually defined as the total weight of the aircraft or the aerodynamic drag. The design variable, meanwhile, can include the external geometry of the structure, the interior components, or a combination thereof. As Othman et al. [88] explain, RBDO imposes a set of reliability constraints and aims to optimise the design such that the constraints are not violated. These constraints are typically associated with a probability of failure, i.e. the likelihood of flutter. RDO, on the other hand, seeks to find an optimum design that maximises the robustness about a mean response. That is, to concentrate the effort of the optimisation on the robustness of the solution, not necessarily just the defined cost function.

RBDO and RDO have now been used in the world of aeroelasticity for a few decades [64] and have seen applications especially for the purposes of aeroelastic tailoring. The general idea of aeroelastic tailoring is to optimise the design of the structure subject to ensuring sufficient freedom from detrimental aeroelastic phenomena, such as flutter or limit cycle oscillations. Othman et al. [88] proposed a multi-level framework for the optimisation of composite aircraft

wings through both RBDO and RDO. Similar work was also considered by Scarth and Cooper [89] and Scarth et al. [90]. Stanford and Beran [91] considered weight optimisation of panels under probabilistic aeroelastic flutter constraints. Missoum et al. [92] studied RBDO for aeroelastic systems with nonlinear constraints.

The main challenge associated with RBDO and RDO is the processing speed required for calculating the probability of failure. In general, design optimisation problems require many iterations to find the best solution. Therefore long computational times can be endured if at each iteration the probability of failure has to be found. One solution to this problem is to use a method known as the first-order reliability method (FORM). The FORM is a technique that is used to approximate the probability of failure without the need of sampling, which other techniques, such as Monte Carlo, rely on [93]. The method works by identifying combinations of uncertain parameters that lead to failure. The boundary between failure and normal conditions is then projected into the space of the uncertain parameters and is approximated by a hyperplane. The minimum distance between the hyperplane and the origin of the parameter space is then used to find the probability of failure. Under the assumption that all uncertain parameters are independent and have a standardised normal distribution,

$$P(\text{failure}) = 1 - \Phi(d), \tag{2.23}$$

where Φ is the cumulative distribution function of the unit Gaussian, and d is the minimum distance between the hyperplane and the origin of the parameter space.

RBDO and RDO methodologies commonly employ the FORM due to its speed and simplicity [94]. However, one must be cautious using this approach. The method only works well if the limit state function is approximately linear. If this is not the case, the probability estimate yielded by FORM can be a gross under- or over-estimate. This problem can be avoided by extending FORM to high dimensions. For example, the second-order reliability method (SORM) attempts to reconstruct the limit state function using a second-order curve. However, in recent years, other UQ approaches have been used for design optimisation. Suryawanshi and Ghosh [85] performed RBDO on a cantilever wing using polynomial chaos expansions to evaluate the probability of flutter. A similar approach using PC expansions was also used by Manan and Cooper [95] on an aeroelastic model with uncertain composite material properties.

In the aeroelasticity literature cited above, the optimisation variables are all physical, passive design elements, i.e. mass, stiffness and damping parameters. In practice, design optimisation procedures are not limited just to these elements; indeed, active modifications such as dynamic controllers can be considered too. This idea of robust optimisation of the system through active control is closely related the problem of robust control and is considered in the latter chapters of this thesis.

2.3 Receptance-Based Control

As established in the previous section, accurate numerical modelling of aeroservoelastic systems is challenging. Errors arising from restrictive assumptions in the physical processes or poor parameter estimation can often lead to inaccurate models that do not closely reflect the true system. If AFS control systems are designed using inaccurate models, the desired control objective can be compromised. Indeed, in the worst-case scenario, it is possible that the AFS system does the opposite of what is intended and drives the flutter speed lower [47].

This problem cannot be completely avoided as long as numerical models are used; in fact,

its effects can only be *reduced* through better understanding of the physics involved or by more accurate parameter estimation. However, even this is not always possible. Firstly, highly accurate modelling of the physics often requires large computational resources, which may not be available. Secondly, the complexities of the physical process may mean that it is simply impractical to model. Finally, some uncertain parameters cannot be reduced. For instance, it is impossible to mitigate or reduce the variability of aleatory uncertainties (see §2.2).

To combat this problem, an alternative approach to active flutter suppression has been developed in recent years. The fundamental principle of this new approach is to avoid constructing numerical models entirely. This is done by using experimental data from real-world systems to facilitate an experiment-driven approach to active control. In this way, the numerical modelling stage of conventional AFS control design is bypassed, thus mitigating the errors associated with this step. Of course, the type of experimental data that is used can in principle take numerous forms. However, following the theme of this thesis, this section will concentrate on receptance-based approaches.

2.3.1 What are Receptance Data?

Before proceeding with a review of receptance-based techniques, it is necessary to first define what receptance data are. Most generally, receptances are data that quantify the frequency domain relationships between the inputs and outputs of an arbitrary dynamic system. The system in question can take any form of inputs and outputs and there is no restriction on the nature of the system nor the number of inputs or output. However, it is important to note that a *single* set of receptance data can only fully encapsulate the relationship between the inputs and outputs if the system is strictly linear.

The formal, mathematical-based definition of receptance data is as follows. Consider an arbitrary black box system, like that shown in Fig. 2.10. Let the time domain vector of inputs

Figure 2.10: Black box system model.

to the system be written as

$$\mathbf{u}(t) = \begin{pmatrix} u_1(t) & \dots & u_m(t) \end{pmatrix}^T. \tag{2.24}$$

Also, let the time domain vector of outputs be written as

$$\mathbf{y}(t) = \begin{pmatrix} y_1(t) & \dots & y_n(t) \end{pmatrix}^T. \tag{2.25}$$

By definition of the Laplace transform,

$$\mathcal{L}[\mathbf{u}(t)] = \mathbf{u}(s) = \int_0^\infty \mathbf{u}(t) e^{-st} dt, \tag{2.26}$$

$$\mathcal{L}[\mathbf{y}(t)] = \mathbf{y}(s) = \int_0^\infty \mathbf{y}(t) e^{-st} dt, \tag{2.27}$$

where s is the complex Laplace variable. Assuming that the system is linear, it is possible to

relate the input and output vectors by the equation

$$\mathbf{y}(s) = \mathbf{R}(s)\mathbf{u}(s), \tag{2.28}$$

where $\mathbf{R}(s)$ is named the input-output transfer function matrix. This matrix $\mathbf{R}(s)$ contains the receptance data relating the system's outputs to the system's inputs. In general, the matrix $\mathbf{R}(s)$ has the structure

$$\mathbf{R}(s) = \begin{pmatrix} r_{11}(s) & r_{12}(s) & \dots & r_{1m}(s) \\ \vdots & \vdots & \dots & \vdots \\ r_{n1}(s) & r_{n2}(s) & \dots & r_{nm}(s) \end{pmatrix} \tag{2.29}$$

where each element $\mathbf{r}_{ij}(s)$ gives the relationship between the i^{th} output and the j^{th} input.

In the literature, $\mathbf{R}(s)$ is commonly referred to as the receptance matrix instead of the input-output transfer function matrix. Strictly speaking, this is only true when the outputs from the system are displacements and the inputs are forces. However, as seems to be convention, the term receptance matrix is used interchangeably to mean both the specific and general form of the matrix $\mathbf{R}(s)$. Throughout this thesis, efforts are made to distinguish between receptance and input-output data, where necessary[4].

It is important to point out that receptance data cannot be obtained immediately through experiments. Instead, only a frequency response function matrix can be collected through standard modal testing techniques, such as stepped-sine testing or random input testing [96]. The FRF matrix is the matrix $\mathbf{R}(s)$ when the complex parameter s is limited to points on the imaginary axis, i.e. $s = i\omega$. To reconstruct the full receptance matrix from the FRF matrix, one must perform rational transfer function (RTF) fitting. There are several different methods to do this; however, a popular algorithm that is used is known as PolyMAX [97]. The above points are illustrated diagrammatically in Fig. 2.11. Further details about RTF fittings are provided in Chapter 6.

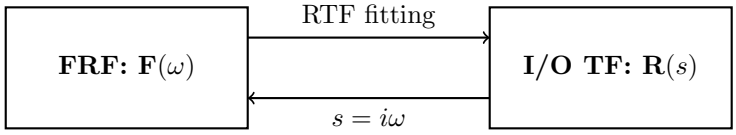

Figure 2.11: Converting between FRF data and receptance data.

2.3.2 Structural Modification Theory

Before considering the topic of receptance-based control, it is first necessary to review the literature and historical origins of another field known as 'receptance-based structural modification theory'. This is for two reasons. Firstly, the theory of receptance-based control is derived from this earlier work. Secondly, Chapters 7 and 8 will consider approaches where uncertainty is modelled using methods from this field.

Receptance-based structural modification theory is the field of study that aims to understand the relationship between the modal properties and spatial properties of a system, using only receptance data [98]. The modal properties include: the eigenvalues, which contain information about the natural frequencies and damping of one or more modes; and the eigenvectors, which

[4]Further details are given in Chapter 3.

contain information about the displacement pattern in each mode. The spatial properties usually include the physical mass, stiffness, and damping parameters.

Structural modification theory is commonly segregated into two separate, but closely related, branches: (i) *direct* structural modification theory, and (ii) *inverse* structural modification theory [99]. Direct structural modification theory concerns the prediction of changes in modal properties when a change to the physical parameters is applied. For example, the changes to the natural frequencies of a cantilever beam as masses are added at points along its span. Inverse structural modification theory, on the other hand, concerns the calculation of the physical modifications required to achieve a desired change in one or more modal properties. For example, the required stiffness modification necessary to assign a desired natural frequency. Both of these branches are visualised in Fig. 2.12.

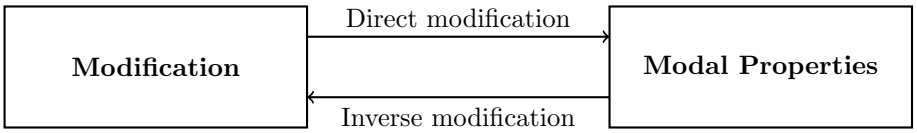

Figure 2.12: Branches of structural modification theory.

Inverse structural modification bares a close resemblance to the generalised control problem. That is, the problem of calculating the required modification to the system that achieves a desired control objective. For this reason, this branch is considered in greater detail here.

Inverse Structural Modification Theory

Early work in the field of receptance-based inverse structural modification theory can be traced back to Duncan [100]. Building on the earlier developed Admittance Method [101], Duncan showed that the natural frequency of a system could be assigned through the coupling of two systems or, equivalently, by a structural modification to a given reference system. The method worked by using admittance data from both subsystems at the point of connection and used the principle of 'equal and opposite admittance' to find the natural frequency of the new, coupled system. In this early paper, Duncan demonstrated the principles of structural modification through applications such as flywheels mounted to elastic shafts, and the examples shown were based on modifications that depended on only a single parameter. However, the idea of modifications with more than one parameter dependency was discussed in this paper. Similar work was also considered by Weissenburger [102], who developed the conceptually similar 'method of local modifications'.

Both Duncan's and Weissenburger's works were early forerunners in structural modification theory. However, their methods considered only simple mass-spring systems and did not consider the effect of damping in a system. In 1971, however, Pomazal and Snyder [103] addressed this issue by expanding the theory to consider systems with linear, viscous damping. By recasting the structural modification problem into a more general matrix form, they were able to re-write the problem so that more arbitrary modifications could be considered. They were also able to remove the restriction of considering only systems with normal modes; complex-valued modes that collectively do not form a spanning set of the vector space could be considered in a general way for the first time.

As mentioned above, initial studies in structural modification theory concentrated primarily on the assignment of natural frequencies using a single modification parameter. For example, a single mass, stiffness or damping change. Also, the modifications considered were rank-one.

That is, modifications with a dynamic stiffness matrix that can be expressed as a dyadic product. In practice, it may be the case that the assignment of the damping in each frequency may also be desired. Furthermore, the use of multiple parameters in the structural modification potentially enables a more flexible, multi-objective approach. For instance, the ability to modify multiple modes simultaneously. Some recent studies have considered multi-parameter approaches to inverse structural modification. For example, Tsai et al. [104] considered an approach based on optimisation. However, even still, these approaches typically have several limitations in their use, which stem from the physicality imposed by the modification parameters. This is considered later on in this discussion.

Despite great progress in the field, real-world applications of structural modification theory have thus far been few and far between and have been limited primarily to experimental settings [104]. Mottershead et al. [105] considered the effect of a large overhanging mass on the coupling in the system responses in a Lynx Mark 7 helicopter tailcone and addressed the practical limitations of structural modification theory in an experimental setting. Tsai et al. [104] applied inverse structural modification theory to a geared rotor-bearing and used an optimisation approach to find the required mass modification to assign specific natural frequencies. Zarraga et al. [106] applied the technique to a brake-clutch model for the purposes of disc squeal noise suppression. A more detailed overview of the history and progress in inverse structural modification theory may be found in the thesis by Tehrani [107].

Active Modifications

The early literature in the field of inverse structural modification theory all consider static, physical modifications to the mass, stiffness and damping parameters. These modifications are collectively referred to as those of the passive kind. Although the type historically used, passive modifications have several restrictions in their use [99]. Firstly, the matrix corresponding to the modification must be symmetric and positive semi-definite. Secondly, the number of poles that can be assigned cannot exceed the rank of the modification [108]. Finally, the modification must conform to a specific pattern of values. Clearly, all of these restrictions limit the choice of the desired eigenvalues and/or eigenvectors. Indeed, these modifications present challenges to the eigenvalue/eigenvector assignment problem and usually a compromise in the performance of the assignment must be accepted if they are to be used.

An alternative type of modification, however, that is not constrained by the above restrictions is known as active modification. As the name suggests, these types of modifications use active controllers to assign the modal properties of a system and is achieved by using one or more actuators placed at strategic locations on the structure. Whilst the concepts and principles of active control techniques for structures have been known for at least 50 years [109], their formulation in terms of structural modification theory or measured receptances was not fully realised until 2007, when Ram and Mottershead [110] presented the Receptance Method for active vibration control.

2.3.3 The Receptance Method

The receptance method, first formalised by Ram and Mottershead [110], [111] is an experiment-based active pole/zero assignment technique. Using either state or output feedback [107], a controller is used to create an active modification to a set of measured receptance data so that the eigenvalues and/or eigenvectors of the closed-loop system are assigned in a desired fashion. The method is advantageous in that there is no need to construct a numerical model of the

system to be controlled. Hence, uncertainties associated with this are mitigated entirely.

In the original formulation of the Receptance Method, a single input, equivalent to a rank-one modification, is used to assign a set of desired closed-loop poles. In this way, the input to the system is related to the outputs by

$$u(s) = \left(s\mathbf{f}^T + \mathbf{g}^T\right)\mathbf{y}(s), \tag{2.30}$$

where $\mathbf{f}, \mathbf{g}$ are control gains that are to be determined. The gains are solved through use of the Sherman-Morrison formula [112]. This expresses the system's closed-loop characteristic equation in terms of the measured input-output transfer function data and the controller's feedback gains. The characteristic equation is then modified, by changing the control gains, to yield solutions corresponding to a set $\{\mu_1\mu_2, \ldots, \mu_l\}$ of l desired closed-loop poles. The necessary control gains are then obtained in a straightforward manner by simply solving a set of linear equations in the unknown variables.

Since the original formulation in 2007, several attempts were made in the years that followed to generalise the Receptance Method to systems with multiple inputs. That is, systems with inputs of the form

$$\mathbf{u}(s) = \left(s\mathbf{F}^T + \mathbf{G}^T\right)\mathbf{x}(s). \tag{2.31}$$

Most of these early methods initially worked on restrictive assumptions about the system or measured receptances, and were not general to arbitrary dynamic systems [113]. However, the problem of receptance-based control with an arbitrary number of inputs and outputs was solved by Ram and Mottershead in 2013 [114]. This new formulation, which is now the most widely used, allows both the eigenvalues and eigenvectors to be assigned independently. Thus, the controller is able to leverage the greater freedom allowed by the extra control inputs. This modern formulation is described mathematically in Chapter 5; for now, however, this section proceeds with a general view of the Receptance Method and its historical development.

The additional freedom granted by more than one input poses the question of how best to distribute the control effort. If, in addition to the eigenvalues, one cares about the assignment of specific eigenvectors, then there is only one unique solution for the control gains. However, it is more usual that the assignment of the eigenvalues is the dominant factor and the eigenvectors may be assigned for other purposes. In this case, there are a theoretically infinite number of solutions to the gains and thus strategies must be developed to choose the most appropriate one. One strategy is based on imposing modal constraints so that the relative displacement associated with a particular degree-of-freedom in one mode is limited. This was the approach considered originally by Ram and Mottershead [114]. An alternative strategy is to assign the eigenvectors such that the system is more robust to external disturbances, poor controller performance, and other sources of uncertainty. This strategy is well known in the realm of conventional, state-space based control models [115] and will be considered later in §2.3.5.

The Receptance Method itself is commonly used for the purposes of vibration suppression [116]. By assigning specific combinations of poles and/or zeros, the 'shape' of the closed-loop response can be modified so that: (i) the damping level is increased in specific modes, and (ii) the natural frequencies are shifted away from operating points, thereby preventing resonance. Tehrani et al. [117] were the first to demonstrate the method experimentally by applying it to a lightweight glass-fibre beam and a 'heavy modular test structure'. The Receptance Method has also been used for the purposes of aeroservoelastic control. However, this is considered in the section that follows.

The original formulation of the Receptance Method was designed for linear, time-invariant

(LTI) systems. However, it is worth noting that the method has also been extended to consider nonlinear systems too. Tehrani et al. [118] have explored the control of nonlinear systems using a receptance-based describing function approach. Zhen et al. [119] presented a method based on the classic feedback linearisation technique. A similar approach was also considered by Lisitano et al. [120].

2.3.4 Applications in Aeroservoelasticity

As the theory continues to mature, the number of numerical and experimental applications of receptance-based control is growing. This section explores the use of receptance-based techniques for the purposes aeroservoelastic control and, more specifically, active flutter suppression [121].

The first numerical application of the Receptance Method to aeroservoelastic systems can be attributed to Singh et al. [122]. In their work, eigenvalue assignment was performed on a three-degree-of-freedom, pitch-plunge system with a single trailing-edge control surface. Using the original formulation in [110], the control gains were calculated at a discrete number of freestream speeds such that either: (i) the damping in the modes were increased, (ii) the frequency separation between modes was increased, or (iii) a combination of both (i) and (ii). In this way, the poles were driven further away from instability and hence the flutter speed was pushed higher.

The work by Singh et al. [122] demonstrated for the first time how receptance-based techniques could be used for AFS. Moreover, it considered some of the key issues in designing the controller, such as: scheduling of the control gains, deciding which inputs and outputs to use, and the effect of actuator dynamics. However, the original study was limited in several ways. Firstly, as the authors point out, they assumed availability of the full input-output transfer function matrix. In other words, the transfer function between each input and output was assumed to be measurable. In practice, this may not be true as the data collected in specific input-output combinations may be susceptible to excessive noise. Moreover, the location of some of the inputs or outputs may be physical inaccessible. Secondly, the study assumed that the transfer function matrices could be collected at speeds close to the flutter speed. In practice, this is unlikely to be true due to low levels of damping, which makes modal testing extremely difficult. Thirdly, their work did not explicitly consider the limitations of the controller. In aeroelastic systems, it is essential that the control surface deflection is not large enough flow separation to occur. If this is the case, adverse aerodynamic effects may be induced and the assumed linear input-output behaviour of the system may become invalid. Furthermore, the control surfaces are frequently used for lateral guidance control and hence there must always be some degree of control effort available for this too.

Since the original work of Singh et al. [122], some of the above-mentioned practical limitations have been addressed. Wei et al. [123] considered the problem of pole placement using receptances when one or more degrees of freedom are inaccessible. By modifying the input to also include acceleration feedback, orthogonality conditions were imposed on the input and feedback gains to yield apparent zeros in the regions corresponding to inaccessible sensing and actuation regions. This was similarly considered by Singh et al. [124], who also investigated receptance-based aeroelastic control with partial measurements. The problem was shown equivalent to an output feedback problem and the same technique of introducing an additional acceleration feedback term was able to address the problem. Moreover, it was demonstrated, by means of a parametric study, that optimal selection of the measurement and sensor locations

could lead to control gains that are minimised in terms of their norm.

Several other numerical studies of receptance-based control of aeroservoelastic systems have been performed. Xia and Li [125] presented a hybrid approach to aeroelastic control, whereby receptances of the structural system are coupled with numerically calculated fluid loads. The receptance method is then used, as normal, for active flutter suppression. Although this does not constitute a 'full' receptance method, since a numerical model of the aerodynamics is required, the requirement of the structural model is still eliminated, and this approach is useful when measurement of receptances from the fluid loaded structure is unfeasible. Singh et al. [126] considered the application of the Receptance Method when the control surfaces themselves are subject to actuator dynamics. It was demonstrated that both the aeroelastic modes and control surface dynamic modes could be simultaneously controlled by means of eigenvalue assignment and that spillover of the controller modes could be avoided.

The earlier studies of receptance-based AFS considered only single input systems. However, as previously discussed, multiple-input systems have greater flexibility over single-input systems. This is because the control effort can be distributed amongst the various inputs. Based on this, it has been suggested that the input distribution can be used advantageously to increase the effectiveness of AFS controllers and thus drive the flutter speed higher, compared to single-input systems. Multiple input receptance-based control on a flexible aeroservoelastic system was considered by Singh et al. [127]. The system used to demonstrate the principles of this approach had three control surfaces, which were used to assign a greater damping and frequency separation in all modes. Whilst the principle of multiple-input receptance control was demonstrated in this paper, it was not discussed how the distribution of the inputs were selected. Furthermore, the study used a numerical gain scheduling approach which, for the same reasons as [122], is not experimentally practical. The problem of a more general multiple input aeroelastic control lay dormant until the work of Mokrani et al. [128], which is discussed later.

The first experimental application of receptance-based control to aeroservoelastic systems can be attributed to Papatheou et al. [129]. In this research, the authors used the receptance method for the purposes of flutter suppression on a wind-tunnel model, which is based at the University of Liverpool. The model is equipped with a single trailing-edge control surface, which is actuated by two V-shaped piezoelectric stacks that allow deflection angles of up to 7 degrees. Unlike the original theory in [110], accelerances were used instead of receptances; that is, FRFs where the output is in the form of acceleration data. Additionally, the true sensitivity of the input was not considered. In other words, the receptances were in the form of voltage relationships. This does not, however, affect the analysis of the receptance method itself and indeed may simplify the analysis since the output data from the sensors can be used directly, without calibration or processing.

The initial experimental applications of the receptance method were limited to rigid systems with a discrete number of degrees-of-freedom. Although sufficient to highlight the effectiveness of the receptance method itself, these systems are not representative of real-world applications. In practice, the number of degrees-of-freedom is aeroelastic systems is extremely large[5] and therefore the effect of using only a limited number of sensors and actuators must be considered. The first major study to consider this was by Fichera et al. [130], who applied receptance-based techniques to a flexible, aeroelastic model, known as MODFLEX. Using the Receptance Method, it was shown that a single control surface located at the trailing edge of the aerofoil was sufficient to increase the flutter speed by 12%. This was done by increasing the damping

[5]Theoretically infinite.

in the first two modes of the system.

An important point to consider with the Receptance Method is that the number of modes that can be independently controlled is limited by the number of sensors that are used in the system. In the case of Fichera et al. [130], only the first two modes were controlled as only two laser displacement sensors were used in the experimental setup. This meant that the higher order modes were uncontrollable and thus the system could have exhibited features such as spillover. In this paper, the solution was to simply apply the controller and then observe the dynamic stability experimentally. However, this approach is arguably not practical in real-world aircraft because of safety limitations. It would be interesting to consider alternative approaches that explicitly address issues related to spillover in future work.

Most recently, the Receptance Method has been re-applied to a modified version of MODFLEX, which now includes both leading- and trailing-edge control surfaces. Mokrani et al. [128] demonstrate the benefits of using the additional control input on MODFLEX and discuss a 'control effort selection' technique, which allows the control gains, and hence control surface deflection, to be optimised. In doing this, maximum control effort is left free for other purposes, such as lateral control.

2.3.5 Uncertainty in the Receptance Method

As previously discussed, the main advantage of receptance-based control techniques is that a numerical model of the system is not required. This is particularly useful for aeroservoelastic systems as the errors associated with modelling of the structure, aerodynamic, and their coupled interaction are mitigated entirely. Based on this, one may therefore assume that receptance-based control is by default more accurate or reliable than conventional control techniques that are based on numerical models. However, this is not necessarily true; due to the nature of the technique, experimental errors are often present and have an impact on the robustness of the final, closed-loop system. This is demonstrated, for instance, in the work by Mokrani et al. [128], where the desired eigenvalues do not match the true values observed in the experimental system.

There have been a limited number of studies investigating the effect of uncertainty in the Receptance Method. The first was by Mottershead et al. [131], and similarly by Tehrani et al. [132], who considered the robustness of the assigned, closed-loop poles to variability in the control gains. Using a perturbation approach, sensitivity formulae were derived and used to assesses the spread of the closed-loop poles as the control gains were modified in a neighbourhood about some nominal values. In other words, expressions of the form

$$\frac{\partial \mu_j}{\partial f_i} = \ldots, \quad \frac{\partial \mu_j}{\partial g_i} = \ldots, \tag{2.32}$$

were obtained. One of the key results from the paper was that the variability of the poles depends on the location of their nominal values. That is, the choice of the desired set $\{\mu_1, \mu_2, \ldots, \mu_l\}$ affects the spread of each true, closed-loop pole.

The method presented by Mottershead et al. [131] did not only quantify the sensitivities of the closed-loop poles, but also considered how they could be reduced. The equivalence between eigenvalue placement and eigenvalue sensitivity was demonstrated and the Receptance Method was extended to show that eigenvalue sensitivities could be assigned, rather than the set of nominal closed-loop poles. The study was however limited to single-input systems and therefore only the nominal poles or their corresponding sensitivities could be independently

assigned.

Sensitivity-based approaches have also been used to quantify the variability that arises from other sources of uncertainty. In 2011, Tehrani et al. [113] addressed the problem of uncertainty arising from measurement errors in input-output transfer function matrices. By modelling uncertainty as small, complex-valued perturbations, the sensitivities of each closed-loop pole with respect to each element in the receptance matrix was calculated, again using analytic formulae. This time, the sensitivities were of the form

$$\frac{\partial \mu_j}{\partial h_{l,m}} = \ldots, \tag{2.33}$$

where $h_{l,m}$ is an arbitrary element in the receptance matrix. For the first time, the effect of the uncertainty on the poles was visualised in the complex plane through the phenomenon of pole clustering. This is where the assigned poles are spread about some nominal points in the complex plane. Fig. 2.13 shows an example of the pole clustering phenomena.

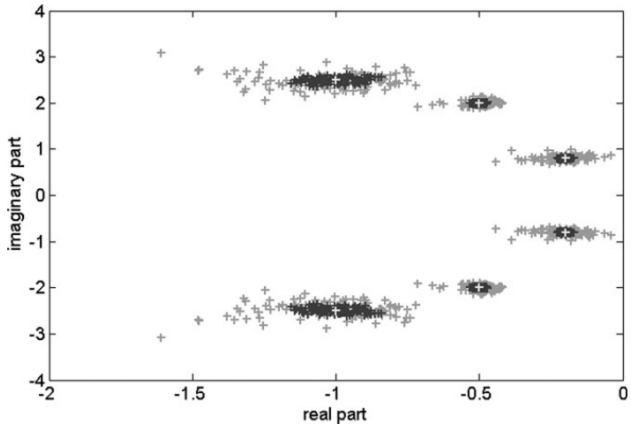

Figure 2.13: An example of pole clustering. *(Image taken from Tehrani et al. [113] with permission from Elsevier.)*

Building on the principles of [131], the paper by Tehrani et al. [113] performed eigenstructure assignment so that the sensitivities of the nominal poles were minimised, subject to them being placed in constrained oval regions in the complex plane. This method was again able to show that a good choice of eigenvalue assignment can reduce the propagation of uncertainty to the poles, further supporting the work of Mottershead et al. [131].

The work of Tehrani et al. [113] also highlighted, for the first time, the usefulness of having multiple-inputs for the purposes of uncertainty minimisation. A quasi multiple-input technique was used, where the poles of the system were placed sequentially, using one input at a time, so that the original formulation of the Receptance Method [110] could still be used. It was shown that the multiple-input system reduced the total sensitivity of the poles to measurement noise and performed better than that of the single-input approach. In other words, it was determined that the eigenvectors, in addition to the eigenvalues, play a role in uncertainty propagation and hence should be selected carefully during the receptance method.

The problem of robustness in receptance-based control with multiple-inputs has also been studied by Lu and Bai [133] and Bai et al. [134]. Similar to the above-mentioned works, analytic sensitivity formulae were derived and used to quantify the uncertainty in the assigned closed-loop eigenvalues. Using a gradient-based optimisation approach, the sensitivities were minimised by assigning the set of closed-loop eigenvalues and eigenvectors. Additionally, the

effect of controller effort was considered through the addition of a weighted norm of the control gains. By contrast with [113], the works of [133] and [134] do not rely upon placing the poles sequentially and hence can be considered the first to fully address the problem of uncertainty with multiple-input receptance-based control. However, it is important to highlight that these approaches require knowledge of the mass, stiffness and damping matrices. In other words, the methods are not purely receptance-based and still require some sort of numerical modelling or system identification techniques. The challenge of robust multiple-input control without the need of sequential placement and using only receptance data remains an open problem.

The literature cited above all considers uncertainty in a fairly holistic manner. Uncertainties are lumped together and treated as a single perturbation to measured data. Whilst usually simpler to implement, the physical meaning of the uncertainty is lost under this approach. Furthermore, it is impossible to explicitly quantify the impact of each individual physical source of uncertainty. Such information could be useful, for instance, in system design, where efforts can be concentrated primarily on the components that cause the largest amount of uncertainty. If UQ techniques are to be used in aeroelastic systems, it is important that one can explain the amount of uncertainty that is modelled. Using physical-based approach, where individual sources of uncertainty at the component level are specified, is arguably a better approach to do this.

One of the first works to consider physical sources of uncertainty at the component level is that of Liang et al. [135], [136]. Similar to Tehrani et al. [113], a sensitivity-based method was used to determine the robustness of the poles when subject to variability in specific physical parameters. In the examples given, the uncertain parameters were contact stiffness coefficients, contact damping coefficients, and friction coefficients. The sensitivity of the closed-loop poles were formulated explicitly in terms of these parameters and not just arbitrary complex perturbations to the measured receptance data. After converting to a non-dimensional form, the sensitivities of each pole with respect to the physical parameters were calculated.

The studies by Liang et al. [135], [136] show the feasibility of considering physical sources of uncertainty in receptance-based methods. Moreover, they demonstrate that the choice of eigenstructure assignment dictates the degree to which uncertainty propagates from physical parameters to the assigned poles and hence frequency and damping characteristics of modes.

Whilst there is an obvious need and scope for the application of uncertainty quantification techniques in receptance-based control of aeroservoelastic systems, little research can be found at present. Indeed, the only work that explicitly addresses this is that of Fichera et al. [137]. This work considered the effect of parameter uncertainties on the design of the feedback controller and the chosen gain vectors. A numerical model of the experimental single-input MODFLEX system [130] was created and uncertainty was introduced into the elastic modulus of the spar. Using a polynomial chaos (PC) expansion, a surrogate model of the flutter V-g diagram was created and the variability of the flutter speed with respect to the uncertain elastic modulus was obtained. The effect of the uncertain elastic modulus on the input-output transfer functions at different freestream speeds was also described using a PC expansion and was visualised by sampling of the expansion. Finally, a separate PC expansion was used to create a surrogate model of the control gains for a fixed control objective. For each outcome of the random elastic modulus, the poles of the system were placed to increase the damping of the first bending and torsional mode and to separate their frequencies. The probability density functions of the control gains were then calculated and compared to the deterministic case. Interestingly, it was shown that the maximum value in the PDF plots did not correspond to the values of the deterministic control gains. This reinforces the idea that designing the controller for the

deterministic system may lead to poor robustness and instead it may be more appropriate to choose the control gains about a condition corresponding to the maximum likelihood.

2.4 Summary

The chapter surveys some of the key literature in the fields of aeroservoelasticity, uncertainty quantification, and receptance-based control techniques. First, the principles of active flutter suppression are described, and its superiority over traditional passive measured is discussed. Next, the effects of uncertainty in AFS is reviewed and some techniques to quantify and mitigate these effects have been introduced. These include both probabilistic and non-probabilistic methods. It is also suggested that design optimisation techniques may be used in the realm of aeroelastic control in order to facilitate a more reliable and robust AFS solution. Finally, receptance-based methodologies are introduced, including both structural modification theory and the Receptance Method. It is shown how the Receptance Method facilitates a experiment-driven approach to active control and eliminated the need for numerical models of the aeroservoelastic system, which are difficult to obtain. Whilst receptance-based control has been considered in aeroelastic settings, further work is needed to better suit these methods for industrial practice. This is the principal aim of this thesis.

Chapter 3

Preliminary Theory

3.1 Introduction

This chapter serves to review some of the fundamental theory that is required in the latter chapters of this thesis. Essential concepts and physical quantities, such as the definition of flutter and its associated speed, are introduced and formalised. The aim here is to introduce a notation that remains consistent throughout this thesis and thus this chapter also serves as a reference for the techniques developed hereinafter.

The outline of this chapter is as follows. First, the equations of motion describing a general, linear aeroservoelastic system are described, both in terms of the time domain and frequency domain. The frequency domain formulation introduces two important quantities: (i) the receptance matrix, and (ii) the input-output transfer function matrix. Both of these matrices form the basis of the receptance-based approaches that are developed in the chapters that follow. After this, a formal definition of flutter is given. The definition introduces two separate, but closely related, quantities: the open-loop flutter speed and the closed-loop flutter speed. It is briefly shown how the application of an arbitrary feedback controller can give rise to a closed-loop flutter speed that is higher than its open-loop counterpart and thus the idea behind active flutter suppression is formalised mathematically. Finally, the effect of uncertainty in structural and/or aerodynamic parameters on the open- and closed-loop flutter speeds is described. The concept of a probabilistic flutter speed is introduced and the idea of treating the aeroservoelastic system as a stochastic dynamic system is considered.

3.2 Aeroelastic Equations of Motion

As discussed in Chapter 2, an AFS system is comprised of three main elements: (i) the structure, (ii) the aerodynamics, and (iii) a controller. Together, the combined structural and aerodynamic equations of motion describe the aeroelastic system. It is this coupled system that the design of the controller is based on. Since the aim here is to describe any arbitrary aeroelastic system, the model given in Fig. 2.4 is simplified to the form given in Fig. 3.1. In other words, one can view the aeroelastic system as a black box with several inputs and outputs. Usually, the outputs from the system are displacements measured at certain locations on the wing. The inputs, on the other hand, are a mixture of two types: (i) deflection angles of one or more control surfaces, and (ii) external disturbance forces. The first of these inputs is what the controller is designed to assign in most aeroservoelastic applications in the literature, as discussed previously.

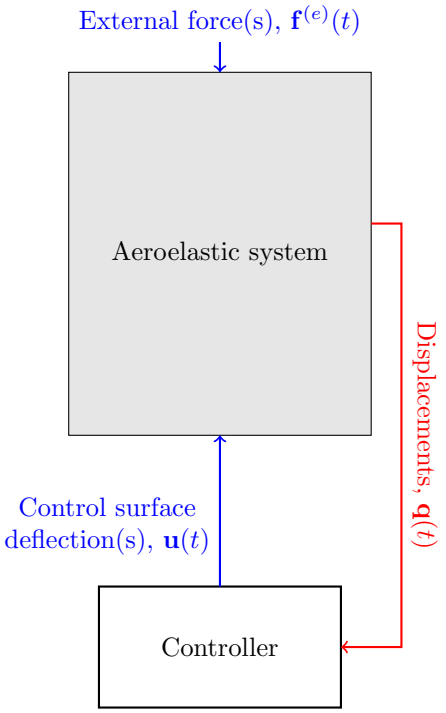

Figure 3.1: Simplified diagram of a typical aeroservoelastic system.

The coupled structural and aerodynamic equations of motion describing the aeroelastic system may be written in the time domain using a generalised state space approach. In this general form,

$$\dot{\mathbf{x}}(t) = f(\mathbf{x}(t), v) + g_1(\mathbf{u}(t), v) + g_2(\mathbf{f}^{(e)}(t), v), \tag{3.1}$$

$$\mathbf{y}(t) = h(\mathbf{x}(t)), \tag{3.2}$$

where $\mathbf{x}(t) \in \mathbb{R}^n$ is the state vector, $\mathbf{u}(t) \in \mathbb{R}^{m_1}$ is the vector of m_1 control surface inputs, $\mathbf{f}^{(e)}(t) \in \mathbb{R}^{m_2}$ is the vector of m_2 external force inputs, $\mathbf{y}(t) \in \mathbb{R}^r$ is the output vector, and $v \in \mathbb{R}$ is the freestream speed. The freestream speed is defined as the speed of the interacting fluid at a distance far away from the aerofoil.

This study is restricted to linear aeroservoelastic systems. That is, systems where the equations of motion describing both the structure and aerodynamic are linear differential equations. Under this restriction, Eqs. 3.1 and 3.2 may be expressed in the form

$$\dot{\mathbf{x}}(t) = \mathbf{A}(v)\mathbf{x}(t) + \mathbf{B}_{\mathrm{CS}}(v)\mathbf{u}(t) + \mathbf{B}_{\mathrm{F}}(v)\mathbf{f}^{(e)}(t), \tag{3.3}$$

$$\mathbf{y}(t) = \mathbf{C}\mathbf{x}(t), \tag{3.4}$$

where $\mathbf{A}(v) \in \mathbb{R}^{n\times n}$, $\mathbf{B}_{\mathrm{CS}}(v) \in \mathbb{R}^{n\times m_1}$, $\mathbf{B}_{\mathrm{F}}(v) \in \mathbb{R}^{n\times m_2}$ and $\mathbf{C} \in \mathbb{R}^{r\times n}$ are collectively named the system matrices.

Taking the Laplace transform of Eqs. 3.3 and 3.4 and dropping the initial value terms gives that

$$s\mathbf{x}(s) = \mathbf{A}(v)\mathbf{x}(s) + \mathbf{B}_{\mathrm{CS}}(v)\mathbf{u}(s) + \mathbf{B}_{\mathrm{F}}(v)\mathbf{f}^{(e)}(s), \tag{3.5}$$

$$\mathbf{y}(s) = \mathbf{C}\mathbf{x}(s), \tag{3.6}$$

where s is the complex Laplace variable. Joining Eqs. 3.5 and 3.6 and eliminating $\mathbf{x}(s)$ leads to

$$\mathbf{y}(s) = \mathbf{C}\left(s\mathbf{I} - \mathbf{A}(v)\right)^{-1}\mathbf{B}_{\mathrm{CS}}(v)\mathbf{u}(s) + \mathbf{C}\left(s\mathbf{I} - \mathbf{A}(v)\right)^{-1}\mathbf{B}_{\mathrm{F}}(v)\mathbf{f}^{(e)}(s), \tag{3.7}$$

or equivalently

$$\mathbf{y}(s) = \mathbf{R}(s, v)\mathbf{u}(s) + \mathbf{H}(s, v)\mathbf{f}^{(e)}(s), \tag{3.8}$$

where

$$\mathbf{H}(s, v) = \mathbf{C}\left(s\mathbf{I} - \mathbf{A}(v)\right)^{-1}\mathbf{B}_{\mathrm{F}}(v), \tag{3.9}$$

$$\mathbf{R}(s, v) = \mathbf{C}\left(s\mathbf{I} - \mathbf{A}(v)\right)^{-1}\mathbf{B}_{\mathrm{CS}}(v). \tag{3.10}$$

The matrix $\mathbf{H}(s, v)$ is named the *receptance matrix* and is a matrix of transfer functions relating the system's outputs to the external force inputs. The matrix $\mathbf{R}(s, v)$ is named the *input-output transfer function matrix* and, by contrast, relates the system's outputs to the control surface deflection inputs. Although these matrices correspond to different types of inputs, they can be related to each other by

$$\mathbf{R}(s, v) = \mathbf{H}(s, v)\mathbf{B}_{\mathrm{CS}\to\mathrm{F}}(s, v), \tag{3.11}$$

where $\mathbf{B}_{\mathrm{CS}\to\mathrm{F}}(s, v)$ is named the force distribution matrix. This matrix serves to map the control surface deflections to equivalent forces acting on the system. The above points are illustrated by means of a block diagram in Fig. 3.2.

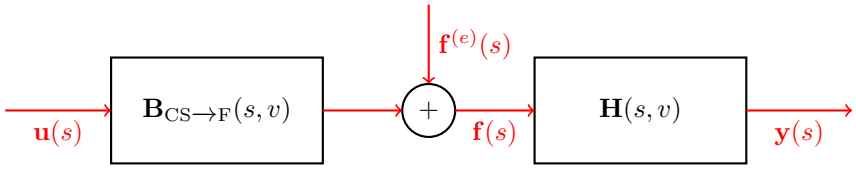

Figure 3.2: Block diagram of the frequency domain formulation.

Suppose that the external force inputs are collocated with the outputs of the system. In this case, $m_2 = r$ and therefore the receptance matrix is square. Under this restriction, the inverse of the receptance matrix $\mathbf{H}(s, v)$ is known as the *dynamic stiffness matrix* and is written as

$$\mathbf{Z}(s, v) = \mathbf{H}^{-1}(s, v). \tag{3.12}$$

Eq. 3.8 can be expressed in terms of the dynamic stiffness matrix by

$$\mathbf{Z}(s, v)\mathbf{y}(s) = \mathbf{f}^{(e)}(s) + \mathbf{Z}(s, v)\mathbf{R}(s, v)\mathbf{u}(s). \tag{3.13}$$

Using Eq. 3.11, Eq. 3.13 can be simplified to

$$\mathbf{Z}(s, v)\mathbf{y}(s) = \mathbf{f}^{(e)}(s) + \mathbf{B}_{\mathrm{CS}\to\mathrm{F}}(s, v)\mathbf{u}(s). \tag{3.14}$$

3.3 Deterministic Flutter Condition

Now that the equations of motion for an arbitrary aeroservoelastic system have been described, it is possible to define the flutter condition and two of its important quantitative features, the flutter speed and the flutter frequency. The flutter speed is the lowest freestream speed at which the system transitions from stable to marginally stable. In other words, one or more poles move

from the left-hand side of the complex plane to points that lie exactly on the imaginary axis. The flutter frequency is defined as the frequency at which the system oscillates, in steady state, when the freestream speed is identically equal to the flutter speed.

In the analysis that follows, the flutter condition is defined for two situations. The first situation corresponds to the open-loop system. This is where there is no external controller and the control inputs are set to zero at all times. The second situation corresponds to the closed-loop system. In this case, there is some external controller that serves to modify the dynamics of the system.

3.3.1 Open-Loop System

Consider the open-loop system, where $\mathbf{u}(s) = \mathbf{0}$. Eq. 3.8 becomes

$$\mathbf{y}(s) = \mathbf{H}(s, v)\mathbf{f}^{(e)}(s), \tag{3.15}$$

and hence the output vector is dependent only on the receptance matrix and the external force inputs. Using Eq. 3.9 and the definition of the matrix inverse, Eq. 3.15 can be written as

$$\mathbf{y}(s) = \frac{1}{\det\left(s\mathbf{I} - \mathbf{A}(v)\right)}\mathbf{C}\mathrm{adj}\left(s\mathbf{I} - \mathbf{A}(v)\right)\mathbf{B}_{\mathrm{F}}(v)\mathbf{f}^{(e)}(s), \tag{3.16}$$

where $\det(\cdot)$ and $\mathrm{adj}(\cdot)$ denote the determinant and adjugate matrix, respectively. The determinant term is also known as the characteristic equation and can be expressed in the form

$$\det\left(s\mathbf{I} - \mathbf{A}(v)\right) = \prod_{i=1}^{l}\left(s - \lambda_i(v)\right), \tag{3.17}$$

where $\lambda_i(v) \in \mathbb{C}$ are the open-loop poles of the system. Collectively, the open-loop poles form a set $\lambda(v) = \{\lambda_1(v), \lambda_2(v), \ldots, \lambda_l(v)\}$. Assuming $\mathbf{A}(v)$ is real for all values of v, the set of open-loop poles are closed under conjugation. Thus, any complex poles appear in conjugate pairs referred to as 'pole pairs' hereinafter.

As indicated by the notation, the open-loop poles are a function of the freestream speed. In other words, there is a different set of open-loop poles at each freestream speed. This allows one to define the flutter speed of the system as follows. Let a function $G_{\mathrm{OL}}(v)$ be written as

$$G_{\mathrm{OL}}(v) = \max_i\left(\mathrm{Re}\left(\lambda_i(v)\right)\right). \tag{3.18}$$

The open-loop flutter speed v^*_{OL} is defined as the freestream speed for which

$$G_{\mathrm{OL}}(v^*_{\mathrm{OL}}) = 0. \tag{3.19}$$

At the flutter speed, a pole pair lies precisely on the imaginary axis and thus there are eigenvalue solutions given by

$$\lambda_{1,2} = \pm\mathrm{i}\omega^*, \tag{3.20}$$

where $\omega^* \in \mathbb{R}$ is the flutter frequency.

It is important to point out that there may be more than one solution to Eq. 3.19. However, it is customary to consider only the smallest solution. This is because, in practice, the lowest value gives the first transition to instability and thus higher values are insignificant as one could not physically achieve this without already experiencing flutter and potentially damaging the

system.

3.3.2 Closed-Loop System

Suppose now that the control surface inputs are not identically zero but are instead related to the output vector by the transfer function

$$\mathbf{u}(s) = \mathbf{G}(s)\mathbf{y}(s). \tag{3.21}$$

Eq. 3.8 becomes

$$\mathbf{y}(s) = \mathbf{H}(s,v)\mathbf{f}^{(e)}(s) + \mathbf{R}(s,v)\mathbf{G}(s)\mathbf{y}(s), \tag{3.22}$$

or equivalently

$$\mathbf{y}(s) = \left(\mathbf{I} - \mathbf{R}(s,v)\mathbf{G}(s)\right)^{-1}\mathbf{H}(s,v)\mathbf{f}^{(e)}(s). \tag{3.23}$$

By inspection, the characteristic equation of the closed-loop system is

$$\det\left(\mathbf{I} - \mathbf{R}(s,v)\mathbf{G}(s)\right) = 0. \tag{3.24}$$

As before, the characteristic equation may be written as

$$\det\left(\mathbf{I} - \mathbf{R}(s,v)\mathbf{G}(s)\right) = \prod_{i=1}^{l}\left(s - \mu_i(v)\right) = 0, \tag{3.25}$$

where $\mu_i(v) \in \mathbb{C}$ are the closed-loop poles of the system. Similar to the open-loop system, the set of closed-loop poles is denoted $\mu(v) = \{\mu_1(v), \mu_2(v), \ldots, \mu_l(v)\}$. In general, the closed-loop poles defined above do not match those of the open-loop system. Indeed, the application of the controller serves to shift the poles to different points in the complex plane at different freestream speeds[1].

A similar function to that in Eq. 3.18 can be defined for the closed-loop system. Let $G_{\mathrm{CL}}(v)$ be written as

$$G_{\mathrm{CL}}(v) = \max_i\left(\mathrm{Re}\left(\mu_i(v)\right)\right). \tag{3.26}$$

The closed-loop flutter speed is then defined as

$$G_{\mathrm{CL}}(v^*_{\mathrm{CL}}) = 0. \tag{3.27}$$

In general, the open-loop and closed-loop flutter speeds are not identical. In other words, the flutter condition is modified by introducing a feedback controller. This gives rise to the principle of active flutter suppression. Simply by applying a controller, the dynamics of the system are modified and the poles are shifted so that the transition to instability arises at a high freestream speed.

3.4 Stochastic Flutter Condition

The above analysis gives the traditional definition of flutter. Although conceptually straightforward and widely used, it assumes that the system matrices, or equivalently the receptance and transfer function matrices, are known a priori. This is why the above analysis is commonly

[1]Some poles, however, may remain unchanged from the open-loop system. This is known as partial pole placement and is discussed further in Chapter 5

referred to as the 'deterministic flutter condition'. As discussed in Chapter 2, complete, deterministic knowledge of the structural and aerodynamic parameters is impossible and there is always some degree of uncertainty. Therefore, as has been previously argued, it is perhaps more suitable to modify the flutter condition to explicitly consider the effect of uncertainties. This modified flutter condition is known as the 'stochastic flutter condition' and is addressed here.

3.4.1 Open-Loop System

Consider again the state space equations of the aeroservoelastic system. However, now suppose that the system matrices are dependent on some uncertain parameters. This is expressed mathematically as

$$\dot{\mathbf{x}}(t) = \mathbf{A}(v, \boldsymbol{\theta})\mathbf{x}(t) + \mathbf{B}_{\mathrm{CS}}(v, \boldsymbol{\theta})\mathbf{u}(t) + \mathbf{B}_{\mathrm{F}}(v, \boldsymbol{\theta})\mathbf{f}^{(e)}(t), \tag{3.28}$$

$$\mathbf{y}(t) = \mathbf{C}\mathbf{x}(t), \tag{3.29}$$

where $\boldsymbol{\theta} \in \mathbb{R}^p$ is a vector of p random variables. As before, the receptance and transfer function matrices are given by

$$\mathbf{H}(s, v, \boldsymbol{\theta}) = \mathbf{C}\left(s\mathbf{I} - \mathbf{A}(v, \boldsymbol{\theta})\right)^{-1}\mathbf{B}_{\mathrm{F}}(v, \boldsymbol{\theta}), \tag{3.30}$$

$$\mathbf{R}(s, v, \boldsymbol{\theta}) = \mathbf{C}\left(s\mathbf{I} - \mathbf{A}(v, \boldsymbol{\theta})\right)^{-1}\mathbf{B}_{\mathrm{CS}}(v, \boldsymbol{\theta}). \tag{3.31}$$

However, by contrast, both of these matrices are now dependent on the vector of random parameters and therefore are also uncertain.

By repeating the same analysis in §3.3.1, the open-loop flutter condition is expressed as

$$G_{\mathrm{OL}}(v^*_{\mathrm{OL}}, \boldsymbol{\theta}) = 0. \tag{3.32}$$

Now, the flutter condition has an explicit dependency on the vector of random parameters. Consequently, the flutter speed depends on the outcome of the random parameters and so

$$v^*_{\mathrm{OL}} = w_{OL}(\boldsymbol{\theta}), \tag{3.33}$$

where $w_{OL}(\boldsymbol{\theta})$ is some function of the random variables.

Due to the probabilistic nature of the random parameters, the open-loop flutter speed is no longer deterministic. Instead, it has a probability distribution. An example of such a distribution is illustrated diagrammatically in Fig. 3.3. In this case, it is no longer possible to define a single, unique flutter speed. One must, instead, treat the flutter speed as a probabilistic variable and use statistics.

There are two main statistics that are used to quantify the flutter speed in the stochastic condition: (i) the mean, and (ii) the variance. The mean denotes the average flutter speed. The variance, on the other hand, gives the variability and indicates how far the true flutter speed may be from the mean value. Let the joint probability density function of the vector of random parameters be written $f(\theta_1, \theta_2, \ldots, \theta_p)$. The mean and variance of the flutter speed are given

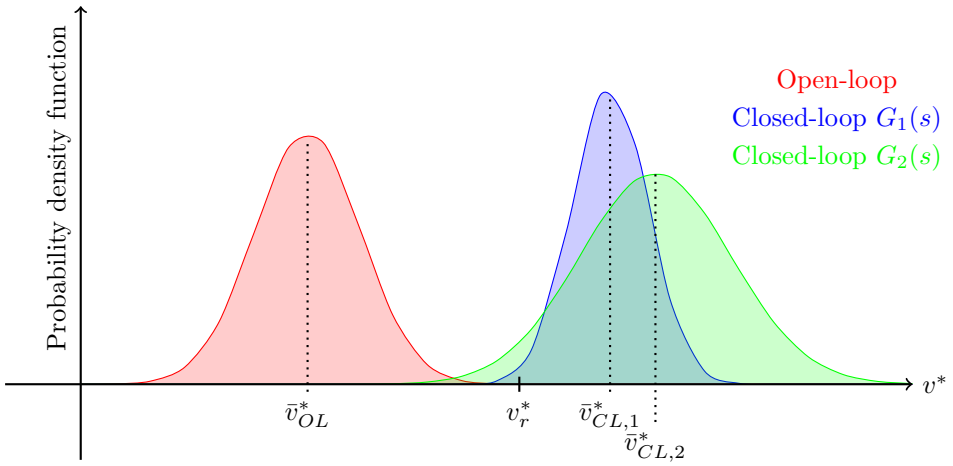

Figure 3.3: Probabilistic flutter distribution in an aeroservoelastic system with uncertainty. $G_1(s)$ and $G_2(s)$ are different control transfer functions.

respectively by

$$\bar{v}^*_{OL} = \mathrm{E}\{v^*_{\mathrm{OL}}\} = \int_{-\infty}^{\infty}\int_{-\infty}^{\infty}\cdots\int_{-\infty}^{\infty} w_{OL}(\boldsymbol{\theta}) f(\theta_1,\theta_2,\ldots,\theta_p)d\theta_1 d\theta_2\ldots d\theta_p, \tag{3.34}$$

$$\mathrm{Var}\{v^*_{\mathrm{OL}}\} = \int_{-\infty}^{\infty}\int_{-\infty}^{\infty}\cdots\int_{-\infty}^{\infty} \left(w_{OL}(\boldsymbol{\theta}) - \bar{v}^*_{OL}\right)^2 f(\theta_1,\theta_2,\ldots,\theta_p)d\theta_1 d\theta_2\ldots d\theta_p. \tag{3.35}$$

The mean and variance require knowledge of the joint probability distribution and the function w_{OL}. In practice, it is difficult, or even impossible, to obtain an analytical expression for w_{OL}. Instead, it is often the case that one has to approximate the probability by estimating the function. The process of estimating or approximating the function is known as surrogate modelling and is one of the strategies that is used in the later chapters to solve the mean and variance integrals.

3.4.2 Closed-Loop System

Suppose now that the feedback controller defined in Eq. 3.21 is again applied to the system. As before, this serves to modify the flutter speed. However, unlike in the deterministic case, one cannot define a simple change in the flutter speed. Instead, one has to consider its effect on the probability distribution.

Following the same procedure as previously, the stochastic flutter condition in the closed-loop system is given by

$$G_{\mathrm{CL}}(v^*_{\mathrm{CL}}, \mathbf{G}(s), \boldsymbol{\theta}) = 0. \tag{3.36}$$

Therefore, the flutter speed is expressed in the form

$$v^*_{\mathrm{OL}} = w_{CL}(\mathbf{G}(s), \boldsymbol{\theta}), \tag{3.37}$$

where $w_{CL}(\mathbf{G}(s), \boldsymbol{\theta})$ is some arbitrary function. By contrast with its open-loop counterpart, the above equation is a function of both the random parameters and the feedback law given by the matrix $\mathbf{G}(s)$. Therefore, the probabilistic distribution of the flutter speed depends on *both* of these quantities.

Figure 3.3 shows an example of the effect of choosing different feedback controllers on the distribution of the flutter speed. The blue curve, corresponding to the feedback matrix $\mathbf{G}_1(s)$,

has a higher mean than its open-loop counterpart. Additionally, its spread is less, meaning that the variance is lower. The green curve, corresponding to the feedback $\mathbf{G}_2(s)$, has a higher mean value than the controller corresponding to the blue curve. However, this is at the expense of the variance. Indeed, at lower speeds, such as that of v_r^* given in Fig. 3.3, is it more likely that flutter arises using the second controller rather than the first. This balance of an increased mean and possibly increased variance lies at the heart of controlling aeroservoelastic systems with uncertainty. One must be able to judge, in a quantitative manner, whether the improvement in the flutter speed is justified with regards to the confidence that one has in knowing its range across all possible random parameters. This is a crucial point that is addressed in the techniques developed in this thesis.

3.5 Summary

The purpose of this chapter is to introduce, define and formalise some of the fundamental concepts that are required in the latter chapters of this thesis. The aeroservoelastic equations of motion are defined in the frequency domain by use of the receptance and input-output transfer function matrices. These matrices give the relationship between the outputs of the system, which are usually displacements, and the external force and control surface inputs. Using these matrices, the flutter speed is defined and the effect of a closed-loop controller is considered. The conventional analysis of flutter assumes that all parameters in the system are known a priori. However, due to uncertainties, this approach is contentious and it is arguably more appropriate to treat the flutter condition in a probabilistic setting. This setting is known as the 'stochastic flutter speed' and gives rise to the concept of a probability density function over the flutter speed. It has been shown that the application of a controller, using conventional feedback control techniques, can modify the mean of the flutter speed, thus permitting active flutter suppression. However, in the stochastic setting, one must also consider the influence of the variance of the flutter speed.

Chapter 4

Aeroservoelastic Models

4.1 Introduction

In Chapters 5 to 8, several examples and case studies are presented to both verify and validate the techniques that are developed. Therefore, before commencing with the main study, it is useful to first introduce the models that are used in such examples. The examples use two separate aeroservoelastic models, one experimental and one numerical.

The experimental model, which is also referred to as the wind-tunnel model, is based on the 'typical section' described by Dowell [16]. It is a two-dimensional aerofoil that is equipped with both a leading- and trailing-edge control surface. The model resides in the University of Liverpool's subsonic wind tunnel facility and is used as the baseline model in the experimental case studies that are presented in the later chapters. Since this thesis is concerned with receptance-based approaches, there is no tuned numerical model accompanying the experimental setup. Indeed, the experimental case studies only use measured data from the system. In this way, the real-world conditions under which the developed techniques would be applied are emulated experimentally; that is, one cannot use information obtained from a numerical model to influence the application of the techniques.

In practice, it is also necessary to have a separate numerical model. This is to permit rapid testing in an environment that is free from the errors associated with the experimental model and its measured data. Therefore, it was decided in the early stages of this project to use a popular reference numerical model from the established literature. In this way, the results from the model are already validated. The specific reference model that is used is that of Platanitis and Strganac [138]. Similar to the experimental model, this model is also a pitch-plunge system with both a leading- and trailing-edge control surface.

Both models are described in detail in this chapter. First, the reference numerical model is described together with a derivation of the equations of motion. The equations of motion are cast into the standard state space form for aeroservoelastic systems (shown in Chapter 3) and the equivalent transfer function representation is given. Key results from the model are stated, including the flutter speed, the variation of the open-loop poles with the freestream speed, and Bode plots of the receptance and input-output transfer function matrices. Following this, the experimental setup is described alongside a discussion of some of the design choices in select components. A summary of the key properties, such as the flutter speed, is also presented and a comparison between the numerical and experimental results is made.

4.2 Numerical Model

In this section, the reference numerical model is described. The aeroservoelastic equations of motion are derived from first principles and then cast into the standard time and frequency domain formulations that were shown in Chapter 3.

The numerical model is illustrated diagrammatically in Figs. 4.1 and 4.2. Assuming that the model is rigid along its span, the position of the system is fully described by four degrees-of-freedom, namely: the plunge displacement h, the pitch angle α, the trailing-edge control surface deflection angle β, and the leading-edge control surface deflection angle γ. The plunge and pitch degrees of freedom are restrained by a vertical and rotational spring, respectively. Although not shown, a damper is also placed in each of these degrees-of-freedom in order to model energy losses, such as friction in mechanical connections and air resistance. The leading- and trailing-edge control surface are not restrained by any mechanical elements. Instead, they are each governed by a motor, which is itself operated by a position controller. That is, a closed-loop controller that assigns a desired control surface deflection angle. This is considered in more detail later on.

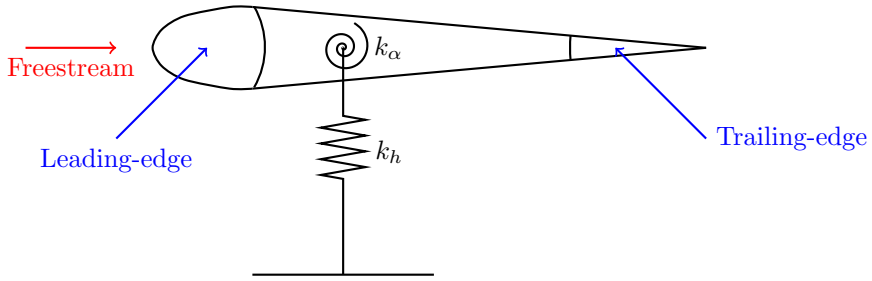

Figure 4.1: Numerical aeroservoelastic system with leading- and trailing-edge control surfaces.

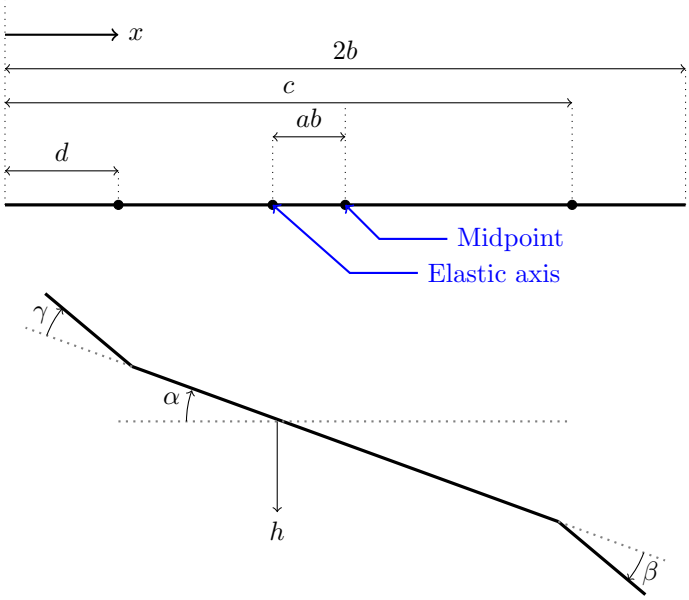

Figure 4.2: Two-dimensional representation of the numerical aeroservoelastic system.

4.2.1 Structural Model

First, the structural equations of motion are derived using a Lagrangian-based approach. Applying Lagrange's equation of the second kind gives that

$$\frac{d}{dt}\left(\frac{\partial T}{\partial \dot{q}_i} - \frac{\partial V}{\partial \dot{q}_i}\right) - \frac{\partial T}{\partial q_i} + \frac{\partial V}{\partial q_i} + \frac{\partial \mathcal{D}}{\partial \dot{q}_i} = f_i, \quad i = 1, 2, \ldots, 4, \tag{4.1}$$

where $\mathbf{q} = \begin{pmatrix} h & \alpha & \beta & \gamma \end{pmatrix}^T$ is the vector of degrees-of-freedom, T is the kinetic energy term, V is the potential energy term, $\mathcal{D}$ is the dissipation term, and f_i is the generalised external force acting in the coordinate q_i. The potential energy term V is simply the energy stored in the springs and thus

$$V = \frac{1}{2}k_h h^2 + \frac{1}{2}k_\alpha \alpha^2, \tag{4.2}$$

where k_h and k_α are the plunge and pitch stiffness parameters, respectively. The dissipation term D is equal to the rate of energy loss through the dampers, and therefore

$$\mathcal{D} = \frac{1}{2}c_h \dot{h}^2 + \frac{1}{2}c_\alpha \dot{\alpha}^2, \tag{4.3}$$

where c_h and c_α are the plunge and pitch damping coefficients, respectively. The kinetic energy term T is derived by dividing the aerofoil into a series of differential elements, as shown in Fig. 4.3. Let the kinetic energy of a differential element be written as

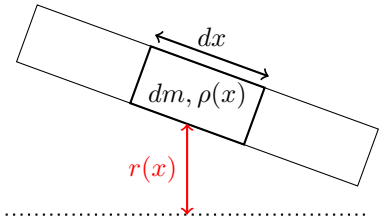

Figure 4.3: Differential aerofoil element.

$$dT = \frac{1}{2}\dot{r}(x)^2 dm, \tag{4.4}$$

where $r(x)$ is the instantaneous displacement of the element. By introducing the mass per unit chord length $\rho(x)$, Eq. 4.4 is equivalent to

$$dT = \frac{1}{2}\dot{r}(x)^2 \rho(x) dx, \tag{4.5}$$

and thus the total kinetic energy is given by

$$T = \int_0^{2b} dT = \frac{1}{2}\int_0^{2b} \dot{r}(x)^2 \rho(x) dx. \tag{4.6}$$

By assuming small deflection angles in the rotational degrees-of-freedom, the instantaneous displacement may be approximated as

$$r(x) \approx \begin{cases} h + (x-e)\alpha + (x-d)\gamma, & 0 \le x \le d, \\ h + (x-e)\alpha, & d \le x \le c, \\ h + (x-e)\alpha + (x-c)\beta, & c \le x \le 2b, \end{cases} \tag{4.7}$$

and hence the instantaneous velocity is given by

$$\dot{r}(x) \approx \begin{cases} \dot{h} + (x-e)\dot{\alpha} + (x-d)\dot{\gamma}, & 0 \le x \le d, \\ \dot{h} + (x-e)\dot{\alpha}, & d \le x \le c, \\ \dot{h} + (x-e)\dot{\alpha} + (x-c)\dot{\beta}, & c \le x \le 2b. \end{cases} \tag{4.8}$$

Using Eq. 4.8 in Eq. 4.6 gives that

$$\begin{aligned} T = &\frac{1}{2}\int_0^d \left(\dot{h} + (x-e)\dot{\alpha} + (x-d)\dot{\gamma}\right)^2 \rho(x)dx \\ &+ \frac{1}{2}\int_d^c \left(\dot{h} + (x-e)\dot{\alpha}\right)^2 \rho(x)dx \\ &+ \frac{1}{2}\int_c^{2b} \left(\dot{h} + (x-e)\dot{\alpha} + (x-c)\dot{\beta}\right)^2 \rho(x)dx, \end{aligned} \tag{4.9}$$

or equivalently

$$T = \frac{1}{2}\left(M\dot{h}^2 + I_\alpha\dot{\alpha}^2 + I_\beta\dot{\beta}^2 + I_\gamma\dot{\gamma}^2\right) + \dot{\alpha}\dot{h}S_\alpha + \dot{h}\dot{\beta}S_{h\beta} + \dot{\alpha}\dot{\beta}S_{\alpha\beta} + \dot{\alpha}\dot{\gamma}S_{\alpha\gamma} + \dot{h}\dot{\gamma}S_{h\gamma}, \tag{4.10}$$

where

$$M = \int_0^{2b} \rho(x)dx, \tag{4.11}$$

$$I_\alpha = \int_0^{2b} (x-e)^2 \rho(x)dx, \tag{4.12}$$

$$S_\alpha = \int_0^{2b} (x-e)\,\rho(x)dx, \tag{4.13}$$

$$I_\beta = \int_c^{2b} (x-c)^2 \rho(x)dx, \tag{4.14}$$

$$I_\gamma = \int_0^{d} (x-d)^2 \rho(x)dx, \tag{4.15}$$

$$S_{h\gamma} = \int_0^{d} (x-d)\,\rho(x)dx, \tag{4.16}$$

$$S_{h\beta} = \int_c^{2b} (x-c)\,\rho(x)dx, \tag{4.17}$$

$$S_{\alpha\beta} = \int_c^{2b} (x-c)\,(x-e)\,\rho(x)dx, \tag{4.18}$$

$$S_{\alpha\gamma} = \int_0^{d} (x-d)\,(x-e)\,\rho(x)dx. \tag{4.19}$$

When it is assumed that either: (i) the mass of the leading- and trailing-edge control surfaces are small, or (ii) the centre of mass of each control surfaces lies close to its respective hinge, the first and second moment of inertia terms associated with the control surfaces are negligibly small. In other words, one can assume that Eqs. 4.14 to 4.19 become zero so that the total kinetic energy term is approximated by

$$T \approx \frac{1}{2}\left(M\dot{h}^2 + I_\alpha\dot{\alpha}^2\right) + S_\alpha\dot{h}\dot{\alpha}. \tag{4.20}$$

By substituting the potential energy, kinetic energy and dissipation terms into Eq. 4.1, the

structural equations of motion are found to be

$$\begin{bmatrix} M & S_\alpha \\ S_\alpha & I_\alpha \end{bmatrix} \begin{bmatrix} \ddot{h} \\ \ddot{\alpha} \end{bmatrix} + \begin{bmatrix} c_h & 0 \\ 0 & c_\alpha \end{bmatrix} \begin{bmatrix} \dot{h} \\ \dot{\alpha} \end{bmatrix} + \begin{bmatrix} k_h & 0 \\ 0 & k_\alpha \end{bmatrix} \begin{bmatrix} h \\ \alpha \end{bmatrix} = \begin{bmatrix} f_h \\ f_\alpha \end{bmatrix}, \tag{4.21}$$

where f_h and f_α are the external forces acting in the h and α degrees-of-freedom, respectively. This is written equivalently in matrix form as

$$\mathbf{M}_s \ddot{\mathbf{q}}_{1:2}(t) + \mathbf{C}_s \dot{\mathbf{q}}_{1:2}(t) + \mathbf{K}_s \mathbf{q}_{1:2}(t) = \mathbf{f}(t), \tag{4.22}$$

with the obvious definitions of $\mathbf{M}_s$, $\mathbf{C}_s$, $\mathbf{K}_s$, $\mathbf{q}_{1:2}(t)$ and $\mathbf{f}(t)$. At this point, it is important to point out that the structural equations of motion describe only the h and α degrees of freedom; there are no dynamic equations associated with the leading- and trailing-edge control surface deflection angles (i.e. β and γ). This is due to the assumption that the first and second moments of inertia of the flaps are negligibly small. It is assumed in the remainder of the analysis that the control surface deflections are input variables to the aeroelastic system. This is equivalent to assuming that the position controllers act to instantaneously assign the control surface deflections to desired values and hence the dynamics of the actuators and controllers are ignored.

For purposes later apparent, the external forces in the pitch and plunge degrees-of-freedom are partitioned into two contributory force types: (i) those that arise from the aerodynamic loading, and (ii) additional external forces, such as those applied during modal testing. Written mathematically,

$$\mathbf{f}(t) = \mathbf{f}^{(a)}(t) + \mathbf{f}^{(e)}(t), \tag{4.23}$$

where $\mathbf{f}^{(a)}(t)$ is the aerodynamic contribution, and $\mathbf{f}^{(e)}(t)$ is the contribution of the external forces. Thus, the final structural equations of motion are

$$\mathbf{M}_s \ddot{\mathbf{q}}_{1:2}(t) + \mathbf{C}_s \dot{\mathbf{q}}_{1:2}(t) + \mathbf{K}_s \mathbf{q}_{1:2}(t) = \mathbf{f}^{(a)}(t) + \mathbf{f}^{(e)}(t), \tag{4.24}$$

or equivalently

$$\ddot{\mathbf{q}}_{1:2}(t) = -\mathbf{M}_s^{-1}\mathbf{C}_s \dot{\mathbf{q}}_{1:2}(t) - \mathbf{M}_s^{-1}\mathbf{K}_s \mathbf{q}_{1:2}(t) + \mathbf{M}_s^{-1}\mathbf{f}^{(a)}(t) + \mathbf{M}_s^{-1}\mathbf{f}^{(e)}(t). \tag{4.25}$$

4.2.2 Aerodynamic Model

With the structural equations of motion derived, one can now consider the influence of the aerodynamic loading. As discussed in Chapter 2, there exists a plethora of different aerodynamic models that are widely used in aeroelastic analyses. Each has its relative advantages, disadvantages, and physical assumptions that make it more or less appropriate to different aeroelastic models. In this particular system, a quasi-steady model is used. This was the choice of the original authors and has been verified experimentally [138].

Under the quasi-steady assumption, the aerodynamic contribution vector is written as

$$\begin{aligned}\mathbf{f}^{(a)}(t) = \rho v b s_p \begin{pmatrix} -C_{l_\alpha} & -\left(\frac{1}{2}-a\right) b C_{l_\alpha} \\ b C_{m_{\alpha-eff}} & \left(\frac{1}{2}-a\right) b^2 C_{m_{\alpha-eff}} \end{pmatrix} \begin{pmatrix} \dot{h} \\ \dot{\alpha} \end{pmatrix} \\ + \rho v^2 b s_p \begin{pmatrix} 0 & -C_{l_\alpha} \\ 0 & b C_{m_{\alpha-eff}} \end{pmatrix} \begin{pmatrix} h \\ \alpha \end{pmatrix} \\ + \rho v^2 b s_p \begin{pmatrix} -C_{l_\beta} & -C_{l_\gamma} \\ b C_{m_{\beta-eff}} & b C_{m_{\gamma-eff}} \end{pmatrix} \begin{pmatrix} \beta \\ \gamma \end{pmatrix},\end{aligned} \tag{4.26}$$

where ρ is the density of air; s_p is the aerofoil span; v is the freestream speed; and C_{l_α}, $C_{m_{\alpha-eff}}$, C_{l_β}, $C_{m_{\beta-eff}}$, C_{l_γ} and $C_{m_{\gamma-eff}}$ are lift and moment coefficients associated with the α, β and γ degrees-of-freedom, respectively. This may be reduced to the matrix form given by

$$\mathbf{f}^{(a)}(t) = -v\mathbf{C}_a\dot{\mathbf{q}}_{1:2}(t) - v^2\mathbf{K}_a\mathbf{q}_{1:2}(t) + v^2\mathbf{B}_a\mathbf{u}(t), \tag{4.27}$$

where

$$\mathbf{C}_a = \rho b s_p \begin{pmatrix} C_{l_\alpha} & \left(\frac{1}{2}-a\right) b C_{l_\alpha} \\ -b C_{m_{\alpha-eff}} & -\left(\frac{1}{2}-a\right) b^2 C_{m_{\alpha-eff}} \end{pmatrix}, \tag{4.28}$$

$$\mathbf{K}_a = \rho b s_p \begin{pmatrix} 0 & C_{l_\alpha} \\ 0 & -b C_{m_{\alpha-eff}} \end{pmatrix}, \tag{4.29}$$

$$\mathbf{B}_a = \rho b s_p \begin{pmatrix} -C_{l_\beta} & -C_{l_\gamma} \\ b C_{m_{\beta-eff}} & b C_{m_{\gamma-eff}} \end{pmatrix}, \tag{4.30}$$

$$\mathbf{u}(t) = \begin{pmatrix} \beta \\ \gamma \end{pmatrix}. \tag{4.31}$$

4.2.3 Coupled Equations of Motion

Finally, it is possible to obtain the coupled equations of motion governing the complete aeroservoelastic system. First, the time-domain formulation using the state-space approach is considered. Following this, the frequency domain formulation is given.

Time-Domain Formulation

Consider again the structural equation of motion, given by

$$\mathbf{M}_s\ddot{\mathbf{q}}_{1:2}(t) + \mathbf{C}_s\dot{\mathbf{q}}_{1:2}(t) + \mathbf{K}_s\mathbf{q}_{1:2}(t) = \mathbf{f}^{(a)}(t) + \mathbf{f}^{(e)}(t). \tag{4.32}$$

Substituting Eq. 4.27 into Eq. 4.32 gives that

$$\mathbf{M}_s\ddot{\mathbf{q}}_{1:2}(t) + \mathbf{C}_s\dot{\mathbf{q}}_{1:2}(t) + \mathbf{K}_s\mathbf{q}_{1:2}(t) = -v\mathbf{C}_a\dot{\mathbf{q}}_{1:2}(t) - v^2\mathbf{K}_a\mathbf{q}_{1:2}(t) + v^2\mathbf{B}_a\mathbf{u}(t) + \mathbf{f}^{(e)}(t), \tag{4.33}$$

or equivalently

$$\mathbf{M}_s\ddot{\mathbf{q}}_{1:2}(t) + \mathbf{C}_t(v)\dot{\mathbf{q}}_{1:2}(t) + \mathbf{K}_t(v)\mathbf{q}_{1:2}(t) = v^2\mathbf{B}_a\mathbf{u}(t) + \mathbf{f}^{(e)}(t), \tag{4.34}$$

where

$$\mathbf{C}_t(v) = \mathbf{C}_s + v\mathbf{C}_a, \tag{4.35}$$

$$\mathbf{K}_t(v) = \mathbf{K}_s + v^2\mathbf{K}_a. \tag{4.36}$$

Let the state vector $\mathbf{x}(t)$ be chosen as

$$\mathbf{x}(t) = \begin{pmatrix} h \\ \alpha \\ \dot{h} \\ \dot{\alpha} \end{pmatrix}. \tag{4.37}$$

The state space formulation is given by

$$\begin{aligned} \begin{pmatrix} \dot{\mathbf{q}}_{1:2}(t) \\ \ddot{\mathbf{q}}_{1:2}(t) \end{pmatrix} = & \begin{pmatrix} \mathbf{0} & \mathbf{I} \\ -\mathbf{M}_s^{-1}\mathbf{K}_t(v) & -\mathbf{M}_s^{-1}\mathbf{C}_t(v) \end{pmatrix} \begin{pmatrix} \mathbf{q}_{1:2}(t) \\ \dot{\mathbf{q}}_{1:2}(t) \end{pmatrix} + \begin{pmatrix} \mathbf{0} \\ v^2\mathbf{M}_s^{-1}\mathbf{B}_a \end{pmatrix} \mathbf{u}(t) \\ & + \begin{pmatrix} \mathbf{0} \\ \mathbf{M}_s^{-1} \end{pmatrix} \mathbf{f}^{(e)}(t), \end{aligned} \tag{4.38}$$

or more compactly

$$\dot{\mathbf{x}}(t) = \mathbf{A}(v)\mathbf{x}(t) + \mathbf{B}_{CS}(v)\mathbf{u}(t) + \mathbf{B}_F\mathbf{f}^{(e)}(t), \tag{4.39}$$

with the obvious definitions of $\mathbf{A}(v)$, $\mathbf{B}_{CS}(v)$, and $\mathbf{B}_F$.

Frequency-Domain Formulation

If one defines the output vector from the aeroelastic system as

$$\mathbf{y}(t) = \begin{pmatrix} h(t) \\ \alpha(t) \end{pmatrix}, \tag{4.40}$$

the corresponding $\mathbf{C}$ matrix satisfying Eq. 3.6 in Chapter 3 is given by

$$\mathbf{C} = \begin{pmatrix} \mathbf{I}_{2\times 2} & \mathbf{0}_{2\times 2} \end{pmatrix}. \tag{4.41}$$

Thus, the receptance matrix and input-output transfer function matrix are given respectively by

$$\mathbf{H}(s, v) = \mathbf{C}\left(s\mathbf{I} - \mathbf{A}(v)\right)^{-1}\mathbf{B}_F, \tag{4.42}$$

$$\mathbf{R}(s, v) = \mathbf{C}\left(s\mathbf{I} - \mathbf{A}(v)\right)^{-1}\mathbf{B}_{CS}(v). \tag{4.43}$$

4.2.4 Results

Here, some of the key results of the numerical model are summarised. The results presented use the structural and aerodynamic parameters that are given in Table 4.1. These are the same as those in the original model presented by Platanitis and Strganac [138] and remain constant throughout all numerical examples in this thesis.

Table 4.1: Structural and aerodynamic parameters in the numerical model.

Parameter	Value	Unit
M	15.57	kg
S_α	0.57	kg m
I_α	0.142	kg m^2
c_h	27.43	Ns/m
c_α	0.036	Nms/rad
k_h	2844	N/m
k_α	12.77	Nm/rad
a	-0.6719	-
b	0.1905	m
s_p	0.5945	m
c_{l_α}	6.757	-
c_{m_α}	0	-
c_{l_β}	3.774	-
c_{m_β}	-0.6719	-
c_{l_γ}	-0.1566	-
c_{m_γ}	-0.1005	-

Open-Loop Pole Variation

First, the variation of the system's poles with the freestream speed v is considered. Figures 4.4 (a) and (b) show the dependency of the real and imaginary parts of the open-loop poles on the freestream speed. That is, the variation of the poles when both control surfaces are set to a deflection angle of zero and there are no external forces. Note that the poles of the system are in conjugate pairs and thus it is only necessary to plot two of them (those with positive imaginary parts).

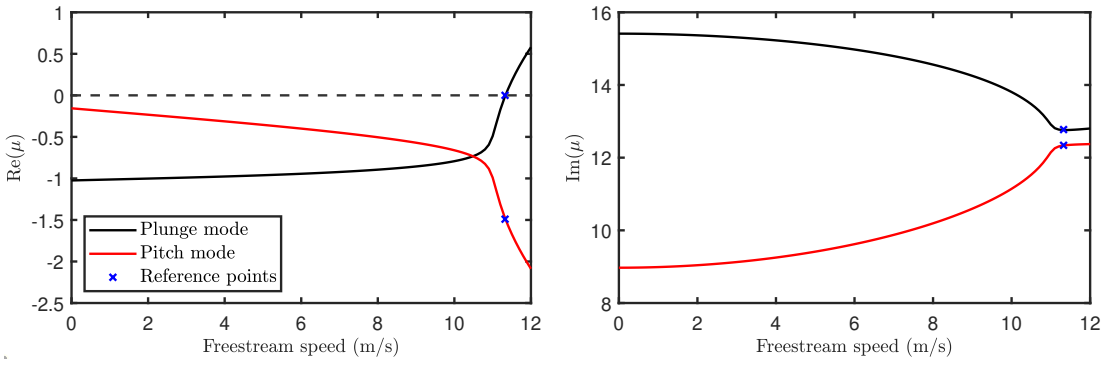

(a) Real part (b) Imaginary part

Figure 4.4: Variation of the open-loop poles in the numerical model with respect to the freestream speed.

Figure 4.4 (a) shows that both pole pairs have negative real parts below speeds of 11.3 m/s and thus the system is stable. However, at this speed one pole pair has a real part of exactly zero and hence the system is marginally stable. Thus, the open-loop flutter speed in the numerical model is $v^*_{OL} = 11.3$ m/s. This matches the value stated by the original authors [138]. Beyond this speed, the pole pair shown by the black line becomes unstable whilst the pole pair shown by the red line continues to increase its damping significantly. The mode corresponding to the black line is the plunge mode; that is, the mode that corresponds mostly to vertical motions[1].

[1] Although, due to the mass coupling in the system, there is also some small movement in the pitch degree-of-freedom as well.

The mode corresponding to the red line represents motions with a large amplitude primarily in the pitch degree-of-freedom.

Figure 4.4 (b) shows the movement of each pole's frequency as the freestream speed increases. As the speed increases, the frequencies of the pitch and plunge modes appear to move together. The rate at which these modes move together increases as the freestream speed increases. This behaviour is typical in binary aeroservoelastic systems, as discussed by Dowell [16].

Both figures show blue points that are named 'reference points'. These points are taken from the work of Lee and Singh [139], who gave precise values of the poles in both the pitch and plunge modes at the flutter speed for the same numerical model. As shown, these points lie exactly on the curves belonging to the numerical model and hence one can consider this as a further verification of the results presented.

Receptance Matrix

Next, the receptance matrix $\mathbf{H}(s, v)$ of the system is considered. Here, the receptance matrix is taken as that when the force inputs are collocated with the outputs, i.e. the pitch and plunge degrees-of-freedom. Figure 4.5 shows its variation as the freestream speed is changed. Initially, at $v = 0$ m/s, the receptance matrix corresponds to that of the structural system. This is because the aerodynamic forces are proportional to v and v^2 and thus do not have any impact. As the freestream speed increases, the two peaks in the receptances move closer together. The rate at which these peaks move closer together increases as the freestream speed increases. This is because effect of the aerodynamic is greater at larger speeds and hence its corresponding forces are more comparable to those generated by the elasticity and inertia of the structural system.

As the freestream speed approaches the flutter speed, the peak of the plunge mode becomes extremely sharp, thus indicating a very small damping value. Meanwhile, at these same speeds, the peak of the pitch mode becomes very small and hence is barely visible in the FRFs. This is due to the large damping that is present in this mode.

An interesting point to consider is the symmetry of the receptance matrix. At the zero freestream speed, the receptances matrix is symmetric about its leading diagonal. This is to be expected as the structural matrices, i.e. the mass, stiffness and damping, are symmetric. However, as the freestream speed increases, one can see that the matrix deviates from the symmetry. This is because the aerodynamic loading is not symmetric and hence large freestream speeds will greatly exhibit asymmetric behaviour in the FRFs.

Transfer Function Matrix

Finally, the transfer function matrix $\mathbf{R}(s, v)$ is considered. Figure 4.6 shows its variation as the freestream speed is modified. Columns one and two are each associated with the β and γ inputs, respectively. Rows one and two are associated with the outputs h and α, respectively. At low speeds, the amplitudes across all frequencies are very small. This is because the aerodynamic forces that the flaps can exert on the system are small and hence have little impact on the system. This is confirmed by the dependency of $\mathbf{B}_{CS}(v)$ on v^2. As the speed increases so too do the amplitudes of the frequency responses. This indicates that the control authorities of the flaps increase as the freestream speed does.

An important point to consider is the behaviour of the transfer function matrix at a zero freestream speed. Substituting $v = 0$ into Eq. 4.43 shows that the matrix collapses to a matrix of zeros. Hence, there is no control input and it is not possible to modify the dynamics of

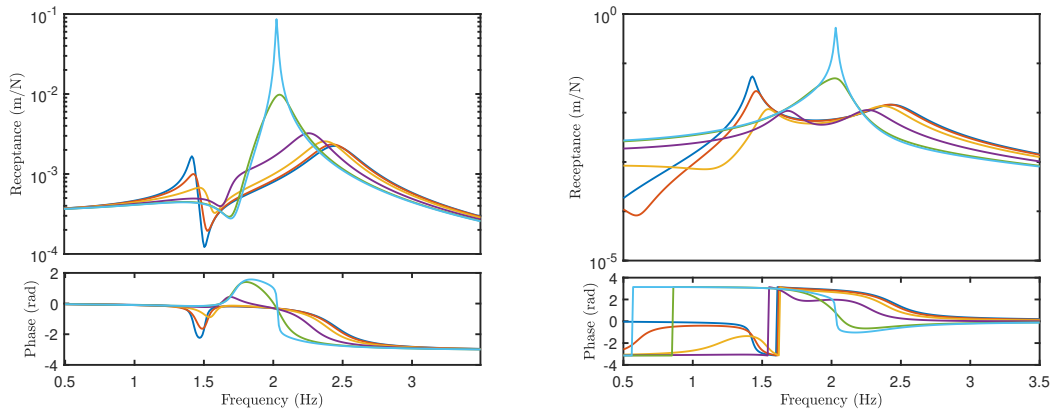

(a) h_{11}

(b) h_{12}

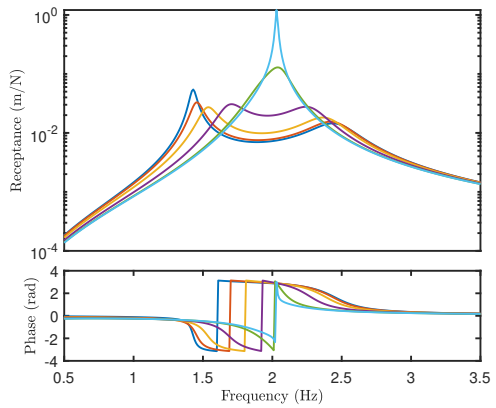

(c) h_{21}

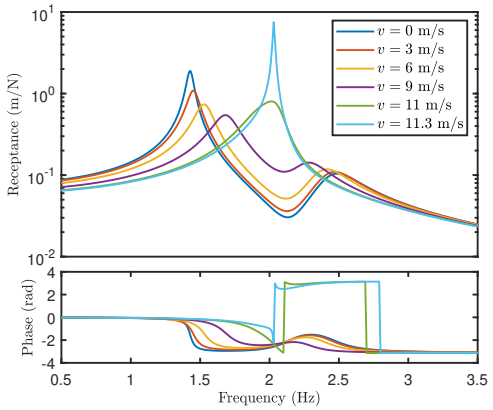

(d) h_{22}

Figure 4.5: Variation of the receptance matrix in the numerical model with respect to the freestream speed.

the system. In practice, one would not expect this to be observed experimentally. Indeed, the inertia of the flap would contribute to the input to the system and hence there would still be a visible FRF. However, the numerical model does not account for this.

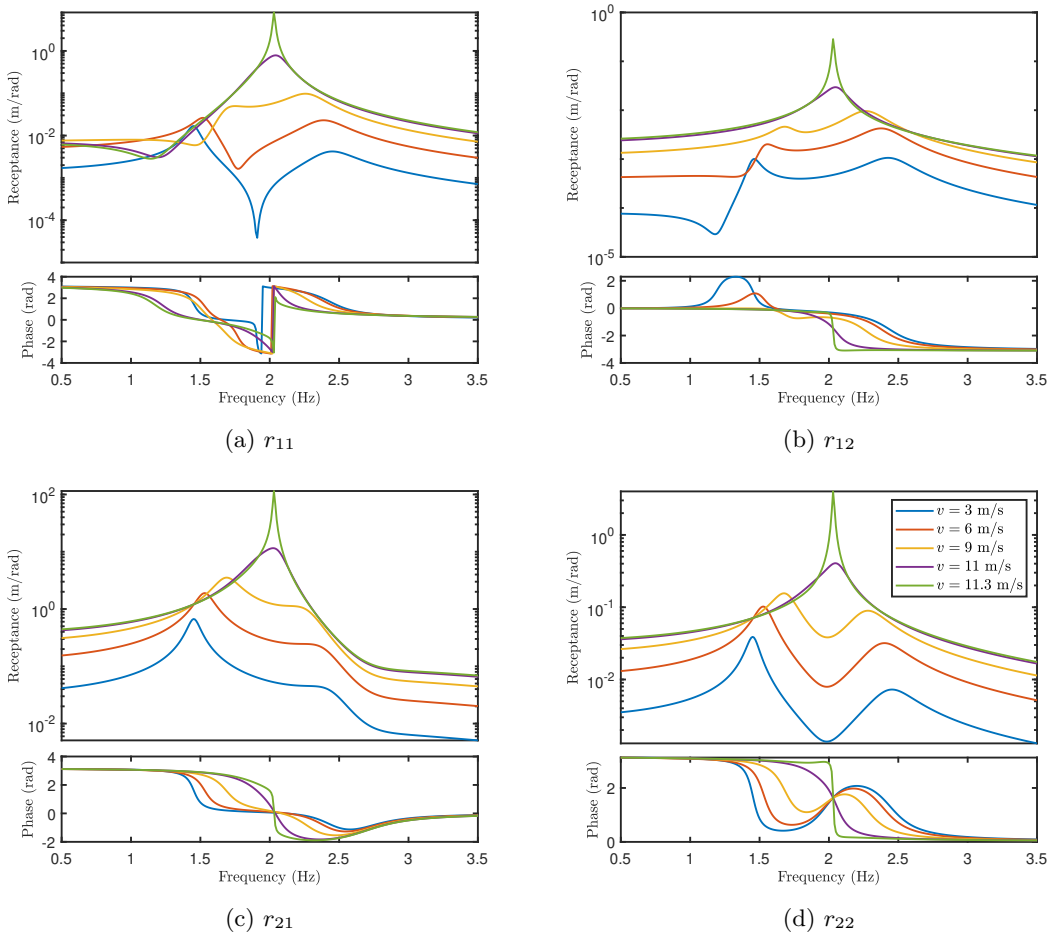

(a) r_{11} (b) r_{12}

(c) r_{21} (d) r_{22}

Figure 4.6: Variation of the input-output transfer function matrix in the numerical model with respect to the freestream speed.

4.3 Experimental Model

Here, the experimental aeroservoelastic model is described. The model is comprised of two main assemblies: (i) the aerofoil, which is placed inside a portable test section; and (ii) the outer support structure, which is fixed to the outside of the test section.

4.3.1 Setup

Aerofoil

The aerofoil is comprised of five 3D printed, ABS aerodynamic sectors. Each sector has a chord length of 0.3 m and a cross section that corresponds to the NACA0018 profile. The internal structure of each profile is as shown in Fig. 4.7. This has been designed so that each sector is both rigid but also lightweight. Each sector is mounted to two aluminium spars, which run parallel to the span of the aerofoil, by means of four bolts that are placed on the underside of the aerofoil. The arrangements of the sectors and the spars are given in Fig. 4.8. In total, the aerofoil has a span of 1.2 m.

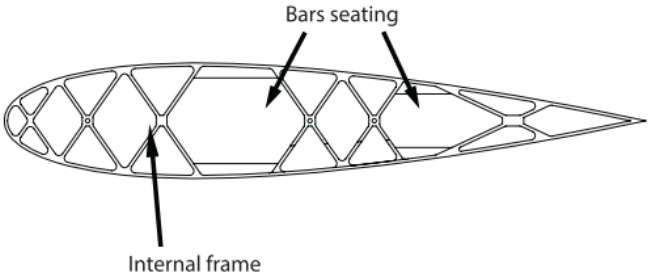

Figure 4.7: Internal structure of the aerodynamic sectors. *[Image taken from [140]]*

Figure 4.8: Arrangement of the aerodynamic sectors.

The two aluminium spars, which are shown in Fig. 4.9, were designed so that there is negligible twisting or bending across the span of the aerofoil. Furthermore, this design ensures

that the fundamental frequency of each beam lies far away from the frequencies of the pitch and plunge modes, which are discussed later.

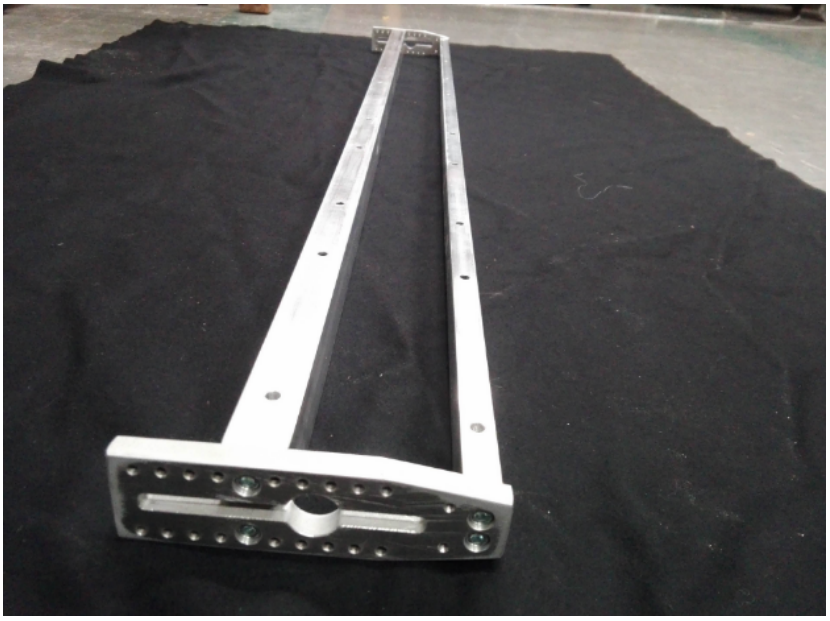

Figure 4.9: Central spars. *[Image taken from [140]]*

The central sector, i.e. that which lies in the middle of the aluminium spars, contains both a leading- and trailing-edge control surface, as shown in Fig. 4.10. These control surfaces are each designed to rotate about fixed axes that lie parallel to the span and are held in place by bearings on both sides of the control surfaces. Two Maxon 60W current controlled, brushless DC motors are housed inside the central sector; one at the interface with the leading-edge and one at interface with the trailing-edge. The control surfaces are clamped internally to each motor shaft and hence the motors are used as the means of actuation. Both motors are equipped with an encoder, which reads the instantaneous rotational displacement of the shaft and hence the angle of deflection of the control surface. The current supplied to each of the motors is controlled by two PID controllers, which are discussed later.

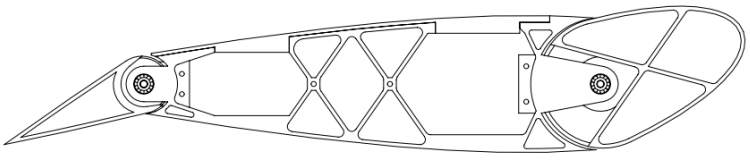

Figure 4.10: Cross section of the central sector with control surfaces. *[Image taken from [140]]*

Support Structure

The aerofoil is mounted to the external support structure through four bolts on both sides of the aerofoil. The support structure consists of a series of horizontal and vertical linkages, as shown in Fig. 4.11. The linkages serve to constrain the movement of the aerofoil to vertical and rotational motions. As in the numerical model, the degrees-of-freedom corresponding to these motions are named the plunge and pitch motions, respectively. The support structure

is designed so that the pitch and plunge displacements are identical across either side of the aerofoil, in the spanwise direction. As a result, there is negligible twisting and bending across the section. This is achieved by use of a torque tube, which lies on top of the test section.

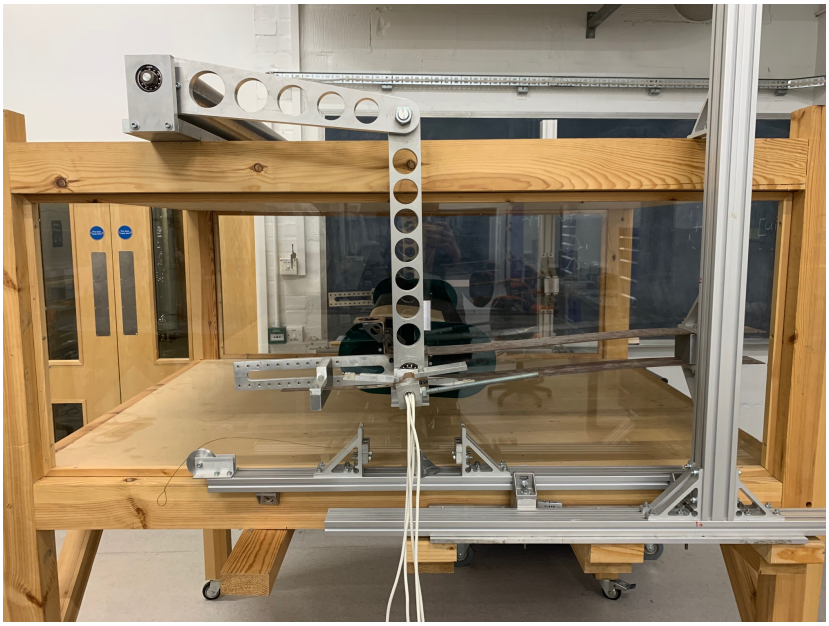

Figure 4.11: Support structure in the experimental system.

The pitch and plunge degrees-of-freedom are restrained by leaf springs that are fixed to both sides of the test section. The springs are designed in a cantilever style, as shown in Fig. 4.12, and can have their length adjusted so that the stiffness is modified. All the springs are made from spring steel. This is to ensure a linear relationship between the structural restoring force and the displacement, both in pitch and plunge.

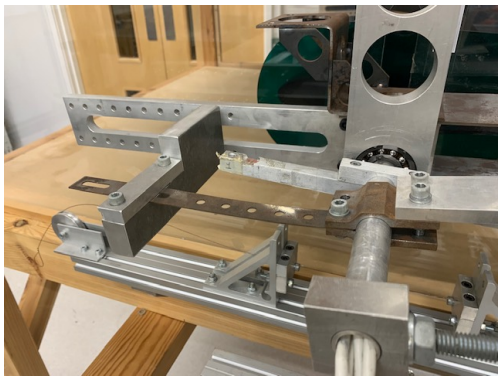

(a) Pitch

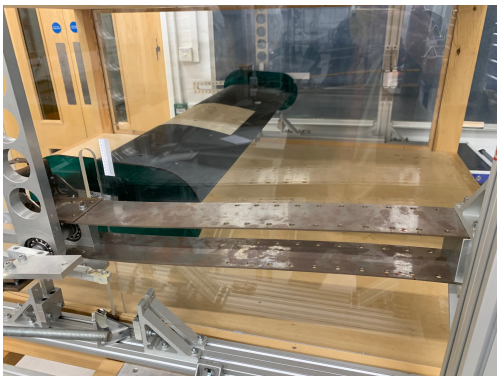

(b) Plunge

Figure 4.12: Cantilever beams of the support structure.

Wind Tunnel Facility & Test Section

The experimental model is situated in the University of Liverpool's low speed, subsonic wind tunnel facility. The wind tunnel is of the blower type and is shown pictorially in Fig. 4.13. The facility is capable of a maximum wind speed of approximately[2] 20 m/s and thus, throughout all experiments, it is assumed that the flow is incompressible.

[2]Note that this can change according to external factors, such as temperature.

Figure 4.13: The University of Liverpool's low-speed, subsonic wind tunnel facility.

In all of the experimental tests, the portable test section was wheeled directly in front of the exit of the wind tunnel. The cross section of the test section matches that of the wind tunnel exit and thus there is no change in cross section, which could otherwise lead to disturbances in the air flow. However, a very small gap of approximately 2mm is used between the exit of the wind tunnel and the test section. This is to ensure that vibrations from the wind tunnel do not transmit through to the test section, which could otherwise affect the results.

A high precision Furness Controls FCO560 pitot tube is mounted inside the wind tunnel. This is used to measure the freestream speed, which is shown on a digital display placed directly above the wind tunnel.

Laser Displacement Sensors

In this work, the outputs from the experimental system are displacements at two reference locations. Two Keyence LK-500 laser displacement sensors were used to measure the displacements at these points. The reading locations are not points directly on the aerofoil but rather points on a bar, external to the test section, that protrudes from the elastic axis. This is illustrated in Fig. 4.14.

The readings from the laser displacement sensors do not correspond directly to the pitch and plunge degrees of freedom. However, they may be easily converted using the relationships

$$h = \frac{y_1 + y_2}{2}, \tag{4.44}$$

$$\alpha = \frac{y_2 - y_1}{0.24}, \tag{4.45}$$

where y_1 and y_2 are the displacements measured by the first and second laser displacement sensor, respectively; and 0.24 is the distance, in m, between the leading- and trailing-edge laser sensors. Of course, the above equation assumes that the displacement in the pitch motion is sufficiently small that the small angle deflection formula may be used.

Throughout the remainder of this thesis, the input-output transfer function matrix is left in terms of the displacement outputs y_1 and y_2. Thus, the transfer function matrix is of a form

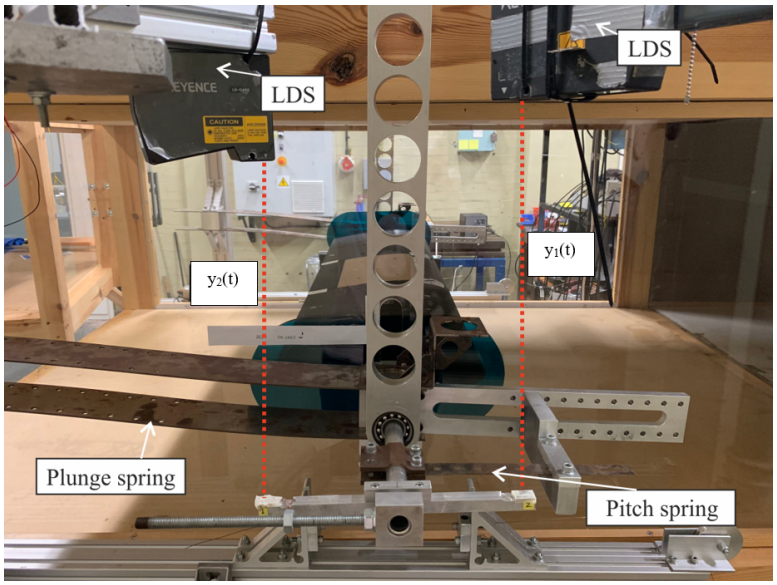

Figure 4.14: Setup of the laser displacement sensors.

that satisfies

$$\begin{pmatrix} y_1(s) \\ y_2(s) \end{pmatrix} = \mathbf{R}(s) \begin{pmatrix} \beta(s) \\ \gamma(s) \end{pmatrix} \tag{4.46}$$

Second-order Butterworth filters with a cutoff frequency of 15Hz were used on both laser signals. This was to reduce the influence of noise, which is especially important when these signals are differentiated. The value of 15Hz was chosen so that the filters have negligible impact on the frequency range of the two structural modes.

Control Systems Implementation & Data Acquisition Systems

The aeroservoelastic contains three independent control systems. The first two relate to the PID controllers that command the deflection of the leading- and trailing-edge control surfaces. The third system relates to the high-level feedback controller, which is used to modify the dynamics of the aeroelastic system. Throughout this work, the three controllers are implemented using dSPACE realtime control hardware. The controllers are created on MATLAB Simulink and then compiled into C code to be run on the hardware at a sample rate of 1 ms.

In addition to the realtime control hardware, it was necessary to use data acquisition equipment in order to perform structural dynamics test, such as impact hammer and shaker experiments. Therefore, a Siemens SCADAS 4 acquisition box was used. The box consists of 16 analogue voltage inputs, of which two were used to read the laser displacement readings, and two outputs, which were used to drive either the control surfaces or an electromechanical shaker. The overall control and data acquisition architecture is shown in Fig. 4.15 in the form of a system interconnection diagram. It is worth noting that in the early stages of this work an older data acquisition known as LMS was used. However, the working principles and system interconnection is the same, regardless.

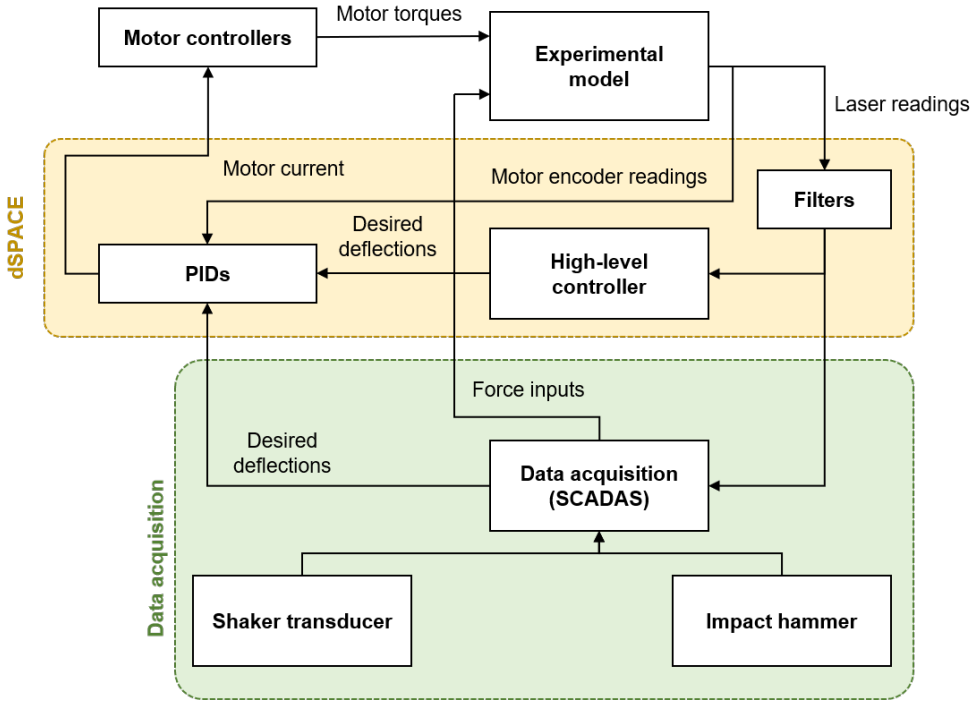

Figure 4.15: System interconnection diagram of the experimental system.

4.3.2 Results

Stiffness Verification

One of the first tests conducted on the experimental model was the verification of the linear assumption in the structure. In particular, the stiffness parameters in the pitch and plunge degrees of freedom were tested. This was done by means of force-displacement tests. Masses were placed in each degree of freedom and the readings from the laser displacement sensors were recorded and converted to the pitch and plunge degrees-of-freedom, using Eqs. 4.44 and 4.45. Figs. 4.16 (a) and (b) show the results from these experiments in the plunge and pitch degree-of-freedom, respectively. In both cases, across the ranges tested, it is clear that the linear approximation is sufficient and thus one can conclude that the assumption of linearity in the stiffness parameters is good. This is further supported by the coefficient of determination (R^2), which is 1.00 in both degrees-of-freedom.

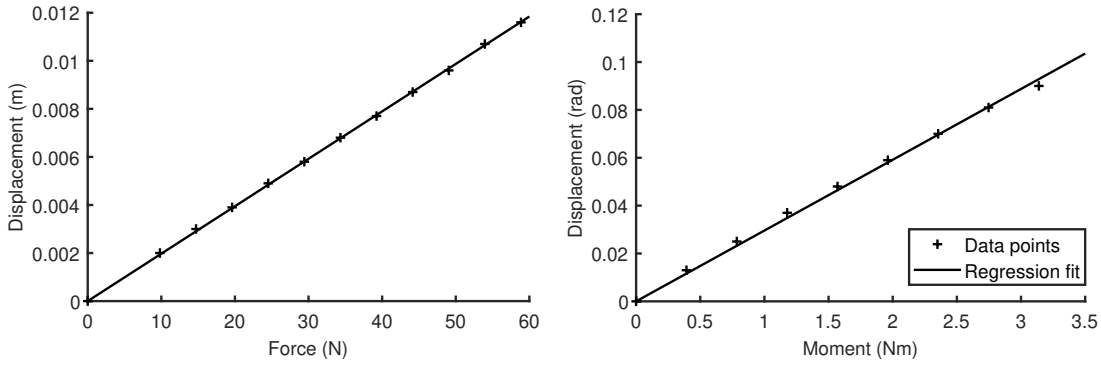

(a) Plunge (b) Pitch

Figure 4.16: Results of the force displacement tests.

PID Tuning & Performance

Tuning of the PIDs was performed by Martinelli [140] using the Ziegler-Nicholas method and then adjusted manually for optimum performance. Table 4.2 gives the final values used for both the leading- and trailing-edge controllers.

Table 4.2: Gains used in the PIDs for the leading- and trailing-edge control surfaces.

PID	Trailing-edge	Leading-edge
k_p	3	3
k_i	10	10
k_d	0.02	0.035

Open-Loop Pole Variation

The variation of the open-loop poles with respect to the freestream speed was also investigated on the experimental system. Impact hammer tests were performed and the Siemens SCADAS data acquisition hardware was used to obtain the frequency response functions from the leading-edge laser sensor. The test was conducted over a series of freestream speeds and the poles corresponding to the measured frequency response functions were identified from the data using the PolyMax fitting algorithm. Figures 4.17 (a) and (b) show the variation of the real and imaginary parts of the open-loop poles, respectively. The data points all show a decreasing (more negative) real part as the freestream speed increases. However, the data point corresponding to 12 m/s shows a slight decrease in the rate at which the damping increases in the plunge mode. This matches the behaviour shown in the numerical model and, more generally, the conventional binary aeroelastic model.

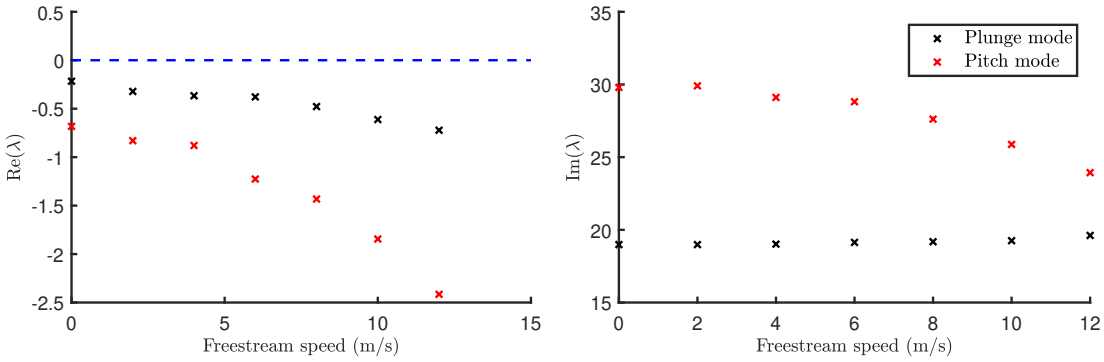

(a) Real part (b) Imaginary part

Figure 4.17: Variation of the open-loop poles in the experimental model with respect to the freestream speed.

Due to issues with collecting frequency response functions at low damping values, it was not possible to obtain experimental data points closer to the flutter speed and thus the above figures do not explicitly indicate the flutter speed. However, it was possible to estimate the flutter speed by disturbing the model at speeds above 12 m/s and observing whether the displacement from the system increased or decreased. Experimentally, it was determined that the flutter speed is in the region of 14 m/s.

Receptance Matrix

Next, the receptance matrix of the system is considered. Impact hammer tests were performed, again using the SCADAS 4 data acquisition hardware, between frequencies of 2 to 6 Hz. The results of these tests are shown in Fig. 4.18. As before, one observes a good degree of symmetry in the model when the freestream speed is set to zero, i.e. wind-off. At 5 m/s, there is only a marginal difference between the measured FRFs at this speed and the FRFs at zero m/s. However, as the freestream speed increases, there is a great increase in the effect of the aerodynamic.

A noticeable feature of the receptance measurements in the experimental system is observed in h_{21}. As the freestrem speed increases, the plunge mode becomes less apparent. Indeed, at 10 m/s, it is very difficult to identify this first mode. As seen in the other measurements at the same speed, the mode is still evident and thus one can conclude that this is not a consequence of a large damping. In fact, this is caused by the asymmetric aerodynamic loading, as was discussed in the results of the numerical model.

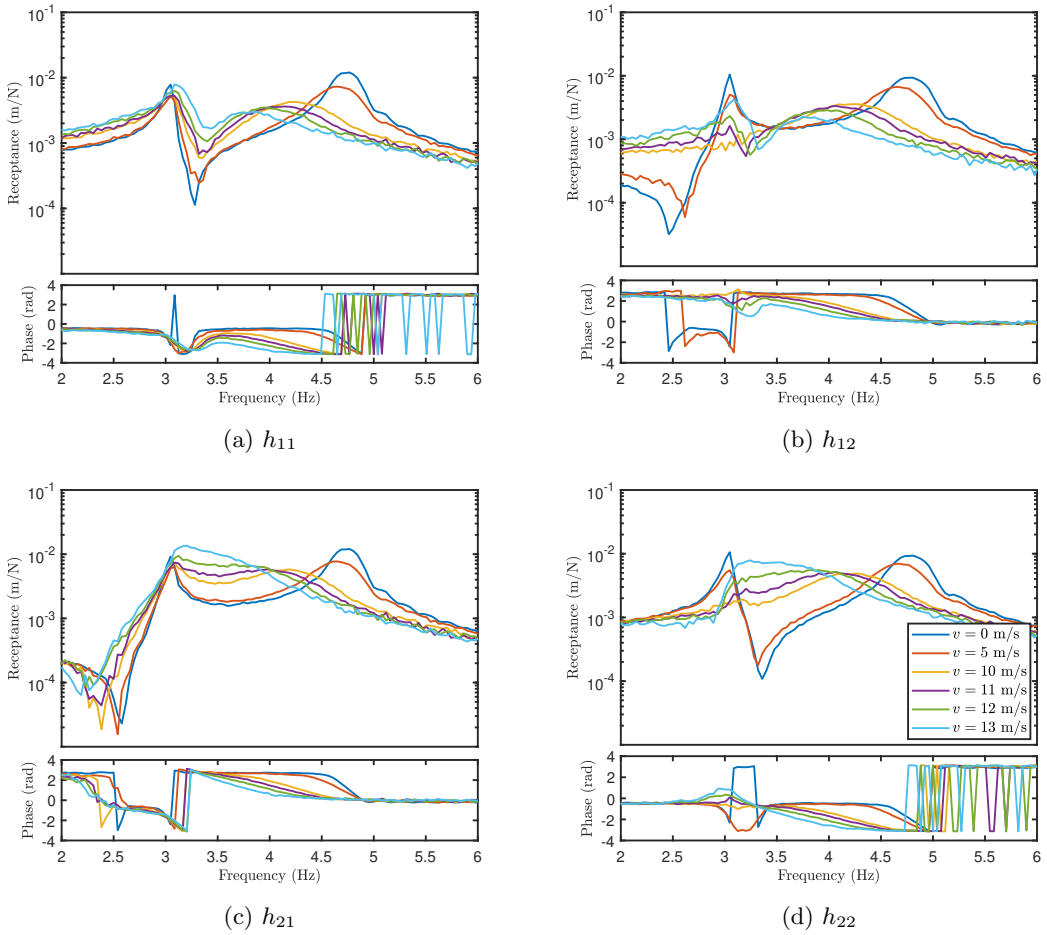

(a) h_{11} (b) h_{12}

(c) h_{21} (d) h_{22}

Figure 4.18: Variation of the receptance matrix in the experimental model with respect to the freestream speed.

Input-Output Transfer Function Matrix

Finally, the variation of the input-output transfer function matrix with the freestream speed is shown in Fig. 4.19. Similar to the numerical, the amplitude of the FRF increases as the

freesteam speed increases. This is due to the increasing influence of the aerodynamics and therefore the flap is able to exert a larger force on the system.

In contrast with the numerical model, there is a visible frequency response at the zero freestream speed. This is due to the inertia of the leading- and trailing-edge control surfaces.

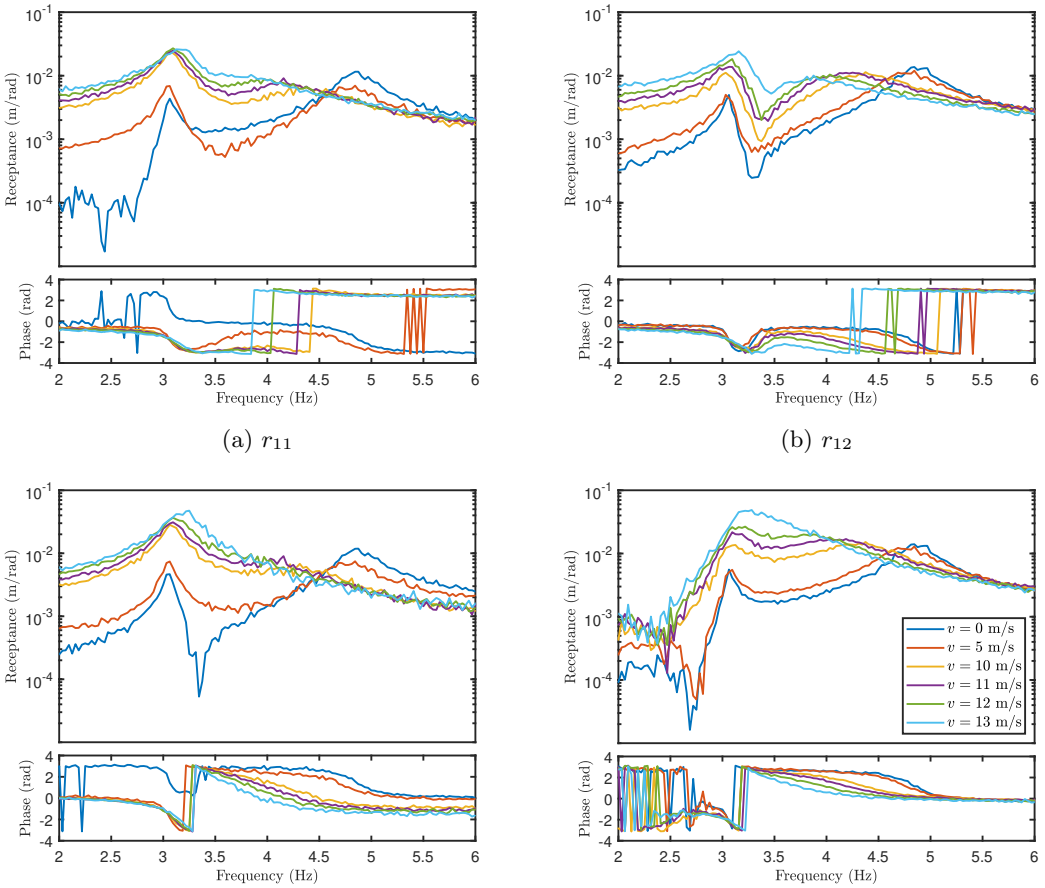

(a) r_{11} (b) r_{12}

(c) r_{21} (d) r_{22}

Figure 4.19: Variation of the input-output transfer function matrix in the experimental model with respect to the freestream speed.

4.4 Summary

This chapter presents two aeroservoelastic models that are used throughout the remainder of this thesis. The first model is numerical and is based on the pitch-plunge model, which is widely used in the literature. The parameters of the model are identical to that of Platanitis and Strganac [138] and hence the model has been verified. This numerical model is used a test bed for the methods presented later in the thesis. The second model is an experimental aeroservoelastic system that is housed at the University of Liverpool. The data from this experimental setup is used in the following chapters to demonstrate how receptance and/or transfer function data can be used to facilitate an experiment-only approach to active flutter suppression and uncertainty quantification.

Chapter 5

Receptance-Based Active Flutter Suppression

5.1 Introduction

This chapter considers the development of receptance-based control techniques for the purpose of active flutter suppression. The basic principles of receptance-based control are reviewed and a formal treatment of eigenstructure assignment using only receptance data is given. Both single- and multiple-input systems are studied and key differences between their respective formulations are highlighted. Unique to this work, two limitations that previously impeded the application of the Receptance Method to large-scale aircraft are addressed. Firstly, the arbitrary approach to assigning both the eigenvalues and eigenvectors is replaced by a global optimisation algorithm. This algorithm simultaneously increases the damping and frequency separation between modes, whilst ensuring that the control effort does not become too large. Secondly, an iterative control scheme is developed. This allows receptance data to be collected well above the open-loop flutter speed. In doing so, the controller is more likely to push the flutter speed higher as it is not designed using data that is far below the original flutter speed, as is current practice.

Both the iteration and optimisation methods are tested numerically on the reference aeroservoelastic system under both single- and multiple-input configurations. The method is also applied experimentally, in the form of a case study, to the University of Liverpool's subsonic aeroelastic wind-tunnel model. It is shown that these new methods address some of the restrictions that inhibit real-world applications of receptance-based control techniques and perform better than direct application of standard receptance-based control methods.

5.2 Receptance-Based Eigenstructure Assignment

First, the fundamental principles of eigenstructure assignment in the frequency domain are studied. Consider a general m-input, n-output linear aeroservoelastic system described by the standard form

$$\mathbf{Z}(s,v)\mathbf{y}(s) = \mathbf{B}_{\mathrm{CS}\rightarrow\mathrm{F}}(s,v)\mathbf{u}(s), \tag{5.1}$$

where $\mathbf{Z}(s,v) \in \mathbb{C}^{n\times n}$, $\mathbf{y}(s) \in \mathbb{C}^n$, $\mathbf{u}(s) \in \mathbb{C}^m$, and $\mathbf{B}_{\mathrm{CS}\to\mathrm{F}}(s,v) \in \mathbb{C}^{n\times m}$ have their usual definitions[1,2]. In the case that $\mathbf{u}(s) = \mathbf{0}$, i.e. the open-loop system, Eq. 5.1 becomes

$$\mathbf{Z}(s,v)\mathbf{y}(s) = \mathbf{0}. \tag{5.2}$$

Hence, the associated open-loop eigenvalue problem is

$$\mathbf{Z}(\lambda_i, v)\mathbf{v}_{R,i} = \mathbf{0}, \quad i = 1, 2, \ldots, l, \tag{5.3}$$

$$\mathbf{v}_{L,i}^T\mathbf{Z}(\lambda_i, v) = \mathbf{0}^T, \quad i = 1, 2, \ldots, l, \tag{5.4}$$

where $\lambda_i \in \mathbb{C}$ are the open-loop poles; and $\mathbf{v}_{L,i}, \mathbf{v}_{R,i} \in \mathbb{C}^n$ are the corresponding left and right eigenvectors, respectively. Note that $\mathbf{v}_{L,i}$ and $\mathbf{v}_{R,i}$ are equal if the dynamic stiffness matrix is symmetric. However, this is generally not the case in aeroelastic systems due to asymmetric aerodynamic loading. Therefore, the analysis proceeds with the generalised left and right eigenvectors.

Suppose now that a linear output feedback controller is selected so that the input becomes

$$\mathbf{u}(s) = \left(s\mathbf{F}^T + \mathbf{G}^T\right)\mathbf{y}(s), \tag{5.5}$$

where $\mathbf{F}, \mathbf{G} \in \mathbb{R}^{n\times m}$ are matrices of control gains. Eq. 5.1 becomes

$$\mathbf{Z}(s,v)\mathbf{y}(s) = \mathbf{B}_{\mathrm{CS}\to\mathrm{F}}(s,v)\left(s\mathbf{F}^T + \mathbf{G}^T\right)\mathbf{y}(s). \tag{5.6}$$

Pre-multiplying both sides of Eq. 5.6 by the receptance matrix $\mathbf{H}(s,v) = \mathbf{Z}(s,v)^{-1}$ gives that

$$\mathbf{y}(s) = \mathbf{R}(s,v)\left(s\mathbf{F}^T + \mathbf{G}^T\right)\mathbf{y}(s), \tag{5.7}$$

where

$$\mathbf{R}(s,v) = \mathbf{H}(s,v)\mathbf{B}_{\mathrm{CS}\to\mathrm{F}}(s,v) \tag{5.8}$$

is the input-output transfer function matrix. Figure 5.1 shows the closed-loop system in block diagram form.

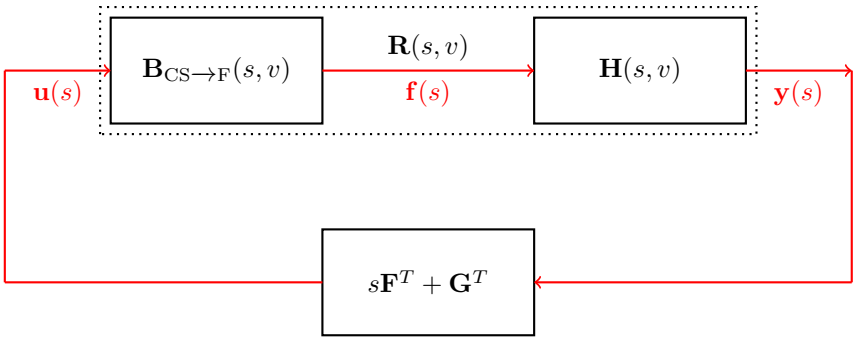

Figure 5.1: Block diagram of the closed-loop system.

[1] See Chapter 3.
[2] Note that the external force input vector in Eq. 3.14 is set to zero here and is not considered.

The eigenvalue problem associated with the closed-loop system is

$$\left(\mathbf{I} - \mathbf{R}(\mu_i, v)\left(\mu_i \mathbf{F}^T + \mathbf{G}^T\right)\right)\mathbf{w}_{R,i} = \mathbf{0}, \quad i = 1, 2, \ldots, l, \tag{5.9}$$

$$\mathbf{w}_{L,i}^T\left(\mathbf{I} - \mathbf{R}(\mu_i, v)\left(\mu_i \mathbf{F}^T + \mathbf{G}^T\right)\right) = \mathbf{0}^T, \quad i = 1, 2, \ldots, l, \tag{5.10}$$

where $\mu_i \in \mathbb{C}$ are the closed-loop poles; and $\mathbf{w}_{L,i}, \mathbf{w}_{R,i} \in \mathbb{C}^n$ are the corresponding left and right eigenvectors of the closed-loop system, respectively. By selecting different control matrices $\mathbf{F}$ and $\mathbf{G}$, it is possible to change the definition of the eigenvalue problem and hence modify the resulting eigenvalues and eigenvectors. Choosing control gains so that the eigenvalues and eigenvectors match desired values is known as eigenstructure assignment and the process of determining these gains is known as the Receptance Method.

5.3 The Receptance Method

Let the set of open-loop poles be denoted $\boldsymbol{\lambda} = \{\lambda_1, \lambda_2, \ldots, \lambda_l\}$ and the set of desired closed-loop poles be denoted $\boldsymbol{\mu} = \{\mu_1, \mu_2, \ldots, \mu_p, \mu_{p+1}, \mu_{p+1}, \ldots, \mu_l\}$. The first p closed-loop poles are those that are distinct from the open-loop (i.e. $\mu_i \notin \boldsymbol{\lambda}, i = 1, 2, \ldots, p$). The remaining $l - p$ poles are those that are unchanged from the open-loop (i.e. $\mu_i \in \boldsymbol{\lambda}, i = p+1, p+2, \ldots, l$). The aim now is to determine the control gains $\mathbf{F}$ and $\mathbf{G}$ such that the poles match the desired closed-loop set. This process depends on whether the system is single-input or multiple-input. Both configurations are considered here.

5.3.1 Single-Input Systems

In single-input systems (i.e. $m = 1$), the input-output transfer function matrix reduces to a vector of the form $\mathbf{r}(s, v) \in \mathbb{C}^n$ and thus so too do the control gains $\mathbf{f}, \mathbf{g} \in \mathbb{R}^n$. This considerably simplifies the analysis for eigenvalue assignment.

Unchanged Poles

First, the $l - p$ unchanged poles are considered. By definition of Eq. 5.3

$$\mathbf{Z}(\mu_i, v)\mathbf{v}_{R,i} = \mathbf{0}, \quad i = p+1, p+2, \ldots, l. \tag{5.11}$$

Hence, since $\mathbf{b}(s, v) \neq \mathbf{0}$ for all s, Eq. 5.6 leads to

$$\left(\mu_i \mathbf{f}^T + \mathbf{g}^T\right)\mathbf{v}_{R,i} = 0, \quad i = p+1, p+2, \ldots, l. \tag{5.12}$$

By taking the transpose, the conditions imposed on the control gains for the unchanged poles are given by

$$\mathbf{v}_{R,i}^T\left(\mu_i \mathbf{f} + \mathbf{g}\right) = 0, \quad i = p+1, p+2, \ldots, l. \tag{5.13}$$

That is, the vectors $(\mu_i \mathbf{f} + \mathbf{g})$ and $\mathbf{v}_{R,i}$ must be orthogonal for all $i = p+1, p+2, \ldots, l$.

Changed Poles

Next, the p changed poles are considered. By virtue of Eq. 5.9, the gains must be selected so that

$$\mathbf{w}_{R,i} = \mathbf{r}(\mu_i, v)\left(\mu_i \mathbf{f}^T + \mathbf{g}^T\right)\mathbf{w}_{R,i}, \quad i = 1, 2, \ldots, p. \tag{5.14}$$

By denoting

$$\alpha_i = \left(\mu_i \mathbf{f}^T + \mathbf{g}^T\right) \mathbf{w}_{R,i}, \quad i = 1, 2, \ldots, p, \tag{5.15}$$

Eq. 5.14 becomes

$$\mathbf{w}_{R,i} = \mathbf{r}(\mu_i, v)\alpha_i, \quad i = 1, 2, \ldots, p. \tag{5.16}$$

Substituting Eq. 5.16 into Eq. 5.15 gives

$$\alpha_i = \left(\mu_i \mathbf{f}^T + \mathbf{g}^T\right) \mathbf{r}(\mu_i, v)\alpha_i, \quad i = 1, 2, \ldots, p, \tag{5.17}$$

and thus by cancellation of the α_i term and taking the transpose of the result

$$\mathbf{r}^T(\mu_i, v)\left(\mu_i \mathbf{f} + \mathbf{g}\right) = 1, \quad i = 1, 2, \ldots, p. \tag{5.18}$$

Control Gains Solution

Now, it is straightforward to compute the control gains necessary to assign the closed-loop poles in the single-input configuration. Let

$$\mathbf{P} = \begin{pmatrix} \mu_1 \mathbf{r}^T(\mu_1, v) & \mathbf{r}^T(\mu_1, v) \\ \vdots & \vdots \\ \mu_p \mathbf{r}^T(\mu_p, v) & \mathbf{r}^T(\mu_p, v) \end{pmatrix}, \tag{5.19}$$

$$\mathbf{Q} = \begin{pmatrix} \mu_{p+1} \mathbf{v}_{R,p+1}^T & \mathbf{v}_{R,p+1}^T \\ \vdots & \vdots \\ \mu_l \mathbf{v}_{R,l}^T & \mathbf{v}_{R,l}^T \end{pmatrix}. \tag{5.20}$$

From Eqs. 5.18 and 5.13,

$$\begin{pmatrix} \mathbf{f} \\ \mathbf{g} \end{pmatrix} = \begin{pmatrix} \mathbf{P} \\ \mathbf{Q} \end{pmatrix}^{-1} \begin{pmatrix} \mathbf{e} \\ \mathbf{0} \end{pmatrix}, \tag{5.21}$$

where $\mathbf{e} \in \mathbb{R}^p$ is a vector with unit entries.

To be physically meaningful, the control gains must be real. Therefore, it is necessary that the set of desired closed-loop poles is closed under conjugation. A proof of this is given in [110].

5.3.2 Multiple-Input Systems

In multiple-input systems (i.e. $m > 1$), the input-output transfer function matrix $\mathbf{R}$ and the control gains $\mathbf{F}$ and $\mathbf{G}$ no longer collapse to vector quantities. Consequently, there is greater flexibility in the eigenvalue assignment, as will be shown in the analysis that follows.

Unchanged Poles

Again, the $l - p$ unchanged poles are considered first. From Eq. 5.3,

$$\mathbf{Z}(\mu_i, v)\mathbf{v}_{R,i} = \mathbf{0}, \quad i = p+1, p+2, \ldots, l \tag{5.22}$$

and hence from Eq. 5.6

$$\left(\mu_i \mathbf{F}^T + \mathbf{G}^T\right) \mathbf{v}_{R,i} = \mathbf{0}, \quad i = p+1, p+2, \ldots, l. \tag{5.23}$$

In other words, the matrix $\left(\mu_i \mathbf{F}^T + \mathbf{G}^T\right)$ must be comprised of the null space of $\mathbf{v}_{R,i}$, for each unchanged pole. By writing the gain matrices as

$$\mathbf{F} = \begin{pmatrix} \mathbf{f}_1 & \mathbf{f}_2 & \dots & \mathbf{f}_m \end{pmatrix}, \quad \mathbf{G} = \begin{pmatrix} \mathbf{g}_1 & \mathbf{g}_2 & \dots & \mathbf{g}_m \end{pmatrix}, \tag{5.24}$$

Eq. 5.23 can be written in matrix form as

$$\mathbf{Q}_i \mathbf{y} = \mathbf{0}, \quad i = p+1, p+2, \dots, l, \tag{5.25}$$

where

$$\mathbf{Q}_i = \begin{pmatrix} \mu_i \mathbf{v}_{R,i}^T & 0 & \dots & 0 & \mathbf{v}_{R,i}^T & 0 & \dots & 0 \\ 0 & \mu_i \mathbf{v}_{R,i}^T & \dots & 0 & 0 & \mathbf{v}_{R,i}^T & \dots & 0 \\ \vdots & \vdots & \dots & \vdots & \vdots & \vdots & \dots & \vdots \\ 0 & 0 & \dots & \mu_i \mathbf{v}_{R,i}^T & 0 & 0 & \dots & \mathbf{v}_{R,i}^T \end{pmatrix}, \quad \mathbf{y} = \begin{pmatrix} \mathbf{f}_1 \\ \vdots \\ \mathbf{f}_m \\ \mathbf{g}_1 \\ \vdots \\ \mathbf{g}_m \end{pmatrix}. \tag{5.26}$$

Changed Poles

Next, the p changed poles are considered. Similar to before, the gains must be selected so that

$$\mathbf{w}_{R,i} = \mathbf{R}(\mu_i, v) \left(\mu_i \mathbf{F}^T + \mathbf{G}^T\right) \mathbf{w}_{R,i}, \quad i = 1, 2, \dots, p. \tag{5.27}$$

By introducing

$$\boldsymbol{\alpha}_i = \left(\mu_i \mathbf{F}^T + \mathbf{G}^T\right) \mathbf{w}_{R,i}, \quad i = 1, 2, \dots, p, \tag{5.28}$$

Eq. 5.27 becomes

$$\mathbf{w}_{R,i} = \mathbf{R}(\mu_i, v) \boldsymbol{\alpha}_i, \quad i = 1, 2, \dots, p, \tag{5.29}$$

and hence

$$\boldsymbol{\alpha}_i = \left(\mu_i \mathbf{F}^T + \mathbf{G}^T\right) \mathbf{R}(\mu_i, v) \boldsymbol{\alpha}_i, \quad i = 1, 2, \dots, p. \tag{5.30}$$

This may be recast in matrix form as

$$\begin{pmatrix} \mu_i \mathbf{w}_{R,i}^T & 0 & \dots & 0 & \mathbf{w}_{R,i}^T & 0 & \dots & 0 \\ 0 & \mu_i \mathbf{w}_{R,i}^T & \dots & 0 & 0 & \mathbf{w}_{R,i}^T & \dots & 0 \\ \vdots & \vdots & \dots & \vdots & \vdots & \vdots & \dots & \vdots \\ 0 & 0 & \dots & \mu_i \mathbf{w}_{R,i}^T & 0 & 0 & \dots & \mathbf{w}_{R,i}^T \end{pmatrix} \begin{pmatrix} \mathbf{f}_1 \\ \vdots \\ \mathbf{f}_m \\ \mathbf{g}_1 \\ \vdots \\ \mathbf{g}_m \end{pmatrix} = \boldsymbol{\alpha}_i \quad i = 1, 2, \dots, p, \tag{5.31}$$

or more compactly

$$\mathbf{P}_i \mathbf{y} = \boldsymbol{\alpha}_i, \quad i = p+1, p+2, \dots, l, \tag{5.32}$$

with the obvious definitions of $\mathbf{P}_i$.

Control Gains Solution

By defining

$$\mathbf{z} = \begin{pmatrix} \boldsymbol{\alpha}_1 \\ \vdots \\ \boldsymbol{\alpha}_p \end{pmatrix}, \tag{5.33}$$

the control gains for the multiple-input version of the Receptance Method are given by

$$\begin{pmatrix} \mathbf{f}_1 \\ \vdots \\ \mathbf{f}_m \\ \mathbf{g}_1 \\ \vdots \\ \mathbf{g}_m \end{pmatrix} = \begin{pmatrix} \mathbf{P}_1 \\ \vdots \\ \mathbf{P}_p \\ \mathbf{Q}_{p+1} \\ \vdots \\ \mathbf{P}_l \end{pmatrix}^{-1} \begin{pmatrix} \mathbf{z} \\ \mathbf{0} \end{pmatrix}. \tag{5.34}$$

The $\boldsymbol{\alpha}_i$ vectors in the above formulation are quantities that must be chosen. As explained by Mokrani et al. [141], for any conjugate pole pair $\{\mu_i, \bar{\mu}_i\}$, the corresponding alpha vectors must be conjugate pairs also, i.e. $\boldsymbol{\alpha}_i, \bar{\boldsymbol{\alpha}}_i$. Apart from this restriction, however, the vectors may be chosen arbitrarily. In the multiple-input formulation of the Receptance Method, Ram and Mottershead [114] suggest an approach based on imposing modal constraints. However, other methods, such as minimising the norm of the control gains, may be used instead [141]. In this work, the alpha vectors are used to achieve optimal eigenstructure assignment, as is discussed in the following section.

5.4 Optimum Eigenstructure Assignment

The main objective of active flutter suppression is to push the flutter speed higher. In traditional control methods, this is reasonably straightforward to do; one can design the controller and use a numerical model to assess its impact on the flutter speed. However, this is not possible in receptance-based methods. Without a numerical model, it is impossible to accurately predict the direct effect a controller has on the flutter speed. Indeed, as shown in the previous section, receptance-based control techniques only consider the assignment of the eigenvalues and eigenvectors; it is not possible to assign a desired flutter speed.

Although the relationship between the eigenstructure assignment and the flutter speed is not known exactly, it is still possible to make some qualitative predictions based on the general behaviour of aeroelastic systems. Firstly, flutter itself arises when one or more modes become unstable. Therefore, it is known that driving the damping higher in certain modes can serve to push the flutter speed higher. Secondly, prior to flutter itself, the frequency separation between two or more modes appears to reduce significantly, at a rate that increases as the freestream speed tends to the flutter speed. Therefore, separating the frequencies between successive modes also usually increases the flutter speed. Based on these observations, two strategies that are usually used for the purposes of AFS are:

1. To push the poles of the system further into the left hand side of the complex plane so that the damping is increased.

2. To increase the imaginary part separation between successive poles so that the frequency separation is increased.

The above two principles have been used to design a variety of receptance-based AFS systems, as discussed in Chapter 2. However, there is still no formal, rigorous method that considers how to implement these points; the process of increasing the flutter speed still largely relies on trial and error. Moreover, a survey of the literature shows that is not usual to consider the limitations of the controller in the process of eigenstructure assignment. It is only an after consideration, once the control gains have been found. To address the above-mentioned issues, a more rigorous method that is based on the principles of optimisation theory is developed here.

5.4.1 Objective Function

The first step in the optimisation method is to create an objective function. The objective function serves as a metric by which to assess the suitability of the controller. As mentioned above, the two methods of increasing the flutter speed are to: (i) increase the damping in one or more modes, or (ii) to increase the frequency separation between successive modes. These two principles are used to design the objective function.

Let each pole in the set $\boldsymbol{\mu}$ be expressed in the standard form

$$\mu_i = -\zeta_i\omega_i(+/-)\omega_i\sqrt{1-\zeta_i^2}\mathrm{i}, \quad i = 1, 2, \ldots, p, \tag{5.35}$$

where ζ_i is the damping ratio, and ω_i is the undamped natural frequency. The objective function is given by

$$\rho = -\min\left(\zeta_i | i = 1, 2, \ldots, p\right) + \zeta^* \max\left(\left(\frac{\max\left(\omega_i, \omega_j\right)}{|\omega_i - \omega_j|}\right)^2 | i, j = 1, 2, \ldots, p\right). \tag{5.36}$$

The aim of the optimisation is to minimise the objective function by performing eigenstructure assignment. The first term in Eq. 5.36 selects the mode with the least damping and takes the negative of its damping ratio. In this way, a better optimisation solution corresponds to one where the minimum damping ratio is as large as possible. The second term corresponds to the frequency separation and is referred to as the *frequency separation metric* hereinafter. This may be viewed as a penalty to the damping term in the objective function. The frequency separation metric works by taking the maximum normalised frequency distance between any two modes. In other words, a lower frequency separation corresponds to a larger penalty in the optimisation. The frequency separation metric is weighted in the objective function by the term ζ^*. This serves to adjust the magnitude of the frequency separation and damping penalties to appropriate relative levels.

5.4.2 Controller Constraint

If the controller were designed based only on the objective function, it is likely that the final solution would be impossible to implement. This is because the controller is limited in its performance. In aeroelastic systems, the control surfaces usually have a limited angle of deflection and hence there exists a point of saturation, which is to be avoided as it would introduce nonlinearities into the system. Additionally, the control surfaces are usually also used for lateral control of the aircraft. Thus, the deflection of the control surfaces demanded by the controller must not be so large that little control effort is left for the lateral control.

In the optimisation, the above points are addressed through the introduction of control constraints. There are a variety of different ways in which to do this. However, here, the constraints are implemented through restrictions placed on the control gains.

It is usual for the controller constraints to be based on the norm of the control gains. Mokrani et al. [141], for example, considered the Frobenius form of the combined gain matrix. That is,

$$||\mathbf{T}||_F, \tag{5.37}$$

where

$$\mathbf{T} = \begin{pmatrix} \mathbf{F} & \mathbf{G} \end{pmatrix}. \tag{5.38}$$

This convention of considering the magnitude of the control gains is followed in this work. However, some modifications are made based on some observations.

Firstly, it is well-known that both $\mathbf{F}$ and $\mathbf{G}$ are generally not the same order of magnitude. This is because the $\mathbf{F}$ term is associated with velocity feedback, and the $\mathbf{G}$ term is associated with displacement feedback. In cases where the velocity is much greater in magnitude than the displacement, the $\mathbf{F}$ terms should be small compared to $\mathbf{G}$. Therefore, if this is not considered, the constraints may not penalise the $\mathbf{F}$ matrix as much as is necessary and could lead to an unacceptable control effort.

Secondly, within each control gain matrix itself, there may be difference in the magnitudes. Each row of the gains is associated with different measured outputs from the system. For instance, in the numerical system, one output is associated with the pitch degree-of-freedom and one output is associated with the plunge degree of freedom. Clearly, it would be inappropriate to weight the impact of these gains equally as one output has a different unit than the other and hence the one with a larger magnitude will tend to dominate the norm.

Based on the above points, the gain constraint used in this work is of the form

$$w||\mathbf{\Lambda F}||_F + ||\mathbf{\Lambda G}||_F \leq c_{max}, \tag{5.39}$$

where w and c are constants, and $\mathbf{\Lambda}$ is a diagonal matrix that is chosen. The purpose of the matrix $\mathbf{\Lambda}$ is to scale each row of the gain matrices to be suitable for each output and the purpose of w is to adjust the magnitude of $||\mathbf{\Lambda F}||_F$ relative to $||\mathbf{\Lambda G}||_F$.

The choice of the constants in the gain constraints is problem dependent and there is no universal approach for how to choose these values. However, general rules may be used to give good scaling of the constraints and to ensure that the weighting of each constraint relative to one another is meaningful. Firstly, choose the diagonal elements of $\mathbf{\Lambda}$ as the maximum value expected in each output. For example, the maximum displacement you would expect from a laser sensor reading. Once included in the Frobenius norm, this weighting will then adjust the gain matrices so that they are representative of maximum expected control output values. The value w can then be chosen as the average natural frequency in the system, which is a good adjustment to convert from displacement to velocity. Finally, the constant c is chosen as the maximum allowable value of the output from the system. For aeroservoelastic systems, this will be the maximum control surface deflection. With this procedure, the units of the constraint are consistent across all terms and therefore have some physical basis.

Whilst giving an informal way to choose the weighting constants, the above approach will likely yield conservative restrictions on the control gains. This is because the outputs from the system are unlikely to be simultaneously at their maximum. This problem is helped slightly by the use of the Frobenius norm, rather than alternatives such as the Manhattan norm. However, it is suggested that fine tune adjusting of the gain constraints may be required in an experimental setting.

5.4.3 Optimisation Problem & Solution Strategy

With the objective function and constraints defined, the question that remains is what variables to optimise. The answer to this depends on whether the system is single-input or multiple-input.

Single-Input Systems

As previously discussed, single-input systems can only assign the eigenvalues. Therefore, these are the only variables that may be optimised. In this case, the optimisation problem is

> **Single-Input Optimisation:** Assign the set of closed-loop eigenvalues such that the objective function in Eq. 5.36 is minimised, without exceeding the constraint specified by Eq. 5.39.

Multiple-Input Systems

In multiple-input systems, one also has the ability to optimally assign the eigenvectors in addition to the eigenvalues. This additional flexibility can therefore be used in the optimisation to yield a better solution. The optimisation problem in this case is therefore

> **Multiple-Input Optimisation:** Assign the set of closed-loop eigenvalues and eigenvectors such that the objective function in Eq. 5.36 is minimised, without exceeding the constraint specified by Eq. 5.39.

It is important to stress that one does not directly optimise the eigenvectors. Indeed, the alpha vectors in the multiple-input formulation are optimised, which in turn affects the eigenvectors.

Optimisation Solution

The solution strategy to optimisation problems is determined by the 'convexity'. A convex objective function has a single, global minimum point across the entire domain of all optimisation parameters. Convex optimisation problems are much simpler to analyse than non-complex optimisation procedures as one can always guarantee that the global optimum is found using gradient-based optimisation techniques. In this work, however, it is impossible to obtain an analytical form for the relationships between the optimisation parameters and the objective function. Therefore, one cannot infer the convexity of the problem and thus it is possible, and indeed likely, that there are multiple minima solutions. For this reason, it is necessary to use global optimisation procedures. Such procedures do not rely on gradient-based methods and instead use alternative approaches. In general, these alternative methods cannot guarantee that the global minima is found. However, it is far less likely to become attracted to local minima solutions that are sub-optimal.

Throughout the following numerical and experimental examples, the Differential Evolution algorithm by Storn and Price is used. This optimisation algorithm is based on the principle of stochastic updating and is shown to observe good performance, even when the objective function is ill-conditioned or contains an extremely large number of local minima [142]. Further details on this optimisation may be found in Appendix A.

5.5 Iterative Control Method

The method developed in the previous section allows the poles to be assigned optimally using only receptance data. However, as previously discussed, the receptance data are dependent on the freestream speed v. Therefore, the question remains as to which reference speed the receptance data should be collected at. In an experimental setting, it is necessary that the receptance data are collected in a practical and safe manner. This is not normally an issue for simple mass, spring, damper systems. However, this is particularly challenging in aeroservoelastic systems. Firstly, data cannot be collected when the system is unstable and hence FRFs cannot be measured at freestream speeds at or above the flutter speed. Secondly, in accordance with strict legislation, data can only be collected at speeds well below the flutter speed. This is due to the low levels of damping exhibited close to the flutter speed, which, whilst stable, could still induce large amplitude vibrations during testing.

In previous works, FRF data has been collected at speeds well below the flutter speed. For instance, Mokrani et al. [128] used receptance data at 10 m/s when the flutter speed in their system was approximately 13.5 m/s. Whilst such an approach has been shown to work, it is likely sub-optimal. This is because the dynamic that is measured at lower speeds is not necessarily representative of that closer to the flutter speed. In other words, the controller is designed about a reference point that does not reflect the system's dynamics at flutter. If one could somehow measure receptances closer to the flutter speed, it is hypothesised that a more optimal controller may be obtained.

In this section, a new approach is developed as an extension to the Receptance Method. Rather than using a fixed reference velocity well below the flutter speed, receptance data close to, at, or above the flutter speed are collected. This is done by repeatedly applying the receptance method in an iterative manner. This allows the flutter speed to be gradually increased and, as a consequence, permits receptance data to be collected in a closed-loop configuration at higher speeds.

5.5.1 Methodology

Consider an arbitrary aeroservoelastic system with an open-loop flutter speed v^*. Above v^*, receptance data cannot be measured. Receptance data also cannot be measured at speeds close to the flutter speed. This is demonstrated graphically in Figure 5.2. The red region represents speeds at which receptance data cannot be collected and the green region represents speeds at which it can. The maximum speed that the data can be collected at is denoted v_{lim} and represents the boundary between the measurable and immeasurable regions.

Suppose that a controller is designed at some reference speed using the optimum eigenstructure assignment method. The input vector at this speed is denoted $\mathbf{u}_0$ and the corresponding control gains are written $\mathbf{F}_0$ and $\mathbf{G}_0$. After the controller has been applied, both v_{lim} and v^* are pushed higher. This is demonstrated graphically in Fig. 5.3.

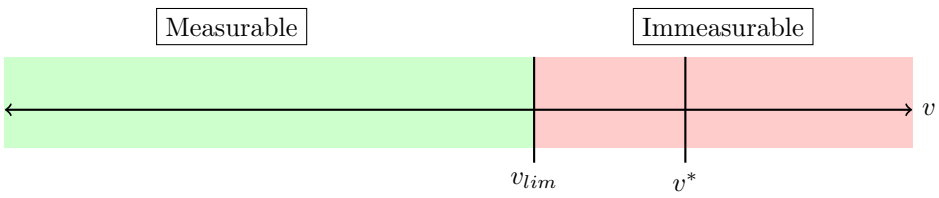

Figure 5.2: Open-loop receptance measurement regions.

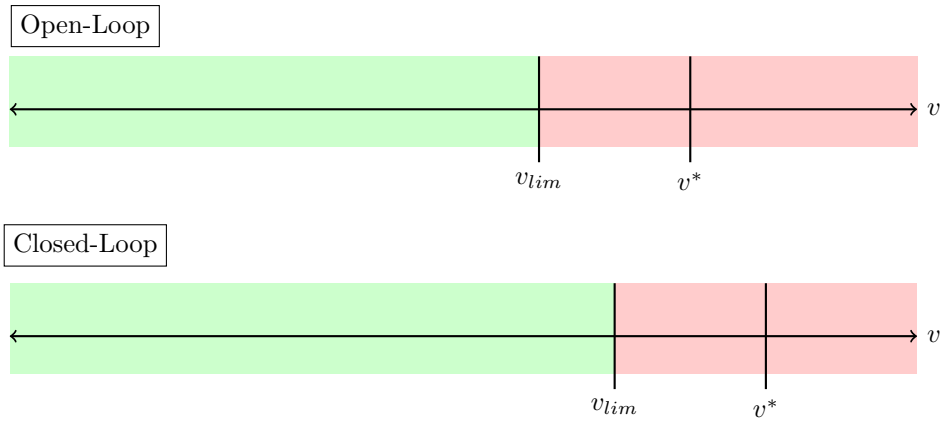

Figure 5.3: Closed-loop receptance measurement regions.

The aim is to now design a new controller using receptance data from the closed-loop configuration, where the limiting speed of receptance measurement is higher than the open-loop.

Suppose that the new input to the system in the closed-loop configuration is given by

$$\mathbf{u}(s) = \mathbf{u}_0(s) + \Delta\mathbf{u}(s), \tag{5.40}$$

or equivalently

$$\mathbf{u}(s) = \left(s\mathbf{F}_0^T + \mathbf{G}_0^T\right)\mathbf{y}(s) + \left(s\Delta\mathbf{F}^T + \Delta\mathbf{G}^T\right)\mathbf{y}(s). \tag{5.41}$$

Following the same procedure as before,

$$\mathbf{y}(s) = \mathbf{R}(s,v)\left(s\mathbf{F}_0^T + \mathbf{G}_0^T\right)\mathbf{y}(s) + \mathbf{R}(s,v)\left(s\Delta\mathbf{F}^T + \Delta\mathbf{G}^T\right)\mathbf{y}(s). \tag{5.42}$$

Re-arranging gives that

$$\mathbf{y}(s) = \left(\mathbf{I} - \mathbf{R}(s,v)\left(s\mathbf{F}_0^T + \mathbf{G}_0^T\right)\right)^{-1}\mathbf{R}(s,v)\left(s\Delta\mathbf{F}^T + \Delta\mathbf{G}^T\right)\mathbf{y}(s), \tag{5.43}$$

or equivalently

$$\mathbf{y}(s) = \hat{\mathbf{R}}_0(s,v)\left(s\Delta\mathbf{F}^T + \Delta\mathbf{G}^T\right)\mathbf{y}(s), \tag{5.44}$$

where

$$\hat{\mathbf{R}}_0(s,v) = \left(\mathbf{I} - \mathbf{R}(s,v)\left(s\mathbf{F}_0^T + \mathbf{G}_0^T\right)\right)^{-1}\mathbf{R}(s,v). \tag{5.45}$$

The term $\hat{\mathbf{R}}_0(s,v)$ corresponds to the input-output transfer function matrix that is measured when the previous control system is active. In other words, the input-output transfer function matrix with the effect of the gains $\mathbf{F}_0$ and $\mathbf{G}_0$ included. Therefore, according to Eq. 5.44, if one can measure this matrix, an additional controller, acting as a perturbation, can be designed using the Receptance Method as normal.

The process of applying a control modification to an already existing controller can be performed in an iterative manner. This causes both the reference limit speed and flutter speed to be gradually pushed higher with each modification to the controller. Of course, when either of these values does not increase, the iterations must stop and the controller has reached its final form and cannot be improved further.

Figure 5.4 shows the principles of the control iteration technique in block diagram form. As shown, the process can be thought of as applying several parallel feedback control loops.

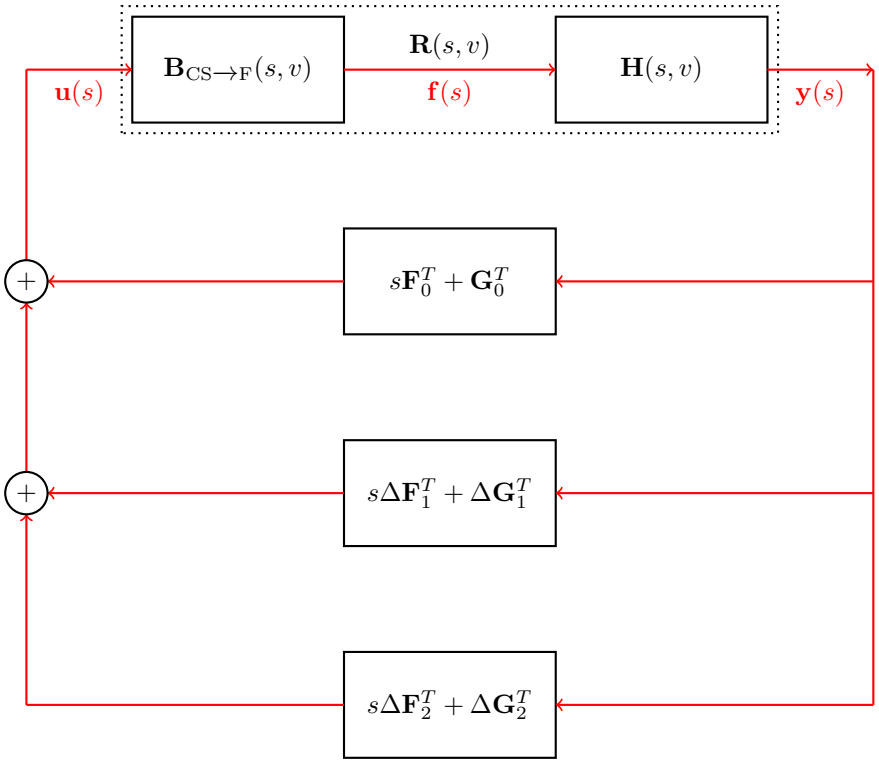

Figure 5.4: Block diagram of the closed-loop system after three control iterations.

It is important to note that the terms $\Delta\mathbf{F}_i$ and $\Delta\mathbf{G}_i$ represent the gain modifications to the closed-loop receptance data. Thus, there are not the total gains of the controller in the iteration. However, by inspection of Eq. 5.40 and Fig. 5.4, it is easy to show that the control gains acting on the open-loop system are simply given by

$$\mathbf{F}_i = \mathbf{F}_o + \sum_{j=1}^{i} \Delta\mathbf{F}_j, \tag{5.46}$$

$$\mathbf{G}_i = \mathbf{G}_o + \sum_{j=1}^{i} \Delta\mathbf{G}_j. \tag{5.47}$$

5.6 Method Overview

Figure 5.5 shows an overview of the proposed method for receptance-based active flutter suppression.

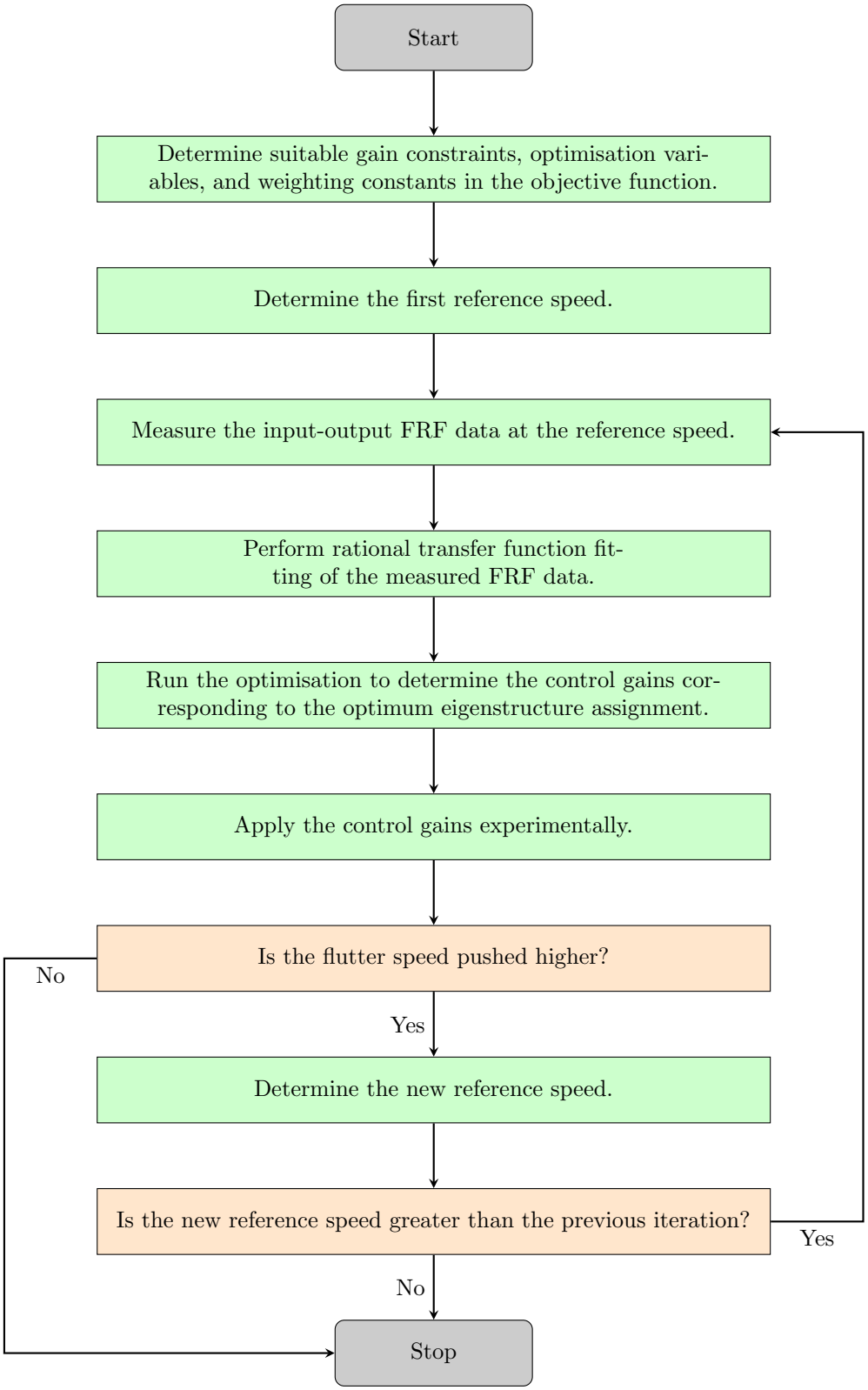

Figure 5.5: Overview of the receptance-based AFS method.

5.7 Numerical Examples

In this section, the control iteration and optimisation methods are applied to the reference aeroservoelastic model by Platanitis and Strganac [138]. Examples are given for the cases of both single- and multiple-input control. The aim here is to demonstrate the workings of the techniques and to discuss the effect of the optimisation parameters on the performance of the final AFS controller.

5.7.1 Single-Input

In this first example, the leading-edge control surface is fixed to a zero angle of deflection. In this way, only the trailing-edge can be used and hence the system is single-input.

As discussed in §5.5, one of the limiting factors in the gain scheduling method is the set of speeds at which the input-output transfer functions can be measured. In particular, data cannot be collected at speeds where the damping in one or more modes is too low. Numerically, this does not present an issue as the FRF data can be collected at any speed. However, to simulate such a constraint, it was decided that data corresponding to speeds where the damping is less than three percent cannot be used. This value may be different experimentally and must be judged on a case by case basis. However, the idea here is to use a constraint that is somewhat representative of the practical implementation.

In what follows, two different objective functions are tested and their impacts on the performance of final controllers are compared. To maintain consistency across both examples, the gain constraints are fixed as

$$14||\mathbf{\Lambda F}||_F + ||\mathbf{\Lambda G}||_F \leq \frac{5\pi}{180}, \tag{5.48}$$

where

$$\mathbf{\Lambda} = \begin{pmatrix} 0.03 & 0 \\ 0 & 0.1745 \end{pmatrix}.$$

The constants in the left hand side of the gain constraint are chosen approximately from the maximum displacement and velocities for the system, which are given in [138]. The right-hand side, meanwhile, corresponds to a maximum angle of deflection of approximately 5 degrees.

Objective Function 1

First, the objective function is selected as

$$\rho = -\min\left(\zeta_{pi}, \zeta_{pl}\right), \tag{5.49}$$

where the subscripts 'pi' and 'pl' represent the pitch and plunge modes, respectively. In contrast with the generalised form given in Eq. 5.36, this objective function does not include a penalty for the frequency separation of the pitch and plunge modes[3]. In this way, the optimisation, only cares about the minimum damping value.

Table 5.1 shows the first six iterations of the control method. v_{lim} denotes the highest speed above which the damping drops below three percent and v^* gives the flutter speed after each iteration. v_{it} denotes the speed at which FRF measurements are taken. As shown, v_{lim} is gradually increased and the input-output transfer functions can eventually be measured above open-loop flutter speed, as demonstrated in iterations three and above. Additionally, the flutter speed increases monotonically with each successive iteration.

[3]It is equivalent to setting $\zeta^* = 0$

Table 5.1: Optimisation 1: Single-input scheduling with no frequency separation metric.

Iteration	v_{it} (m/s)	v_{lim} (m/s)	v^* (m/s)
Open-loop	0	11.0	11.3
1	11.0	11.2	11.6
2	11.2	11.3	11.8
3	11.3	11.4	11.9
4	11.4	11.5	12.0
5	11.5	11.7	12.1
6	11.7	11.8	12.3

After 30 iterations, the flutter speed converges to a value of 15.2 m/s. The final gains corresponding to this flutter speed are

$$\mathbf{f} = \begin{pmatrix} -5.36 \times 10^{-5} & 8.98 \times 10^{-6} \end{pmatrix}^T, \quad \mathbf{g} = \begin{pmatrix} 1.4151 & -0.4364 \end{pmatrix}^T.$$

Although the optimisation shown above does gradually increase the flutter speed, there are some limitations in its practical use. As shown, the speed difference between successive iterations is very small; in most cases, it is as low as 0.1 m/s. Experimentally, increasing the speed with such small steps is unlikely to be possible due to the accuracy of the measurement equipment and stability of the wind tunnel. Additionally, the difference between the measured input-output transfer function matrices between two successive iterations is likely to be very small. Consequently, between iterations, errors in the data are likely to have more of an impact on the placement of the poles than the change in speed. In this case, ensuring that the flutter speed increases at each iteration becomes much more difficult.

Objective Function 2

In order to address the issues associated with optimisation one, the objective function is changed to

$$\rho = -\min\left(\zeta_{pi}, \zeta_{pl}\right) + 0.0002 \max\left(\left(\frac{\min\left(\omega_{pi}, \omega_{pl}\right)}{|\omega_{pi} - \omega_{pl}|}\right)^2\right). \tag{5.50}$$

Now, the objective function includes a frequency separation metric. This means that the result of the optimisation should not push the frequencies of the pitch and plunge modes as close together. The weighting constant used in the frequency metric was chosen manually so that the flutter speed increased maximally whilst the difference between successive iteration speeds was sufficient.

Table 5.2 shows the results with the new objective function. In comparison with Table 5.1, the velocity difference between successive iterations is now much larger. Consequently, the controller converges to the final solution in fewer steps. At the fifth iteration, the flutter speed decreases from the previous iteration. Therefore, this satisfies the stopping condition of the optimisation and iteration five is taken as the final controller.

Table 5.2: Optimisation 2: Single-input scheduling with a frequency separation metric.

Iteration	v_{it} (m/s)	v_{lim} (m/s)	v^* (m/s)
1	11.0	12.0	12.4
2	12.0	13.1	13.5
3	13.1	14.2	14.7
4	14.2	14.7	15.2
5	14.7	14.3	14.9

The final control gains for this objective function are

$$\mathbf{f} = \begin{pmatrix} 3.5771 \times 10^{-4} & -1.4537 \times 10^{-4} \end{pmatrix}^T, \quad \mathbf{g} = \begin{pmatrix} 1.4678 & -0.4292 \end{pmatrix}^T.$$

These values lie very close to the solution obtained from optimisation one. This suggests that the frequency separation metric does not always affect the final flutter speed but significantly affects the measurement speeds of the iteration technique.

Figures 5.6 and 5.7 show the variation of the real and imaginary part of the poles in the open-loop and final closed-loop configurations. As shown, the speed at which one of the poles crosses the imaginary axis is increased in the closed-loop. As expected, the frequency separation between the modes increases up to speed of around 14 m/s. However, this is at the expense of the damping of the first mode. Indeed, at speeds above 8 m/s, the damping of the least stable mode is lower. This suggests that, at these speeds, the frequency separation metric is the dominant factor in the optimisation. This is further supported by the final control gains, which are dominant in the displacement feedback; this is mainly associated with frequency/stiffness modifications.

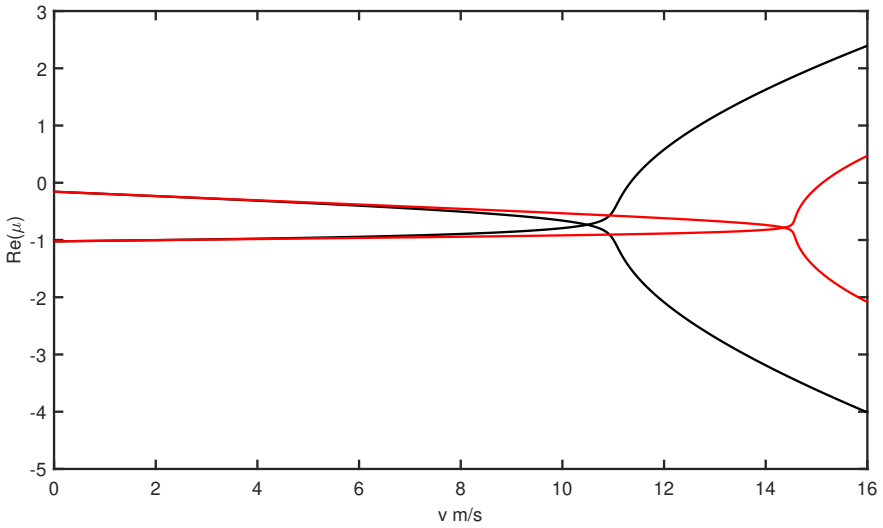

Figure 5.6: Real part variation of the poles in the open- and closed-loop configurations. (See legend in Fig. 5.7)

In general, it was found that changing the weighting of the frequency separation metric has very little effect on the final flutter speed. Figure 5.8 shows the effect of the weighting parameter on the final flutter speed and the number of iterations required to find the final controller. As shown, there is negligible impact on the flutter speed itself. However, the number of iterations required to reach the final solution decreases with a larger weighting. This may be useful in the experimental setting as one would likely want to minimise the number of experimental measurements required.

An interesting point to consider is the control effort at each step of the iteration. By substituting the control gains at each iteration into Eq. 5.48, the difference between the observed and maximum control effort is obtained. In both optimisation one and two, the maximum control effort is used at each iteration. This means that the controller is at its limit and hence cannot increase the damping or separate the frequencies, according to the objective function, any further. It is hypothesised, therefore, that by relaxing the control constraints it is possible to obtain a higher flutter speed. This is tested later.

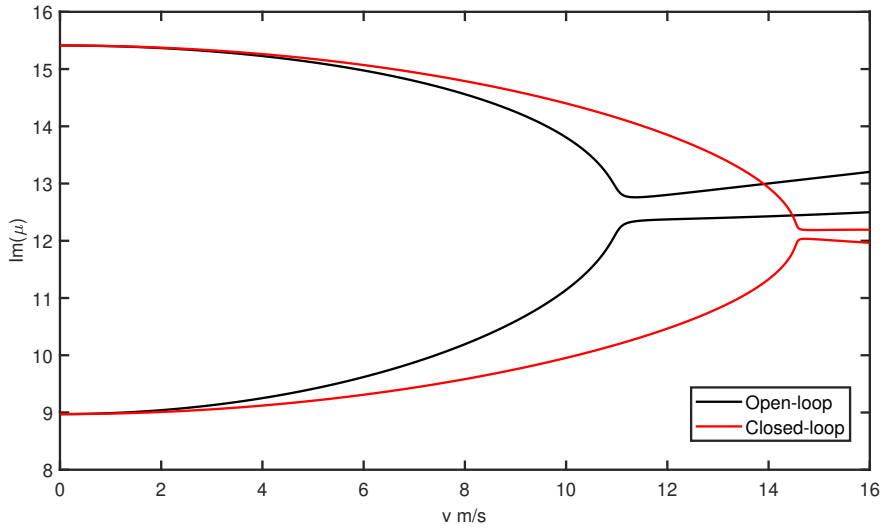

Figure 5.7: Imaginary part variation of the poles in the open- and closed-loop configurations.

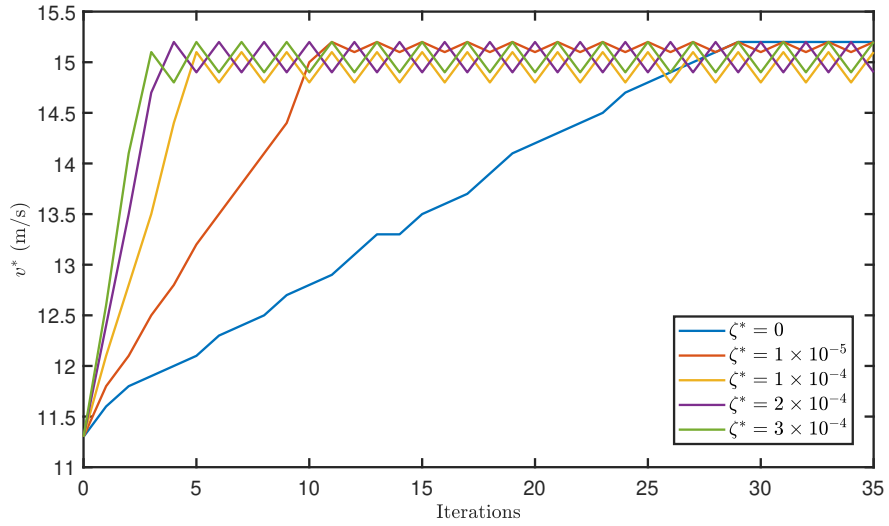

Figure 5.8: Effect of the frequency separation metric weighting parameter on the flutter speed at each iteration.

5.7.2 Multiple-Input

In this second example, the leading-edge control surface is reactivated. Now, the system returns to multiple-input. The gain constraints and objective function are initially kept unchanged[4]. In addition to the placement of the poles, the alpha vectors in the multiple-input formulation can be optimised.

Table 5.3 shows the results of the optimisation after five iterations. As shown, the final closed-loop flutter speed is 15.2 m/s. Notably, this is the same value as that obtained from the single-input example. The reason for this is the limited extra control effort that is introduced by the leading-edge control surface. In chapter 4, the force distribution matrix associated with the numerical model was written as

$$\mathbf{B}_a = \rho b s_p \begin{pmatrix} -C_{l_\beta} & -C_{l_\gamma} \\ bC_{m_{\beta-eff}} & bC_{m_{\gamma-eff}} \end{pmatrix}, \tag{5.51}$$

where the first column is associated with the trailing-edge input and the second column is associated with the leading-edge input. Substituting the parameters from the numerical model into this matrix gives that

$$\mathbf{B}_a = \begin{pmatrix} -0.5236 & 0.0217 \\ -0.0527 & -0.0046 \end{pmatrix}. \tag{5.52}$$

As shown, the values associated with the trailing-edge are an order of magnitude larger than the leading-edge, both in the pitch and plunge degrees-of-freedom. Since the optimisation relies upon minimising the control effort in order to improve the objective function, it is logical that most control effort will be assigned to the trailing edge. This is further confirmed by the final control gains, which are

$$\mathbf{F} = \begin{pmatrix} 1.680 \times 10^{-4} & -2.373 \times 10^{-4} \\ -1.4283 \times 10^{-4} & 0.100 \times 10^{-4} \end{pmatrix}, \quad \mathbf{G} = \begin{pmatrix} 1.4756 & 0.0252 \\ -0.4468 & -0.0095 \end{pmatrix} \tag{5.53}$$

Note that the first column of both control matrices, corresponding to the trailing-edge input, closely matches the final result obtained from optimisation two.

A confirmatory study of this is shown in Appendix B, where the single-input example is repeated but with the leading-edge instead of the trailing-edge. As expected, the leading-edge has very little impact on the closed-loop system.

Table 5.3: Optimisation 3: Multiple-input optimisation.

Iteration	v_{it} (m/s)	v_{lim} (m/s)	v^* (m/s)
1	11.0	12.0	12.5
2	12.0	13.1	13.6
3	13.1	14.2	14.7
4	14.2	14.7	15.2
5	14.7	14.6	15.2

Whilst this example does not show the benefits of multiple-input AFS control, it does show that the optimisation works as intended. The final controller, found through this method, does not waste effort on the actuation of the leading-edge control surface.

[4] Objective function two is used.

The Effect of the Control Constraints

Throughout the numerical examples, it has been observed that the control effort is always maximised and that the limit of the gain constraints is reached at each iteration. Based on this, it has been hypothesised that relaxing the gain constraint will increase the final flutter speed, and vice-versa. To test this, the multiple input optimisation was run again with the same objective function as before, but with different constants on the right hand side of Eq. 5.48. Table 5.4 shows the results of this test. As anticipated, the relaxation of the gain constraints leads to a higher closed-loop flutter speed.

Table 5.4: The effect of the gain constraints on the flutter speed.

Constraint value	v^* (m/s)
$\frac{4\pi}{180}$	13.9
$\frac{5\pi}{180}$	15.2
$\frac{6\pi}{180}$	17.7

5.8 Experimental Case Study

The optimum eigenstructure assignment and iterative control techniques described in the previous sections were also tested experimentally on the University of Liverpool's pitch-plunge aeroelastic wind-tunnel model. The aim was to demonstrate the practicality of the technique and to highlight some of the limiting factors and remaining challenges in its implementation. This section details the experimental procedure and the results obtained.

5.8.1 Methodology

The first step in the iterative control method is to collect frequency response function data from the open-loop system. All FRF data referenced hereinafter were collected through MIMO random testing using the Siemens SCADAS data acquisition system. White noise signals, with frequencies between 2 to 5 Hz, were passed to the PID controller of both the leading and trailing edge control surfaces. The displacements of two positions on the structure, which are discussed in Chapter 4, were then measured and automatically converted to FRF data. To reduce the impact of noise, measurements were repeated 20 times. The FRF data shown hereinafter gives the averaged values.

First Iteration

The first control iteration was performed at a freestream speed of 12.7 m/s. This was chosen to give a sufficient margin from the open-loop flutter speed (14.5 m/s)[5], without having too small a speed that a controller would not have any significant impact. Figure 5.9 shows the FRF data at this speed and the corresponding rational transfer function (RTF) fitting. The RTF fitting was done using the Siemens PolyMAX algorithm [97], which is included in the SCADAS data acquisition software. In addition to the two modes corresponding to the pitch and plunge degrees-of-freedom, upper and lower residuals were used in the fitting to improve its accuracy. Across all four FRFs, it is was found that the final fitting was good in both the amplitude and

[5]This value is slightly different to that stated in Chapter 4 as the experiment was dismantled and re-setup during the Covid pandemic.

phase[6]. However, measurement noise from the FRFs meant that it was almost impossible to obtain an exact fit and there is some degree of uncertainty in the best fitting available.

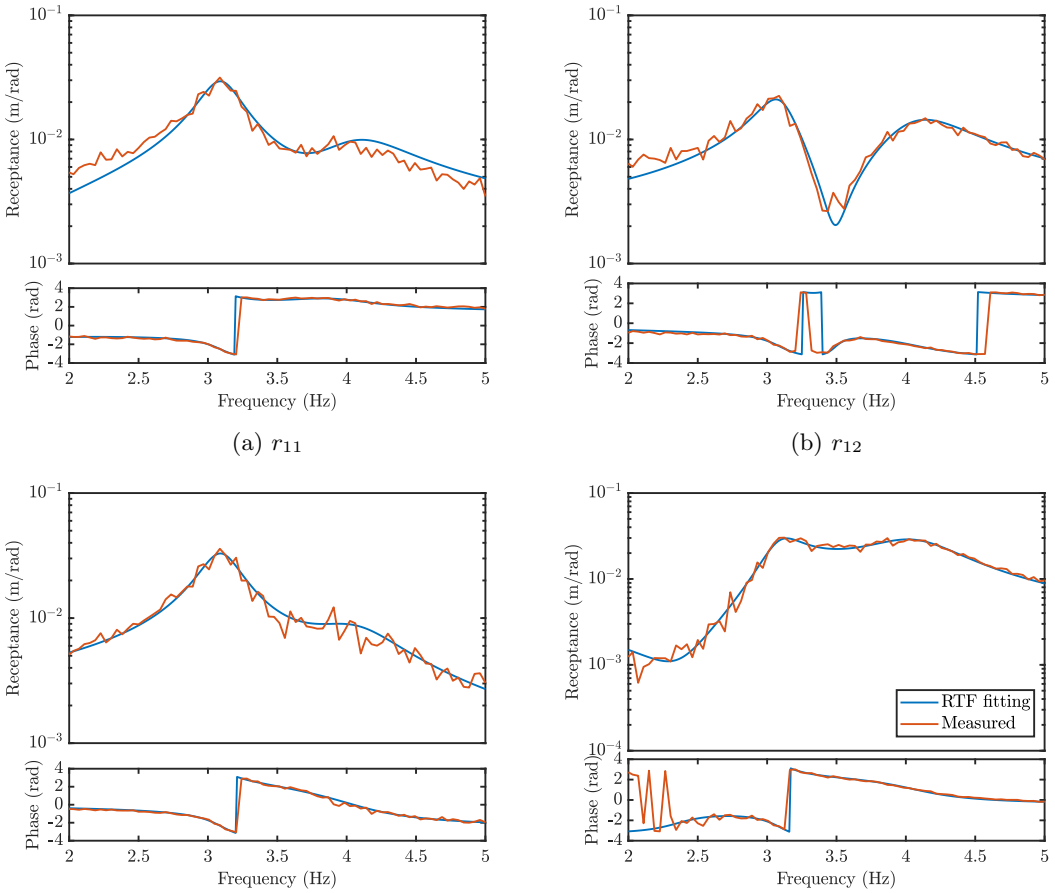

(a) r_{11} (b) r_{12}

(c) r_{21} (d) r_{22}

Figure 5.9: Rational transfer function fitting of the FRF data at 12.7 m/s.

With the RTF fitting complete, the next step was to define the objective function. In this work, the final objective function was taken as

$$\rho = -\min\left(\zeta_{pi}, \zeta_{pl}\right) + \zeta^* \max\left(\left(\frac{\min\left(\omega_{pi}, \omega_{pl}\right)}{|\omega_{pi} - \omega_{pl}|}\right)^2\right), \tag{5.54}$$

where the subscripts 'pi' and 'pl' represent the pitch and plunge modes, respectively. The constant ζ^* that weights the frequency separation metric was chosen empirically. After conducting several tests to chose a suitable value for the experiment, a final value of 0.0003 was selected. This constant is in the same order of magnitude as the one used in the numerical examples. Therefore, it appears that the non-dimensional form of the objective function is appropriate, with only small adjustments, in terms of scalability, to other aeroservoelastic systems of a similar kind.

The gain constraints used in this work were chosen as

$$2\pi * 3.5||\mathbf{\Lambda F}||_F + ||\mathbf{\Lambda G}||_F \leq 15, \tag{5.55}$$

[6]This is verified later in the results.

where

$$\mathbf{\Lambda} = \begin{pmatrix} 20 & 0 \\ 0 & 20 \end{pmatrix}.$$

The value of 15 was chosen on the right hand side of the gain constraints based on a rough maximum deflection angle of 7.5 degrees in each flap. The values in the $\mathbf{\Lambda}$ were chosen based on assumed maximum deflections at the positions of the lasers. The constant before the $\mathbf{F}$ term was selected as roughly the averaged values of the two natural frequencies, in rad/s. It is important to note that the gains in Eq. 5.55 are expressed in the units of deg/mm and deg.s/mm. These will be the standard units used throughout the rest of this case study.

After running the optimisation using data from the RTF fitting at 12.7 m/s, the optimum closed-loop poles after the first control iteration were found to be

$$\mu_{1,2} = -1.4083 \pm 18.9788\text{i},$$
$$\mu_{3,4} = -1.9156 \pm 25.8150\text{i}.$$

The corresponding optimum alpha vectors were

$$\boldsymbol{\alpha}_{1,2} = \begin{pmatrix} 1 \\ 0.84 \pm 0.1\text{i} \end{pmatrix}, \quad \boldsymbol{\alpha}_{3,4} = \begin{pmatrix} 1 \\ 5 \pm 3.52\text{i} \end{pmatrix}.$$

Before the optimisation (with the open-loop poles), the objective function was -0.0441. After optimisation, the objective function decreased to -0.0717 and hence the performance metric was improved by 63%.

In this first iteration, the frequency separation between the pitch and plunge modes increased from 6.1409 rad/s to 6.8550 rad/s. Additionally, the damping in the lowest mode (plunge) increased from 0.0471 to 0.0740. These points are illustrated in Fig. 5.10, which shows the FRFs before and after the controller was applied. It is interesting to note that the damping in the pitch mode decreased from 0.0853 to 0.0740. Of course, the maximum damping is not specified in the objective function and, as in the numerical example, it is expected that the damping in the pitch mode may be reduced in order to facilitate a greater damping in the plunge mode or a greater frequency separation between the modes.

Other Iterations

The process described above was repeated across three further iterations with the objective function and constraints kept constant. Table 5.5 shows the reference speeds at which FRFs were measured in each iteration and the corresponding new flutter speed, once the optimum controller has been applied. Tables 5.7 and 5.8 show the variation of the control gains in each iteration. As shown, the flutter speed increases with each iteration and thus one can conclude that the choice of objective function is sufficient. Between the first and second iteration it is noted that the flutter speed barely changes. This is because the reference speeds lie close to each other and hence the difference between the FRFs at these respective speeds is not significant. In iteration 3 and 4, FRFs are collected above the flutter speed and hence the iteration method is shown to work in an experimental setting.

The final flutter speed after applying the final controller was approximately 17.7 m/s. In principle, further iterations could be been done to enable further FRF measurements and a potentially higher flutter speed. However, due to the physical limitations of the wind-tunnel, it was decided to stop at the fourth iteration. Furthermore, at the fourth iteration it was observed

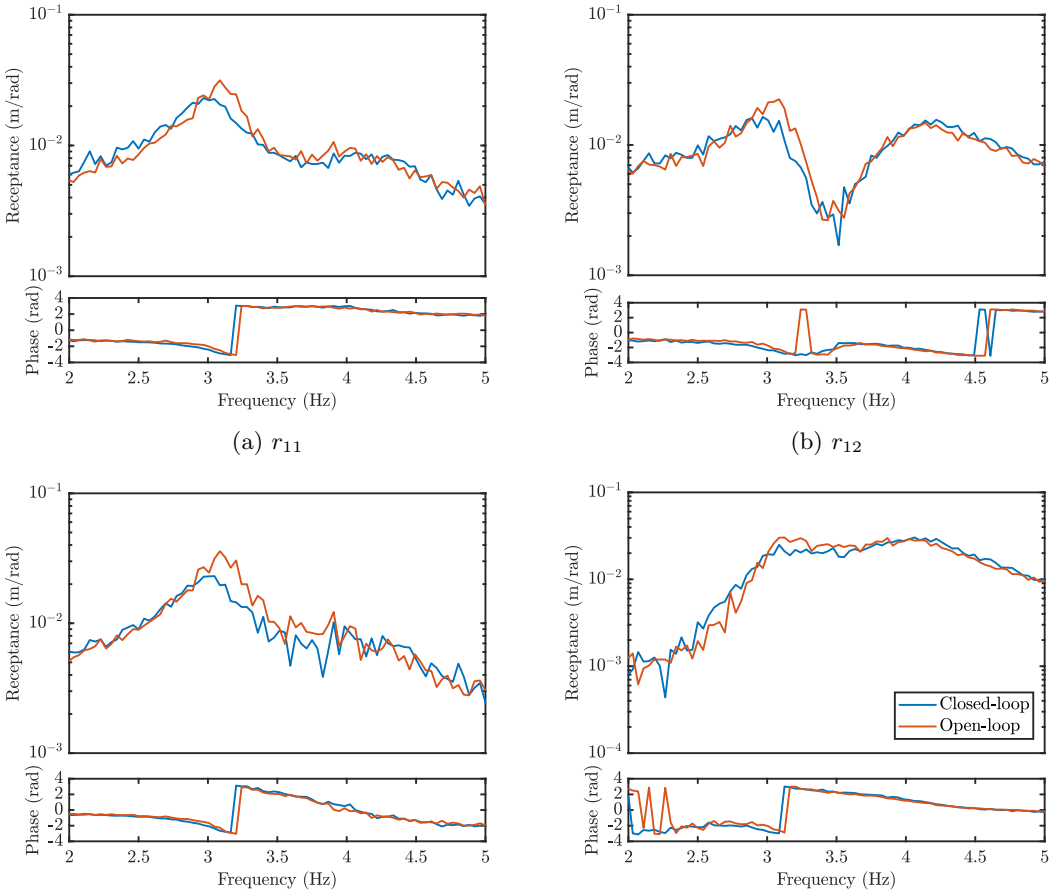

(a) r_{11} (b) r_{12}

(c) r_{21} (d) r_{22}

Figure 5.10: FRFs at 12.7 m/s, before and after the control iteration.

that the angle of deflection of the aerofoil itself was so great that separation of the flow was likely to occur and damage to the pitch springs may have arisen if pushed further.

Table 5.5: Reference speeds and new closed-loop flutter speed in each control iteration.

Iteration	v_{ref} (m/s)	$v^*(m/s)$
1	12.7	16.7
2	13.4	16.8
3	14.7	17.2
4	16	17.7

To verify the performance of the controller, FRF tests were conducted at the various iteration speeds with their respective control gains active. Table 5.6 shows a comparison of the desired and actual poles in the closed-loop for each iteration speed. As shown, there is a good agreement between the desired and actual controller. This indicates that the RTF in each speed is representative of the true system and hence leads to a reasonably accurate controller. At higher speeds, the difference between the true and desired poles is slightly greater than at lower speeds. This is most likely due to increased difficulty in fitting data at the higher speeds due to increased measurement noise. For example, this is illustrated in the final FRF and RTF fitting at 16 m/s, which is given in Fig 5.11. Additionally, it is to be noted that the percentage error in the real part of the assigned poles is smaller than the real part. Such an effect has also been observed experimentally in [128].

Table 5.6: Comparison of desired and true pole placement at each iteration.

Iteration	Desired Poles		Actual poles	
	$\mu_{1,2}$	$\mu_{3,4}$	$\mu_{1,2}$	$\mu_{3,4}$
1	$-1.408 \pm 18.98i$	$-1.916 \pm 25.82i$	$-1.351 \pm 18.95i$	$-1.995 \pm 25.95i$
2	$-1.668 \pm 18.88i$	$-2.207 \pm 24.99i$	$-1.680 \pm 18.89i$	$-2.142 \pm 25.17i$
3	$-1.966 \pm 18.99i$	$-2.447 \pm 23.63i$	$-1.673 \pm 18.93i$	$-2.293 \pm 23.64i$
4	$-1.840 \pm 19.07i$	$-2.291 \pm 23.75i$	$-1.632 \pm 19.05i$	$-2.015 \pm 24.28i$

Table 5.7: Variation of the gains in the **G** matrix with each iteration.

Iteration	g_{11} (deg/mm)	g_{12} (deg/mm)	g_{21} (deg/mm)	g_{22} (deg/mm)
1	0.4698	0.1391	0.3090	0.4727
2	0.4707	0.2907	0.3483	0.3471
3	0.4536	0.4009	0.1694	0.0815
4	0.1982	0.1622	0.0928	0.0396

Table 5.8: Variation of the gains in the **F** matrix with each iteration.

Iteration	f_{11} (deg· s/mm)	f_{12} (deg· s/mm)	f_{21} (deg· s/mm)	f_{22} (deg· s/mm)
1	0.0000194	-0.0000688	0.0000458	0.0000594
2	0.0000236	-0.0002029	-0.0000682	0.0003908
3	-0.0010000	-0.0024000	-0.0014000	0.0044000
4	-0.0043000	-0.0128000	-0.0079000	0.0149000

5.8.2 Final Result & Discussion

FRF testing was repeated across a range of different freestream speeds with the final control gains applied. The PolyMAX algorithm was then used again to identify the poles of the system

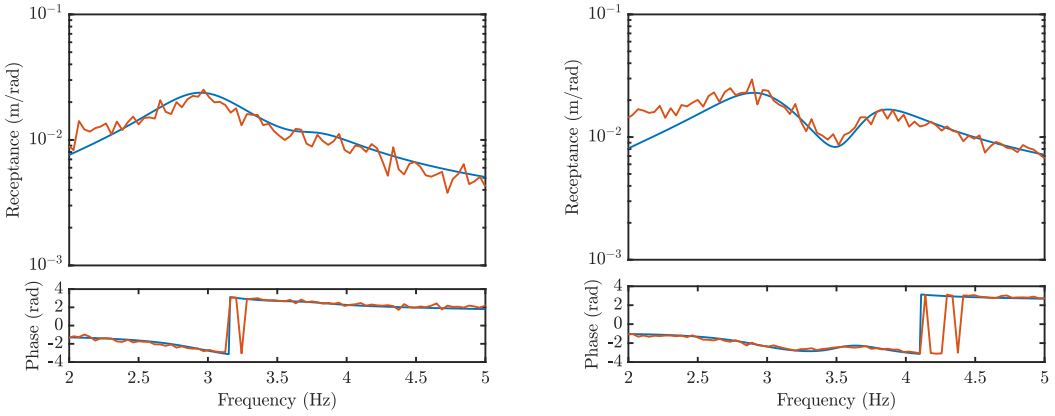

(a) r_{11}

(b) r_{12}

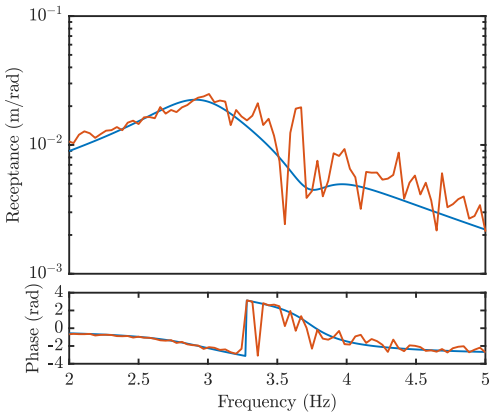

(c) r_{21}

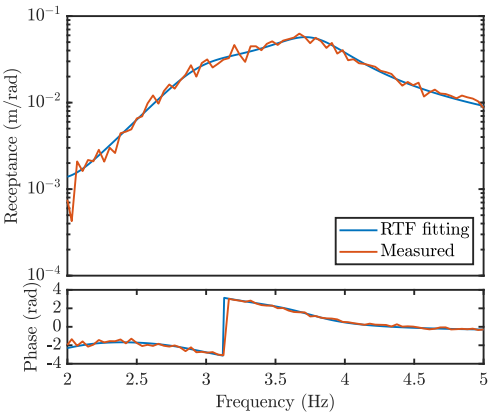

(d) r_{22}

Figure 5.11: Rational transfer function fitting of the FRF data at 16.0 m/s.

at each measured freestream speed. Figures 5.12 and 5.13 show the real and imaginary part variation of the poles with respect to the freestream speed in both the closed-loop and open-loop configurations.

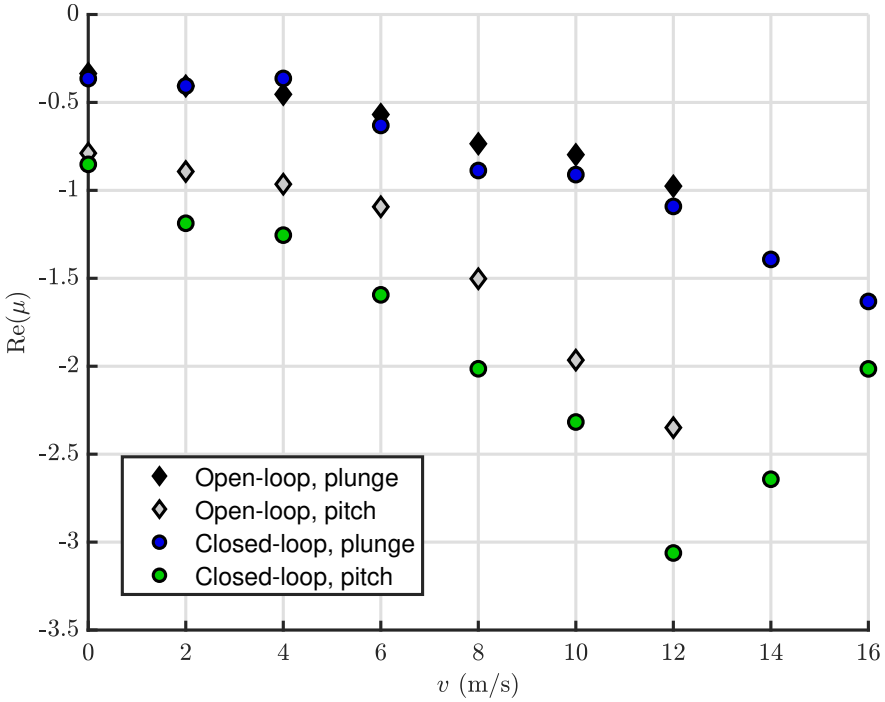

Figure 5.12: Real part variation of the poles in the open- and closed-loop configurations.

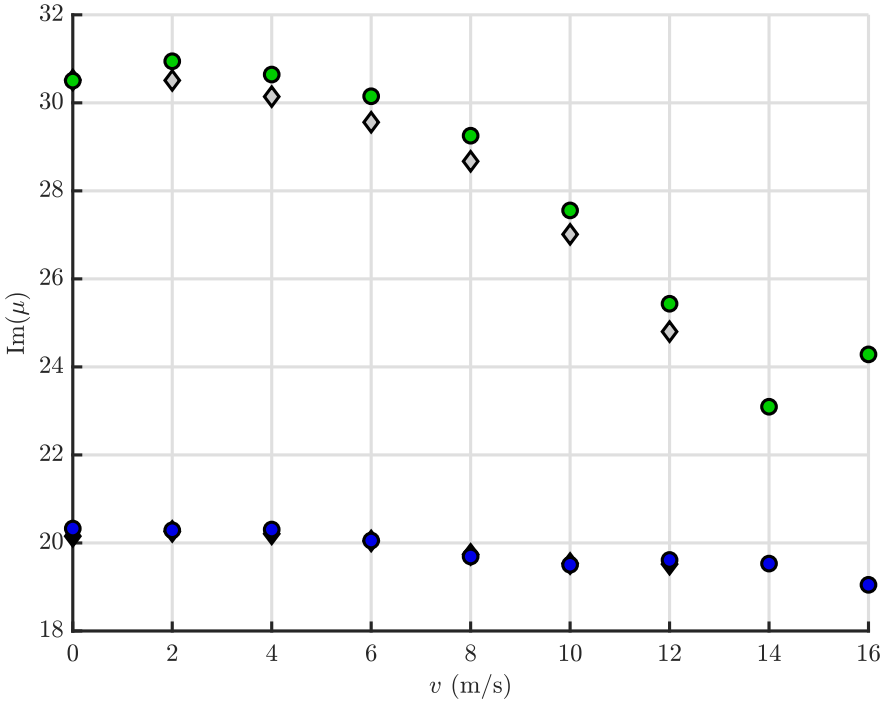

Figure 5.13: Imaginary part variation of the poles in the open- and closed-loop configurations. (see legend in Fig. 5.12)

The most obvious feature in Fig. 5.12 is that the real part of both the pitch and plunge modes is more negative across the full range of speeds tested. In other words, the damping in

both modes has been increased. It is reasonable to conclude, therefore, that the action of the controller in the final iteration is concentrated mainly on increasing the damping, particular in the pitch mode.

In figure 5.13, it is shown that the plunge frequency is barely modified in between the open- and closed-loop. However, the pitch frequency appears to be modified and increased slightly. In this way, the frequency separation of the modes is increased. As discussed previously, this is one of the strategies known to increase the flutter speed.

By contrast with the numerical example, the pitch frequency is modified slightly at lower speeds. There may be several reasons for this. Firstly, it is possible that the inertia of the flap is sufficient to exert a force on system when it moves. Consequently, the inertia force may create a force that is proportional to the displacement of the pitch motion and hence increase its frequency. Secondly, throughout the tests it was necessary to re-tighten the pitch springs. This was due to slippage in the clamp that arose when the system was tested at high speeds. As a result of this, different tightening could have caused the pitch stiffness to be changed slightly; especially as the springs on either side of the test section are not perfectly identical. Finally, at lower speeds the displacement of the system is small during FRF testing. Consequently, the FRFs can contain some noisy artefacts and exact identification of the pitch frequency can be difficult.

Gain Scheduling

It is worthwhile to note that the desired poles given in Table 5.6 do not match the true values shown in Figs. 5.12 and 5.13 for the first three iterations. Indeed, the only iteration for which they do match is the final, fourth one. This is because the control gains change between the iterations and hence the action of the controller at lower speeds no longer matches what was achieved with the gains found at previous iterations. In this particular system, this does not present an issue as the system remains stable up to the final flutter speed. However, in other aeroelastic systems, this may not always be the case. If the system has a larger number of degrees-of-freedom, it may be possible that different control gains are required at different speeds to suppress different modes that could become unstable in different regions. Moreover, if the inertia of the flap is large, there can be a transition behaviour between the inertia of the flap and the aerodynamic.

In the situations mentioned above, it may be necessary to vary the objective of the controller with the freestream speed. In this way, the control gains would also vary with the freestream speed in some way. Such an approach is known as gain-scheduling and is an approach that has been used in a variety of different applications. It is suggested, perhaps, that this may be necessary for real-world applications and presents an open area of research to consider in future work.

5.9 Summary

This chapter considers the development of receptance-based control techniques for the purpose of active flutter suppression in aeroservoelastic systems. Two new methodologies are developed to address some of the current limitations in applying such methods to real world systems. Firstly, an optimum eigenstructure assignment method is developed, where the eigenvalues and eigenvectors are assigned optimally according to a user-defined objective function, which penalises low damping and low frequency separation between modes. The optimisation also

takes into account the maximum effort of the controller, something that was previously an afterthought of the eigenstructure assignment. Secondly, a control iteration strategy is developed. This allows receptances to be collected close to, at, or even above the flutter speed. In this way, the controller is far more likely to be optimal in terms of flutter suppression performance.

The methods were applied both numerically and experimentally to test their performance. In the numerical examples, it was shown that the technique was able to successfully increase the flutter speed. Moreover, it was shown that using receptance data from speeds at or above the open-loop flutter speed led to a better AFS controller. The effect of the weighting constant in the objective function was considered and shown to have little effect on the final flutter speed. However, the weighting parameter did affect the convergence of the final solution and the number of iteration steps required. It was also shown that the control effort at each stage of the iteration was at the limit defined by the gain constraints. Consequently, it was shown that a better AFS solution could be obtained by relaxing the gain constraints. In other words, more control effort leads to a higher final flutter speed.

In the experimental case study, it was shown that the flutter speed could be increased by approximately 22%. Furthermore, as in the numerical example, the performance of the controller was also better when using receptance data at higher speeds, well above the open-loop flutter speed. It was noted, however, that limitations in terms of FRF measurement noise and physical factors, such as spring variability, affected the robustness of the AFS controller and hence further work is required to address these points.

It is suggested that this work may be extended in future research through the implementation of a gain scheduling scheme, which would allow the control gains to vary with the freestream speed and hence permit different control objectives at different speed. Furthermore, the complexity of the optimisation could be reduced by automatically assigning the alpha vectors through some deterministic method that minimises the control effort. In this way, regardless of whether the system is single- or multiple-input, only the closed-loop eigenvalues would be the optimisation variables.

This page is intentionally left blank.

Chapter 6

Uncertainty in the Receptance Method: RTF Fittings

6.1 Introduction

In the previous chapter, an experiment-based approach to eigenstructure assignment in aeroservoelastic systems was developed. The Receptance Method was extended for the purposes of active flutter suppression through the creation of a new control iteration technique and an optimum eigenstructure assignment procedure. As previously mentioned, the main advantage of receptance-based techniques is that there is no need to create a numerical model of the system. Consequently, errors arising from restrictive modelling assumptions and poorly estimated structural and aerodynamic parameters are eliminated. However, despite mitigating said uncertainties, the Receptance Method is still subject to various errors. Indeed, by virtue of the experimental-only nature of the technique, uncertainties arising from experimental sources are prominent and must be considered. The problems associated with these types of uncertainties will be addressed in the following two chapters. The sources of the uncertainties and their effects on the eigenstructure assignment will be quantified. Furthermore, methodologies will be developed to reduce their influence on the eigenstructure assignment.

In this chapter, the uncertainty that arises from errors in rational transfer function fittings (RTFs) of measured FRF data is considered. Such errors occur due to poor fitting algorithms and ill-conditioned, noisy experimental FRF data. The relationship between the variability in the parameters of the RTFs and the resulting spread of the closed-loop poles is quantified by means of analytic sensitivity formulae, which are derived for the first time. A robustness metric, which is constructed using the above-mentioned sensitivity formulae, is defined. This metric is then used for optimal eigenstructure assignment, which is performed using a global optimisation algorithm. The proposed technique is applied numerically on a simple mass-spring-damper system in both single- and multiple-input configurations. The technique is also applied to experimental data from the aerservoelastic rig described in Chapter 4.

6.2 Uncertainty in Rational Transfer Function (RTF) Fittings

Consider again the steps of the Receptance Method. In order to calculate the control gains $\mathbf{F}$ and $\mathbf{G}$, it is necessary to evaluate the input-output transfer function matrix $\mathbf{R}(s)$ at each closed-loop pole μ_i. When $\mathrm{Re}(\mu_i) = 0$, or in other words the desired closed-loop pole lies on the imaginary axis, $\mathbf{R}(\mu_i) = \mathbf{R}(i\omega_i)$ and hence the transfer function matrix is simply equal to the matrix of measured frequency response functions. Therefore, in this special case, one can proceed with the Receptance Method directly using the measured FRF data. However, in the more general and usual case that $\mathrm{Re}\,(\mu_i) \neq 0$, the input-output transfer function matrix does not correspond to the measured FRFs and RTF fitting is required.

RTF fitting is a numerical technique that extends the domain of the frequency response functions, which is originally purely imaginary points (i.e. $\mathbf{F}(i\omega)$), to any general point in the complex plane, i.e. $\mathbf{F}(s), s \in \mathbb{C}$. There are a plethora of different techniques to do this. However, the underlying principle of RTF fitting is to construct a transfer function model, which depends on some chosen parameters, and to minimise the error between the model prediction of the FRF and the true, experimental FRF data.

In practice, the goodness of fit in the RTF model depends on a number of factors. Firstly, the quality of the measured, experimental data must be sufficient. If the experimental data is noisy, incomplete or has too small a frequency domain, it may be difficult to fit an RTF model and thus the model may not truly reflect the experimental system. Secondly, as discussed by Ewins [96], RTF approximations have difficulty in accurately estimating the damping. This is especially true if the damping is very small, leading to large peaks in the FRF data, or if the damping is very large, making the identification of a peak very difficult in the first place. Moreover, numerous fitting algorithms require that a user must manually choose the peaks in the FRF and thus an element of human error is introduced too. Finally, RTF fitting usually requires an initial model form. Indeed, it is often the case that one must determine the number of modes in the system and specify whether the modes are normal, complex, etc. This also introduces an element of uncertainty in the RTF. If one does not select an appropriate model structure, it is possible that the fitting is sub-optimal, regardless of the final fitting parameters.

In practice, the parameters of the fitting are assumed to be deterministic. However, due to the above-mentioned sources of uncertainty, it is arguably more appropriate to consider the parameters as non-deterministic values, such as intervals or random variables. In the remainder of this section, a generalised formulation of the RTF fitting is given and the consequences of treating the fitting parameters as non-deterministic quantities is considered.

6.2.1 Mathematical Formulation

In its most general form, the input-output transfer function matrix may be expressed as

$$\mathbf{R}(s) = \frac{\mathbf{N}(s)}{d(s)}, \tag{6.1}$$

where $\mathbf{N}(s) \in \mathbb{C}^{n\times m}$ is the matrix numerator term; and $d(s) \in \mathbb{C}$ is the scalar denominator term, which is also known as the characteristic polynomial. The scalar denominator term is a

monic polynomial whose roots are the open-loop poles of the system. Therefore

$$d(s) = \prod_{i=1}^{l} (s - \lambda_i)\,, \tag{6.2}$$

where l is the total number of poles. The matrix numerator term is a matrix of possibly non-monic polynomials, whose roots are the open-loop zeros of the system. In other words, each element $n_{ij}(s)$ of the matrix $\mathbf{N}(s)$ may be expressed as

$$n_{ij}(s) = \eta_{ij} \prod_{k=1}^{K_{ij}} (s - z_{ij_k})\,, \tag{6.3}$$

where z_{ij_k} is the k^{th} zero belonging to the element ij, K_{ij} is the total number of zeros in the ij^{th} element, and η_{ij} is named the scaling parameter. The input-output transfer function matrix is therefore fully described by the open-loop poles, open-loop zeros, and scaling parameters, which are all selected during RTF fitting.

Let the fitted poles, zeros and scaling parameters be compiled into a vector of fitting parameters $\boldsymbol{\theta} \in \mathbb{C}^p$. To show the dependency of the input-output transfer function matrix on the fitting parameters, the notation for $\mathbf{R}(s)$ is now replaced by $\mathbf{R}(s, \boldsymbol{\theta})$. Hence, the eigenvalue problem is rewritten as

$$\left(\mathbf{I} - \mathbf{R}(\mu_i, \boldsymbol{\theta}) \left(\mu_i \mathbf{F}^T + \mathbf{G}^T\right)\right) \mathbf{w}_{R,i} = \mathbf{0}, \quad i = 1, 2, \ldots, l, \tag{6.4}$$

$$\mathbf{w}_{L,i}^T \left(\mathbf{I} - \mathbf{R}(\mu_i, \boldsymbol{\theta}) \left(\mu_i \mathbf{F}^T + \mathbf{G}^T\right)\right) = \mathbf{0}^T, \quad i = 1, 2, \ldots, l. \tag{6.5}$$

In this form, it is clear that the eigenvalue problem depends on the chosen parameters. This means that the parameters in the fitting dictate the eigensolutions of the closed-loop system. In general, the relationships between the fitting parameters and the closed-loop poles, or eigensolutions, cannot be expressed in analytic form. Therefore, in order to understand the effects of the parameters on the closed-loop poles, one must use computational or approximation methods. One such method is presented in the following section and is based on the principles of local sensitivity analysis.

6.3 Local Sensitivity Analysis

The number of fitting parameters in the transfer function matrix may be in the order of tens, hundreds, or possibly thousands. This is especially true for systems with a large number of inputs, outputs, or modes that lie within the frequency range of interest. Therefore, bearing in mind computational effort, a sensitivity-based approach is used to quantify the relationship between the fitting parameters and the eigenvalue solutions. In this way, the computation of the uncertainty is order one. That is, doubling the number of sensitivity parameters doubles the computational time.

Consider a small perturbation of *one* of the fitting parameters about the nominal value obtained by RTF fitting, so that: $\theta \to \theta + \delta\theta$, $\mu_i \to \mu_i + \delta\mu_i$ and $\mathbf{w}_{R,i} \to \mathbf{w}_{R,i} + \delta\mathbf{w}_{R,i}$. The eigenvalue problem associated with the perturbed system is given by

$$\left(\mathbf{I} - \mathbf{R}(\mu_i + \delta\mu_i, \theta + \delta\theta) \left((\mu_i + \delta\mu_i)\, \mathbf{F}^T + \mathbf{G}^T\right)\right) (\mathbf{w}_{R,i} + \delta\mathbf{w}_{R,i}) = \mathbf{0}, \quad i = 1, 2, \ldots, l. \tag{6.6}$$

If one assumes that $\delta\theta$ and $\delta\mu_i$ are small

$$\mathbf{R}(\mu_i + \delta\mu_i, \theta + \delta\theta) \approx \mathbf{R}(\mu_i, \theta) + \frac{\partial \mathbf{R}}{\partial s}\delta\mu_i + \frac{\partial \mathbf{R}}{\partial \theta}\delta\theta, \quad i = 1, 2, \ldots, l, \tag{6.7}$$

and thus

$$\left(\mathbf{I} - \left(\mathbf{R}(\mu_i, \theta) + \frac{\partial \mathbf{R}}{\partial s}\delta\mu_i + \frac{\partial \mathbf{R}}{\partial \theta}\delta\theta\right)\left(\left(\mu_i + \delta\mu_i\right)\mathbf{F}^T + \mathbf{G}^T\right)\right)\left(\mathbf{w}_{R,i} + \delta\mathbf{w}_{R,i}\right) = \mathbf{0}, \quad i = 1, 2, \ldots, l. \tag{6.8}$$

Expanding Eq. 6.8 and dropping the second- and higher-order terms gives that

$$\begin{aligned}&\left(\mathbf{I} - \mathbf{R}(\mu_i, \theta)\left(\mu_i\mathbf{F}^T + \mathbf{G}^T\right)\right)\left(\mathbf{w}_{R,i} + \delta\mathbf{w}_{R,i}\right)\\ &+ \left(-\mathbf{R}\left(\mu_i, \theta\right)\mathbf{F}^T\delta\mu_i - \left(\frac{\partial \mathbf{R}}{\partial s}\delta\mu_i + \frac{\partial \mathbf{R}}{\partial \theta}\delta\theta\right)\left(\mu_i\mathbf{F}^T + \mathbf{G}^T\right)\right)\mathbf{w}_{R,i} = \mathbf{0}, \quad i = 1, 2, \ldots, l,\end{aligned} \tag{6.9}$$

and thus, by making use of the definition of the left eigenvector in Eq. 6.5, Eq. 6.9 may be reduced to

$$\mathbf{w}_{L,i}^T\left(-\mathbf{R}\left(\mu_i, \theta\right)\mathbf{F}^T\delta\mu_i - \left(\frac{\partial \mathbf{R}}{\partial s}\delta\mu_i + \frac{\partial \mathbf{R}}{\partial \theta}\delta\theta\right)\left(\mu_i\mathbf{F}^T + \mathbf{G}^T\right)\right)\mathbf{w}_{R,i} = 0, \quad i = 1, 2, \ldots, l. \tag{6.10}$$

By rearranging and taking the limit as $\delta\theta$ tends to zero, the sensitivity of a closed-loop pole with respect to an arbitrary fitting parameter in the transfer function matrix is given by

$$\frac{\partial \mu_i}{\partial \theta} = -\frac{\mathbf{w}_{L,i}^T\frac{\partial \mathbf{R}}{\partial \theta}\left(\mu_i\mathbf{F}^T + \mathbf{G}^T\right)\mathbf{w}_{R,i}}{\mathbf{w}_{L,i}^T\left(\mathbf{R}\left(\mu_i, \theta\right)\mathbf{F}^T + \frac{\partial \mathbf{R}}{\partial s}\left(\mu_i\mathbf{F}^T + \mathbf{G}^T\right)\right)\mathbf{w}_{R,i}}, \quad i = 1, 2, \ldots, l. \tag{6.11}$$

In the form given above, the sensitivity of a closed-loop pole can be found by using only the nominal transfer function matrix obtained by RTF. First, the right and left eigenvectors are found from the null space of

$$\mathbf{I} - \mathbf{R}(\mu_i, \theta)\left(\mu_i\mathbf{F}^T + \mathbf{G}^T\right) \tag{6.12}$$

and

$$\left(\mathbf{I} - \mathbf{R}(\mu_i, \theta)\left(\mu_i\mathbf{F}^T + \mathbf{G}^T\right)\right)^T, \tag{6.13}$$

respectively. Additionally, the term $\frac{\partial \mathbf{R}}{\partial s}$ is found by differentiating the the fitted, nominal input-output transfer function matrix $\mathbf{R}(s)$ by the Laplace variable s. The term $\frac{\partial \mathbf{R}}{\partial \theta}$ depends on the type of fitting parameter that is chosen. Still, however, it can be expressed in terms of the nominal transfer function matrix. Expressions for this sensitivity term are derived in the following subsections for the cases of open-loop poles, zeros and scaling parameters.

6.3.1 Sensitivity to Open-Loop Poles

First, the sensitivity of the closed-loop poles to the open-loop poles in the RTF is considered. Let the transfer function matrix be written in the form

$$\mathbf{R}\left(s\right) = \frac{\mathbf{N}(s)}{\prod_{i=1}^{l}\left(s - \lambda_i\right)} \tag{6.14}$$

and suppose that one of the fitted poles, λ_j, is uncertain. By writing Eq. 6.14 as

$$\mathbf{R}\left(s,\lambda_j\right)=\frac{\mathbf{N}(s)}{\left(s-\lambda_j\right)\prod_{i=1,i\neq j}^{l}\left(s-\lambda_i\right)}, \tag{6.15}$$

the partial derivative with respect to λ_j is simply

$$\frac{\partial\mathbf{R}}{\partial\lambda_j}=\frac{\mathbf{N}(s)}{\left(s-\lambda_j\right)^2\prod_{i=1,i\neq j}^{l}\left(s-\lambda_i\right)}=\frac{\mathbf{R}(s)}{s-\lambda_j}. \tag{6.16}$$

Substituting this into Eq. 6.11 gives that

$$\frac{\partial\mu_i}{\partial\lambda_j}=-\frac{\mathbf{w}_{L,i}^T\mathbf{R}(\mu)\left(\mu_i\mathbf{F}^T+\mathbf{G}^T\right)\mathbf{w}_{R,i}}{\left(\mu_i-\lambda_j\right)\mathbf{w}_{L,i}^T\left(\mathbf{R}\left(\mu_i,\theta\right)\mathbf{F}^T+\frac{\partial\mathbf{R}}{\partial s}\left(\mu_i\mathbf{F}^T+\mathbf{G}^T\right)\right)\mathbf{w}_R},\quad i=1,2,\ldots,l, \tag{6.17}$$

which, by definition of the right eigenvector, reduces to

$$\frac{\partial\mu_i}{\partial\lambda_j}=-\frac{\mathbf{w}_{L,i}^T\mathbf{w}_{R,i}}{\left(\mu_i-\lambda_j\right)\mathbf{w}_{L,i}^T\left(\mathbf{R}\left(\mu_i,\theta\right)\mathbf{F}^T+\frac{\partial\mathbf{R}}{\partial s}\left(\mu_i\mathbf{F}^T+\mathbf{G}^T\right)\right)\mathbf{w}_{R,i}},\quad i=1,2,\ldots,l. \tag{6.18}$$

6.3.2 Sensitivity to Open-Loop Zeros

Next, the sensitivity of the closed-loop poles to the fitted zeros is considered. Suppose that the transfer function matrix is expressed as

$$\mathbf{R}(s)=\frac{\mathbf{N}(s)}{d(s)} \tag{6.19}$$

and further suppose that the k^{th} zero $z_{ij,k}$ belonging to the ij^{th} element of $\mathbf{N}(s)$ is variable. The derivative of $\mathbf{R}(s)$ with respect to $z_{ij,k}$ is given by

$$\frac{\partial\mathbf{R}}{\partial z_{ij,k}}=\frac{1}{d(s)}\frac{\partial\mathbf{N}(s)}{\partial z_{ij,k}}=\frac{1}{d(s)}\frac{\partial n_{ij}(s)}{\partial z_{ij,k}}\mathbf{e}_i\mathbf{e}_j^T, \tag{6.20}$$

where $\mathbf{e}_i\in\mathbb{R}^n$ and $\mathbf{e}_j\in\mathbb{R}^m$ are vectors with unit entries belonging to the i^{th} and j^{th} coordinates of the zero, respectively. Using the definition of $n_{ij}(s)$

$$\frac{\partial\mathbf{R}}{\partial z_{ij,k}}=-\frac{\eta_{ij}}{d(s)}\prod_{p=1,p\neq k}^{K_{ij}}\left(s-z_{ij,p}\right)\mathbf{e}_i\mathbf{e}_j^T=-\frac{r_{ij}(s)}{s-z_{ij,k}}\mathbf{e}_i\mathbf{e}_j^T. \tag{6.21}$$

Therefore, by substituting Eq. 6.21 into Eq. 6.11, the sensitivity of a closed-loop pole to a fitted open-loop zero is given by

$$\frac{\partial\mu_i}{\partial z_{ij,k}}=\frac{\mathbf{w}_{L,i}^T r_{ij}(s)\mathbf{e}_i\mathbf{e}_j^T\left(\mu_i\mathbf{F}^T+\mathbf{G}^T\right)\mathbf{w}_{R,i}}{\left(s-z_{ij,k}\right)\mathbf{w}_{L,i}^T\left(\mathbf{R}\left(\mu_i,\theta\right)\mathbf{F}^T+\frac{\partial\mathbf{R}}{\partial s}\left(\mu_i\mathbf{F}^T+\mathbf{G}^T\right)\right)\mathbf{w}_{R,i}}. \tag{6.22}$$

6.3.3 Sensitivity to Scaling Parameters

Finally, the sensitivity to the ij^{th} scaling parameter η_{ij} of $\mathbf{N}(s)$ is considered. Again, writing the transfer function matrix as

$$\mathbf{R}(s)=\frac{\mathbf{N}(s)}{d(s)} \tag{6.23}$$

allows the sensitivity to be expressed as

$$\frac{\partial \mathbf{R}}{\partial \eta_{ij}} = \frac{1}{d(s)} \frac{\partial \mathbf{N}(s)}{\partial \eta_{ij}} = \frac{1}{d(s)} \frac{\partial n_{ij}(s)}{\partial \eta_{ij}} \mathbf{e}_i \mathbf{e}_j^T \tag{6.24}$$

Using the definition of $n_{ij}(s)$, the above can be expressed as

$$\frac{\partial \mathbf{R}}{\partial \eta_{ij}} = \frac{1}{d(s)} \prod_{p=1}^{K_{ij}} (s - z_{ij,p}) \, \mathbf{e}_i \mathbf{e}_j^T = \frac{r_{ij}(s)}{\eta_{ij}} \mathbf{e}_i \mathbf{e}_j^T, \tag{6.25}$$

and hence the sensitivity of a closed-loop pole to a chosen scaling parameter is

$$\frac{\partial \mu_i}{\partial \eta_{ij}} = -\frac{\mathbf{w}_{L,i}^T r_{ij}(s) \mathbf{e}_i \mathbf{e}_j^T \left(\mu_i \mathbf{F}^T + \mathbf{G}^T \right) \mathbf{w}_{R,i}}{\eta_{ij} \mathbf{w}_{L,i}^T \left(\mathbf{R}\left(\mu_i, \theta\right) \mathbf{F}^T + \frac{\partial \mathbf{R}}{\partial s} \left(\mu_i \mathbf{F}^T + \mathbf{G}^T \right) \right) \mathbf{w}_{R,i}}. \tag{6.26}$$

6.4 Robustness Metric

The analytic formulae derived in the previous section consider only the sensitivity of each closed-loop pole to a single fitting parameter at one time. In practice, however, the combined effect of all fitting parameters must be considered. Therefore, in this section, a robustness metric is defined to address this problem. The metric is based on a weighted first-order expansion of each closed-loop pole with respect to the fitting parameters.

Assuming that the control gains $\mathbf{F}$ and $\mathbf{G}$ are fixed, each of the l closed-loop poles are a function of the p fitting parameters, and hence

$$\mu_i = \mu_i(\theta_1, \theta_2, \ldots, \theta_p), \quad i = 1, 2, \ldots, l. \tag{6.27}$$

Therefore, the total differential of each closed-loop pole is given by

$$d\mu_i = \sum_{j=1}^{p} \frac{\partial \mu_i}{\partial \theta_j} d\theta_j, \quad i = 1, 2, \ldots, l. \tag{6.28}$$

If one extends the differential of each fitting parameter, Eq. 6.28 becomes

$$\Delta\mu_i \approx \sum_{j=1}^{p} \frac{\partial \mu_i}{\partial \theta_j} \Delta\theta_j, \quad i = 1, 2, \ldots, l. \tag{6.29}$$

Taking the real and imaginary part gives that

$$\mathrm{Re}\left(\Delta\mu_i\right) \approx \sum_{j=1}^{p} \mathrm{Re}\left(\frac{\partial \mu_i}{\partial \theta_j} \Delta\theta_j \right), \quad i = 1, 2, \ldots, l, \tag{6.30}$$

$$\mathrm{Im}\left(\Delta\mu_i\right) \approx \sum_{j=1}^{p} \mathrm{Im}\left(\frac{\partial \mu_i}{\partial \theta_j} \Delta\theta_j \right), \quad i = 1, 2, \ldots, l, \tag{6.31}$$

and therefore, by expanding,

$$\mathrm{Re}\left(\Delta\mu_i\right) \approx \sum_{j} \left(\mathrm{Re}\left(\frac{\partial \mu_i}{\partial \theta_j} \right) \mathrm{Re}\left(\Delta\theta_j\right) - \mathrm{Im}\left(\frac{\partial \mu_i}{\partial \theta_j} \right) \mathrm{Im}\left(\Delta\theta_j\right) \right), \quad i = 1, 2, \ldots, l, \tag{6.32}$$

$$\mathrm{Im}\left(\Delta\mu_i\right) \approx \sum_{j} \left(\mathrm{Re}\left(\frac{\partial \mu_i}{\partial \theta_j} \right) \mathrm{Im}\left(\Delta\theta_j\right) + \mathrm{Im}\left(\frac{\partial \mu_i}{\partial \theta_j} \right) \mathrm{Re}\left(\Delta\theta_j\right) \right), \quad i = 1, 2, \ldots, l, \tag{6.33}$$

Suppose that each fitting parameter $\Delta\theta_j$ is within an interval given by

$$\Delta\theta_j = \pm x_j \pm y_j \mathrm{i}, \tag{6.34}$$

where $x_j, y_j \in \mathbb{R}^+$. The maximum values of the real and imaginary part of the variation of the closed-loop poles are given by

$$\mathrm{Re}\,(\Delta\mu_i)_{\max} \approx \sum_j \left(\left| \mathrm{Re}\left(\frac{\partial \mu_i}{\partial \theta_j}\right) \right| x_j + \left| \mathrm{Im}\left(\frac{\partial \mu_i}{\partial \theta_j}\right) \right| y_j \right), \quad i = 1, 2, \ldots, l, \tag{6.35}$$

$$\mathrm{Im}\,(\Delta\mu_i)_{\max} \approx \sum_j \left(\left| \mathrm{Re}\left(\frac{\partial \mu_i}{\partial \theta_j}\right) \right| y_j + \left| \mathrm{Im}\left(\frac{\partial \mu_i}{\partial \theta_j}\right) \right| x_j \right), \quad i = 1, 2, \ldots, l. \tag{6.36}$$

Let the *pole robustness metric* for each closed-loop pole be defined as

$$J_i = \beta_i \frac{\mathrm{Re}\,(\Delta\mu_i)_{\max}}{|\mathrm{Re}\,(\mu_i)|} + \gamma_i \frac{\mathrm{Im}\,(\Delta\mu_i)_{\max}}{|\mathrm{Im}\,(\mu_i)|}, \quad i = 1, 2, \ldots, l, \tag{6.37}$$

where $\beta_i, \gamma_i \in \mathbb{R}^+$ are constants that are chosen. The pole robustness metric serves to weight the percentage variation of the real and imaginary part of each closed-loop pole. For example one would choose $\beta_m > \gamma_m$ if the real part variation of the closed-loop pole μ_m is more important that the imaginary part variation. Likewise, one would choose $\beta_m < \gamma_m$ if the imaginary part variation is more important than the real part variation.

Finally, one can define the *total robustness metric* as

$$T_T = \sum_{i=1}^{l} \rho_i J_i, \tag{6.38}$$

where $\rho_i \in \mathbb{R}^+$ are named the pole weighting constants. The pole weighting constants serve to weight the relative important of each pole. For example, $\rho_1 > \rho_3$ if it is more important for the first pole to be more robust than the third pole. It is this metric that is used to assess the net effect of uncertainty in the closed-loop poles.

In the above formulation, it is assumed that the variation in the closed-loop poles is well approximated by a first-order expansion, i.e. the differential, with respect to the fitting parameters. This may not be true. Indeed, the variation of the closed-loop poles with respect to the fitting parameters may be highly nonlinear and thus estimates of the maximum real and imaginary part variation may be erroneous using this approach. Despite this, however, the purpose of the robustness metric is to weight the relative importance of each of the closed-loop poles and their respective real and imaginary parts. That is, to adjust the total robustness metric so that well known, or highly confident, fitting parameters have less of an impact on the assessment of the system's variability. Generally, one should not use the robustness metric alone to find the maximum deviation of a closed-loop pole.

6.5 Optimisation Strategies

The total robustness metric, derived in the previous section, serves merely as a means by which to quantitatively assess the variability of the closed-loop poles of the system. However, when coupled with an optimisation procedure, the metric can also be used to influence the eigenstructure assignment that is performed. In this section, three optimisation procedures are developed for the purpose of optimal eigenstructure assignment.

6.5.1 Single-Input Systems

First, single-input systems are considered. In this case, the force distribution matrix $\mathbf{B}(s)$ reduces to a vector $\mathbf{b}(s) \in \mathbb{C}^n$ and hence so too does the input-output transfer function matrix $\mathbf{r}(s) \in \mathbf{C}^n$ and the vector of control gains $\mathbf{f} \in \mathbb{R}^n$ and $\mathbf{g} \in \mathbb{R}^n$. As discussed in Chapter 5, single-input systems are only capable of assigning the closed-loop poles and not the corresponding closed-loop eigenvectors. Therefore, the only possible approach to minimise the robustness metric is to assign the closed-loop poles to optimal points in the complex plane.

In practice, of course, one cannot simply assign the closed-loop poles to any arbitrary points within the complex plane. Firstly, it is necessary to enforce the condition of stability and thus it is required that the closed-loop poles are assigned within the left hand side of the complex plane; that is $\mathrm{Re}(\mu_i) \leq 0 \,\forall\, i$. Secondly, the physical limitations of the controller mean that the closed-loop poles cannot be moved at great distances away from their original open-loop values. Finally, the closed-loop poles are usually assigned to certain locations in the complex plane that allow desired modal properties, such as natural frequencies and damping values, to be obtained. Therefore, if one is to perform optimal pole placement, the poles must be placed subject to a set of constraints that enforces this.

In this work, the constraints take the form of rectangular boxes that appear in the complex plane. That is, the open-loop poles are shifted to closed-loop locations that satisfy

$$\mu_i \in [\underline{\mathrm{Re}}(\mu_i), \overline{\mathrm{Re}}(\mu_i)] + [\underline{\mathrm{Im}}(\mu_i), \overline{\mathrm{Im}}(\mu_i)]\mathrm{i}, \quad i = 1, 2, \ldots, l \tag{6.39}$$

where $\underline{\mathrm{Re}}(\mu_i)$ and $\overline{\mathrm{Re}}(\mu_i)$ represent the minimum and maximum real part of the i^{th} closed-loop pole, respectively; and $\underline{\mathrm{Im}}(\mu_i)$ and $\overline{\mathrm{Im}}(\mu_i)$ represent the minimum and maximum imaginary part of the i^{th} closed-loop pole, respectively.

The optimisation strategy for single-input system is defined as follows:

> **Optimisation 1 (Single-Input):** Minimise the total robustness metric in Eq. 6.38 subject to placing the closed-loop poles within the rectangular regions defined by Eq. 6.39.

6.5.2 Multiple-Input Systems

Now, the more general case of $m > 1$ inputs is considered. Compared to single-input systems, the extra flexibility of multiple inputs allows the closed-loop eigenvectors to be assigned in addition to the eigenvalues. Thus, the optimisation procedure in multiple-input systems can take advantage of this.

For clarity, it is restated here that one accounts for the extra inputs in multiple-input systems using the $\boldsymbol{\alpha}_i$ vectors, which are defined in the Receptance Method. Therefore, in addition to the closed-loop poles, these vectors are also considered optimisation variables that may be used to reduce the total robustness metric.

Strategy 1: Fixed Closed-Loop Poles

In this first strategy, the closed-loop poles are assigned to fixed locations in the complex plane. That is, the practitioner decides specific points in the complex plane where the closed-loop poles are desired to be. Thus, it is no longer possible to optimally assign the closed-loop poles. However, unlike before, the $\boldsymbol{\alpha}_i$ vectors are now chosen optimally.

In general, the $\boldsymbol{\alpha}_i$ vectors may be chosen arbitrarily[1]. However, in practice, certain combinations of these vectors can lead to exceptionally large control gains and hence an unfeasible control effort. To account for this, the gain constraints from Chapter 5 are used again here. For clarity, this is repeated below.

$$w||\boldsymbol{\Lambda}\mathbf{F}||_F + ||\boldsymbol{\Lambda}\mathbf{G}||_F \leq c. \tag{6.40}$$

This first optimisation strategy for multiple-input systems is defined as follows:

Optimisation 2 (Multiple-Input): Minimise the total robustness metric in Eq. 6.38 by assigning the closed-loop poles at fixed locations in the complex plane and optimally choosing the $\boldsymbol{\alpha}_i$ vectors subject to the gain constraint in Eq. 6.40.

Strategy 2: Variable Closed-Loop Poles

In the second, and final, strategy for multiple-input systems, a combination of both optimisation one and two is considered. Now, both the closed-loop poles are assigned in addition to the $\boldsymbol{\alpha}_i$ vectors. More formally:

Optimisation 3 (Multiple-Input): Minimise the total robustness metric in Eq. 6.38 by assigning the closed-loop poles within rectangular regions in the complex plane defined by Eq. 6.39 and optimally choosing the $\boldsymbol{\alpha}_i$ vectors subject to the gain constraint in Eq. 6.40.

This optimisation procedure increases the number of optimisation variables and thus should, in theory, be able to reduce the robustness metric to a greater extent compared to optimisation 2. This is investigated in the examples presented later.

For the same reasons given in Chapter 5, the Differential Evolution algorithm is used again for this optimisation problem. Further details are given in Appendix A.

6.6 Numerical Examples

The three optimisation strategies presented above are applied numerically in this section. For simplicity, they are tested on a simple three-degree-of-freedom mass-spring-damper system. Throughout all of the following examples, the mass, damping and stiffness matrices are given respectively by

$$\mathbf{M} = \begin{pmatrix} 2 & 0 & 0 \\ 0 & 1 & 0 \\ 0 & 0 & 3 \end{pmatrix}, \quad \mathbf{C} = 0.5 \begin{pmatrix} 1 & 0 & 0 \\ 0 & 1 & -1 \\ 0 & -1 & 1 \end{pmatrix}, \quad \mathbf{K} = \begin{pmatrix} 6 & -2 & -1 \\ -2 & 4 & -2 \\ -1 & -2 & 3 \end{pmatrix}.$$

Thus, the open-loop poles are as given in Table 6.1. This system is the same as that presented in [113] and is referred to as the 'standard reference system' hereinafter.

[1] Provided that they satisfy the conjugate requirement (see Chap. 5).

Table 6.1: Open-loop poles.

Pole	Value
$\lambda_{1,2}$	-0.0166 ± 0.5516i
$\lambda_{3,4}$	-0.1890 ± 1.6044i
$\lambda_{5,6}$	-0.2528 ± 2.2289i

6.6.1 Single-Input

First, the case of a single input is considered. Suppose that the force distribution vector is selected as

$$\mathbf{b} = \begin{pmatrix} 1 \\ 1 \\ 1 \end{pmatrix}.$$

The input-output transfer function matrix is written as

$$\mathbf{R}(s) = \frac{1}{\prod_{i=1}^{6}(s-\lambda_i)} \begin{pmatrix} \frac{1}{2}\left(s^4 + \frac{2}{3}s^3 + \frac{22}{3}s^2 + \frac{3}{2}s + 8\right) \\ s^4 + \frac{7}{12}s^3 + \frac{23}{4}s^2 + \frac{5}{3}s + \frac{13}{2} \\ \frac{1}{3}\left(s^4 + \frac{5}{4}s^3 + \frac{39}{4}s^2 + \frac{21}{4}s + 21\right) \end{pmatrix}$$

and hence the open-loop zeros and scaling parameters are as given in Tables 6.2 and 6.3, respectively.

Table 6.2: Open-loop zeros (single-input).

Element ij	$z_{ij,1}$	$z_{ij,2}$	$z_{ij,3}$	$z_{ij,4}$
11	-0.2678+2.4161i	-0.2678-2.4161i	-0.0656+1.1617i	-0.0656-1.1617i
21	-0.1429+2.0115i	-0.1429-2.0115i	-0.1487+1.2555i	-0.1487-1.2555i
31	-0.1690+1.8863	-0.1690-1.8863	-0.4560+2.3764i	-0.4560-2.3764i

Table 6.3: Scaling parameters (single-input).

Scaling parameter	Value
η_{11}	$\frac{1}{2}$
η_{21}	1
η_{31}	$\frac{1}{3}$

For the purposes of comparison later on, a reference closed-loop eigenstructure assignment is defined as that which assigns the closed-loop poles to the set defined in Table 6.4. The control gains necessary to assign said set are computed, using the Receptance Method, as

$$\mathbf{f}_{\text{ref}} = \begin{pmatrix} -4.2265 \\ -0.5163 \\ 0.4387 \end{pmatrix}, \quad \mathbf{g}_{\text{ref}} = \begin{pmatrix} -0.3915 \\ -6.8904 \\ 4.2002 \end{pmatrix}. \tag{6.41}$$

These values match those found by Tehrani et al. [113][2].

[2]Note that the values by Tehrani et al. are negated due to their definition of the feedback controller

Table 6.4: Reference closed-loop poles.

Pole	Value
$\mu_{1,2}$	-0.2 ± 0.8i
$\mu_{3,4}$	-0.5 ± 2i
$\mu_{5,6}$	-1 ± 2.5i

Example 1: Equal Weighting

In this first example, the pole placement is relaxed from the reference condition so that the closed-loop poles are instead assigned within rectangular regions defined by

$$\begin{aligned}\mu_{1,2} &= [-0.5, -0.2] \pm [0.6, 1]\text{i},\\ \mu_{3,4} &= [-0.7, -0.3] \pm [1.7, 2.3]\text{i},\\ \mu_{5,6} &= [-1.2, -0.8] \pm [2.2, 2.8]\text{i}.\end{aligned}$$

These regions have been chosen so that: (i) the reference pole placement in Table 6.4 is included within the rectangular regions, and (ii) the entirety of each rectangular box has a lower (more negative) real part than its open-loop counterpart. This second condition enforces a stabilising control objective and is representative of the type of pole placement that would be used in practice.

With the rectangular regions chosen, one can now define the robustness metric. For the sake of simplicity, equal weighting is initially given to all of the parameters in the optimisation. That is, β_i, γ_i, and ρ_i are set to one, for all i. This means that there is no priority of any pole nor is there priority of each pole's real and imaginary part. Mathematically,

$$T_T = \sum_{i=1}^{6} \left(\frac{\text{Re}\left(\Delta\mu_i\right)_{\max}}{|\text{Re}\left(\mu_i\right)|} + \frac{\text{Im}\left(\Delta\mu_i\right)_{\max}}{|\text{Im}\left(\mu_i\right)|} \right). \tag{6.42}$$

If one assumes that the nominal values obtained in Tables 6.1, 6.2 and 6.3 are variable by 3% in both the real and imaginary part, the initial objective function in the reference condition is computed as 4.64. Using the Differential Evolution algorithm, the poles are now placed optimally according to the rectangular constraints given above. The final, optimum poles are found to be

$$\begin{aligned}\mu_{1,2} &= -0.2 \pm 1\text{i},\\ \mu_{3,4} &= -0.3 \pm 2.245\text{i},\\ \mu_{5,6} &= -1.2 \pm 2.8\text{i}.\end{aligned}$$

which corresponds to control gains of

$$\mathbf{f} = \begin{pmatrix} -3.1986 \\ -0.2951 \\ -1.7668 \end{pmatrix}, \quad \mathbf{g} = \begin{pmatrix} -9.6234 \\ -4.0595 \\ 2.7671 \end{pmatrix}.$$

With the poles placed optimally, the total robustness metric reduces to 2.19 (a 53% reduction). This reduction is confirmed visually in Fig. 6.1, which shows the variation of the poles between ±3% of the nominal values using one thousand samples[3]. As shown, the clusters of the

[3]A uniform distribution was used here. However, this is merely for visualisation purposes; the method does not require knowledge of the parameter distributions.

optimised poles appear to be more centred about the nominal points and thus one can conclude that there is less variation, as was required.

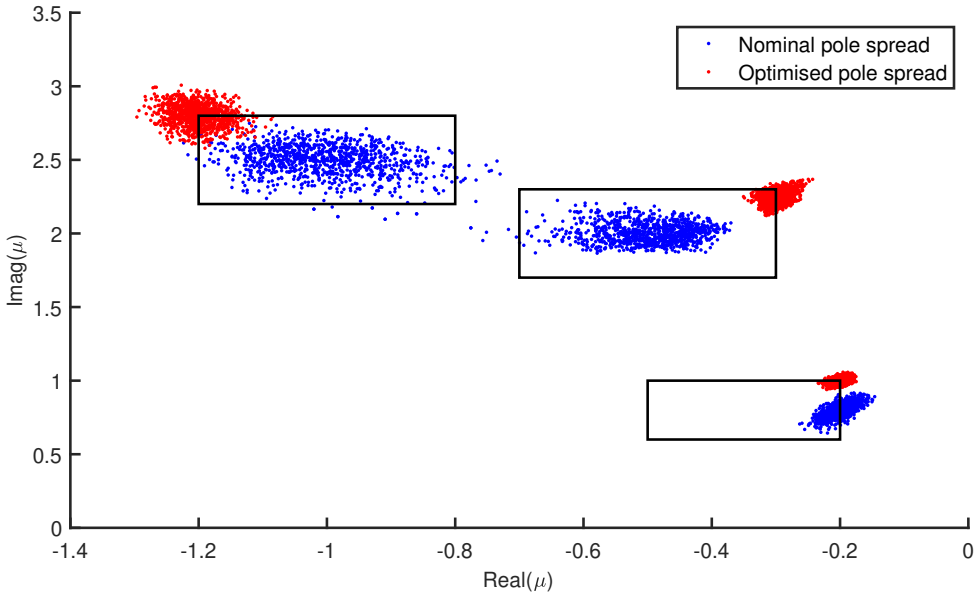

Figure 6.1: Pole clusters (numerical example 1).

It is interesting to note that the optimal solutions obtained above lie in the corners of the optimisation regions. That is, the real and imaginary parts are at the limits of the constraints. This suggests that the global minimum of the optimisation problem lies beyond the rectangular regions and thus the reduction in the poles is limited by the constraints. Indeed, a relaxation of the constraints would likely yield a better solution. This hypothesis was briefly tested by increasing the size of the pole rectangles to

$$\mu_{1,2} = [-0.55, -0.15] \pm [0.4, 1.1]\text{i}$$
$$\mu_{3,4} = [-0.75, -0.25] \pm [1.5, 2.5]\text{i}$$
$$\mu_{5,6} = [-1.3, -0.7] \pm [2.1, 2.9]\text{i}.$$

Running the optimisation again, with the same settings, gave new solutions at

$$\mu_{1,2} = -0.15 \pm 1.1i$$
$$\mu_{3,4} = -0.25 \pm 2.185i$$
$$\mu_{5,6} = -1.3 \pm 2.9i$$

which reduces the robustness metric to 1.607, thus confirming the above hypothesis.

In this example, it was found that the Differential Evolution algorithm proved to be a robust optimisation technique. Different starting positions of the closed-loop poles always converged to the optimal solutions found above. Of course, this is problem specific and one cannot conclude that this will always be the case in general.

Example 2: First Pole Pair Priority, Real Part Priority

In this second example, the total robustness metric definition is modified. Instead, β_1,β_2, ρ_1 and ρ_2 are set to one and all other weighting parameters are set to zero. In other words, the metric depends only on the real part variation of the first pole pair (μ_1, μ_2).

The initial robustness metric for the reference pole placement in this example is 1.29. After running the optimisation again using the same constraints as in example 1, the metric is reduced to 0.38 using gains of

$$\mathbf{f} = \begin{pmatrix} -0.6273 \\ -1.3065 \\ -0.1896 \end{pmatrix}, \quad \mathbf{g} = \begin{pmatrix} -0.3197 \\ -2.9580 \\ 0.3633 \end{pmatrix}.$$

This corresponds to assigned closed-loop poles of

$$\begin{aligned} \mu_{1,2} &= -0.2 \pm 1\text{i}, \\ \mu_{3,4} &= -0.3 \pm 1.94\text{i}, \\ \mu_{5,6} &= -0.8 \pm 2.2\text{i}. \end{aligned}$$

Fig. 6.2 shows the new pole clusters for this example. As expected, the real part variation of the first pole pair is slightly smaller. However, this is at the expense of the variation of the other poles, since they were not considered in the new robustness metric. One can see that the location of the first pole pair remains the same but that the other poles move, especially in the third pole pair. This suggests that there is an interdependency between all of the poles and their variation. In other words, one cannot optimise the variation of a chosen pole pair simply by assigning its nominal value independently of the other poles. However, it does imply that its own location in the complex plane is the most significant factor in this particular case.

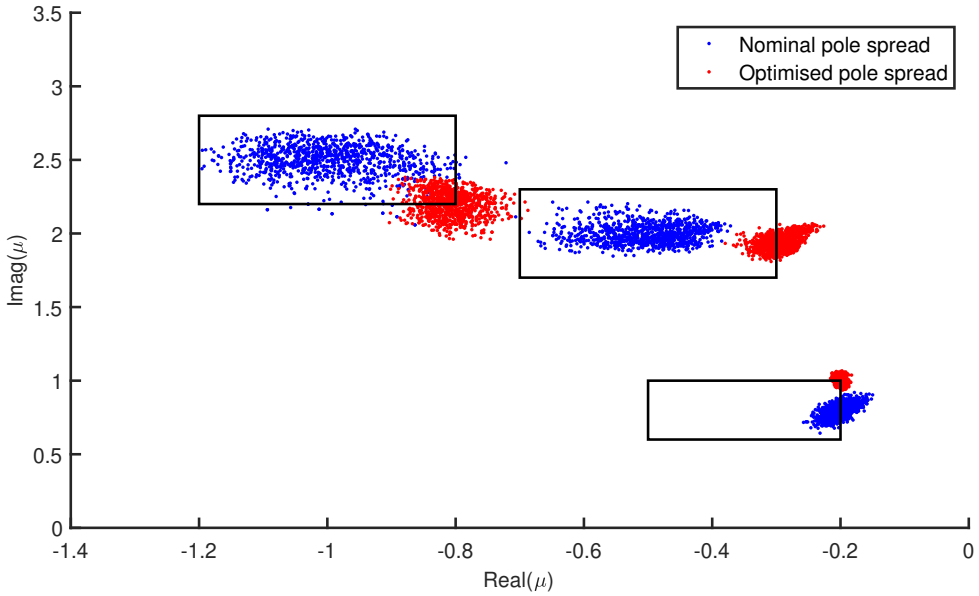

Figure 6.2: Pole clusters (numerical example 2).

6.6.2 Multiple-Input Case

Next, the case of multiple inputs is considered. Suppose that there are three inputs and that the force distribution matrix is given by

$$\mathbf{B} = \begin{pmatrix} 1 & 0 & 0 \\ 0 & 2 & 0 \\ 0 & 0 & 3 \end{pmatrix}$$

The new input-output transfer function matrix is given by

$$\mathbf{R}(s) = \frac{1}{\prod_{i=1}^{6}(s-\lambda_i)} \begin{pmatrix} r_{11}(s) & r_{12}(s) & r_{13}(s) \\ r_{21}(s) & r_{22}(s) & r_{23}(s) \\ r_{31}(s) & r_{32}(s) & r_{33}(s) \end{pmatrix}$$

where

$$\begin{aligned}
r_{11}(s) &= \frac{1}{2}\left(s^4 + \frac{2}{3}s^3 + 5s^2 + \frac{1}{2}s + \frac{8}{3}\right), \\
r_{12}(s) &= 2\left(s^2 + \frac{1}{4}s + \frac{4}{3}\right), \\
r_{13}(s) &= \frac{1}{2}\left(s^2 + \frac{3}{2}s + 8\right), \\
r_{21}(s) &= s^2 + \frac{1}{4}s + \frac{4}{3}, \\
r_{22}(s) &= 2\left(s^4 + \frac{5}{12}s^3 + \frac{97}{24}s^2 + \frac{3}{4}s + \frac{17}{6}\right), \\
r_{23}(s) &= \frac{1}{2}\left(s^3 + \frac{17}{4}s^2 + 4s + 14\right), \\
r_{31}(s) &= \frac{1}{6}\left(s^2 + \frac{3}{2}s + 8\right), \\
r_{32}(s) &= \frac{1}{3}\left(s^3 + \frac{17}{4}s^2 + 4s + 14\right), \\
r_{33}(s) &= s^4 + \frac{3}{4}s^3 + \frac{57}{8}s^2 + \frac{5}{2}s + 10.
\end{aligned}$$

Hence, the zeros and scaling parameters in this case are as given in Tables 6.5 and 6.6, respectively.

Table 6.5: Open-loop zeros (multiple-input).

Element ij	$z_{ij,1}$	$z_{ij,2}$	$z_{ij,3}$	$z_{ij,4}$
11	-0.3209+2.0668i	-0.3209+2.0668i	-0.0124+0.7807i	-0.0124-0.7807i
12	-0.125+1.1479i	-0.125-1.1479i		
13	-0.75+2.7272i	-0.75-2.7272i		
21	-0.125+1.1479i	-0.125-1.1479i		
22	-0.1234+1.7506i	-0.1234-1.7506i	-0.0849+0.9554i	-0.0849-0.9554i
23	-4.1062	-0.0719+1.8451i	-0.0719-1.8451i	
31	-0.75+2.7272i	-0.75-2.7272i		
32	-4.1062	-0.0719+1.8451i	-0.0719-1.8451i	
33	-0.2077+2.2211i	-0.2077-2.2211i	-0.1673+1.4076i	-0.1673-1.4076i

Example 3: Fixed Poles

First, consider the case where the poles are fixed to the locations

$$\begin{aligned}
\mu_{1,2} &= -0.2 \pm 0.8\text{i}, \\
\mu_{3,4} &= -0.5 \pm 2\text{i}, \\
\mu_{5,6} &= -1 \pm 2.5\text{i},
\end{aligned}$$

Table 6.6: Scaling parameters (multiple-input).

Scaling parameter	Value
η_{11}	$\frac{1}{2}$
η_{12}	2
η_{13}	$\frac{1}{2}$
η_{21}	1
η_{22}	2
η_{23}	$\frac{1}{2}$
η_{31}	$\frac{1}{6}$
η_{32}	$\frac{1}{3}$
η_{33}	1

and the eigenvectors are to be optimally assigned. This is an example of Optimisation 2, which is described in §6.5.

Let the gain constraint be written as

$$3||\mathbf{F}||_F + ||\mathbf{G}||_F \leq 7,$$

and suppose that the same metric as in example one is used to assess the robustness of the system. Using the same optimisation procedure as before, the optimum set of $\boldsymbol{\alpha}_i$ vectors is computed as

$$\boldsymbol{\alpha}_{1,2} = \begin{pmatrix} 1 \\ -0.16 \\ -1.6613 \pm 4.2788i \end{pmatrix}, \quad \boldsymbol{\alpha}_{3,4} = \begin{pmatrix} 1 \\ 0.0541 \pm 0.2543 \\ -1.3277 \pm 1.1091i \end{pmatrix}, \quad \boldsymbol{\alpha}_{5,6} = \begin{pmatrix} 1 \\ -9.6961 \pm 2.4055i \\ 0 \end{pmatrix},$$

which corresponds to control gains of

$$\mathbf{F} = \begin{pmatrix} -0.5758 & 0.3000 & 0.1308 \\ 0.0510 & -0.7657 & -0.1349 \\ 0.3297 & 0.6033 & -0.6640 \end{pmatrix}, \quad \mathbf{G} = \begin{pmatrix} -0.5572 & 1.5169 & 1.4346 \\ -0.1247 & -1.2435 & -0.0245 \\ 0.5684 & 0.1341 & -1.4786 \end{pmatrix}$$

and right eigenvectors of

$$\mathbf{w}_{1,2} = \begin{pmatrix} 1 \\ 1.4959 \pm 0.0385i \\ 1.5297 \pm 0.2102i \end{pmatrix}, \quad \mathbf{w}_{3,4} = \begin{pmatrix} 1 \\ 0.0283 \pm 0.9508i \\ -0.97 \pm 0.3930i \end{pmatrix}, \quad \mathbf{w}_{5,6} = \begin{pmatrix} 1 \\ -3.0714 \pm 4.2318i \\ 0.3231 \pm 0.4319i \end{pmatrix},$$

Note here that the first element in the $\boldsymbol{\alpha}_i$ vectors is always one. This scaling is allowed since the corresponding eigenvectors may be scaled arbitrarily.

The spread of the optimised closed-loop poles is shown in Fig. 6.3. The green cross in each pole cluster shows the position of the fixed, nominal pole locations. To allow a comparison, a reference case is shown for the case of where $\alpha_{k,i} = 1 \forall k, i$. As shown, despite the same fixed nominal pole locations, the uncertainty in the poles is reduced simply by appropriate assignment of the closed-loop eigenvectors. Indeed, the robustness metric in this example reduces from 7.73 to 2.77 (a 64% reduction).

Substituting the optimum control gains into the left-hand side gain constraint, one finds that $3||\mathbf{F}||_F + ||\mathbf{G}||_F = 7.1$ and thus the gain constraint is slightly violated. This violation arises from the implementation of the constraint, which is expressed as a cost penalty to the

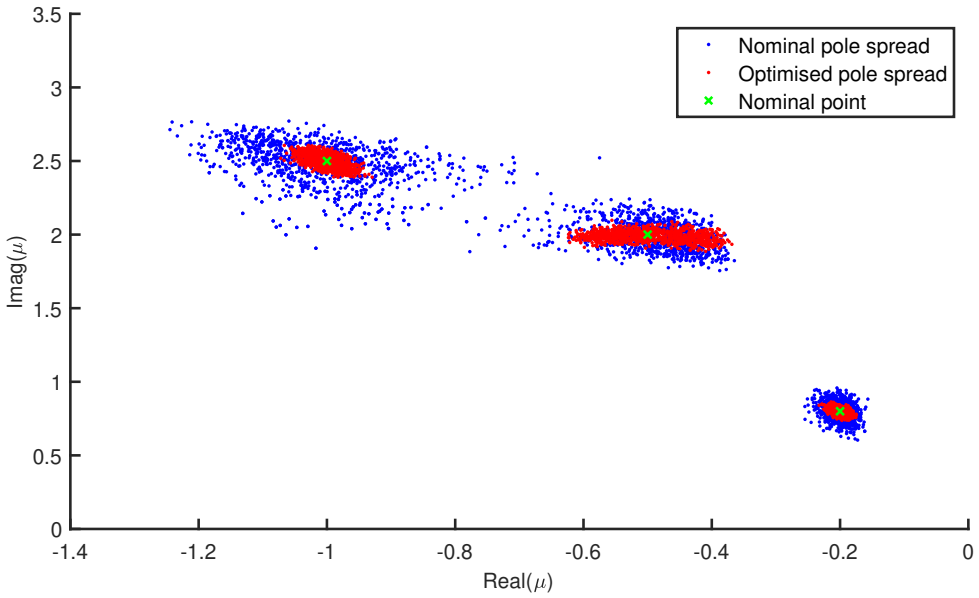

Figure 6.3: Pole clusters (numerical example 3).

robustness metric[4] [143]. Regardless, however, it is clear that the controller is at the limit of its performance and thus one can infer that increasing this limit will improve the performance of the optimisation. Again, this hypothesis was tested briefly by gradually relaxing the gain constraints, optimising and find the new total robustness metric in each case. Table 6.7 shows the results of this test. As shown, relaxing the gain constraint leads to a better performance as one would expect.

Table 6.7: Effect of relaxing the gain constraint on the total robustness metric.

Gain constraint	Total robustness metric
$3\|\|\mathbf{F}\|\|_F + \|\|\mathbf{G}\|\|_F \leq 7$	2.77
$3\|\|\mathbf{F}\|\|_F + \|\|\mathbf{G}\|\|_F \leq 8$	2.59
$3\|\|\mathbf{F}\|\|_F + \|\|\mathbf{G}\|\|_F \leq 9$	2.19

Despite using the same definition of robustness metric, it is to be noted that the initial value of the objective function in examples 1 and 3 are different. This is due to the added uncertainty that is introduced through the parameters of the other two inputs.

Example 4: Eigenstructure Assignment

Finally, the case of Optimisation 3 is considered. This is where both the closed-loop poles and eigenvectors are optimally assigned. Suppose that the poles are to be placed within regions specified by

$$\mu_{1,2} = [-0.5, -0.2] \pm [0.6, 1]\text{i},$$
$$\mu_{1,2} = [-0.7, -0.3] \pm [1.7, 2.3]\text{i},$$
$$\mu_{1,2} = [-1.2, -0.8] \pm [2.2, 2.8]\text{i}.$$

To enable a fair comparison of the results, the same robustness metric and gains constraints from example 3 are used here.

[4]See Appendix A.

Running the new optimisation, the optimum set of closed-loop poles are computed as

$$\begin{aligned}\mu_{1,2} &= -0.2 \pm 0.6\text{i},\\ \mu_{3,4} &= -0.3 \pm 1.7\text{i},\\ \mu_{5,6} &= -0.8 \pm 2.3631\text{i}.\end{aligned}$$

Additionally, the optimum $\boldsymbol{\alpha}_i$ vectors are given by

$$\boldsymbol{\alpha}_{1,2} = \begin{pmatrix} 1 \\ -6.1699 \pm 0.0249i \\ -8.0772 \pm 0.7286i \end{pmatrix}, \quad \boldsymbol{\alpha}_{3,4} = \begin{pmatrix} 1 \\ -0.0099 \pm 0.0017 \\ 0 \end{pmatrix}, \quad \boldsymbol{\alpha}_{5,6} = \begin{pmatrix} 1 \\ -9.57 \\ 1.6021 \pm 0.8635 \end{pmatrix},$$

which corresponds to control gains of

$$\mathbf{F} = \begin{pmatrix} -0.5795 & 0.4785 & -0.1507 \\ 0.0662 & -0.5496 & -0.0176 \\ 0.2963 & 0.0985 & -0.2943 \end{pmatrix}, \quad \mathbf{G} = \begin{pmatrix} -0.9245 & 0.6526 & -0.2264 \\ -0.1820 & -0.5489 & 0.1528 \\ 0.6079 & 0.0347 & -0.0998 \end{pmatrix},$$

and right-eigenvectors of

$$\mathbf{w}_{1,2} = \begin{pmatrix} 1 \\ 1.6061 \pm -0.0803i \\ 2.0365 \pm -0.0730i \end{pmatrix}, \quad \mathbf{w}_{3,4} = \begin{pmatrix} 1 \\ 0.9976 \pm -0.0985i \\ -0.5046 \pm 0.0752i \end{pmatrix}, \quad \mathbf{w}_{5,6} = \begin{pmatrix} 1 \\ -2.5269 \pm 3.2459i \\ 0.4014 \pm 0.6070i \end{pmatrix}.$$

Under these new gains, the robustness metric decreases from 7.73 to 1.69 (a 79% reduction). As expected, this gives a better results than example 3 due to the added flexibility in the optimisation of being able to assign the closed-loop poles.

The pole spreads for the reference and optimised system are shown in Fig 6.4. As one expects, the spread of the poles in each cluster is reduced. However, it is interesting to note that the assigned closed-loop poles are not the same as those found in example 1. This suggests that there is a dependency between the poles and the eigenvectors in the optimum solution; in other words, one cannot optimise the poles and eigenvectors independently.

An interesting feature of Fig. 6.4 is the shape of the pole cluster associated with the first pole pair. As shown, the cluster is flatter and seems to be aligned to the imaginary axis. Such a situation arises when either a particular sensitivity is dominant or the combined effect of the sensitivities, collectively, tend to align in a particular direction. In this particular case, it is that the sensitivities combine so that the real part variation is greater than the imaginary part variation.

6.7 Experimental Case Study

In this section, the robust pole placement technique is applied to the experimental aeroservoelastic system. The example presented here is not exhaustive, like the numerical examples. Rather, the aim here is to highlight the practicalities of the technique and to illustrate how it may be used in real-world applications.

The first step is to collect the experimental frequency response functions. In this work, the FRFs were collected at a freestream speed of 12 m/s. This speed was chosen so that: (i) it does not lie too close to the open-loop flutter speed, and (ii) it is large enough to enable a reasonable

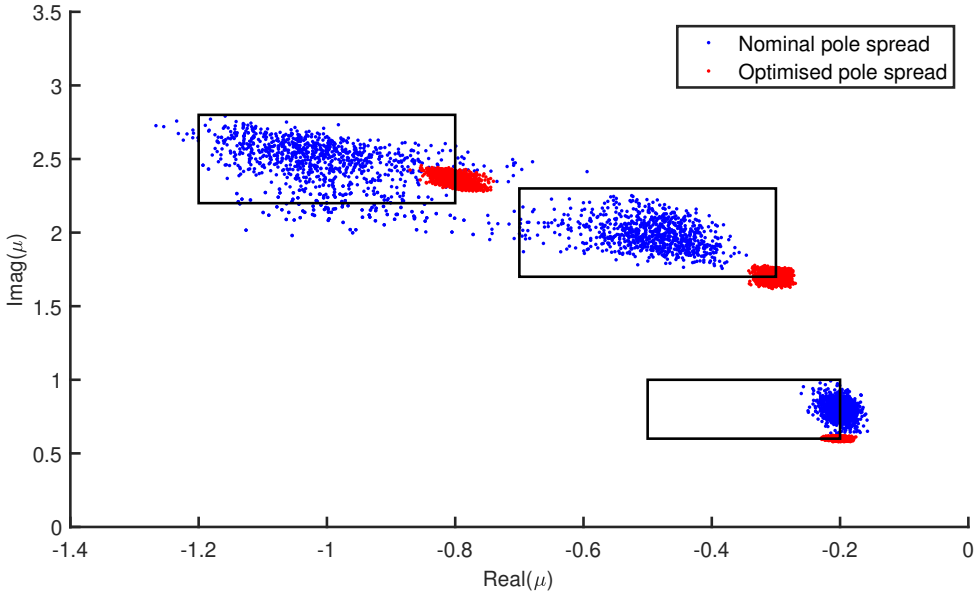

Figure 6.4: Pole clusters (numerical example 4).

level of actuation from the control surfaces. Figure 6.5 shows the input-output FRFs for both the leading- and trailing-edge control surfaces between the frequencies of 2 to 5 Hz. These were collected using random, white-noise MIMO testing through the Siemens SCADAS data acquisition system.

Figure 6.5 also shows the rational transfer function fittings corresponding to the measured FRF data. These fittings were done using Siemens' PolyMAX algorithm [97]. Complex modes were used in the fitting and, as shown, there is a good agreement between the measured and fitted data. Furthermore, it was found that lower and upper residuals had little effect on the performance of the fitting and were thus excluded since the system is two degrees-of-freedom. Tables 6.8, 6.9 and 6.10 show the poles, zeros and scaling parameters of the fitting, respectively.

Table 6.8: Open-loop poles (experimental).

Pole	Value
$\lambda_{1,2}$	-0.7662 $\pm$ 19.59i
$\lambda_{3,4}$	-2.4801 $\pm$ 24.95i

Table 6.9: Open-loop zeros (experimental).

Element ij	$z_{ij,1}$	$z_{ij,2}$	$z_{ij,3}$
11	-2.0588+22.2145i	-2.0588-22.2145i	18.2539
12	-0.3809+21.449i	-0.3809-21.449i	33.889
21	3.6266+23.6293i	3.6266-23.6293i	-32.3123
22	-1.5577+15.0279i	-1.5577-15.0279i	60.1262

Table 6.10: Open-loop scaling parameters (experimental).

Scaling parameter	Value
η_{11}	-0.0560
η_{12}	-0.0413
η_{21}	0.0321
η_{22}	0.0207

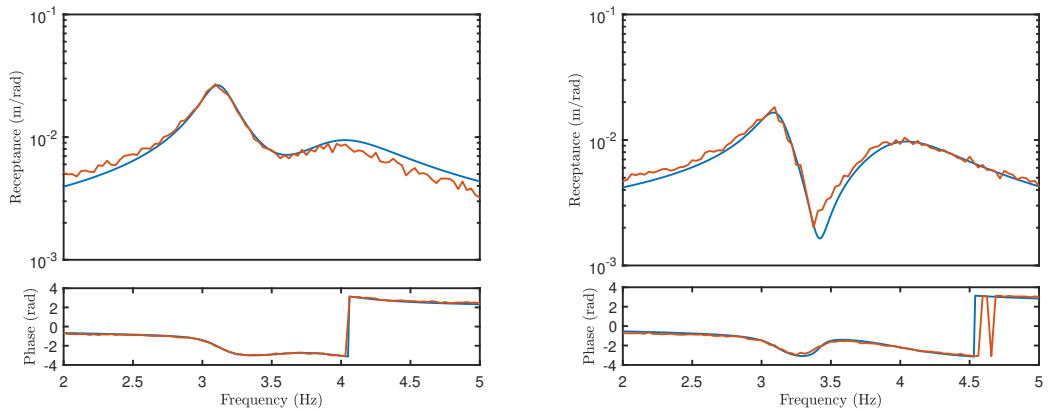

(a) r_{11}

(b) r_{12}

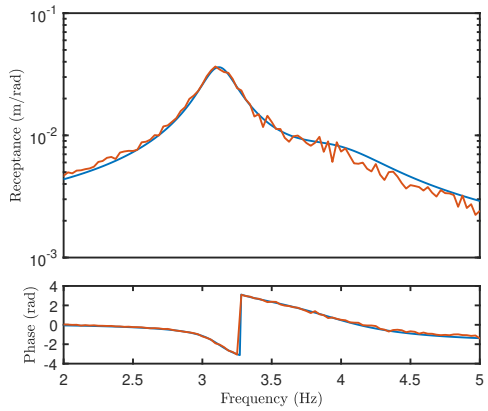

(c) r_{21}

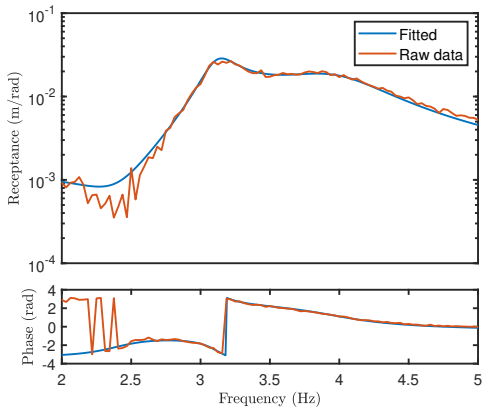

(d) r_{22}

Figure 6.5: Measured and fitted input-output transfer function matrix in the experimental model at 12 m/s.

With the RTF fitting complete, the next step is to choose the percentage variation in the fitting parameters. By inspection of Fig. 6.5, it is clear that there is a good agreement in the first mode across all measured FRFs. However, in the first column, there is more difficulty in the fitting of the second mode, which lies at approximately 4 Hz. To reflect this, all parameters in the fitting are set to 5% variation except for the real and imaginary part of the pole corresponding to the second mode. This is instead set to a 10% variation.

Suppose that the poles are to be shifted to points satisfying

$$\mu_{1,2} = [-1.1, -0.9] \pm [18.5, 20.5]\text{i},$$
$$\mu_{3,4} = [-3, -2.5] \pm [24, 26]\text{i}.$$

Also, let the constraints on the control gains be written as

$$2\pi \times 3.5||\mathbf{\Lambda F}||_F + ||\mathbf{\Lambda G}||_F \leq \frac{15\pi}{180},$$

where

$$\mathbf{\Lambda} = \begin{pmatrix} 0.02 & 0 \\ 0 & 0.02 \end{pmatrix}.$$

Note that these constraints are the same as those presented in the experimental case study in Chapter 5.

For this case study, the objective function is selected as

$$T_T = \frac{\text{Re}\,(\Delta\mu_1)_{\max}}{|\text{Re}\,(\mu_1)|} + \frac{\text{Re}\,(\Delta\mu_3)_{\max}}{|\text{Re}\,(\mu_3)|} + \frac{\text{Im}\,(\Delta\mu_1)_{\max}}{|\text{Im}\,(\mu_1)|} + \frac{\text{Im}\,(\Delta\mu_3)_{\max}}{|\text{Im}\,(\mu_3)|}.$$

That is, equal priority is given the variation in the real and imaginary part of each pole pair. In practice, it may be better to weight these contributions separately. However, this is not considered in this simple case study and is left as an area of future study.

Using 300 iterations of the Differential Evolution algorithm, the optimum poles were found to be

$$\mu_{1,2} = -0.900 \pm 19.723\text{i},$$
$$\mu_{3,4} = -2.500 \pm 24.871\text{i}.$$

The optimum alpha vectors were found to be

$$\boldsymbol{\alpha}_{1,2} = \begin{pmatrix} 1 \\ -0.2818 \pm 0.2818i \end{pmatrix}, \quad \boldsymbol{\alpha}_{3,4} = \begin{pmatrix} 1 \\ -24.0 \mp 100i \end{pmatrix},$$

which yields control gains of

$$\mathbf{F} = \begin{pmatrix} -0.2301 & 0.0413 \\ -0.1564 & 0.0218 \end{pmatrix}, \quad \mathbf{G} = \begin{pmatrix} -3.5744 & 3.6519 \\ -1.2727 & 0.3441 \end{pmatrix}.$$

The gains obtained by the optimisation satisfy the constraints define above. However, it is interesting to note that constraint is satisfied with a 12% buffer and the gains are therefore not at the limit of the control effort. There are potentially a number of reasons for this. Firstly, in the optimisation code it was necessary to constrain the values in the alpha vector so that the optimisation does not go to extreme, non-physical values. In the result given above, the

second term in the second alpha vector is saturated in terms of the imaginary value ($\mp 100i$). Secondly, it may be the case that there is a true minimum solution there. Of course, this cannot be proven due to the complexity of the defined objective function.

The final robustness metric after optimisation is 0.445. On its own, this value gives little information as there is presently nothing to compare it to. Therefore, to give some context to this result, the optimisation was repeated. Now, the robustness metric was negated. In this way, the optimisation gives the result corresponding to the worst-case assignment and hence minimum robustness.

The optimisation corresponding to the worst-case assignment gave a final metric of 4.213. Figure 6.6 shows the spread of the poles in both the optimum and worst-case optimisations. As expected, the optimum poles have a lower spread in both modes. Hence, although one cannot prove that the global solution has been found, the optimisation is assigning the poles and alpha values sensibly, in terms of robustness.

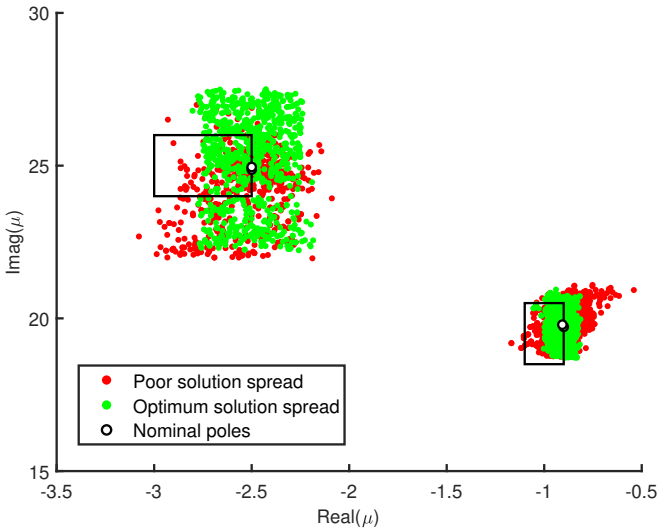

Figure 6.6: Multiple-input pole spread (experimental).

It is worth noting that the spread corresponding to the higher frequency mode is larger than that of the lower frequency mode. This is because of the 10% interval that is used for the open-loop poles for this mode compared to the 5% for the other mode.

At this point, it is important to point out that these examples have considered the robustness of the poles at one specific speed. In general, one cannot guarantee that a robust eigenvalue assignment at one speed leads to robustness at greater speeds. Indeed, the inverse may be true in certain situations. This should be considered in future research.

6.8 Summary

This chapter considers the effect of uncertainty in rational transfer function fittings on the spread of closed-loop poles that have been assigned using the Receptance Method. A sensitivity-based approach is used to quantify the variability of the poles and a metric is used to weight the relative robustness of the system in terms of the real and imaginary parts of each pole. A global optimisation procedure is then used to assign the poles and/or eigenvectors so that the metric is minimised and thus the propagation of uncertainty from the RTF to the assigned poles is reduced.

The developed technique is applied numerically to a standard reference system and show that one is able to successfully reduce the impact of uncertainty simply by robust eigenstructure assignment. Furthermore, the examples show that one can prioritise the robustness in certain poles by selecting suitable weighting constants in the metric. The technique is also tested in the form of a experimental case study, which uses receptance data from the experimental aeroservoelastic system. This case study emphasises the crucial role the eigenvectors play in the robustness of the closed-loop poles and highlights the practical nature of the technique.

Chapter 7

Uncertainty in the Receptance Method: Physical Modifications

7.1 Introduction

In the previous chapter, the problem of uncertainty in the Receptance Method was considered. It was shown that, despite the method's model-free characteristic, experimental errors play a significant role in the assignment of the closed-loop eigenvalues and eigenvectors. In general, uncertainty in receptance-based methods manifests itself through so-called pole clustering, where poles no longer appear as deterministic points in the complex plane but instead as clusters centred on nominal locations. By optimisation of the assigned nominal set of eigenvalues and eigenvectors, these clusters can be minimised in size so that the propagation of uncertainty is reduced. This in turn reduces variability in the frequency and damping characteristics of certain modes in the closed-loop system.

In this chapter, the study of uncertainty in the Receptance Method is continued, but now considering an alternative source. Here, physical sources of uncertainty, such as manufacturing tolerances, damage and degradation, are addressed and their effects on the results of the eigenstructure assignment are quantified. As in Chapter 6, the uncertainty is modelled through a receptance-based approach, thereby preserving the model-free nature of the technique. This is achieved by treating the uncertainty as a direct structural modification to measured receptance data and then finding the perturbation of the closed-loop poles. Unlike the previous chapter, the physical modifications are treated as random variables that contain probabilistic information. In this way, the approach allows one to assess the variation of the poles using statistical information, such as the mean and variance. The main benefit of this new approach is that it is not restricted to small perturbations, as was the case in Chapter 6. Indeed, the uncertainty is quantified globally by using a surrogate model that can capture the nonlinear variability of the poles with respect to the random parameters.

The remaining sections of this chapter are structured as follows. First, a discussion is made about the suitability of the Receptance Method when physical sources of uncertainty are present. Following this, a new method is presented that aims to incorporate the effect of physical uncertainty into the Receptance Method by means of stochastic structural modifications. Next, the problem of robustness in the closed-loop poles is framed in a probabilistic setting and an optimisation strategy is developed to reduce the impact of the physical uncertainties. This

optimisation technique is then applied to the numerical system from Chapter 6 and a discussion is made about the advantages of the technique. Finally, some of the current limitations of the method, which partially impede its application to real-world systems, are discussed and areas of future research are identified.

7.2 Physical Sources of Uncertainty

One of the most fruitful properties of the Receptance Method is that only a single set of experimental measurements is required[1]. More specifically, after performing rational transfer function fitting of the measured FRF data, the gains used in the high-level feedback controller are found using only one input-output transfer function matrix. Although presenting clear advantages in terms of cost and resources, this is equivalent to assuming that the measured system is completely determined by the single set of measurements[2]. This assumption is referred to hereinafter as the '*single data assumption*'. In this section, the credibility and consequences of this assumption are considered.

Variability Between Nominal Systems

Consider the case where an AFS system is being developed for a commercial aircraft using the Receptance Method. Under the single data assumption, FRF measurements are taken from one reference aircraft and the gains in the high-level controller, which enforce a higher flutter speed, are computed. When the controller is applied experimentally to the reference aircraft, the poles of the eigenstructure assignment are as desired and hence the flutter speed is increased. This is the case because the experimental data belongs to this system and thus the method should work well, within the limits of fitting errors. However, now suppose that the same controller is applied to another aircraft of the same type. If one were to inspect the results of the controller, one would see that the measured and desired closed-loop poles are different. In fact, the closed-loop dynamic would be slightly different to what is anticipated and thus the flutter speed will likely differ slightly. The reason for such discrepancy is variability between nominal systems. In practice, supposedly identical systems will not be the same. This is due to manufacturing tolerances, the impact of human error in assembly, and variability in material properties. Consequently, the system that the controller is designed for does not match the system on which the controller is being applied and hence the eigenstructure assignment is not exactly as desired. This leads to uncertain controller performance.

Damage and Degradation

Now, consider only the reference aircraft on which the Receptance Method was applied. At the time of application, the experimental results of the eigenstructure assignment is as predicted; that is, the closed-loop poles and eigenvectors match the desired values. However, over a prolonged period of time, one may notice that the true poles no longer match the desired values. Such deviation from the original closed-loop poles arises due to time-based changes in the structure. This occurs due to damage, degradation, and changes in environmental conditions. Therefore, considering the receptance matrix or input-output transfer function matrix from a measured system as static is only acceptable if the time after which the controller is applied is relatively small.

[1] Provided the system is linear.
[2] Assuming that the measurements are error free.

7.3 Stochastic Structural Modifications

With the qualitative features described, a quantitative approach is now developed to model the physical sources of uncertainty. Consider again the frequency-domain equations of motion of the closed-loop aeroservoelastic system, which are expressed in matrix form as

$$\mathbf{Z}(s,v)\mathbf{y}(s) = \mathbf{B}_{\mathrm{CS}\to F}(s)\left(s\mathbf{F}^T + \mathbf{G}^T\right)\mathbf{y}(s), \tag{7.1}$$

or equivalently,

$$\left(\mathbf{Z}(s,v) - \mathbf{B}_{\mathrm{CS}\to F}(s)\left(s\mathbf{F}^T + \mathbf{G}^T\right)\right)\mathbf{y}(s) = \mathbf{0}. \tag{7.2}$$

Due to variability between supposedly nominal systems, the dynamic stiffness matrix becomes a function of one or more random parameters and hence Eq. 7.2 is now rewritten as

$$\left(\mathbf{Z}(s,v,\boldsymbol{\theta}) - \mathbf{B}_{\mathrm{CS}\to F}(s)\left(s\mathbf{F}^T + \mathbf{G}^T\right)\right)\mathbf{y}(s) = \mathbf{0}, \tag{7.3}$$

where $\boldsymbol{\theta} \in \mathbb{R}^p$ is a vector of p random variables. This random vector is a collection of the uncertain structural mass, stiffness and damping parameters. It is important to note that, in this work, the force distribution matrix $\mathbf{B}_{\mathrm{CS}\to F}(s)$ is assumed to be free from uncertainty; that is, it does not depend of the vector of random variables. This will be considered in future work.

If one were to measure the receptance matrix of one of the systems described by Eq. 7.3, one sample from the random vector would be selected. That is, by the act of measurement, a specific set of mass, stiffness and damping values would be obtained. To highlight this, a measured receptance matrix is written as

$$\mathbf{H}_m(s,v) = \mathbf{Z}(s,v,\hat{\boldsymbol{\theta}})^{-1}, \tag{7.4}$$

where the subscript m denotes a measured value, and $\hat{\boldsymbol{\theta}}$ is used to indicate one sample from the random vector. $\hat{\boldsymbol{\theta}}$ is a deterministic quantity that corresponds to a specific set of mass, stiffness and damping outcomes. This term will be considered in more detail later.

Pre-multiplying Eq. 7.3 by the measured receptance matrix gives that

$$\mathbf{H}_m(s,v)\left(\mathbf{Z}(s,v,\boldsymbol{\theta}) - \mathbf{B}_{\mathrm{CS}\to F}(s)\left(s\mathbf{F}^T + \mathbf{G}^T\right)\right)\mathbf{y}(s) = \mathbf{0}, \tag{7.5}$$

which may be expanded as

$$\left(\mathbf{H}_m(s,v)\mathbf{Z}(s,v,\boldsymbol{\theta}) - \mathbf{R}_m(s,v)\left(s\mathbf{F}^T + \mathbf{G}^T\right)\right)\mathbf{y}(s) = \mathbf{0}, \tag{7.6}$$

where

$$\mathbf{R}_m(s,v) = \mathbf{H}_m(s,v)\mathbf{B}_{\mathrm{CS}\to F}(s) \tag{7.7}$$

is the input-output transfer function matrix belonging to the measured system. By definition of Eq. 7.4, the term $\mathbf{H}_m(s,v)\mathbf{Z}(s,v,\boldsymbol{\theta})$ in Eq. 7.6 is only equal to the identity matrix when $\boldsymbol{\theta} = \hat{\boldsymbol{\theta}}$; that is, only when the random vector is identically equal to the sample corresponding to the measured system. Therefore, in its current form Eq. 7.6 does not guarantee cancellation of the dynamic stiffness matrix and hence its knowledge is required. This contradicts the model-free property of receptance methods. However, it is possible to adapt Eq. 7.6 such that the *complete* dynamic stiffness matrix is not explicitly required.

Let the dynamic stiffness matrix be decomposed as the sum of a nominal and random

contribution, such that

$$\mathbf{Z}(s,v,\boldsymbol{\theta}) = \mathbf{Z}_n(s,v) + \Delta\mathbf{Z}_r(s,v,\boldsymbol{\theta}), \tag{7.8}$$

where $\mathbf{Z}_n(s,v)$ is the nominal dynamic stiffness, which does not contain any of the random parameters; and $\Delta\mathbf{Z}(s,v,\boldsymbol{\theta})$ is the random contribution, which contains the isolated random terms. For the purposes of simplicity, and without affecting the proceeding analysis, it is assumed that the random contribution is independent of the freestream speed and thus Eq. 7.8 is rewritten as

$$\mathbf{Z}(s,v,\boldsymbol{\theta}) = \mathbf{Z}_n(s,v) + \Delta\mathbf{Z}_r(s,\boldsymbol{\theta}). \tag{7.9}$$

By adding and subtracting the random contribution corresponding to the measured system, it can be easily shown that

$$\mathbf{Z}(s,v,\boldsymbol{\theta}) = \left(\mathbf{Z}_n(s,v) + \Delta\mathbf{Z}_r(s,\hat{\boldsymbol{\theta}})\right) + \Delta\mathbf{Z}_r(s,v,\boldsymbol{\theta}) - \Delta\mathbf{Z}_r(s,\hat{\boldsymbol{\theta}}). \tag{7.10}$$

By definition of Eq. 7.9,

$$\mathbf{Z}(s,v,\hat{\boldsymbol{\theta}}) = \mathbf{Z}_n(s,v) + \Delta\mathbf{Z}_r(s,\hat{\boldsymbol{\theta}}), \tag{7.11}$$

and thus

$$\mathbf{Z}(s,v,\boldsymbol{\theta}) = \mathbf{Z}(s,v,\hat{\boldsymbol{\theta}}) + \Delta\mathbf{Z}_r(s,\boldsymbol{\theta}) - \Delta\mathbf{Z}_r(s,\hat{\boldsymbol{\theta}}). \tag{7.12}$$

Using the definition of the measured receptance matrix

$$\mathbf{H}_m(s,v)\mathbf{Z}(s,v,\boldsymbol{\theta}) = \mathbf{I} + \mathbf{H}_m(s,v)\left(\Delta\mathbf{Z}_r(s,\boldsymbol{\theta}) - \Delta\mathbf{Z}_r(s,\hat{\boldsymbol{\theta}})\right), \tag{7.13}$$

and thus Eq. 7.6 is equivalent to

$$\left(\mathbf{I} + \mathbf{H}_m(s,v)\left(\Delta\mathbf{Z}_r(s,\boldsymbol{\theta}) - \Delta\mathbf{Z}_r(s,\hat{\boldsymbol{\theta}})\right) - \mathbf{R}_m(s,v)\left(s\mathbf{F}^T + \mathbf{G}^T\right)\right)\mathbf{y}(s) = \mathbf{0}. \tag{7.14}$$

The corresponding characteristic equation is therefore

$$\det\left(\mathbf{I} + \mathbf{H}_m(s,v)\left(\Delta\mathbf{Z}_r(s,\boldsymbol{\theta}) - \Delta\mathbf{Z}_r(s,\hat{\boldsymbol{\theta}})\right) - \mathbf{R}_m(s,v)\left(s\mathbf{F}^T + \mathbf{G}^T\right)\right) = 0. \tag{7.15}$$

In the form given by Eq. 7.15, the characteristic equation is written in terms of the measured receptance matrix, the measured input-output transfer function matrix, and two additional dynamic stiffness matrix perturbation terms. The dynamic stiffness perturbation terms correspond only to the random parameters and thus may be viewed as a structural modification to the nominal dynamic stiffness. Therefore, there is no need to model the system itself; rather, it is only necessary to model the random modification, which is simulated.

7.3.1 Sample Modification Term

In its current form, the characteristic equation (Eq. 7.15) contains the perturbation contribution of the measured system. Therefore, it is necessary to know the sample outcome vector $\hat{\boldsymbol{\theta}}$ in order to find the random poles. Whilst this vector is deterministic, it is often difficult to measure. For instance, in complex systems the uncertain components may lie in inaccessible locations once manufactured and hence are immeasurable. Furthermore, even if one is able to measure the outcome of the random parameters, it would usually require dismantling and then reassembling the system, which could result in different system dynamics before and after.

In the following analysis, it is assumed that the sample random vector is immeasurable and instead is treated as a second random vector with the same probability distribution as $\boldsymbol{\theta}$. In

this way, the measured receptance matrix is *simulated* as belonging to any possible outcome of the random vector.

Let a new vector $\tilde{\boldsymbol{\theta}}$ be defined as

$$\tilde{\boldsymbol{\theta}} := \boldsymbol{\theta} - \hat{\boldsymbol{\theta}}. \tag{7.16}$$

Assuming that $\Delta\mathbf{Z}_r$ is a linear operator in the random parameters

$$\Delta\mathbf{Z}_r(s,\boldsymbol{\theta}) - \Delta\mathbf{Z}_r(s,\hat{\boldsymbol{\theta}}) = \Delta\mathbf{Z}_r(s,\tilde{\boldsymbol{\theta}}), \tag{7.17}$$

and hence Eq. 7.15 is re-expressed in terms of the new vector $\tilde{\boldsymbol{\theta}}$ as

$$\det\left(\mathbf{I} + \mathbf{H}_m(s,v)\Delta\mathbf{Z}_r(s,\tilde{\boldsymbol{\theta}}) - \mathbf{R}_m(s,v)\left(s\mathbf{F}^T + \mathbf{G}^T\right)\right) = 0. \tag{7.18}$$

Eq. 7.18 is referred to as the stochastic structural modification equation hereinafter. It combines the effects of the original uncertainty in the dynamic stiffness matrix and the uncertainty in the sample random vector through a new auxiliary random vector $\tilde{\boldsymbol{\theta}}$.

To observe the impact of using this new formulation, the first two probabilistic moments of the auxiliary random vector are considered.

Expectation

Using the expectation operator on Eq. 7.16 gives that

$$\mathrm{E}[\tilde{\boldsymbol{\theta}}] = \mathrm{E}[\boldsymbol{\theta}] - \mathrm{E}[\hat{\boldsymbol{\theta}}]. \tag{7.19}$$

Since $\hat{\boldsymbol{\theta}}$ is a random vector with distribution equal to $\boldsymbol{\theta}$

$$\mathrm{E}[\boldsymbol{\theta}] = \mathrm{E}[\hat{\boldsymbol{\theta}}], \tag{7.20}$$

and hence

$$\mathrm{E}[\tilde{\boldsymbol{\theta}}] = \mathbf{0}. \tag{7.21}$$

Covariance

By definition

$$\mathrm{Cov}[\tilde{\theta}_i,\tilde{\theta}_j] = \mathrm{E}[\left(\tilde{\theta}_i - \mathrm{E}[\tilde{\theta}_i]\right)\left(\tilde{\theta}_j - \mathrm{E}[\tilde{\theta}_j]\right)] = \mathrm{E}[\tilde{\theta}_i\tilde{\theta}_j] - \mathrm{E}[\tilde{\theta}_i]\mathrm{E}[\tilde{\theta}_j]. \tag{7.22}$$

Therefore, by using Eq. 7.16

$$\mathrm{Cov}[\tilde{\theta}_i,\tilde{\theta}_j] = \mathrm{E}[\left(\theta_i - \hat{\theta}_i\right)\left(\theta_j - \hat{\theta}_j\right)] - \mathrm{E}[\theta_i - \hat{\theta}_i]\mathrm{E}[\theta_j - \hat{\theta}_j]. \tag{7.23}$$

Expanding gives that

$$\mathrm{Cov}[\tilde{\theta}_i,\tilde{\theta}_j] = \mathrm{E}[\theta_i\theta_j - \theta_i\hat{\theta}_j - \hat{\theta}_i\theta_j + \hat{\theta}_i\hat{\theta}_j] - \mathrm{E}[\theta_i]\mathrm{E}[\theta_j] + \mathrm{E}[\theta_i]\mathrm{E}[\hat{\theta}_j] + \mathrm{E}[\hat{\theta}_i]\mathrm{E}[\theta_j] - \mathrm{E}[\hat{\theta}_i]\mathrm{E}[\hat{\theta}_j], \tag{7.24}$$

and hence

$$\mathrm{Cov}[\tilde{\theta}_i,\tilde{\theta}_j] = \mathrm{Cov}[\theta_i,\theta_j] - \mathrm{Cov}[\theta_i,\hat{\theta}_j] - \mathrm{Cov}[\hat{\theta}_i,\theta_j] + \mathrm{Cov}[\hat{\theta}_i,\hat{\theta}_j]. \tag{7.25}$$

Since $\boldsymbol{\theta}$ and $\hat{\boldsymbol{\theta}}$ are independent

$$\mathrm{Cov}[\theta_i,\hat{\theta}_j] = \mathrm{Cov}[\hat{\theta}_i,\theta_j] = 0, \tag{7.26}$$

and hence

$$\mathrm{Cov}[\tilde{\theta}_i, \tilde{\theta}_j] = \mathrm{Cov}[\theta_i, \theta_j] + \mathrm{Cov}[\hat{\theta}_i, \hat{\theta}_j]. \tag{7.27}$$

Since $\boldsymbol{\theta}$ and $\hat{\boldsymbol{\theta}}$ are identically distributed

$$\mathrm{Cov}[\theta_i, \theta_j] = \mathrm{Cov}[\hat{\theta}_i, \hat{\theta}_j] \tag{7.28}$$

and thus

$$\mathrm{Cov}[\tilde{\theta}_i, \tilde{\theta}_j] = 2\mathrm{Cov}[\theta_i, \theta_j]. \tag{7.29}$$

Therefore, by treating the sample vector as random, the covariance is doubled.

7.3.2 Solving the Stochastic Structural Modification Equation

In principle, the stochastic structural modification equation can be solved in a number of ways. For example, it is possible to use a numerical method, similar to Chapter 6. It is also possible to consider using symbolic methods, which construct the random characteristic equation from the measured receptance data. These solution strategies are considered in more detail later on in §7.7.

7.4 Probabilistic Response

Using numerical methods to solve the stochastic structural modification equation produces only one deterministic solution at a time. Moreover, this solution corresponds to only one outcome of the auxiliary random vector. In practice, however, the random vector has a probabilistic distribution. Therefore, the vector permits an infinite number of outcomes and there is a probability distribution that propagates to each of the closed-loop pole solutions. Knowledge of the distribution of the poles is useful when performing eigenstructure assignment since the robustness can be considered in a quantitative manner. Therefore, extensions to the solution strategy that permit the probabilistic information to be extracted are developed here.

The simplest approach is to use a Monte Carlo simulation (MCS). This is where a given number of samples are taken from the random vector and statistics are obtained for the corresponding sampled solutions of the closed-loop poles. Although conceptually simple and easy to implement, this approach can be computationally intensive. Indeed, accurate estimates of the mean, variance and higher order probability moments may require hundreds of thousands of samples. In this work, an alternative strategy is considered and is based on the principle of surrogate modelling.

7.4.1 Surrogate Modelling

Consider again the characteristic equation of the closed-loop system with a stochastic structural modification. The outcome of the auxiliary random vector $\tilde{\boldsymbol{\theta}}$ defines the eigenvalue problem associated with the system and hence determines the set of closed-loop poles.

Let the dependency between the closed-loop poles and the random vector be expressed mathematically as

$$\mu_i = \mu_i(\tilde{\boldsymbol{\theta}}), \quad i = 1, 2, \ldots, l. \tag{7.30}$$

By splitting into the real and imaginary part of each pole,

$$\mu_i(\tilde{\boldsymbol{\theta}}) = \mathrm{Re}[\mu_i(\tilde{\boldsymbol{\theta}})] + \mathrm{Im}[\mu_i(\tilde{\boldsymbol{\theta}})]\mathrm{i}, \quad i = 1, 2, \ldots, l. \tag{7.31}$$

In general, the dependency of the real and imaginary parts of the random parameters is a complicated function and is usually non-analytic. Therefore, is it not possible to directly access their statistics in a straightforward manner. To solve this problem, however, one can create a surrogate model. In this approach, the complex dependencies between the real and imaginary parts of the poles and the random parameters are approximated by simpler models. This allows the statistics of the parameters to be obtained in a more computationally efficient way.

7.4.2 Polynomial Chaos Expansion

There are a plethora of different types of surrogate models. However, one that is widely used in structural dynamics is that of the polynomial chaos (PC) expansion. The PC expansion attempts to form the relationship between a dependent variable and one or more independent random variables using a series of weighted, orthogonal polynomials. Written mathematically [86]

$$y = a_o\Gamma_0 + \sum_{i_1=1}^{p} a_{i_1}\Gamma_1(\theta_{i_1}) + \sum_{i_1=1}^{p}\sum_{i_2=1}^{i_1} a_{i_1 i_2}\Gamma_2(\theta_{i_1},\theta_{i_2}) + \sum_{i_1=1}^{p}\sum_{i_2=1}^{i_1}\sum_{i_3=1}^{i_2} a_{i_1 i_2 i_3}\Gamma_3(\theta_{i_1},\theta_{i_2},\theta_{i_3}) + \ldots, \tag{7.32}$$

where y is the response variable, a_i are weighting constants, and Γ are multivariate, orthogonal functions of the random variables. In the case that the random variables are independent and have a zero mean, unit variance Gaussian distribution, the orthogonal polynomials are the multidimensional Hermite polynomials, given by

$$\Gamma_n(\theta_{i_1},\theta_{i_2},\ldots,\theta_{i_n}) = (-1)^n \frac{\partial^n e^{-\frac{1}{2}\boldsymbol{\theta}^T\boldsymbol{\theta}}}{\partial\theta_{i_1}\partial\theta_{i_2}\ldots\partial\theta_{i_n}} e^{\frac{1}{2}\boldsymbol{\theta}^T\boldsymbol{\theta}}. \tag{7.33}$$

As stated above, the Hermite polynomials may only be used when the independent random variables are standardised Gaussian. In the following examples, it is assumed that the random mass, stiffness and damping parameters are all independent and Gaussian. Therefore, one can easily map the random variables to standardised values using the relationship

$$\hat{\tilde{\boldsymbol{\theta}}} = \frac{\tilde{\boldsymbol{\theta}} - \mathrm{E}[\tilde{\boldsymbol{\theta}}]}{\sqrt{\mathrm{Var}[\tilde{\boldsymbol{\theta}}]}}. \tag{7.34}$$

In general, the random variables may not be independent Gaussian and therefore the use of the Hermite polynomials may be invalid. However, in such cases one can either: (i) use an alternative set of orthogonal polynomials that matches the distribution of the random parameters, or (ii) use techniques to transform the variables to standardised Gaussian. One such transformation technique is known as the Rosenblatt transform and is discussed in greater detail in Chapter 8.

In practice, it is usual to rewrite the expansion given into the form

$$y = \sum_{i=0}^{\infty} b_i\Psi_i(\boldsymbol{\theta}), \tag{7.35}$$

where there is a one-to-one correspondence between the coefficients a_i and b_i, and the functions Γ_i and Ψ_i. For the sake of computational implementation, the expansion is truncated to the

first N terms, so that

$$y \approx \sum_{i=0}^{N-1} b_i \Psi_i(\boldsymbol{\theta}). \tag{7.36}$$

Of course, the number of terms used in the expansion determines the accuracy of the surrogate model. A small number of terms may not be able to encapsulate highly nonlinear terms and hence the surrogate model may be poor. On the contrary, however, too many terms in the expansion may potentially yield a severe overfitting of the model.

There are numerous approaches to calculate the coefficients of the expansion. In this work, however, a simplistic least squares approach is employed. First, a set number of samples is taken from the random parameters. Next, the eigenvalues corresponding to these parameters are calculated. Once the order of the PC expansion is chosen, the coefficients are calculated by finding the least squares estimate between the surrogate model and the true eigenvalue variability.

After the coefficients of the expansion have been obtained, it is straightforward to calculate the statistical information of the dependent random variable. Using the principle of orthogonality, it may be shown that the mean is given by

$$\mathrm{E}[y] = b_0. \tag{7.37}$$

Likewise, the variance is given by

$$\mathrm{Var}[y] = \sum_{i=1}^{N-1} b_i^2 \mathrm{E}[\Psi_i^2(\boldsymbol{\theta})]. \tag{7.38}$$

The term $\mathrm{E}[\Psi_i^2(\boldsymbol{\theta})]$ does not depend upon the coefficients of the expansion and therefore can be obtained from a standard reference list, such as that presented in [80].

In this work, the PC expansion is used to create a surrogate model of the real and imaginary part of each pole. Therefore, in principle, there is a maximum of $2l$ surrogate models. In practice, however, it is not usually necessary to create so many expansions since the real or imaginary part of one or more poles may not be of interest. This is further discussed in the following section.

7.5 Optimisation Strategies

As in Chapter 6, one may consider strategies to maximise the robustness of the closed-loop poles to uncertainty. Unlike before, however, the uncertainty is defined in a probabilistic sense, as opposed to using only sensitivities, and thus the new optimisation strategy must reflect this.

7.5.1 Robustness Metric

Here, a new objective function is used and is composed of two elements: first, the *local* robustness metric, and secondly, the *total* robustness metric. The local robustness metric is defined as

$$J_i = \beta_i \frac{\sqrt{\mathrm{Var}[\mathrm{Re}(\mu_i)]}}{|\mathrm{E}[\mathrm{Re}(\mu_i)]|} + \gamma_i \frac{\sqrt{\mathrm{Var}[\mathrm{Im}(\mu_i)]}}{|\mathrm{E}[\mathrm{Im}(\mu_i)]|}, \quad i = 1, 2, \ldots, l, \tag{7.39}$$

where $\beta_i, \gamma_i \in \mathbb{R}^+$. This first metric serves to weight the relative importance of the robustness of the real and imaginary part of each pole. However, the crucial difference is that this is defined in terms of the variance and expectation of each pole's real and imaginary parts. Indeed, the

weighting parameters β_i and γ_i act on the coefficient of variation of the real and imaginary parts, respectively. The total robustness metric is then defined using the local metrics as

$$T_T = \sum_{i=1}^{l} \rho_i J_i \tag{7.40}$$

where, again, $\rho_i \in \mathbb{R}^+$ are constants that weight the relative importance of each pole with respect to one another.

7.5.2 Optimisation Procedures

The new probabilistic-based robustness metric allows one to perform optimal eigenstructure assignment in a manner that is almost identical to that of the previous chapter. Indeed, the principles of the optimisation technique and the optimisation variables themselves remain unchanged. Therefore, a brief review of the optimisation strategies is given here and adapted slightly for the new robustness metric, or objective function. More complete details may be found in §6.5.

Single-Input Systems

The only optimisation variables in the single-input system are the positions of the closed-loop poles in the complex plane. Therefore, the optimisation is defined as:

Optimisation 1 (Single-Input): Minimise the total robustness metric in Eq. 7.40 subject to placing the closed-loop poles within enclosed rectangular regions.

Multiple-Input Systems

In addition to the closed-loop poles, the $\boldsymbol{\alpha}_i$ vectors are also optimisation variables and thus, as before, the optimisation strategies are:

Optimisation 2 (Multiple-Input): Minimise the total robustness metric in Eq. 7.40 by assigning the closed-loop poles at fixed locations in the complex plane and optimally choosing the $\boldsymbol{\alpha}_i$ vectors subject to a set of gain constraints.

Optimisation 3 (Multiple-Input): Minimise the total robustness metric in Eq. 7.40 by assigning the closed-loop poles within rectangular regions and optimally choosing the $\boldsymbol{\alpha}_i$ vectors subject to gain constraints.

Throughout this work, the gain constraints are the same as those used in the previous chapter and thus are given by

$$w||\boldsymbol{\Lambda}\mathbf{F}||_F + ||\boldsymbol{\Lambda}\mathbf{G}||_F \leq c_{max}. \tag{7.41}$$

Likewise, the pole constraints are

$$\mu_i \in [\underline{\mathrm{Re}}(\mu_i), \overline{\mathrm{Re}}(\mu_i)] + [\underline{\mathrm{Im}}(\mu_i), \overline{\mathrm{Im}}(\mu_i)]\mathrm{i}, \quad i = 1, 2, \ldots, l. \tag{7.42}$$

Optimisation Method

In both the single-input and multiple-input systems, the geometrical form of the optimisation cannot be inferred and therefore it is best to assume that the objective function is: (i) non-convex, and (ii) contains a potentially large number of stationary points. Therefore, it is most suitable to use a global optimisation approach and thus the Differential Evolution algorithm is again used throughout all examples. More details on this algorithm are given in Appendix A.

7.6 Numerical Examples

The techniques developed above are now tested on the reference mass-spring-damper system given in Chapter 6. That is, the system with matrices given by

$$\mathbf{M} = \begin{pmatrix} 2 & 0 & 0 \\ 0 & 1 & 0 \\ 0 & 0 & 3 \end{pmatrix}, \quad \mathbf{C} = 0.5 \begin{pmatrix} 1 & 0 & 0 \\ 0 & 1 & -1 \\ 0 & -1 & 1 \end{pmatrix}, \quad \mathbf{K} = \begin{pmatrix} 6 & -2 & -1 \\ -2 & 4 & -2 \\ -1 & -2 & 3 \end{pmatrix},$$

and corresponding open-loop poles as given in Table 7.1.

Table 7.1: Open-loop poles.

Pole	Value
$\lambda_{1,2}$	-0.0166 ± 0.5516i
$\lambda_{3,4}$	-0.1890 ± 1.6044i
$\lambda_{5,6}$	-0.2528 ± 2.2289i

7.6.1 One Random Parameter

The first three examples consider a single random parameter. More specifically, the collocated stiffness belonging to the 2 kg mass is treated as uncertain. Now, the stiffness matrix is written as

$$\mathbf{K} = \begin{pmatrix} k & -2 & -1 \\ -2 & 4 & -2 \\ -1 & -2 & 3 \end{pmatrix},$$

where

$$k \sim \mathcal{N}(6, 0.4^2).$$

Following the procedure given in §7.2, the dynamic stiffness modification corresponding to the variable stiffness is

$$\Delta\mathbf{Z}_r(s, \tilde{k}) = \begin{pmatrix} \tilde{k} & 0 & 0 \\ 0 & 0 & 0 \\ 0 & 0 & 0 \end{pmatrix},$$

where

$$\tilde{k} \sim \mathcal{N}(0, 2 * 0.4^2).$$

Note again that the random variable $\tilde{\theta}$ is used to account for the uncertainty in the random stiffness and the uncertainty in the outcome of the random parameter in the measured dynamic stiffness matrix.

Throughout these examples, the measured dynamic stiffness matrix is taken as

$$\mathbf{H}_m(s) = \begin{pmatrix} 2s^2 + 0.5s + 6.2 & -2 & -1 \\ -2 & s^2 + 0.5s + 4 & -0.5s - 2 \\ -1 & -0.5s - 2 & 3s^2 + 0.5s + 3 \end{pmatrix}^{-1}.$$

It is important to emphasise here that, in this example, one is able to see the outcome of the random stiffness (6.2 N/m). In practice, however, this is not the case and the outcome is unknown.

Case 1: Single-Input, Single Pole Pair Priority

First, a single-input is considered. Here, the force distribution vector is selected as

$$\mathbf{b} = \begin{pmatrix} 1 \\ 0 \\ 0 \end{pmatrix}.$$

As per optimisation one, the optimisation variables are the closed-loop poles. Therefore, one must define the rectangular constraints in the complex plane. However, before performing optimal pole placement, it is first necessary to introduce a reference pole placement. This is used to quantitatively assess the results of the optimisation. Here, the reference poles are assigned to the values specified in Table 7.2 using control gains of

$$\mathbf{f}_{ref} = \begin{pmatrix} -4.9667 \\ -2.2092 \\ -6.6540 \end{pmatrix}, \quad \mathbf{g}_{ref} = \begin{pmatrix} -10.9156 \\ 1.0144 \\ -2.6132 \end{pmatrix}.$$

Table 7.2: Reference closed-loop poles.

Pole	Value
$\lambda_{1,2}$	-0.2 ± 0.8i
$\lambda_{3,4}$	-0.5 ± 2i
$\lambda_{5,6}$	-1 ± 2.5i

Suppose that the total robustness metric is defined as

$$T_T = \frac{\sqrt{\text{Var}[\text{Re}(\mu_1)]}}{|\text{E}[\text{Re}(\mu_1)]|}.$$

This metric considers only the real part variation of the first pole pair and is representative of the type that would be used in applications where the stability of the system is most crucial. Using a third order polynomial chaos expansion, constructed using 40 Latin hypercube samples between ±3 standard deviations of the random stiffness, the initial robustness metric for the reference case is computed as 0.0423.

Suppose now that the poles are to be re-placed in the rectangular regions specified by

$$\mu_{1,2} = [-0.5, -0.2] \pm [0.6, 1]\text{i},$$
$$\mu_{3,4} = [-0.7, -0.3] \pm [1.7, 2.3]\text{i},$$
$$\mu_{5,6} = [-1.2, -0.8] \pm [2.2, 2.8]\text{i}.$$

After optimisation, again using the Differential Evolution algorithm, the poles are assigned to the points

$$\mu_{1,2} = -0.2 \pm 1i,$$
$$\mu_{3,4} = -0.7 \pm 1.7i,$$
$$\mu_{5,6} = -1.2 \pm 2.259i,$$

using control gains of

$$\mathbf{f} = \begin{pmatrix} -6.5667 \\ -1.3833 \\ -8.5617 \end{pmatrix}, \quad \mathbf{g} = \begin{pmatrix} -10.9475 \\ 5.8900 \\ -9.2200 \end{pmatrix}.$$

This reduces the robustness metric to 0.0090 (a reduction of 79%). Figure 7.1 shows the variation of the poles in the reference and optimised cases. As shown, the optimised poles have a lower spread in the real part of the first pole pair, as was desired. However, this is notably at the expense of the variation of the second and third pole pairs. This is because the robustness metric did not consider their variation and therefore the optimisation result was independent of their spread.

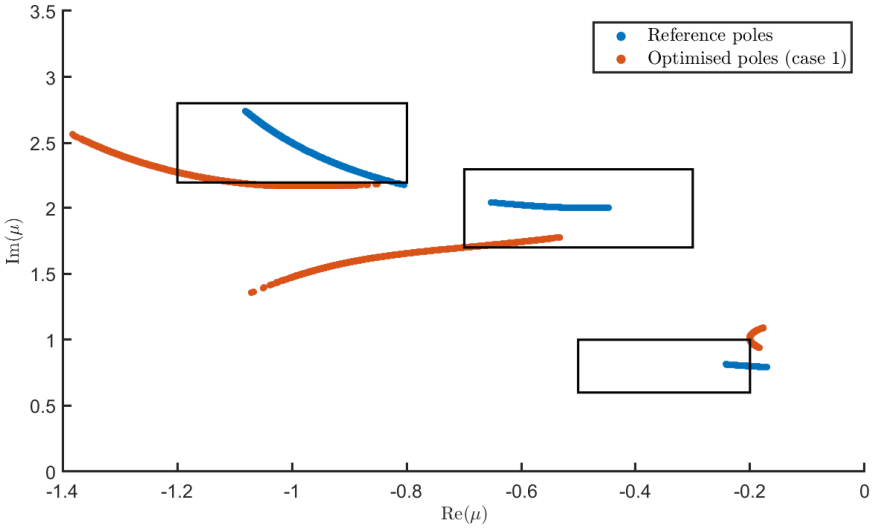

Figure 7.1: Optimisation 1.

An interesting point to consider is the new, optimised shape of the first pole pair. This is emphasised in Fig. 7.2, which shows a zoomed in view of this pole. As shown, the variation of the pole in the real axis direction is curved and is thus highly nonlinear. Therefore, in order to accurately estimate the total robustness metric correctly, one must choose a suitable order polynomial chaos expansion. Indeed, a sensitivity-based approach would be unlikely to give an accurate estimate of the pole variability.

As previously mentioned, it was decided to use a third order expansion throughout the optimisation. This was found to give a good performance in estimating the variability of the poles, without risking the problems associated with overfitting. Figure 7.3 shows a graph of the PC expansion fitting in the real part of the optimised, first pole pair. As shown, there is an excellent agreement between the sampled data and the fitted expansion and thus the estimate of the total robustness metric is likely to be accurate.

The results of this optimisation were verified using an independent Monte Carlo simulation.

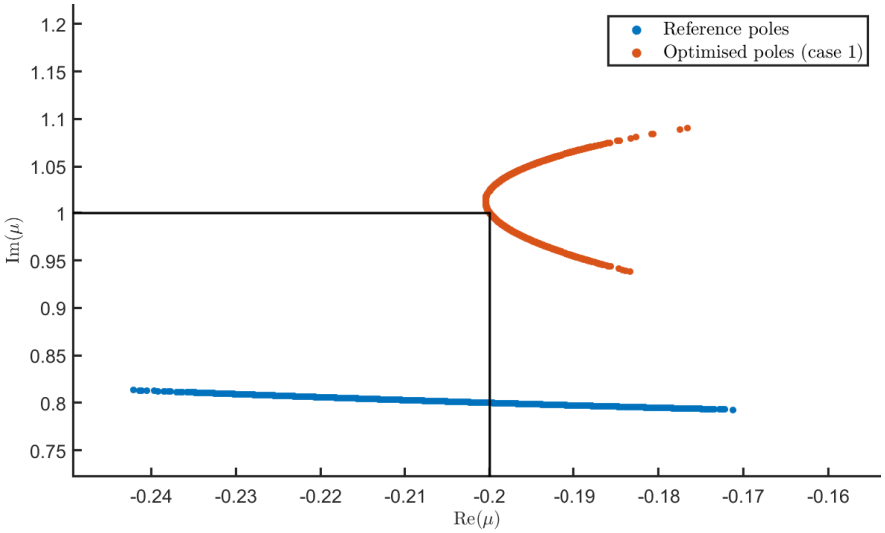

Figure 7.2: Optimisation 1 (Zoomed-in on the first pole).

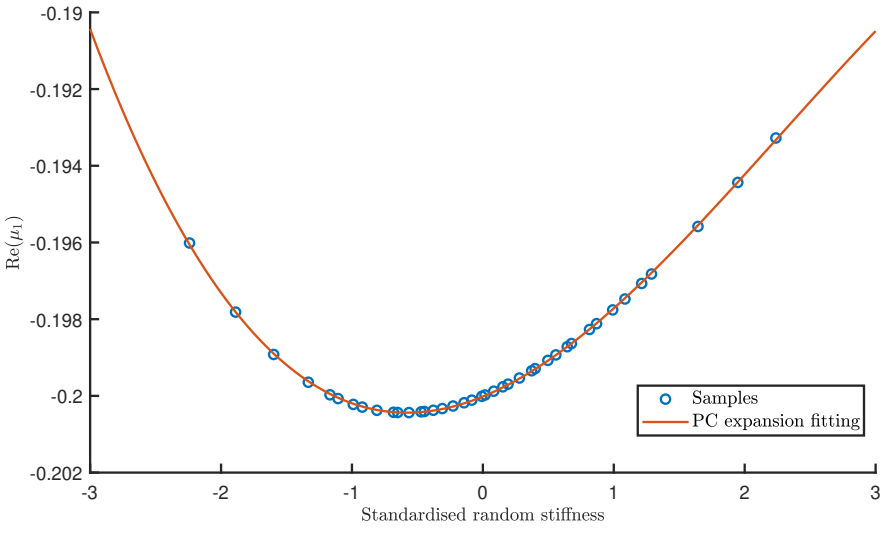

Figure 7.3: PC expansion fitting of the real part pole variation.

100,000 samples of the random stiffness were taken and the resulting closed-loop poles were obtained. The expectation and variance of the first pole pair were then used to compute the total robustness metric. In this case, the metric computed by MCS was 0.0091. This is an error of approximately 1% and therefore one can conclude a high degree of accuracy in the method.

Case 2: Single-Input, Multiple Pole Pair Priority

In the previous optimisation, the objective function was chosen to be the coefficient of variation of the real part of the first pole pair. Consequently, the variation of the other poles was not included and the final result led to a worse variation in these poles compared to the reference condition. Here, an adjustment to the optimisation is considered.

Suppose that the objective function is changed to

$$T_T = 4\frac{\sqrt{\text{Var}[\text{Re}(\mu_1)]}}{|\text{E}[\text{Re}(\mu_1)]|} + \frac{\sqrt{\text{Var}[\text{Re}(\mu_3)]}}{|\text{E}[\text{Re}(\mu_3)]|} + \frac{\sqrt{\text{Var}[\text{Re}(\mu_5)]}}{|\text{E}[\text{Re}(\mu_5)]|}.$$

Now, the real part variation of the other pole pairs is included and thus the optimisation will attempt to ensure that they do not become disproportionately large. Note, however, that the first pole pair is scaled be a factor of four and is therefore still considered to be more important.

Using the same optimisation procedure as before, the optimum poles are found to be

$$\begin{aligned}\mu_{1,2} &= -0.2 \pm 1i,\\ \mu_{3,4} &= -0.5 \pm 2.3i,\\ \mu_{5,6} &= -1.2 \pm 2.8i.\end{aligned}$$

which are assigned using control gains of

$$\mathbf{f} = \begin{pmatrix} -5.7667 \\ -6.3257 \\ -12.9214 \end{pmatrix}, \quad \mathbf{g} = \begin{pmatrix} -18.8622 \\ -6.9720 \\ -11.0665 \end{pmatrix}.$$

This reduces the objective function from 0.24 to 0.071 (a reduction of 70%).

Figure 7.4 shows the variation of the poles in the reference case, the previous optimisation (example 1), and the current optimisation. As shown, the variation of the second and third pole pairs in the real direction is significantly lower than the reference case and that of optimisation one. Thus, one can conclude that the weighting constants serve well to incorporate the variation of the other poles. It is to be noted that the new coefficient of variation of the real part of the first pole pair, which is 0.0162, is larger than the previous optimisation. However, this is to be expected as the optimisation must also balance the variation of the other poles too.

As before, the results obtained above were verified using an independent MCS. Using 100,000 samples, the total robustness metric was computed as 0.071, which matches the value obtained by the PC expansion method.

Case 3: Multiple-Input, Multiple Pole Pair Priority

Here, the case of multiple inputs is considered. Now, the force distribution matrix is selected as

$$\mathbf{B} = \begin{pmatrix} 1 & 0 & 0 \\ 0 & 1 & 0 \\ 0 & 0 & 1 \end{pmatrix}.$$

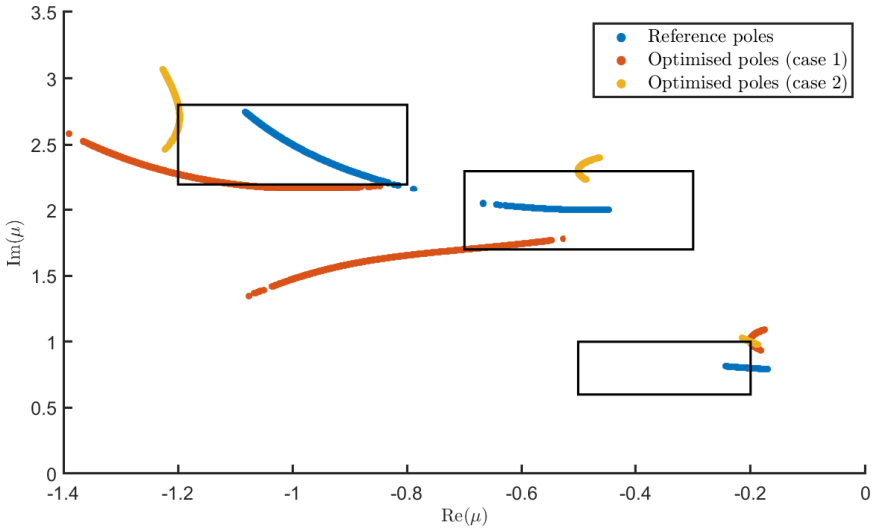

Figure 7.4: Optimisation 2.

This allows the eigenvectors, or more specifically the $\boldsymbol{\alpha}_i$ vectors, to be optimised in addition to the closed-loop poles. As is necessary in multiple input optimisations, gains constraints are used and are given by

$$3||\mathbf{F}||_F + ||\mathbf{G}||_F \leq 7.$$

Performing the optimisation again with the additional optimisation parameters, the new closed-loop poles are found to be

$$\begin{aligned}\mu_{1,2} &= -0.2 \pm 0.618i,\\ \mu_{3,4} &= -0.3 \pm 1.7i,\\ \mu_{5,6} &= -0.8 \pm 2.2i.\end{aligned}$$

This reduces the total robustness to 0.0223, an improvement on the previous optimisation. The corresponding optimum $\boldsymbol{\alpha}_i$ vectors are

$$\boldsymbol{\alpha}_{1,2} = \begin{pmatrix} 1 \\ -7.1500 \pm 0.0003i \\ -5.8900 \mp 0.0238i \end{pmatrix}, \quad \boldsymbol{\alpha}_{3,4} = \begin{pmatrix} 1 \\ 4.7806 \mp 7.4121i \\ -8.5607 \mp 1.0915i \end{pmatrix}, \quad \boldsymbol{\alpha}_{5,6} = \begin{pmatrix} 1 \\ 0.0403 \pm 1.5995i \\ 0.0067 \mp 0.0074i \end{pmatrix}.$$

The control gains in this case are

$$\mathbf{F} = \begin{pmatrix} -0.5340 & -0.1769 & 0.3402 \\ 0.0324 & -1.1252 & -0.1000 \\ 0.1533 & -0.1392 & -0.8735 \end{pmatrix}, \quad \mathbf{G} = \begin{pmatrix} 0.6412 & 0.5414 & 0.0221 \\ -1.3752 & -1.1013 & -0.0327 \\ 0.7529 & 0.3345 & -0.2225 \end{pmatrix},$$

and the corresponding right eigenvectors of the optimised system are

$$\mathbf{w}_{1,2} = \begin{pmatrix} 0.9392 \mp 5.5346i \\ 0.4895 \mp 9.2064i \\ 2.0818 \mp 11.7375i \end{pmatrix}, \quad \mathbf{w}_{3,4} = \begin{pmatrix} -0.5038 \pm 8.2132i \\ 4.5275 \mp 3.6418i \\ -0.5081 \mp 2.9882i \end{pmatrix}, \quad \mathbf{w}_{5,6} = \begin{pmatrix} 0.0317 \mp 0.0261i \\ -0.6656 \mp 0.0590i \\ 0.0937 \mp 0.0026i \end{pmatrix}.$$

Figure 7.5 shows the newly optimised pole spreads. As shown, the additional inputs are able to significantly reduce the variation of the real part of the poles. However, one can observe

that the imaginary part variation of the poles has increased. In practice, it would be necessary to also include a term to ensure that these terms do not become exceptionally large. This is especially true in aeroservoelastic systems where the separation of the modes, in terms of frequency, is also essential.

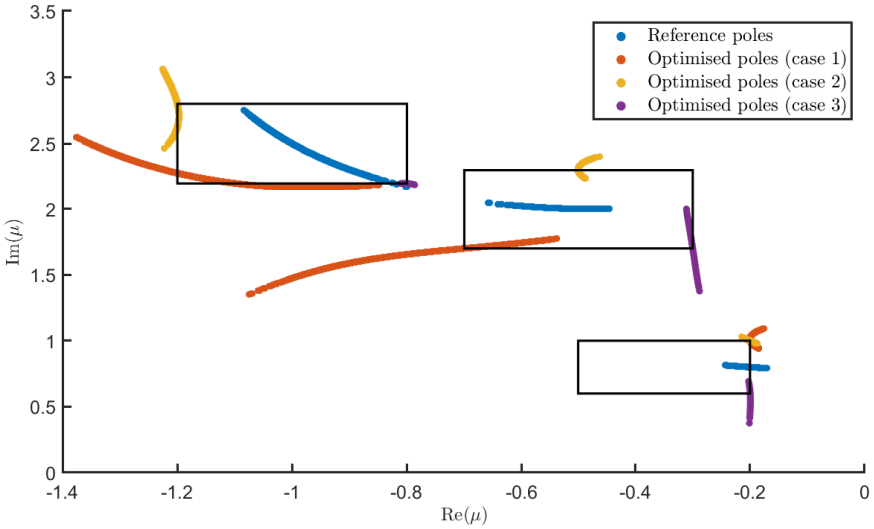

Figure 7.5: Optimisation 3

The results of the optimisation were again verified using MCS. It was found that the total robustness metric matched to two significant figures and therefore it can be deduced that the PC expansions perform well in estimating the mean and variance of the real part of the poles.

Interestingly, substituting the poles into the gains constraints gives that

$$3||\mathbf{F}||_F + ||\mathbf{G}||_F = 6.9.$$

This suggests that, as in Chapter 6, the controller is at the limit of its performance and thus the optimisation is trying to utilise the full control authority that is available to minimise the robustness metric.

7.6.2 Multiple Random Parameters

Finally, the case of multiple random parameters is considered. Now, the stiffness matrix is now written as

$$\mathbf{K} = \begin{pmatrix} k_1 + k_2 + 1 & -k_2 & -1 \\ -k_2 & k_2 + k_3 & -k_3 \\ -1 & -k_3 & k_3 + 1 \end{pmatrix}$$

where

$$k_1 \sim \mathcal{N}(3, 0.3^2), \quad k_2 \sim \mathcal{N}(2, 0.2^2), \quad k_3 \sim \mathcal{N}(2, 0.2^2)$$

This means that the new structural modification matrix becomes

$$\Delta\mathbf{Z}_r(s, \tilde{k}_1, \tilde{k}_2, \tilde{k}_3) = \begin{pmatrix} k_1 + k_2 & -k_2 & 0 \\ -k_2 & k_2 + k_3 & -k_3 \\ 0 & -k_3 & k_3 \end{pmatrix}$$

where

$$\tilde{m}_1 \sim \mathcal{N}(0, 2 * 0.3^2), \quad \tilde{m}_2 \sim \mathcal{N}(0, 2 * 0.2^2), \quad \tilde{m}_3 \sim \mathcal{N}(0, 2 * 0.2^2)$$

Let a reference eigenstructure assignment be defined as that which places the poles at the points defined in Table 7.2 and has $\alpha_{k,i} = 1 \forall k, i$. Supposing that the same metric as given example 2 is used, the initial value of the objective function in the reference case is 0.69.

Now, the eigenstructure assignment can be optimised. Suppose that the poles are to be placed within the same rectangular regions specified in examples 1 to 3. Also, suppose that the control gains are restricted by the constraint given in example 3.

Using the same optimisation procedure, but now with the added uncertain parameters, the optimum poles are found to be

$$\begin{aligned}\mu_{1,2} &= -0.2 \pm 0.751i \\ \mu_{3,4} &= -0.3 \pm 1.7i \\ \mu_{5,6} &= -0.338 \pm 2.2i\end{aligned}$$

The optimum set of alpha vectors are

$$\boldsymbol{\alpha}_{1,2} = \begin{pmatrix} 1 \\ 7.2624 \mp 6.8744i \\ 9.9295 \mp 1.1858i \end{pmatrix}, \quad \boldsymbol{\alpha}_{3,4} = \begin{pmatrix} 1 \\ -0.0100 \\ 0.0065 \mp 0.0076i \end{pmatrix}, \quad \boldsymbol{\alpha}_{5,6} = \begin{pmatrix} 1 \\ 2.4935 \pm 6.2079i \\ 0.0024 \pm 0.0097i \end{pmatrix},$$

The control gains in this case are

$$\mathbf{F} = \begin{pmatrix} -0.5809 & 0.8260 & -0.2556 \\ -0.0922 & -1.1828 & -0.1635 \\ 0.2250 & -0.0300 & -0.8283 \end{pmatrix}, \quad \mathbf{G} = \begin{pmatrix} -0.2182 & 0.4082 & -0.0987 \\ -0.6138 & -0.7869 & -0.2171 \\ 0.4386 & -0.5194 & -0.2672 \end{pmatrix}$$

and the corresponding right eigenvectors of the optimised system are

$$\mathbf{w}_{1,2} = \begin{pmatrix} -2.2695 \pm 4.9367i \\ -3.2188 \pm 7.1486i \\ -4.8787 \pm 11.1032i \end{pmatrix}, \quad \mathbf{w}_{3,4} = \begin{pmatrix} -0.3473 \pm 0.6418i \\ -0.2125 \pm 0.4571i \\ 0.0941 \pm 0.3132i \end{pmatrix}, \quad \mathbf{w}_{5,6} = \begin{pmatrix} -0.0202 \pm 0.4466i \\ -2.2529 \pm 0.8839i \\ 0.3296 \mp 0.2106i \end{pmatrix},$$

This reduces the objective function to 0.111 (an 84% reduction from the reference case). Figure 7.6 shows the variation of the poles before and after optimisation. As shown, the real part variation in each cluster has been minimised and thus the desired action of the optimisation has been achieved.

To verify the results, MCS was performed to estimate the total robustness metric. Using 100,000 samples, the metric was calculated as 0.102. This lies close to the value predicted by the PC expansion (a 7% error) and therefore one can conclude that: (i) a good number of samples (1000) were used to estimate the parameters of the PC expansion, and (ii) the order of the expansion is sufficient to estimate the variability of the real part of the poles.

Substituting the optimum control gains into the gain constraint gives 6.8. Again, the controller effort lies very close to the maximum allowable value.

7.7 Experimental Limitations

As shown in the previous section, the coefficients of the polynomial chaos expansion are found by sampling the random auxiliary vector and its corresponding closed-loop poles. In numerical settings, the random poles can be found in a straightforward manner. The mass, stiffness or

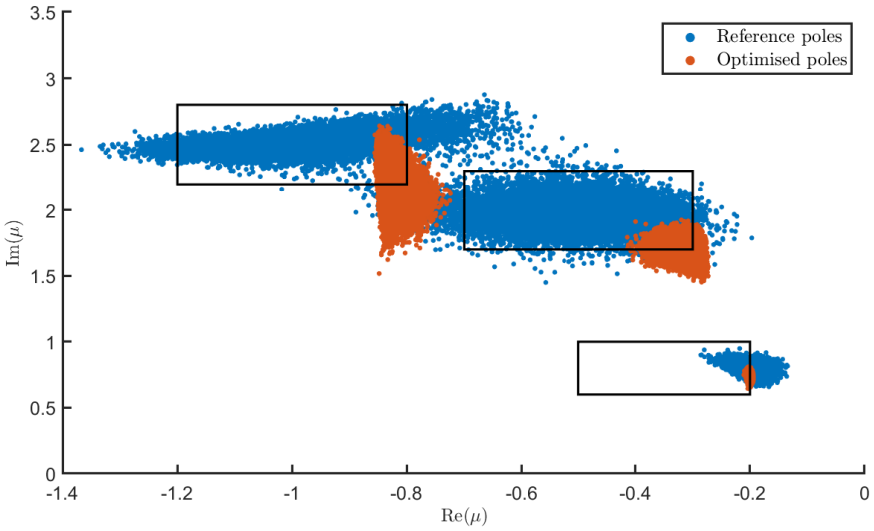

Figure 7.6: Optimisation 4

damping modification can be added to the nominal system matrices and the eigenvalues then computed through standard numerical schemes. For example, in MATLAB, it is possible to use the *polyeig* function directly on the system matrices. However, in experimental settings, this is not possible since the system matrices are not directly available. In such cases, it is then necessary to solve the stochastic structural modification equation using only receptance data.

Consider again the stochastic structural modification equation, which is repeated below

$$\det\left(\mathbf{I}+\mathbf{H}_m(s,v)\Delta\mathbf{Z}_r(s,\tilde{\boldsymbol{\theta}})-\mathbf{R}_m(s,v)\left(s\mathbf{F}^T+\mathbf{G}^T\right)\right)=0. \tag{7.43}$$

The independent variable that is to be solved is s, which in general has l solutions. Each solution $s=\mu_i$ must satisfy

$$\det\left(\mathbf{I}+\mathbf{H}_m(\mu_i,v)\Delta\mathbf{Z}_r(\mu_i,\tilde{\boldsymbol{\theta}})-\mathbf{R}_m(\mu_i,v)\left(\mu_i\mathbf{F}^T+\mathbf{G}^T\right)\right)=0,\quad \mu_i=1,2,\ldots,l. \tag{7.44}$$

In Chapter 6, a form similar to this was solved to visualise the pole spreads[3] This was done by taking the left-hand side of equation 7.44 and separating it into its constituent real and imaginary parts. The uncertain pole solution μ_i was then found by determining the values of s for which the determinant is zero both in the real and imaginary part. This process was then repeated for every pole. Whilst this method works well in principle, it does have several restrictions. Firstly, numerical methods often require the user to input initial search locations. Thus, for the uncertain pole problem, one must give an initial value in the complex plane about which the numerical method will search. The main issue with this is that there is no guarantee that the correct solution will be found. Indeed, the numerical solver may tend towards a 'dominant solution' due to the local behaviour of the objective function[4]. Additionally, there may be issues related to ill-conditioning and the physicality of the solution. These are discussed in the following subsections.

[3]It is to be noted again that the method itself, however, does not require this.
[4]This behaviour was observed in the experimental case study of Chapter 6.

7.7.1 Ill-conditioning

As established in Chapter 6, the input-output transfer function matrix can be expressed in the generalised form

$$\mathbf{R}(s,v) = \frac{1}{d(s,v)}\mathbf{N}_R(s,v). \tag{7.45}$$

Likewise, the receptance matrix can also be written as

$$\mathbf{H}(s,v) = \frac{1}{d(s,v)}\mathbf{N}_H(s,v). \tag{7.46}$$

Substituting Eqs. 7.45 and 7.46 into the structural modification equation gives that

$$\det\left(\mathbf{I} + \frac{1}{d(s,v)}\mathbf{N}_H(s,v)\Delta\mathbf{Z}_r(s,\tilde{\boldsymbol{\theta}}) - \frac{1}{d(s,v)}\mathbf{N}_R(s,v)\left(s\mathbf{F}^T + \mathbf{G}^T\right)\right) = 0. \tag{7.47}$$

or equivalently

$$\frac{1}{(d(s,v))^n}\det\left(d(s,v)\mathbf{I} + \mathbf{N}_H(s,v)\Delta\mathbf{Z}_r(s,\tilde{\boldsymbol{\theta}}) - \mathbf{N}_R(s,v)\left(s\mathbf{F}^T + \mathbf{G}^T\right)\right) = 0. \tag{7.48}$$

The term $d(s,v)$ describes the characteristic equation of the open-loop system. Thus,

$$d(s,v) = 0, \quad \forall s \in \boldsymbol{\lambda}. \tag{7.49}$$

where $\boldsymbol{\lambda}$ is the set of open-loop poles.

Suppose that one of the pole solutions is given by $\mu = \lambda$. The left-hand side of the characteristic equation corresponding to this solution is

$$\frac{1}{(d(\lambda,v))^n}\det\left(d(\lambda,v)\mathbf{I} + \mathbf{N}_H(\lambda,v)\Delta\mathbf{Z}_r(\lambda,\tilde{\boldsymbol{\theta}}) - \mathbf{N}_R(\lambda,v)\left(\lambda\mathbf{F}^T + \mathbf{G}^T\right)\right). \tag{7.50}$$

By virtue of Eq. 7.49, Eq. 7.50 becomes

$$\frac{1}{0}\det\left(\mathbf{N}_H(\lambda,v)\Delta\mathbf{Z}_r(\lambda,\tilde{\boldsymbol{\theta}}) - \mathbf{N}_R(\lambda,v)\left(\lambda\mathbf{F}^T + \mathbf{G}^T\right)\right). \tag{7.51}$$

Using the relationship,

$$\mathbf{N}_R(\lambda,v) = \mathbf{N}_H(\lambda,v)\mathbf{B}_{CS\to F}, \tag{7.52}$$

it is easily shown that

$$\frac{1}{0}\det\left(\mathbf{N}_H(\lambda,v)\right)\det\left(\Delta\mathbf{Z}_r(\lambda,\tilde{\boldsymbol{\theta}}) - \mathbf{B}_{CS\to F}(\lambda,v)\left(\lambda\mathbf{F}^T + \mathbf{G}^T\right)\right). \tag{7.53}$$

As shown in [117],

$$\operatorname{rank}(\mathbf{N}_H(\lambda,v)) = 1. \tag{7.54}$$

Thus, due to rank deficiency,

$$\det\left(\mathbf{N}_H(\lambda,v)\right) = 0, \quad \text{if} \quad n > 1. \tag{7.55}$$

This means that the determinant equation reduces to an indeterminate form $(0/0)$.

Whilst the form is indeterminate at the open-loop poles, the problem may be present at other pole solutions. In regions close to this, i.e. $\mu_i = \lambda_i + \epsilon_i$, the limited precision of the computer may yield erroneous estimates of the random poles due to ill-conditioning. This

should be investigated and quantified in further work.

7.7.2 Solution Physicality

There is also an issue related to the physicality of the solution. At present, the method requires the collection of two forms of data: pure receptance data and the input-output transfer function matrix. As shown previously, these terms must both be constructed by RTF fitting and require that one is able to measure the open-loop poles. In practice, these two fittings are done independently and hence the open-loop poles will be slightly different due to measurement errors and other such sources. This is contrary to theory, which states that the open-loop poles should match identically. Of course, one may argue that the open-loop poles of the fitting may be adjusted post RTF so that they match. However, doing so will sacrifice the goodness of the fitting and hence increase errors associated fitting parameters.

7.8 Summary

This chapter considers the development of a receptance-based optimum eigenstructure assignment technique. Alike Chapter 6, uncertainty in the Receptance Method is considered. However, the uncertainty arising from variability between nominal systems is described instead. Using polynomial chaos expansions, the coefficient of variation of the real and imaginary part of each pole is collected and used to construct a robustness metric. This metric is then optimised by assignment of the closed-loop poles, eigenvectors, or a combination thereof.

The proposed technique has been tested numerically on a simple mass-spring-damper, three-degree-of-freedom system. It is shown how the desired eigenstructure assignment significantly affects the spread of the poles and thus optimal placement of the poles and eigenvectors forms an important aspect of controller design. Additionally, it shown that the method is able to capture the nonlinear mapping between the random parameters and the resulting closed-loop poles. Thus, the method is capable of global optimisation and does not suffer from the issues associated with using sensitivities.

At present, experimental applications of this technique are limited by computational issues that arise when solving the stochastic determinant equation. Firstly, numerical schemes are inappropriate to use when the closed-loop poles lie close to the open-loop values. This is due to the ill-conditioning of the input-output transfer function matrices at these points. Secondly, symbolic methods rely upon cancellation of numerator and denominator terms in the determinant equation. This is usually impossible to achieve due to the limit precision of the computer. Future work will consider these points.

Chapter 8

Probabilistic Flutter Speed Uncertainty Quantification

8.1 Introduction

In Chapters 6 and 7, the problem of uncertainty in the Receptance Method was addressed and considered from two perspectives. Firstly, uncertainties arising from rational transfer function fitting of frequency response function data. Secondly, uncertainties arising from physical sources, such as manufacturing tolerances, damage and degradation. In both cases, the uncertainties were shown to propagate to the open- and closed-loop poles, thus causing variable natural frequencies, damping ratios and mode shapes. The effect of uncertainty in the poles was visualised in the complex plane as pole clustering. This is where the poles are distributed in clusters that are centred on nominal points that correspond to the eigenvalues of the deterministic system. The variability in the pole clusters was quantified in two ways: (i) using sensitivities to evaluate the worst-case deviation from the nominal points, and (ii) using a polynomial chaos expansion to determine the variance of the cluster in the direction of both the real and imaginary axes.

Although allowing one to assess the variability of the system's dynamic response, uncertainty quantification of the poles does not, explicitly, predict the variability of important aeroelastic variables, such as the flutter speed. However, in practice, it is the variability of the flutter speed that would likely be required in industry if uncertainty quantification techniques were to become widely used. Therefore, the earlier developed techniques need to be modified to address this problem. This is the subject of the present chapter.

In this work, the problem of uncertainty quantification in aeroservoelastic systems is reformulated. Alike before, the developed methods use receptance data, thus preserving the model-free superiority of such approaches. However, by contrast, the uncertainty is quantified by evaluating the likelihood of flutter arising at or below a given reference speed, which is chosen. The uncertainty is modelled as a stochastic structural modification, as in Chapter 7, and the characteristic equation of the modified system is obtained and expressed in terms of the uncertain parameters. When the modification matrix is rank-one and arises from a single mechanical element, a graphical method can be used to determine the parameter solutions that cause marginally stable modifications. These solutions are then used to define parameter intervals that correspond to stable and unstable modifications. The probability of flutter can then

be evaluated by integrating the probability density function of the uncertain parameter over the unstable regions. When the modification arises from more than one mechanical element, an alternative technique must be used since, in general, the modification matrix has a rank greater than one and hence the Sherman-Morrison formula cannot be used. This alternative technique projects the characteristic equation into the space of the uncertain parameters. A first-order reliability method is then used to estimate the probability of flutter.

The developed techniques are useful in that they have the potential to permit quantitative risk assessment (QRA) to be performed in real-time decision-making safety systems in future aircraft. Furthermore, they provide, for the first time, an experimental framework on which to perform uncertainty quantification in aeroservoelastic systems using receptance data. This is done without the need for a very large data set, as would be required for conventional techniques such as Monte Carlo simulation.

The remainder of this chapter is structured as follows. Firstly, the equations of motion describing the aeroservoelastic system with a stochastic structural modification are described and the problem of uncertainty quantification is formulated. Following this, a graphical solution method is illustrated for systems with a single-element, rank-one modification. Next, the theory describing the more general case of multiple-element, multiple-rank modifications is considered and a solution strategy based on the projection method is described. Finally, the techniques are tested on the reference numerical model before then being applied experimentally in the form of two case studies.

8.2 Problem Formulation

Consider again the frequency-domain equation of motion of the closed-loop aeroservoelastic system, which is expressed in matrix form as

$$\mathbf{Z}(s,v)\mathbf{y}(s) = \mathbf{B}_{\mathrm{CS}\to\mathrm{F}}(s,v)\left(s\mathbf{F}^T + \mathbf{G}^T\right)\mathbf{y}(s), \tag{8.1}$$

or equivalently,

$$\left(\mathbf{Z}(s,v) - \mathbf{B}_{\mathrm{CS}\to\mathrm{F}}(s,v)\left(s\mathbf{F}^T + \mathbf{G}^T\right)\right)\mathbf{y}(s) = \mathbf{0}. \tag{8.2}$$

For simplicity, the open-loop dynamic stiffness matrix and the control modification term are joined together as a single, effective dynamic stiffness, so that

$$\check{\mathbf{Z}}(s,v)\mathbf{y}(s) = \mathbf{0}, \tag{8.3}$$

where

$$\check{\mathbf{Z}}(s,v) = \mathbf{Z}(s,v) - \mathbf{B}_{\mathrm{CS}\to\mathrm{F}}(s,v)\left(s\mathbf{F}^T + \mathbf{G}^T\right). \tag{8.4}$$

In this way, the analysis presented hereinafter is universal for both open-loop and closed-loop systems.

As in Chapter 7, the dynamic stiffness matrix is considered uncertain and is dependent on a vector $\boldsymbol{\theta} \in \mathbb{R}^p$ of p random variables. Therefore, Eq. 8.3 is written as

$$\check{\mathbf{Z}}(s,v,\boldsymbol{\theta})\mathbf{y}(s) = \mathbf{0}. \tag{8.5}$$

Using the same procedure as in §7.2, the effect of the uncertainty may be considered as a

stochastic structural modification to a measured receptance matrix, so that

$$\left(\mathbf{I} + \check{\mathbf{H}}_m(s,v)\Delta\mathbf{Z}_r(s,\boldsymbol{\theta})\right)\mathbf{y}(s) = \mathbf{0}, \tag{8.6}$$

where

$$\check{\mathbf{H}}_m(s,v) = \check{\mathbf{Z}}(s,v,\hat{\boldsymbol{\theta}})^{-1}. \tag{8.7}$$

As before, $\hat{\boldsymbol{\theta}}$ is the sample vector belonging to the random parameters in the measured system and it is assumed again here that this term is immeasurable. However, for the sake of simplicity and without loss of generality, the analysis continues using the vector of random parameters $\boldsymbol{\theta}$ rather than the modified vector accounting for uncertainty in the sample vector[1]. The characteristic equation of the closed-loop system with a stochastic structural modification is

$$\det\left(\mathbf{I} + \check{\mathbf{H}}_m(s,v)\Delta\mathbf{Z}_r(s,\boldsymbol{\theta})\right) = 0. \tag{8.8}$$

Suppose that the receptance matrix belonging to a single aeroservoelastic system is measured at some chosen reference freestream speed v_{ref}. Also, suppose that the system is initially stable at this reference speed; that is, all poles lie in the left hand side of the complex plane. The aim of this work is to consider whether it is possible for some modification, contained in $\Delta\mathbf{Z}_r(s,\boldsymbol{\theta})$, to render the system unstable and hence enter flutter at v_{ref}. Moreover, if the probability distribution of the random vector is known, to evaluate the probability of such an event occurring.

In the following sections, the analysis is broken down into two situations. First, the case of a single-parameter modification is considered for simple situations where the structural modification matrix is rank-one. Following this, the more general case of a multiple-parameter, multiple-rank modification is considered.

8.3 Single-Element, Rank-One Modifications

First, the case of a single-element ($p = 1$), rank-one modification is considered. Let the structural modification term $\Delta\mathbf{Z}_r(s,\theta)$ be expressed in the form

$$\Delta\mathbf{Z}_r(s,\theta) = z_r(s,\theta)\mathbf{e}\mathbf{e}^T, \tag{8.9}$$

where $z_r(s,\theta) \in \mathbb{C}$ is the scalar dynamic stiffness of the modification element, and $\mathbf{e} \in \mathbb{R}^n$ is a vector with unit entries corresponding to the coordinates of the modification [99]. The scalar dynamic stiffness term may be written as

$$z_r(s,\theta) = \theta g(s), \tag{8.10}$$

where $g(s)$ is some function of the complex Laplace variable. For example, a damper modification is written as

$$z_r(s,c) = c \times s, \tag{8.11}$$

By substituting Eq. 8.9 into Eq. 8.8, the characteristic equation at the reference speed v_{ref} is given by

$$\det\left(\mathbf{I} + \check{\mathbf{H}}_m(s,v_{\text{ref}})z_r(s,\theta)\mathbf{e}\mathbf{e}^T\right) = 0, \tag{8.12}$$

[1] One may account for this uncertainty using the same procedure given in Chapter 7

or equivalently, by definition of Eq. 8.10,

$$\det\left(\mathbf{I}+\check{\mathbf{H}}_m(s,v_{\text{ref}})\theta g(s)\mathbf{e}\mathbf{e}^T\right)=0. \tag{8.13}$$

By definition of the receptance matrix, Eq. 8.13 may be written as

$$\det\left(\check{\mathbf{H}}_m(s,v_{\text{ref}})\right)\det\left(\check{\mathbf{Z}}(s,v_{\text{ref}},\hat{\boldsymbol{\theta}})+\theta g(s)\mathbf{e}\mathbf{e}^T\right)=0. \tag{8.14}$$

Using the matrix determinant lemma [144],

$$\det\left(\check{\mathbf{H}}_m(s,v_{\text{ref}})\right)\det\left(\check{\mathbf{Z}}(s,v_{\text{ref}},\hat{\boldsymbol{\theta}})\right)\left(1+\theta g(s)(s,\theta)\mathbf{e}^T\check{\mathbf{H}}_m(s,v_{\text{ref}})\mathbf{e}\right)=0, \tag{8.15}$$

and thus, since

$$\det\left(\check{\mathbf{H}}_m(s,v_{\text{ref}})\right)\det\left(\check{\mathbf{Z}}(s,v_{\text{ref}},\hat{\boldsymbol{\theta}})\right)=\det\left(\check{\mathbf{H}}_m(s,v_{\text{ref}})\check{\mathbf{Z}}(s,v_{\text{ref}},\hat{\boldsymbol{\theta}})\right)=\det\left(\mathbf{I}\right)=1, \tag{8.16}$$

the characteristic equation is simplified to

$$1+\theta g(s)\mathbf{e}^T\check{\mathbf{H}}_m(s,v_{\text{ref}})\mathbf{e}=0. \tag{8.17}$$

Eq. 8.17 represents the characteristic equation of the system with a stochastic structural modification. The form given is advantageous as it is expressed, linearly, in terms of the random mechanical element. This simplification allows the analysis of flutter speed uncertainty to be performed in a straightforward manner.

8.3.1 Marginally Stable Modifications

Consider the case where the modification causes the flutter speed v^* to be at the reference speed v_{ref}. By definition of the flutter speed, one or more poles lie precisely on the imaginary axis and thus there is an eigenvalue solution $s=i\omega^*$ that satisfies

$$1+\theta g(i\omega^*)\mathbf{e}^T\check{\mathbf{H}}_m(i\omega^*,v_{\text{ref}})\mathbf{e}=0, \tag{8.18}$$

where ω^* is the flutter frequency. By rearranging, the modification parameter that causes one or more marginally stable poles is

$$\theta=-\frac{1}{g(i\omega^*)\mathbf{e}^T\check{\mathbf{H}}_m(i\omega^*,v_{\text{ref}})\mathbf{e}}. \tag{8.19}$$

Eq. 8.19 is unsolvable on initial inspection due to the unknown flutter frequency ω^*. However, this may be resolved by considering the physicality of the parameter solutions. By definition, each random parameter is real. Therefore, since receptances are generally complex, it must be enforced that only values of ω^* that yield a real solution are valid. That is, the frequency must be chosen to satisfy

$$\text{Im}\left(g(i\omega^*)\mathbf{e}^T\check{\mathbf{H}}_m(i\omega^*,v_{\text{ref}})\mathbf{e}\right)=0. \tag{8.20}$$

8.3.2 Probability of Flutter

The solutions to Eq. 8.19 correspond to the parameters that cause the flutter speed to lie exactly at v_{ref}. On its own, this does not give the set of parameters that lead to flutter since it

may be the case that $v^* < v_{\text{ref}}$ and hence flutter is still observed at v_{ref}. Despite this, however, one may use these solutions in order to determine all flutter yielding parameters solutions (i.e. $v^* \leq v_{\text{ref}}$).

Let the solutions to Eq. 8.19 be denoted $\theta_1^*, \theta_2^*, \ldots, \theta_m^*$, where $\theta_1^* < \theta_2^* < \cdots < \theta_m^*$ and $m \geq 1$ is the total number of solutions. These solutions divide the real numbers into intervals given by

$$(-\infty, \theta_1^*], [\theta_1^*, \theta_2^*], [\theta_2^*, \theta_3^*], \ldots, [\theta_{m-1}^*, \theta_m^*], [\theta_m^*, \infty). \tag{8.21}$$

In the analysis that follows, the notation $\mathbb{P}_j$ refers to the interval

$$\mathbb{P}_j = \begin{cases} [\theta_j^*, \theta_{j+1}^*], & 0 < j < m, \\ (-\infty, \theta_1^*], & j = 0, \\ [\theta_m^*, \infty), & j = m. \end{cases} \tag{8.22}$$

This is illustrated diagrammatically in Fig. 8.1 for the case of three parameter solutions.

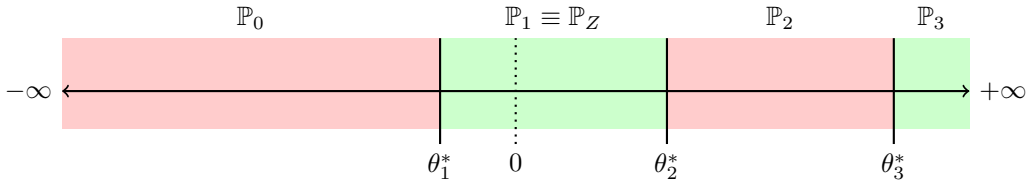

Figure 8.1: Single-element, rank-one parameter intervals. (Green = stable modifications, red = unstable modifications)

Let the interval that contains 0 be denoted $\mathbb{P}_Z$. Since this interval corresponds to the unmodified system, which is stable, all parameters in $\mathbb{P}_Z$ lead to a stable modification and hence no flutter. Since the boundaries of the interval $\mathbb{P}_Z$ correspond to solutions that yield marginally stable modifications, one can conclude that the neighbouring intervals yield unstable modifications. In other words, $\mathbb{P}_{Z\pm1}$ are intervals that correspond to flutter. Extending this further leads to the conclusion that:

1. $\ldots$,$\mathbb{P}_{Z-2}$,$\mathbb{P}_Z$,$\mathbb{P}_{Z+2}$,$\ldots$ are intervals that give *stable* modifications and hence no flutter.

2. $\ldots$,$\mathbb{P}_{Z-1}$,$\mathbb{P}_{Z+1}$,$\ldots$ are intervals that give *unstable* modifications and hence exhibit flutter.

In other words, the regions alternate consecutively between stable and unstable modifications.

Defining the above intervals allows the probability of flutter at v_{ref} to be found. Let the probability density function of the random parameter be denoted $f(\theta)$. Using the above, the probability of flutter is given by

$$P(v^* \leq v_{\text{ref}}) = \sum_{\mathbb{P}_j = \ldots, \mathbb{P}_{Z-1}, \mathbb{P}_{Z+1}, \ldots} \left(\int_{\mathbb{P}_j} f(\theta) d\theta \right). \tag{8.23}$$

In the above analysis, it is assumed that the parameter solutions $\theta_1^*, \theta_2^*, \ldots, \theta_m^*$ all have multiplicity one. However, if the multiplicity of any of the solutions is greater than one, this means that the stable-unstable switching behaviour discussed above may not necessarily hold true. For example, a solution with a multiplicity of two will have connecting intervals that are both stable or both unstable and thus this affects the integration region in Eq. 8.23. However, such situations are not considered in the remainder of this work.

8.4 Multiple-Element, Multiple-Rank Modifications

Next, the more general case of a multiple-element, multiple-rank modification is considered. Unlike before, one cannot employ a simplistic linear analysis since the modification matrix cannot be expressed in the form given in Eq. 8.9. Therefore, an alternative approach is considered.

In the proceeding sections, the multiple-element modification analysis is broken down into two situations. The first considers modifications that are simple mechanical elements, i.e. mass, stiffness and damping modifications. These modifications are simple to analyse since they are linear with respect to the random parameter. Furthermore, the effect of each parameter, considered alone, is a rank-one modification to the measured receptance matrix. The second case considers more complex modifications where the modifications are nonlinear with respect to the random parameter and each parameter, again considered alone, is not necessarily rank-one.

Case 1: Modifications that are linear in the random parameters

Suppose that the structural modification term $\Delta\mathbf{Z}_r(s,\boldsymbol{\theta})$ is comprised of p random variables, which are mass, stiffness and damping parameters. In general, the modification is rank-m $(1 \leq m \leq n)$, where n is the number of degrees-of-freedom of the system. However, it may be decomposed as the sum of p rank-one elements, so that

$$\Delta\mathbf{Z}_r(s,\boldsymbol{\theta}) = \sum_{i=1}^{p} \theta_i g_i(s)\mathbf{e}_i\mathbf{e}_i^T. \tag{8.24}$$

By defining

$$\mathbf{A}_k = \check{\mathbf{Z}}(s, v_{\text{ref}}, \hat{\boldsymbol{\theta}}) + \sum_{i=1}^{k-1} \theta_i g_i(s)\mathbf{e}_i\mathbf{e}_i^T, \tag{8.25}$$

the receptance matrix corresponding to the system with a stochastic structural modification is

$$\hat{\mathbf{H}}(s, v_{\text{ref}}, \boldsymbol{\theta}) = \left(\check{\mathbf{Z}}(s, v_{\text{ref}}, \hat{\boldsymbol{\theta}}) + \sum_{i=1}^{p} \theta_i g_i(s)\mathbf{e}_i\mathbf{e}_i^T\right)^{-1} = \left(\mathbf{A}_p + \theta_p g_p(s)\mathbf{e}_p\mathbf{e}_p^T\right)^{-1}. \tag{8.26}$$

Using the Sherman-Morrison formula [145]

$$\hat{\mathbf{H}}(s, v, \boldsymbol{\theta}) = \mathbf{A}_p^{-1} - \frac{\theta_p g_p(s)\mathbf{A}_p^{-1}\mathbf{e}_p\mathbf{e}_p^T\mathbf{A}_p^{-1}}{1 + \theta_p g_p(s)\mathbf{e}_p^T\mathbf{A}_p^{-1}\mathbf{e}_p}, \tag{8.27}$$

and hence the characteristic equations of the modified system is given by

$$1 + \theta_p g_p(s)\mathbf{e}_p^T\mathbf{A}_p^{-1}\mathbf{e}_p = 0. \tag{8.28}$$

By definition of Eq. 8.25

$$\mathbf{A}_p^{-1} = \left(\mathbf{A}_{p-1} + \theta_{p-1} g_{p-1}(s)\mathbf{e}_{p-1}\mathbf{e}_{p-1}^T\right)^{-1}, \tag{8.29}$$

$$\mathbf{A}_{p-1}^{-1} = \left(\mathbf{A}_{p-2} + \theta_{p-2} g_{p-2}(s)\mathbf{e}_{p-2}\mathbf{e}_{p-2}^T\right)^{-1}, \tag{8.30}$$

$$\vdots$$

$$\mathbf{A}_2^{-1} = \left(\check{\mathbf{Z}}(s, v_{\text{ref}}, \hat{\boldsymbol{\theta}}) + \theta_1 g_1(s)\mathbf{e}_1\mathbf{e}_1^T\right)^{-1}, \tag{8.31}$$

and

$$\check{\mathbf{Z}}(s, v_{\text{ref}}, \hat{\boldsymbol{\theta}})^{-1} = \check{\mathbf{H}}_m(s, v_{\text{ref}}), \tag{8.32}$$

the Sherman-Morrison formula can be used in an iterative manner to find the characteristic equation of the modified system in terms of the random modification parameters and the receptances of the measured system.

Once the iterative approach has been applied, the general form of the characteristic equation is given by

$$1 + \sum_{i_1=1}^{p} \theta_{i_1} f_{i_1}(s, v) + \sum_{i_1=1}^{p} \sum_{i_2=1}^{p} \theta_{i_1}\theta_{i_2} f_{i_1,i_2}(s, v) + \cdots = 0, \tag{8.33}$$

where $f_{i_j}(s, v)$ are functions of the elements in the measured receptance matrix.

Case 2: Modifications that are nonlinear in the random parameters

In the above analysis it has been assumed that: (i) the modification matrix is linear in each parameter, so that $z_r(s, \theta_i) = \theta_i g_i(s)$; and (ii) the modification corresponding to each parameter can be expressed in rank-one form. These assumptions are valid for simple cases such as mass, stiffness or damping modifications. However, they are not necessarily true for more complex situations such as beam length modifications. Here, a more generalised analysis is given.

Let the modification matrix be decomposed as

$$\Delta\mathbf{Z}_r(s, \boldsymbol{\theta}) = \sum_{i=1}^{n} \sum_{j=1}^{n} z_{r_{ij}}(s, \boldsymbol{\theta}) \mathbf{u}_i \mathbf{v}_j^T, \tag{8.34}$$

where $z_{r_{ij}}(s, \boldsymbol{\theta})$ is the ij^{th} element of the modification matrix and $\mathbf{u}_i$ and $\mathbf{v}_j$ are vectors with unit entries corresponding to the i and j positions of the element in the modification matrix, respectively. Alike case one, the dynamic stiffness matrix of each element can be separated as

$$z_{r_{ij}}(s, \boldsymbol{\theta}) = l_{ij}(\boldsymbol{\theta}) g_{ij}(s), \tag{8.35}$$

noting now the use of the nonlinear function $l_{ij}(\boldsymbol{\theta})$ of the random parameters. Using Eq. 8.35 in Eq. 8.34 gives that

$$\Delta\mathbf{Z}_r(s, \boldsymbol{\theta}) = \sum_{i=1}^{n} \sum_{j=1}^{n} l_{ij}(\boldsymbol{\theta}) g_{ij}(s) \mathbf{u}_i \mathbf{v}_j^T, \tag{8.36}$$

and therefore the matrix is expressed as the sum of rank-one modifications using the dyadic product $\mathbf{u}_i\mathbf{v}_j^T$. One can now continue, as before, using the Sherman-Morrison formula in an iterative fashion, noting that the final characteristic equation will be of the form

$$1 + \sum_{i_1=1}^{n} \sum_{j_1=1}^{n} l_{i_1 j_1}(\boldsymbol{\theta}) f_{i_1,j_1}(s, v) + \sum_{i_1=1}^{n} \sum_{j_1=1}^{n} \sum_{i_2=1}^{n} \sum_{j_2=1}^{n} l_{i_1 j_1}(\boldsymbol{\theta}) l_{i_2 j_2}(\boldsymbol{\theta}) f_{i_1,j_1,i_2,j_2}(s, v) + \cdots = 0, \tag{8.37}$$

where $f_{i_j}(s, v)$ are again functions of the elements in the measured receptance matrix. One can see the equivalence between the characteristic equations in case one and two. They both lead to a similar form, except that the random parameters arise in nonlinear combinations in the second case, as one would expect.

8.4.1 Marginally Stable Modifications

For the sake of simplicity, the analysis presented hereinafter concentrates on modifications that are linear in the random parameters (i.e. case 1). However, it is to be noted that the analysis for the other case follows the same process and the results ultimately lead to a very similar form.

Consider again the characteristic equation of the modified system. At the flutter speed, $v^* = v_{\text{ref}}$, one or more poles lie on the imaginary axis and thus the characteristic equation must satisfy

$$L(\theta_1, \theta_2, \ldots, \theta_p, \omega^*, v_{\text{ref}}) = 1 + \sum_{i_1=1}^{p} \theta_{i_1} f_{i_1}(i\omega^*, v_{\text{ref}}) + \sum_{i_1=1}^{p} \sum_{i_2=1}^{p} \theta_{i_1}\theta_{i_2} f_{i_1,i_2}(i\omega^*, v_{\text{ref}}) + \cdots = 0, \tag{8.38}$$

where ω^* is the, initially unknown, flutter frequency. This form of the characteristic equation is referred to as the non-standardised limit-state function hereinafter and is geometrically equivalent to a hypersurface in the $\theta_1, \theta_2, \ldots, \theta_p, \omega^*$ space at each reference speed.

Up until this point, the probability distributions of each random variable, and hence the joint distribution of all variables, have been treated as arbitrary. However, to make the technique universal, it is now necessary to manipulate the random variables into a standardised form. Let a new set of standardised random variables be defined as

$$\begin{pmatrix} \hat{\theta}_1 \\ \hat{\theta}_2 \\ \vdots \\ \hat{\theta}_p \end{pmatrix} = \begin{pmatrix} \Phi^{-1}\left(F_1(\theta_1)\right) \\ \Phi^{-1}\left(F_{2|1}(\theta_2|\theta_1)\right) \\ \vdots \\ \Phi^{-1}\left(F_{p|p-1,\ldots,1}(\theta_p|\theta_{p-1}, \ldots, \theta_1)\right) \end{pmatrix}, \tag{8.39}$$

and

$$\begin{pmatrix} \theta_1 \\ \theta_2 \\ \vdots \\ \theta_p \end{pmatrix} = \begin{pmatrix} F_1^{-1}\left(\Phi(\hat{\theta}_1)\right) \\ F_{2|1}^{-1}\left(\Phi(\hat{\theta}_2)|\theta_1\right)\right) \\ \vdots \\ F_{p|p-1,\ldots,1}^{-1}\left(\Phi(\hat{\theta}_p)|\theta_{p-1}, \ldots, \theta_1\right)\right) \end{pmatrix}, \tag{8.40}$$

where $\hat{\theta}_i$ is the standardised random parameter of θ_i; Φ and Φ^{-1} is the forward and inverse unit variance, zero mean Gaussian cumulative distribution function; and $F_{p|p-1,\ldots,1}$ and $F_{p|p-1,\ldots,1}^{-1}$ are the forward and inverse cumulative distribution functions of the conditional random variable $\theta_p|\theta_{p-1}, \ldots, \theta_1$. This transformation is known as the Rosenblatt transform [81] and serves to standardise the random parameters so that they are each independent Gaussian with a zero mean and unit variance. Using Eq. 8.40 in Eq. 8.38 allows the limit-state function to be expressed in terms of the standardised variables and is hence referred to as the 'standardised limit-state function', i.e. $L(\hat{\theta}_1, \hat{\theta}_2, \ldots, \hat{\theta}_p, \omega^*, v_{\text{ref}})$.

The standardised limit-state function gives the combinations of random parameters, at each frequency ω^*, that cause the system to become marginally stable at v_{ref}. As in the case of single-rank modifications, the receptances are generally complex and therefore the parameter solutions according to the limit-state function are also complex. Therefore, for physically meaningful solutions, one must enforce the constraint that the modification parameters are real.

8.4.2 Probability of Flutter

Let the standardised limit-state function $L(\hat{\theta}_1, \hat{\theta}_2, \ldots, \hat{\theta}_p, \omega^*, v_{\text{ref}})$ be projected into the $\hat{\theta}_1$,$\hat{\theta}_2$,...,$\hat{\theta}_p$ space and the resulting curve be denoted the projected, standardised limit-state function $\bar{L}(\hat{\theta}_1, \hat{\theta}_2, \ldots, \hat{\theta}_p)$. The projection creates a boundary in the standardised parameter space that divides it into two regions. The region encompassing the origin is denoted $\mathbb{S}$ and the other region is denoted $\mathbb{U}$. Region $\mathbb{S}$ corresponds to parameter modifications, in the standardised space, that keep the system stable. Region $\mathbb{U}$, on the other hand, corresponds to parameter solutions that render the system unstable and hence enter flutter. The above points are illustrated diagrammatically in Fig. 8.2 for the case of two random parameters.

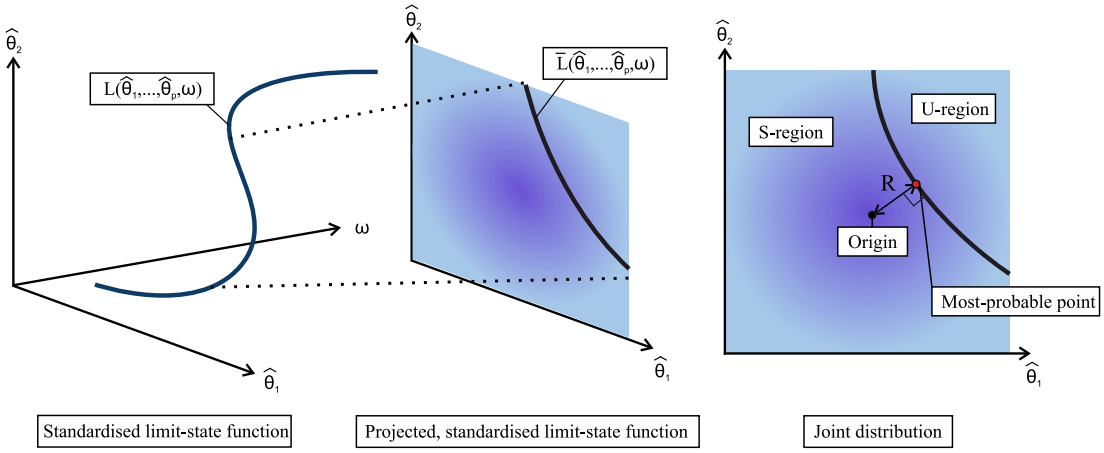

Figure 8.2: Illustration of the limit-state function for two random parameters.

The probability of flutter is found simply by integrating the joint probability density function of the standardised random parameters over the region $\mathbb{U}$. Written mathematically,

$$P(v^* \leq v_{\text{ref}}) = \int \int \cdots \int_{\mathbb{U}} f(\hat{\theta}_1, \hat{\theta}_2, \ldots, \hat{\theta}_p) d\hat{\theta}_1 d\hat{\theta}_2 \ldots d\hat{\theta}_p, \tag{8.41}$$

where $f(\hat{\theta}_1, \hat{\theta}_2, \ldots, \hat{\theta}_p)$ is the joint distribution of the standardised random parameters, which corresponds to a p-multivariate, zero mean, unit variance Gaussian distribution.

8.4.3 First-Order Reliability Method Estimation

In practice, evaluating the probability of flutter directly from Eq. 8.41 is cumbersome. Firstly, the boundary of the region $\mathbb{U}$ may be complex and may not lend itself well to analytical methods. Secondly, a large number of modification parameters in the limit-state function may lead to large computational times if conventional numerical methods, such as Monte-Carlo simulation (MCS), are used. Therefore, in this work, an alternative method is applied; the probability of flutter is estimated using a first-order reliability method.

Let the most probable point (MPP) be defined as the point $\hat{\theta}^* = \left(\hat{\theta}_1^*, \hat{\theta}_2^*, \ldots, \hat{\theta}_p^*\right)^T$ on the projected limit-state function that minimises the function

$$R = \sqrt{\hat{\theta}_1^2 + \hat{\theta}_2^2 + \cdots + \hat{\theta}_p^2}. \tag{8.42}$$

By definition, the tangent to the projected limit-state function at the MPP is perpendicular to the line connecting the MPP to the origin. If the projected limit-state function is well approximated by the tangent, i.e. the function is approximately linear in the standardised

parameters, then the probability of flutter can be approximated by

$$P(v^* \leq v_{\text{ref}}) \approx 1 - \Phi(R^*), \tag{8.43}$$

where Φ is again the cumulative distribution function of the zero mean, unit variance Gaussian; and R^* is the Euclidean distance of between the origin and the MPP.

The first-order reliability method provides a quick and efficient method to estimate the probability of flutter at the reference speed. However, it is important to point out two limiting factors. Firstly, it is usually necessary to obtain the most probable point using optimisation techniques and thus there is a computational cost associated with this. Secondly, there is no general assurance that the projected limit-state function is well approximated by the tangent at the MPP. Indeed, if the curve is highly nonlinear, the technique may over- or underestimate the integral in Eq. 8.41 thus yielding an erroneous estimate of the probability of flutter. It is noted in passing here that second- or higher-order reliability methods [93] may be suitable in such cases. This is left as an area of future work.

8.5 Numerical Examples

In this section, the techniques developed above are tested on the reference numerical aeroservoelastic model. The case of no controller is considered; that is, the control gains $\mathbf{F}$ and $\mathbf{G}$ are set to zero and the flutter speed is taken as the open-loop value, which is 11.3 m/s. Throughout all examples, the probability of flutter is assessed at the freestream speed of 9.6 m/s. This represents a 15% margin from the nominal value and matches that of the current FAA regulations [7].

8.5.1 Single-Rank, Single-Element Modification

First, a single-rank, single-element modification is considered. Suppose that the stiffness of the plunge spring is uncertain. The scalar modification term is written as

$$z_r(s, \tilde{k}_h) = \tilde{k}_h,$$

and hence the stiffness required to render a marginally stable modification is given by

$$\tilde{k}_h = -\frac{1}{\mathbf{e}^T \check{\mathbf{H}}_m(i\omega^*, v_{\text{ref}})\mathbf{e}}.$$

Since the plunge stiffness modification acts at the plunge coordinate,

$$\mathbf{e}^T = \begin{pmatrix} 1 & 0 \end{pmatrix},$$

and thus

$$\tilde{k}_h = -\frac{1}{h_{11}(i\omega^*, v_{\text{ref}})}. \tag{8.44}$$

Figure 8.3 shows the Bode plot of the receptance h_{11} at the reference speed $v_{\text{ref}} = 9.6$ m/s. In order to satisfy the zero imaginary part condition of Eq. 8.20, only parameter solutions at $\omega^* = 0.000, 1.616, 1.887$ Hz are valid. The parameter solutions corresponding to these frequencies, according to Eq. 8.44, are -2844, -2646 and -641 N/m, respectively. The solution at -641 N/m is the first stiffness modification value that would cause the system to transition from stable to

marginally stable. The system is then unstable for modifications between this value and the modification corresponding to -2646 N/m. Between -2646 and -2844 N/m, the system is again stable. It is interesting to note that the solution corresponding to -2844 N/m is identically equal to the plunge stiffness. Of course, this is physically meaningful as removing the spring completely in the plunge degree-of-freedom would cause the system to become unstable. In real life applications, one could not have a modification below this final solution and therefore such situations are dropped hereinafter.

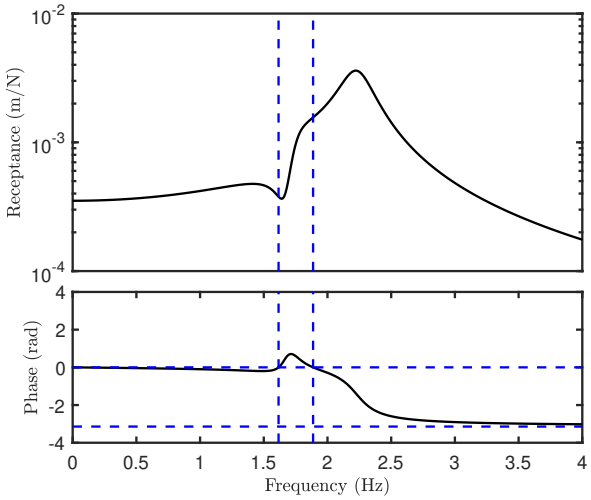

Figure 8.3: Bode plot of h_{11} at 9.6 m/s.

Figure 8.4 shows the root locus of the system as the modification stiffness is changed. The black line shows the numerically computed poles between stiffness modifications of -2844 and 2844 N/m. The red points correspond to the marginally stable poles predicted by the method. As shown, the predicted poles identically match the crossing points of the computed poles with the imaginary axis.

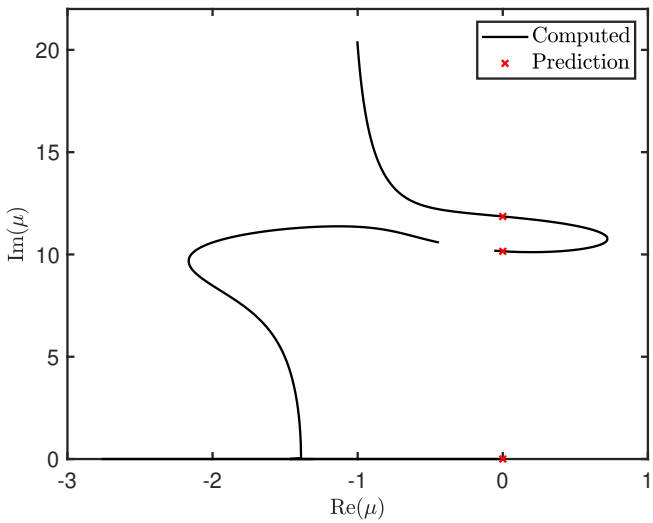

Figure 8.4: Root locus with respect to the modification stiffness.

Figures 8.5 (a) and (b) show the FRFs corresponding to h_{11} but now with the -641 N/m and -2646 N/m modifications added. As shown, the peak in the modified FRFs now arises at the predicted modification frequency in both cases. Furthermore, the peaks indicate that

the damping is incredibly small, thus indicating that a pole pair lies at, or very close to, the imaginary axis.

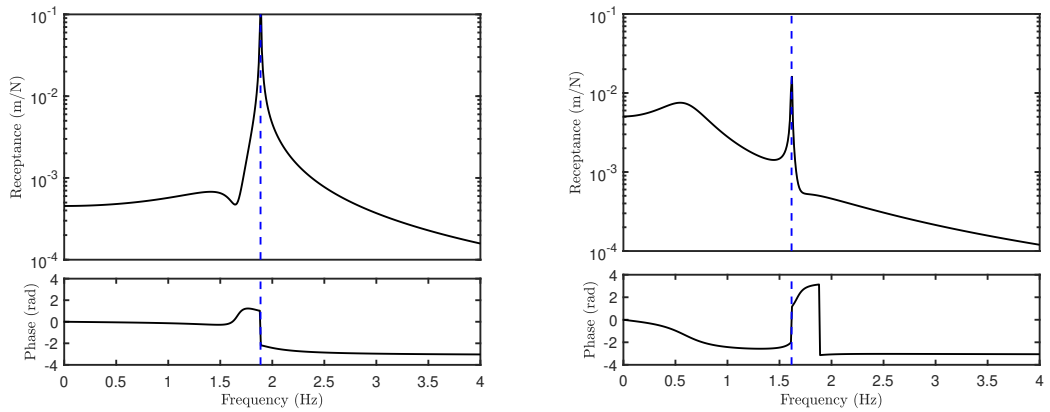

(a) -641 N/m modification.

(b) -2646 N/m modification.

Figure 8.5: FRF at h_{11} with modifications added.

To verify the parameter solutions, the modifications were added to the numerical model and the eigenvalues of the system were computed. Table 8.1 gives the original poles and the poles at the two feasible parameter solutions. As shown, the real part of one pole pair lies very close to zero at the modification, thus validating the solutions.

Table 8.1: Poles at each modification.

$\tilde{k}_h$ (N/m)	$\lambda_{1,2}$	$\lambda_{3,4}$
0	-0.6197 ± 10.90i	-0.8230 ± 14.01i
-641	-1.4438 ± 11.28i	-0.0010 ± 11.86i
-2646	-1.4437 ± 3.7089i	-0.0010 ± 10.16i

The parameter solutions given above allow one to define the stable and unstable parameter regions as

$$\begin{aligned}\mathbb{P}_0 &= [-2844, -2646],\\ \mathbb{P}_1 &= [-2646, -641],\\ \mathbb{P}_2 &= [-641, \infty).\end{aligned}$$

Since $\mathbb{P}_2$ contains zero, $\mathbb{P}_Z = \mathbb{P}_2$ and therefore the probability of flutter at the reference speed is given by

$$P(v^* \leq v_{\text{ref}}) = \int_{-2646}^{-641} f(\tilde{k}_h) d\tilde{k}_h,$$

where $f(\tilde{k}_h)$ is the probability density function of the stiffness modification $\tilde{k}_h$.

8.5.2 Multiple-Rank, Multiple-Element Modification

Next, a multiple-element, multiple-rank modification is considered. The modification is to the plunge mass and the pitch stiffness, so that

$$\Delta\mathbf{Z}_r(s, \tilde{M}, \tilde{k}_\alpha) = \tilde{M}s^2\mathbf{e}_1\mathbf{e}_1^T + \tilde{k}_\alpha\mathbf{e}_2\mathbf{e}_2^T,$$

where

$$\mathbf{e}_1^T = \begin{pmatrix} 1 & 0 \end{pmatrix},$$
$$\mathbf{e}_2^T = \begin{pmatrix} 0 & 1 \end{pmatrix}.$$

Throughout this example, the modification parameters are Gaussian with mean and standard deviation as given in Table 8.2.

Table 8.2: Random modification parameters.

Parameter	Mean	Standard Deviation
$\tilde{M}$	0	3 kg
$\tilde{k}_\alpha$	0	1 N m rad^{-1}

Using the Sherman-Morrison formula iteratively, the characteristic equation of the modified system is given by

$$1 + h_{11}(s)\tilde{M}_h s^2 + h_{22}(s)\tilde{k}_\alpha + \tilde{m}_h\tilde{k}_\alpha s^2 \left(h_{11}(s)h_{22}(s) - h_{12}(s)h_{21}(s)\right) = 0.$$

Therefore, the non-standardised limit-state function is written as

$$L = 1 - h_{11}(i\omega)\tilde{M}_h\omega^2 + h_{22}(i\omega)\tilde{k}_\alpha - \tilde{m}_h\tilde{k}_\alpha\omega^2 \left(h_{11}(i\omega)h_{22}(i\omega) - h_{12}(i\omega)h_{21}(i\omega)\right).$$

As the parameters are Gaussian and zero mean, they can be easily standardised using the formulae

$$\hat{M}_h = \frac{\tilde{M}_h}{\sqrt{\mathrm{Var}[\tilde{M}_h]}},$$
$$\hat{k}_\alpha = \frac{\tilde{k}_\alpha}{\sqrt{\mathrm{Var}[\tilde{k}_\alpha]}}.$$

Therefore, the standardised limit-state function is given by

$$L = 1 - h_{11}\sqrt{\mathrm{Var}[\tilde{M}_h]}\hat{M}_h\omega^2 + h_{22}\sqrt{\mathrm{Var}[\tilde{k}_\alpha]}\hat{k}_\alpha - \sqrt{\mathrm{Var}[\tilde{M}_h]\mathrm{Var}[\tilde{k}_\alpha]}\hat{M}_h\hat{k}_\alpha\left(h_{11}h_{22} - h_{12}h_{21}\right)\omega^2.$$

where the receptances $h_{11}, h_{12}, h_{21}, h_{22}$ are evaluated at $s = i\omega$.

Using MATLAB's *fminsearch* algorithm, the MPP was found by means of numerical optimisation at $(1.4783, 0.2392)^T$ from a starting position of $(2, 0.4)^T$ in a time of 0.17 seconds on a standard desktop computer. The corresponding R value at this MPP is 1.49. Therefore, the probability of flutter is calculated as

$$P(v^* \leq v_{\mathrm{ref}}) = 1 - \Phi(1.49) = 0.0681.$$

Figure 8.6 shows the projection of the limit-state function in the standardised parameter space. The white point corresponds to the MPP calculated above and, as shown, lies on the projected limit-state function at the point closest to the origin, as expected. The projected function has a slight convex curve. However, it is likely well approximated as linear and thus the first order reliability method is predicted to give a reasonable answer.

The results from the first order reliability method were verified using Monte Carlo simula-

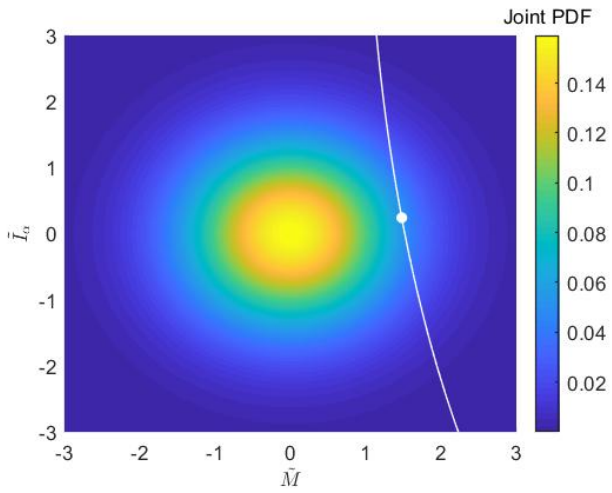

Figure 8.6: Projected, standardised limit-state function (numerical).

tion. Using 1,000,000 samples, the probability of flutter was calculated numerically as 0.0653. This is a 4% difference from the first-order method and thus one can conclude that the first order reliability method gives a good degree of accuracy. An interesting point to consider is that the MCS result is slightly lower than the value predicted by the first-order method. This is to be expected since the projected limit state function curves in a direction away from the origin. Therefore, the unstable region estimated by the tangent at the MPP is larger than its true value.

8.6 Experimental Case Study

The techniques were also tested and verified on the experimental aeroservoelastic system that is described in §4.3. All tests were conducted on the open-loop system; that is, with both control surfaces inactive and set to a zero-deflection angle. The flutter speed of the open-loop system is 14.0 m/s[2]. Throughout all the following examples, the modification is taken at a freestream speed of 12.4 m/s.

8.6.1 Receptance Measurements

The examples that follow utilise FRFs in the wind-off condition (0 m/s) and at the modification speed (12.4 m/s). Therefore, these were measured experimentally by means of stepped-sine testing, using an electromechanical shaker. The shaker was connected to the structure at the location of the front and rear laser sensors using a stinger and a load cell. The stinger was made of stainless steel and was 1 mm in diameter. This was to minimise the effect of any additional pitch stiffness added to the system by attachment of the stinger. This setup is shown in Fig. 8.7. An LMS data acquisition setup was used to process the data from the laser sensors and produce the FRFs. All tests were conducted between frequencies of 2 to 7 Hz. This range allowed sufficient identification of the two modes in the system.

[2]This experimental case study was completed before the Covid pandemic. Since then, the experimental model has been re-setup and consequently the flutter speed does not identically match that stated in Chapter 4.

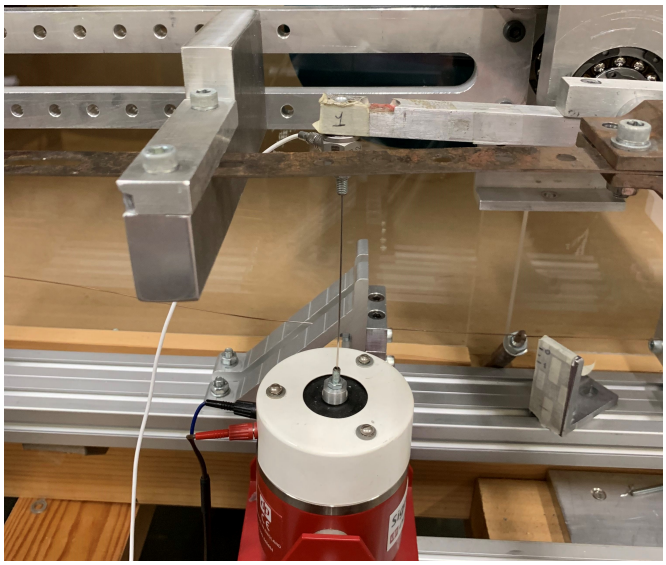

Figure 8.7: Experimental setup for stepped-sine testing.

The measured receptances throughout all the following examples are of the form

$$\mathbf{H}_m(s,v) = \begin{pmatrix} h_{11}(s,v) & h_{12}(s,v) \\ h_{21}(s,v) & h_{22}(s,v) \end{pmatrix}.$$

8.6.2 Single-Element, Rank-One Modification

First, a single-element, rank-one modification was considered. The modification consisted of the addition of a 1 kg mass to a bar protruding out from the elastic axis, as shown in Fig. 8.8. The position of the mass on the bar matches identically the distance between the trailing-edge laser sensor and the elastic axis. In this way, the modification is collocated with the trailing-edge laser sensor.

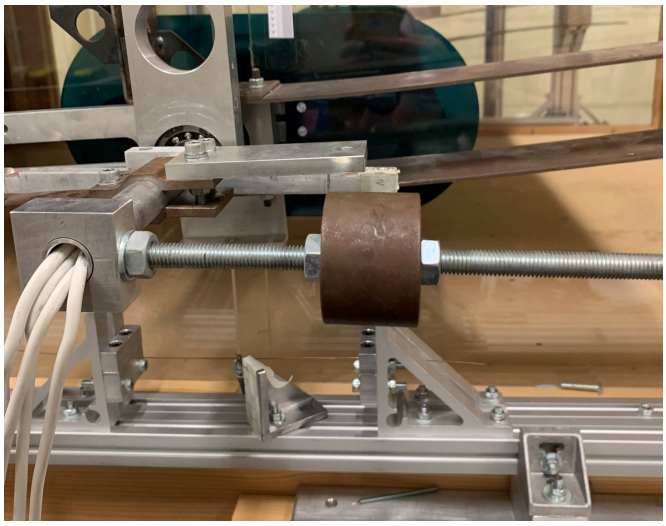

Figure 8.8: Collocated mass modification.

Modification Model

The matrix corresponding to the rank-one modification is given by

$$\Delta \mathbf{Z}_r(s, \boldsymbol{\theta}) = \begin{pmatrix} 0 & 0 \\ 0 & ms^2 \end{pmatrix},$$

or equivalently, in rank-one form,

$$\Delta \mathbf{Z}_r(s, \boldsymbol{\theta}) = ms^2 \begin{pmatrix} 0 \\ 1 \end{pmatrix} \begin{pmatrix} 0 & 1 \end{pmatrix}.$$

Using the Sherman-Morrison formula, the receptance matrix corresponding to the modified system is given by

$$\hat{h}_{22}(s, v) = h_{22}(s, v) - \frac{ms^2 h_{22}(s, v)^2}{1 + ms^2 h_{22}(s, v)},$$

where $\hat{h}(s)$ is the receptance of the modified system and $h(s)$ is the original receptance, before modification.

In order to test the model of the modification, FRFs were collected from the system with and without the modification, both with no wind (i.e. $v = 0$ m/s). Figure 8.9 shows these frequency response functions together with the numerically predicted FRF using the above formula. As shown, there is a good agreement across the frequencies tested in terms of both amplitude and phase. Therefore, one can conclude that the model is sufficient to describe the modification to the system.

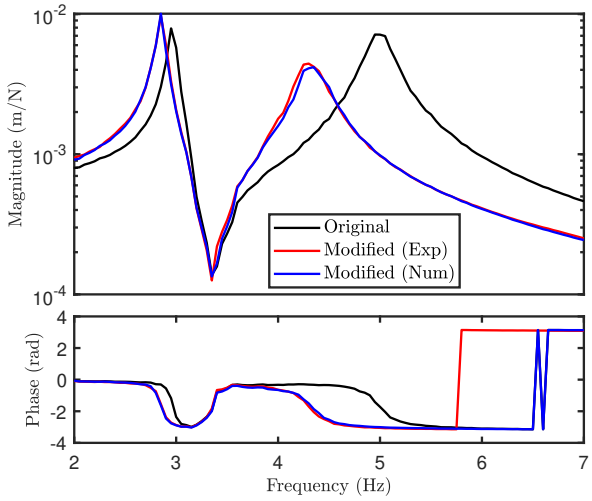

Figure 8.9: Measured and predicted modified FRF at a zero freestream speed.

Flutter Speed Prediction

Next, the effect of the modification on the flutter speed was considered. Experimentally, it was determined that the new flutter speed, with the modification added, was approximately 12.4 m/s.

Consider the FRF corresponding to h_{22} at a freestream speed of 12.4 m/s, as shown in Fig. 8.10. The aim was to determine the necessary mass modification required to shift the flutter

speed to this value. By use of Eq. 8.19, the modification at this speed must satisfy

$$\tilde{m} = \frac{1}{\omega^{*2} h_{22}(i\omega^*)}.$$

For physically meaningful solutions, it is required that the modification parameter is real and thus only solutions where the phase of $h_{22}(i\omega^*)$ is $0 \pm n\pi$ are valid. The flutter frequency solutions, using Fig. 8.10, are therefore given by $\omega^* = 2.66$ Hz and 3.08 Hz. At 3.08 Hz the magnitude of the FRF is 2.73×10^{-3} m/N and so the predicted mass modification is 0.98 kg. This closely matches the true modification of 1 kg with an error of only 2%. The solution corresponding to the higher frequency of 2.66 Hz requires a mass modification of approximately 4 kg. However, this was not tested as the large mass would have potentially damaged the pitch springs in the system and therefore was considered unfeasible.

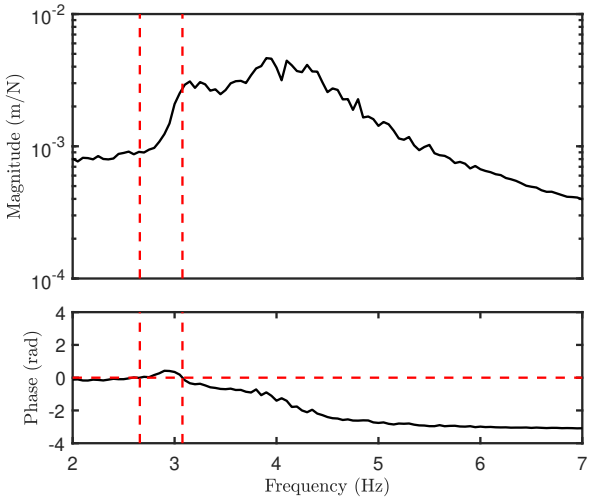

Figure 8.10: Bode plot of h_{22} at v = 12.4 m/s.

At this point it is important to point out some of the practical limitations of this case study. Firstly, the electro-mechanical shaker was placed outside of the wind-tunnel and thus had no impact on the aerodynamics. In real applications on full scale aircraft, one could not do this and it is suggested that inertial shakers placed inside the wing would have to be used instead. Secondly, this work has been restricted to subsonic flows that are well approximated as linear. In practice, one may encounter nonlinear phenomena such as shock waves and flow separation. However, this is left as an area of future research.

8.6.3 Multiple-Element, Multiple-Rank Modification

Next, a multiple-element, multiple-rank modification was considered. The modification consisted of a simultaneous pitch and plunge stiffness modification of the form

$$\Delta\mathbf{Z}_r(s, \boldsymbol{\theta}) = \begin{pmatrix} k_h & 0 \\ 0 & k_\alpha \end{pmatrix}.$$

The parameters k_h and k_α are the random plunge and pitch stiffness modification parameters, respectively, and have probability distributions given by

$$k_h \sim \mathcal{N}(2000, 150^2),$$
$$k_\alpha \sim \mathcal{N}(0, 2^2),$$

where $\mathcal{N}(\mu, \sigma^2)$ denotes a Gaussian distribution with mean μ and standard deviation σ.

In the form given above, the modification matrix is given in units that satisfy

$$\Delta\mathbf{Z}_r(s, \boldsymbol{\theta}) \begin{pmatrix} h \\ \alpha \end{pmatrix} = \begin{pmatrix} f_h \\ f_\alpha \end{pmatrix},$$

where h is the plunge degree-of-freedom, α is the pitch degree-of-freedom, and f_x is the force in the x degree-of-freedom. In practice, however, the receptance measurements correspond to the laser displacement readings. Furthermore, the forces in the receptance measurements correspond to collocated forces in the coordinate system of the lasers. Therefore, it is necessary to change the basis of the modification. Assuming small angle deflections, the relationship between the pitch and plunge coordinates and the laser reading coordinates is given by

$$\begin{pmatrix} h \\ \alpha \end{pmatrix} = \begin{pmatrix} 0.5 & 0.5 \\ -1/(0.24) & 1/(0.24) \end{pmatrix} \begin{pmatrix} x_1 \\ x_2 \end{pmatrix},$$

where x_1 and x_2 are the displacement readings from laser sensors one and two, respectively. Similarly, the force and moment in the plunge and pitch degrees of freedom are related to the collocated forces by

$$\begin{pmatrix} F_h \\ M_\alpha \end{pmatrix} = \begin{pmatrix} 1 & 1 \\ -0.12 & 0.12 \end{pmatrix} \begin{pmatrix} F_1 \\ F_2 \end{pmatrix},$$

where F_1 and F_2 are force inputs collocated at laser positions one and two, respectively. Therefore, the modification is given in the laser coordinates by

$$\Delta\mathbf{Z}_r(s, \boldsymbol{\theta}) = \begin{pmatrix} 1 & 1 \\ -0.12 & 0.12 \end{pmatrix}^{-1} \begin{pmatrix} k_h & 0 \\ 0 & k_\alpha \end{pmatrix} \begin{pmatrix} 0.5 & 0.5 \\ -1/(0.24) & 1/(0.24) \end{pmatrix},$$

or equivalently

$$\Delta\mathbf{Z}_r(s, \boldsymbol{\theta}) = \begin{pmatrix} \frac{625}{36}k_\alpha + \frac{1}{4}k_h & -\frac{625}{36}k_\alpha + \frac{1}{4}k_h \\ -\frac{625}{36}k_\alpha + \frac{1}{4}k_h & \frac{625}{36}k_\alpha + \frac{1}{4}k_h \end{pmatrix}.$$

The modification matrix given above may be broken down into a series of rank-one modifications, as in Eq. 8.24, by

$$\Delta\mathbf{Z}_r(s, \boldsymbol{\theta}) = \frac{1}{4}k_h(1 \quad 1)^T(1 \quad 1) + \frac{625}{36}k_\alpha(1 \quad -1)^T(1 \quad -1),$$

and therefore, by using the iterative Sherman-Morrison approach, the characteristic equation of the modified system is given by

$$1 + \frac{1}{4}k_h(h_{11} + h_{12} + h_{21} + h_{22}) + \frac{625}{36}k_\alpha(h_{11} - h_{12} - h_{21} + h_{22}) + \frac{625}{36}k_\alpha k_h(h_{11}h_{22} - h_{12}h_{21}) = 0.$$

Figure 8.11 shows the frequency response functions in the unmodified system at 12.4 m/s. In order to reduce the impact of noise in the measurements, the FRFs were fitted with rational transfer functions using SDTools.

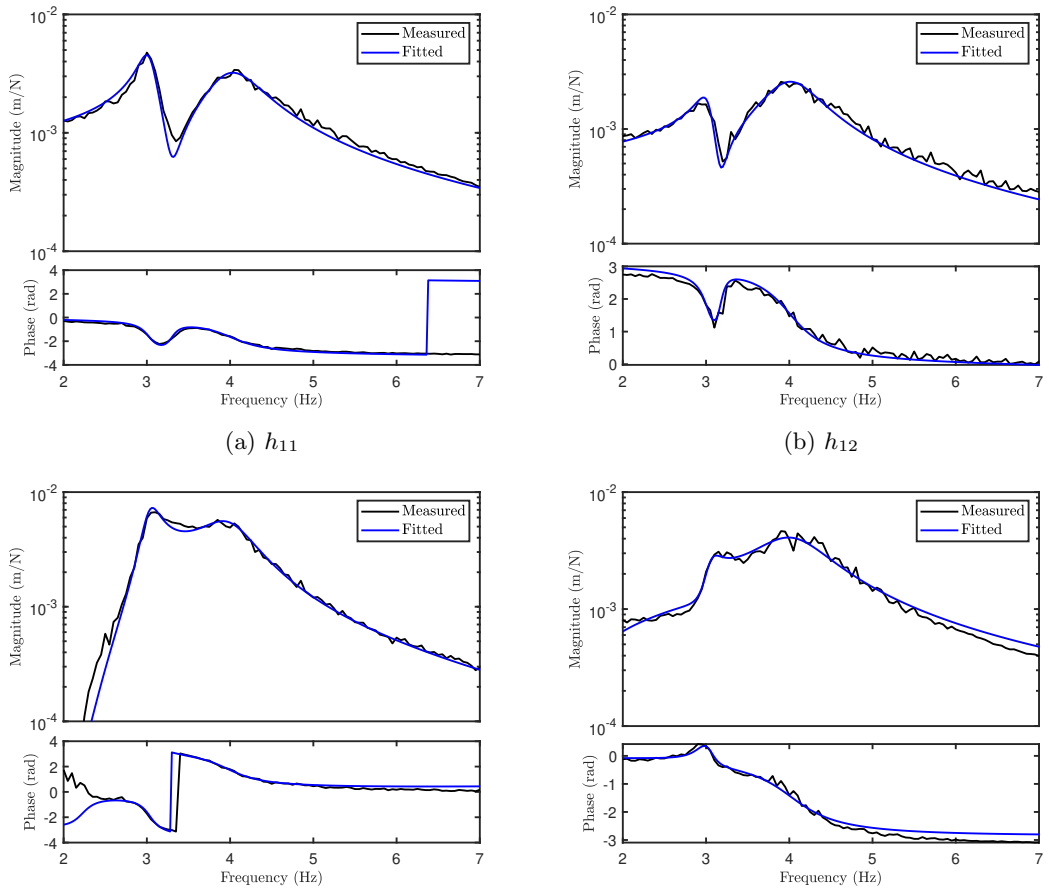

(a) h_{11} (b) h_{12}

(c) h_{21} (d) h_{22}

Figure 8.11: Measured and fitted FRFs at 12.4 m/s.

Figure 8.12 shows the projected, standardised limit-state function. Between ±3 standard deviations of the random parameters, the projected function is well approximated as linear and therefore it is appropriate to use the first-order reliability method to estimate the probability of flutter. Using the same optimisation procedure as given in the numerical examples, the MPP is determined as $(0.1509, -1.7237, 22.6862)^T$. This matches that found geometrically in Fig. 8.12. The distance R corresponding to the MPP is 1.73 and thus the probability of flutter is calculated as 0.0418.

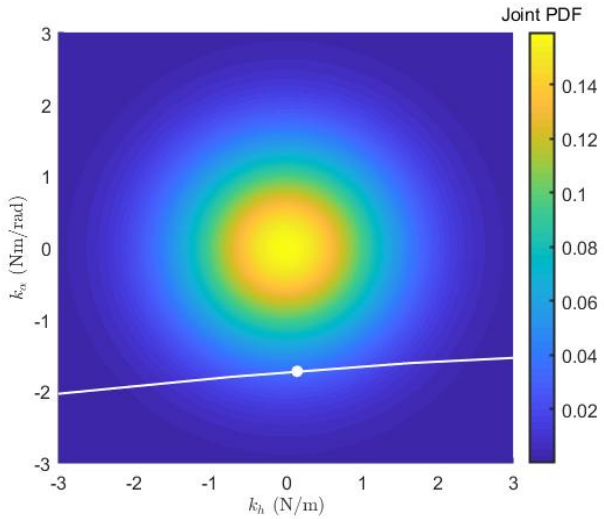

Figure 8.12: Projected, standardised limit-state function (experimental).

It is to be noted that the results presented above cannot be verified experimentally using Monte-Carlo simulation, as was done in the numerical examples. This is because, for such a small probability, it would require many thousands of experimental samples to obtain reliable results and is therefore physically unfeasible. However, since the projected limit-state function is approximately linear, it is highly likely to yield a good estimate of the flutter probability.

8.7 Summary

This chapter considers the development of an experimental-based uncertainty quantification technique for aeroservoelastic systems with uncertainty. Unlike previous work, the likelihood of flutter at a given reference speed is evaluated directly from measured frequency response function data. Two cases are considered: (i) uncertainty due to rank-one modifications to the dynamic stiffness matrix, and (ii) uncertainty due to higher-rank modifications. In the first case, the modification parameters that cause flutter can be found graphically, direct from the measured FRF data. This allows the probability of flutter to be evaluated simply by integration of the flutter yielding parameter solutions. In the second case, a projection-based approach is used where the characteristic equation is mapped to the parameter space, which is standardised using techniques such as the Rosenblatt transform. The region of instability is then integrated to find the probability of flutter. Due to several issues with integration of this region, a first-order reliability approach is used to estimate the probability of flutter and is advantageous due to its simplicity and low computational effort compared to conventional techniques, such as MCS.

The developed techniques have been applied both numerically and experimentally. In the numerical examples, there is a good agreement between the predicted and actual probabilities

of flutter. The limiting factor in the accuracy of such methods is the degree of nonlinearity in the projected limit state function, which, if significant, can yield erroneous solutions. The experimental case studies also showed a good agreement between the true and predicted modifications required for flutter. However, some areas of future work have been identified so that this technique can be potentially applied to full-scale aircraft in the future.

This page is intentionally left blank.

Chapter 9

Conclusions and Future Work

9.1 Conclusions

This thesis explores the development of receptance-based techniques for applications in aeroservoelastic systems. The underlying principle of receptance-based techniques is that frequency response function data, collected by means of standard modal testing, is used to facilitate a purely experiment-based approach to control and uncertainty quantification. In this way, there is no need to construct a numerical model of the structure, aerodynamics, or their coupled interaction. Consequently, issues associated with numerical modelling are avoided.

The first section of the thesis considers receptance-based control techniques. To date, there have been a small number of applications of receptance-based active flutter suppression. However, these applications have been all been limited to numerical models or small experimental systems. This is due to restrictive limitations in the conventional formulation of the Receptance Method, which was originally designed for systems with fixed mass, stiffness and damping properties. In this research, the Receptance Method is extended to better suit aeroservoelastic systems. This is done in two ways. Firstly, an optimum eigenstructure assignment technique is developed, where the closed-loop poles are chosen to maximise the flutter speed. Secondly, a procedure that allows the poles to be assigned iteratively, using receptance data with a prior controller active, is developed. The optimum eigenstructure assignment method replaces the previously-used trial and error approach to AFS and provides a more rigorous framework. The control iteration method allows receptance data to be collected at speeds above the open-loop flutter speed, thereby allowing the Receptance Method to be applied at speeds much higher than previously possible. When used together, both techniques allow the flutter speed to be increased significantly in the closed-loop. Indeed, it is demonstrated in both the numerical and experimental case studies that using the Receptance Method at speeds below the open-loop flutter speed leads to inefficient AFS controllers that do not best utilise the full control effort available.

Despite avoiding issues related to modelling errors, receptance-based control techniques are not completely free from uncertainty. As shown in Chapter 5, experimental sources of uncertainty are prevalent and often have a considerable impact on the robustness of the controller and the closed-loop system. One of the ways in which uncertainty manifests itself is through so-called pole clustering. This is where the poles of the system are scattered about a set of nominal points in the complex plane. The pole clustering phenomenon leads to uncertain natural frequencies and random damping ratios. Consequently, in aeroservoelastic systems, the binary

stability property becomes stochastic and hence the flutter speed becomes non-deterministic.

A review of the literature shows that some attempts have been made to incorporate uncertainty quantification methods into receptance-based control techniques. However, these approaches have been largely holistic; usually, they model uncertainty as arbitrary, complex-valued perturbations and do not account for the physical origins of the uncertainty. In this thesis, alternative techniques for receptance-based control in the presence of uncertainty are developed. Each technique is designed for different purposes, depending on the nature of uncertainty that is present. The first technique is for systems that exhibit uncertainty arising from erroneous rational transfer function fitting of frequency response function data. Such uncertainty typically occurs because of poor quality frequency response function data or ill-behaved fitting algorithms. The second considers uncertainty that arises from physical sources, such as manufacturing tolerances, damage, degradation, and environmental variation. Both of these sources of uncertainty are modelled in different ways and each have relative advantages and disadvantages. In Chapter 6, errors arising from poor RTF fittings are modelled through a non-probabilistic approach. The uncertain parameters in the RTF are treated as complex-valued perturbations to a set of nominal values. Sensitivity formulae are then used to estimate the maximum real and imaginary part variation of each pole. In Chapter 7, errors arising from physical sources are modelled probabilistically. Uncertain mass, stiffness, and damping properties are modelled as random variables, with a defined probability distribution, and then lumped together as a single stochastic structural modification to the set of measured repentance data. Using a polynomial chaos expansion, surrogate models of the poles spreads are created. This then allows the mean and variance of the real and imaginary part of each pole to be extracted.

In both of the above-mentioned situations, it has been shown that the set of assigned, closed-loop eigenvalues and eigenvectors have a direct impact on the spread of the pole clusters. Moreover, it has been shown that eigenstructure assignment can be performed optimally to reduce the spread in the real part, imaginary part, or a combination thereof. This principle of optimum eigenstructure assignment is demonstrated in both Chapters 6 and 7. In cases where the system is single-input, the closed-loop poles can be assigned so that the size and shape of the pole clusters are minimised according to some defined robustness metric, which is chosen. In multiple-input systems, the eigenvectors of the system can be also be assigned and this extra control effort can be used to further reduce the robustness metric and hence minimise the effect of uncertainty in the system.

Whilst required to perform optimum eigenstructure assignment, uncertainty quantification of the system's poles is unlikely to be used in practice as a metric by which to assess the robustness of an aeroelastic system. Instead, it is more meaningful to consider the direct impact of the uncertainty on the stability of the system and to determine the likelihood of instability arising. Whilst conventional UQ methods aim to find the probabilistic distribution of the flutter speed, such an approach is impossible in receptance-based methods. This is because one only has access to information about the system's poles at the specific speeds at which the receptance data were collected. Despite this, however, it is still possible to determine the *likelihood* of flutter at a given airspeed. In Chapter 8, a new receptance-based flutter likelihood evaluation technique is presented. Using only measured frequency response function data, the likelihood of flutter arising due to uncertain physical modifications is quantified. This is done by projecting the uncertain characteristic equation of the system into the random parameter space. The resulting curve in the parameter space is named the limit state function and physically represents the boundary between stable and unstable modification parameters. The region corresponding to the unstable modifications is then integrated with respect to the

joint distribution of the random parameters to obtain the probability of flutter at that specific airspeed. For computational efficiency, a first-order reliability method is used to perform the integration. However, it is shown that this approach only works well if the projection of the limit state curve in the parameter space is approximately linear.

Overall, this thesis demonstrates the usefulness of receptance-based techniques in aeroservoelastic systems. With further developments, these techniques could be used to facilitate an experiment-based approach to active control for the purposes of flutter suppression. Additionally, uncertainty quantification could be performed using real world data, without the use of numerical models. This in turn could lead to new experiment-based quantitative risk assessment measures for aeroelastic systems with uncertainty.

9.2 Future Work

Despite progress in the field, there remains several open challenges that inhibit the use of receptance-based techniques in real-world aeroservoelastic systems. Some of these challenges are summarised below and are suggested as areas of future research:

1. **Nonlinearities** - The scope of this thesis is limited to linear aeroservoelastic systems. In practice, the assumption of linearity is restrictive and unlikely to be true. This is especially the case for highly-flexible aeroservoelastic systems, which are becoming increasingly common. The main impact that nonlinearities have on the methods developed in this work is that the measured FRF data becomes dependent on the amplitude of the input and hence so too do the receptance data. In such situations, the methods would need to be adapted to account for such behaviour. It is suggested that techniques such as 'describing functions' may be useful in such situations [118].

2. **Combined uncertainty** - In Chapters 6 and 7, two different sources of uncertainty were considered. In each case, the effects the uncertainties had on the system's poles were quantified through different approaches and an optimisation procedure was used to reduce their impact. Whilst it was shown possible to reduce the impact of uncertainty in each case, they were considered independently. In practice, it may be that the optimum solution corresponding to variability between nominal systems may not match the optimum solution corresponding to errors in rational transfer function fitting. In future work, it would be interesting to consider a unified approach under which multiple sources of uncertainty are considered simultaneously.

3. **Uncontrollable or inaccessible modes** - Both the numerical and experimental examples presented in this thesis have been based on binary aeroservoelastic systems, which only have two degrees-of-freedom. In real world systems, there are an infinite number of modes and hence there is much greater difficulty in the design of the controller. It is well known that the maximum number of modes that can be controlled is limited by the number of inputs. Consequently, with a limited number of control surfaces, problems such as spillover in high frequency modes may occur and render the system unstable. Future research should consider the effects of spillover in receptance-based methods. Additionally, they should look at approaches to minimise the probability of this happening. It may be useful, perhaps, to consider the optimum placement of the control surfaces on the structure.

4. **Dynamic controllers** - The controllers used throughout this work have been static. In other words, the control gains have been fixed and do not vary according the conditions in which the system operations. Whilst this approach has been shown to increase the flutter speed, it is possible that such an approach would not be suitable in real world applications. In cases where aeroelastic systems have a large number of modes in a limited frequency range, it is possible that the mode that becomes unstable switches, depending on the action of the controller. In these cases, it may then be necessary to schedule the controller according to some parameter, such as the freestream speed, dynamic pressure or Mach number. Receptance-based gain scheduling has been considered in a limited number of numerical applications. However, it is yet to be demonstrated in a practical setting due to difficulties imposed by the lack of a numerical model.

Bibliography

[1] ICAO, "Presentation of 2018 Air Transport Statistical Results," ICAO, Tech. Rep., 2018. [Online]. Available: https://www.icao.int/annual-report-2018/Documents/Annual.Report.2018%7B%5C_%7DAir%20Transport%20Statistics.pdf.

[2] ICAO, *The World of Air Transport in 2017*, 2017. [Online]. Available: https://www.icao.int/annual-report-2017/Pages/the-world-of-air-transport-in-2017.aspx (visited on 01/22/2021).

[3] IATA, *Working Towards Ambitious Targets*. [Online]. Available: https://www.iata.org/en/programs/environment/climate-change/ (visited on 01/21/2021).

[4] K. Button, "Low-Cost Airlines: A Failed Business Model?" *Transp. J.*, vol. 51, no. 2, pp. 197–219, 2012.

[5] H. Justin, "Boeing 787 From The Ground Up," *Aeromagazine*, 2006.

[6] Airbus, *A350 Family*. [Online]. Available: https://www.airbus.com/aircraft/passenger-aircraft/a350xwb-family.html (visited on 01/21/2021).

[7] FAA, "Aeroelastic Stability Substantiation of Transport Category Airplanes (AC 25.629-1B)," Federal Aviation Administration, Tech. Rep., 2014.

[8] C. L. Pettit, "Uncertainty Quantification for Airframes: Current Status, Needs, and Suggested Directions," *J. Mater. Manuf.*, vol. 112, pp. 439–451, 2003.

[9] R. P. Hallion, "World War I: An air war of consequence," *Endeavour*, vol. 38, no. 2, pp. 77–90, 2014.

[10] G. Brewer, "The Collapse of Monoplane Wings," *Flight*, p. 33, Jan. 1913.

[11] I. E. Garrick and W. H. Reed, "Historical development of aircraft flutter," *J. Aircr.*, vol. 18, no. 11, pp. 897–912, 1981.

[12] I. E. Garrick, "Aeroelasticity-frontiers and beyond," *J. Aircr.*, vol. 13, no. 9, pp. 641–657, Sep. 1976.

[13] P. P. Friedmann, "Renaissance of Aeroelasticity and Its Future," *J. Aircr.*, vol. 36, no. 1, pp. 105–121, 1999.

[14] J. A. Dunnmon, S. C. Stanton, B. P. Mann, and E. H. Dowell, "Power extraction from aeroelastic limit cycle oscillations," *J. Fluids Struct.*, vol. 27, no. 8, pp. 1182–1198, 2011.

[15] T. Wu and A. Kareem, "Bridge aerodynamics and aeroelasticity: A comparison of modeling schemes," *J. Fluids Struct.*, vol. 43, pp. 347–370, 2013.

[16] E. H. Dowell, *A Modern Course in Aeroelasticity*, 5th ed., E. H. Dowell, Ed., ser. Solid Mechanics and Its Applications. New York: Springer, 2015, vol. 217.

[17] A. R. Collar, "The First Fifty Years of Aeroelasticity," *Aerospace*, vol. 5, pp. 12–20, 1978.

[18] Y. C. Fung, *An Introduction to the Theory of Aeroelasticity*. New York: Dover Publications Inc, 1993.

[19] A. C. Von Baumhauer and C. Koning, "On the stability of oscillations of an airplane wing," National Advisory Committee for Aeronautics, Tech. Rep., 1923.

[20] Y. Wang, A. Da Ronch, and M. G. Tehrani, "Adaptive feedforward control for gust-induced aeroelastic vibrations," *Aerospace*, vol. 5, no. 3, 2018.

[21] W. Bollay, "Aerodynamic Stability and Automatic Control: The Fourteenth Wright Brothers Lecture," *J. Aeronaut. Sci.*, vol. 18, no. 9, pp. 569–617, Sep. 1951.

[22] P. J. Lu and L. J. Huang, "Flutter suppression of thin airfoils using active acoustic excitations," *AIAA J.*, vol. 30, no. 12, pp. 2873–2881, 1992.

[23] K. B. Lazarus, E. F. Crawley, and C. Y. Lin, "Fundamental mechanisms of aeroelastic control with control surface and strain actuation," *J. Guid. Control. Dyn.*, vol. 18, no. 1, pp. 10–17, 1995.

[24] E. V. Ardelean, M. A. McEver, D. G. Cole, and R. L. Clark, "Active flutter control with V-stack piezoelectric flap actuator," *J. Aircr.*, vol. 43, no. 2, pp. 482–486, 2006.

[25] P. P. Rao, T. W. Strganac, and O. K. Rediniotis, "Control of aeroelastic response via synthetic jet actuators," in *41st Struct. Struct. Dyn. Mater. Conf. Exhib.*, Atlanta, USA, 2000.

[26] S. Fichera, I. Isnardi, and J. E. Mottershead, "High-bandwidth morphing actuator for aeroelastic model control," *Aerospace*, vol. 6, no. 2, 2019.

[27] E. Nissim and J. J. Burken, "Control surface spanwise placement in active flutter suppression systems," NASA, Tech. Rep. 2873, 1988.

[28] E. Livne, "Integrated aeroservoelastic optimization: status and direction," *J. Aircr.*, vol. 36, no. 1, pp. 122–145, 1999.

[29] Q. Wenmin, H. Rui, H. Haiyan, and Z. Yonghui, "Active flutter suppression of a multiple-actuated-wing wind tunnel model," *Chinese J. Aeronaut.*, vol. 27, no. 6, pp. 1451–1460, 2014.

[30] J. J. Ryan and J. T. Bosworth, "Current and Future Research in Active Control of Lightweight, Flexible Structures Using the X-56 Aircraft," in *AIAA 52nd Aerosp. Sci. Meet.*, Maryland, 2014.

[31] J. R. Wright and J. E. Cooper, *Introduction to Aeroelasticity and Loads*, 2nd ed. Chichester: Wiley, 2014.

[32] T. Theodorsen, "General Theory of Aerodynamic Instability and the Mechanism of Flutter," National Advisory Committee for Aeronautics, Tech. Rep., 1949.

[33] E. Albano and W. P. Hodden, "A doublet-lattice method for calculating lift distributions on oscillating surfaces in subsonic flows," *AIAA J.*, vol. 7, no. 2, pp. 279–285, 1969.

[34] H. Ashley and G. Zartarian, "Piston Theory-A New Aerodynamic Tool for the Aeroelastician," *J. Aeronaut. Sci.*, vol. 23, no. 12, pp. 1109–1118, 1956.

[35] A. Tewari, *Aeroservoelasticity*, 1st ed. New York: Springer-Verlag, 2015.

[36] E. Livne, "Aircraft active flutter suppression: State of the art and technology maturation needs," *J. Aircr.*, vol. 55, no. 1, pp. 410–450, 2018.

[37] E. Nissim, "Flutter Suppression Using Active Controls Based on the Concept of Aerodynamic Energy," NASA, Tech. Rep., 1971.

[38] O. O. Bendiksen, "Energy approach to flutter suppression and aeroelastic control," *J. Guid. Control. Dyn.*, vol. 24, no. 1, pp. 176–184, 2001.

[39] S. Kuzmina, F. Ishmuratov, and O. Karas, "Energy approach to transonic flutter and LCO with shock waves movement," *IOP Conf. Ser. Mater. Sci. Eng.*, vol. 1024, no. 1, 2021.

[40] W. P. Lock, E. E. Kordes, J. M. Mckay, and J. H. Wykes, "Flight investigation of a structural mode control system for the XB-70 aircraft," NASA, Tech. Rep. October, 1973.

[41] J. H. Wykes, L. U. Nan, and A. S. Mori, "XB-70 Structural Mode Control System Design and Performance Analyses," NASA, Tech. Rep., 1970.

[42] L. Librescu and P. Marzocca, "Advances in the linear/nonlinear control of aeroelastic structural systems," *Acta Mech.*, vol. 178, no. 3-4, pp. 147–186, 2005.

[43] J. K. Mahesh, C. R. Stone, W. L. Garrard, and H. J. Dunn, "Control law synthesis for flutter suppression using linear quadratic gaussian theory," *J. Guid. Control. Dyn.*, vol. 4, no. 4, pp. 415–422, 1981.

[44] F. Niel, A. Seuret, L. Zaccarian, and C. Fagley, "Robust LQR control for stall flutter suppression: A polytopic approach," *IFAC*, vol. 50, no. 1, pp. 11 367–11 372, 2017.

[45] H. Buschek and A. J. Calise, "Uncertainty modeling and fixed-order controller design for a hypersonic vehicle model," *J. Guid. Control. Dyn.*, vol. 20, no. 1, pp. 42–48, 1997.

[46] M. R. Waszak, "Robust multivariable flutter suppression for Benchmark Active Control Technology wind-tunnel model," *J. Guid. Control. Dyn.*, vol. 24, no. 1, pp. 147–153, 2001.

[47] L. J. Adamson, S. Fichera, and J. E. Mottershead, "Probabilistic control optimization of aeroservoelastic systems with uncertainty," in *AIAA Scitech 2019 Forum*, American Institute of Aeronautics and Astronautics Inc, AIAA, 2019.

[48] W. H. Xing and S. N. Singh, "Adaptive output feedback control of a nonlinear aeroelastic structure," *J. Guid. Control. Dyn.*, vol. 23, no. 6, pp. 1109–1116, 2000.

[49] K. K. Reddy, J. Chen, A. Behal, and P. Marzocca, "Multi-input/multi-output adaptive output feedback control design for aeroelastic vibration suppression," *J. Guid. Control. Dyn.*, vol. 30, no. 4, pp. 1040–1048, 2007.

[50] A. Mannarino and P. Mantegazza, "Nonlinear aeroelastic reduced order modeling by recurrent neural networks," *J. Fluids Struct.*, vol. 48, pp. 103–121, 2014.

[51] R. C. Scott and L. E. Pado, "Active control of wind-tunnel model aeroelastic response using neural networks," *J. Guid. Control. Dyn.*, vol. 23, no. 6, pp. 1100–1108, 2000.

[52] C. M. Lin and W. L. Chin, "Adaptive decoupled fuzzy sliding-mode control of a nonlinear aeroelastic system," *J. Guid. Control. Dyn.*, vol. 29, no. 1, pp. 206–209, 2006.

[53] J. Yuan, N. Qi, Z. Qiu, and F. Wang, "Adaptive RBF observer-sliding mode controller design for a two dimensional aeroelastic system with unsteady aerodynamics," *Aerosp. Sci. Technol.*, vol. 80, pp. 482–495, 2018.

[54] G. L. Ghiringhelli, M. Lanz, P. Mantegazza, and S. Ricci, "Active Flutter Suppression Techniques in Aircraft Wings," *Control Dyn. Syst.*, vol. 52, pp. 57–115, 1992.

[55] N. H. Zimmerman and J. T. Weissenburger, "Prediction of flutter onset speed based on flight testing at subcritical speeds," *J. Aircr.*, vol. 1, no. 4, pp. 190–202, 1964.

[56] R. Lind and M. Brenner, "Flutterometer: an on-line tool to predict robust flutter margins," *J. Aircr.*, vol. 37, no. 6, pp. 1105–1112, 2000.

[57] J. E. Cooper, P. R. Emmett, J. R. Wright, and M. J. Schofield, "Envelope function - A tool for analyzing flutter data," *J. Aircr.*, vol. 30, no. 5, pp. 785–790, 1993.

[58] R. P. Peloubet, R. L. Haller, and R. M. Bolding, "Recent developments in the F-16 flutter suppression with active control program," *J. Aircr.*, vol. 21, no. 9, pp. 716–721, 1984.

[59] FAA, "Special Conditions: Boeing 747-8/8F Airplanes, Interaction of Systems and Structures - 14 CFR Part 25 [Docket No. NM400; Special Conditions No. 25–388A–SC]," FAA, Tech. Rep. 102, 2011, pp. 30 523–30 529.

[60] Siemens, *Simcenter Nastran*.

[61] T. J. Sullivan, *Introduction to Uncertainty Quantification*, 1st ed. Cham Switzerland: Springer International Publishing, 2015.

[62] P. S. Beran, C. L. Pettit, and D. R. Millman, "Uncertainty quantification of limit-cycle oscillations," *J. Comput. Phys.*, vol. 217, no. 1, pp. 217–247, 2006.

[63] C. L. Pettit, "Uncertainty Quantification in Aeroelasticity: Recent Results and Research Challenges," *J. Aircr.*, vol. 41, no. 5, pp. 1217–1229, 2004.

[64] P. Beran, B. Stanford, and C. Schrock, "Uncertainty Quantification in Aeroelasticity," *Annu. Rev. Fluid Mech.*, vol. 49, no. 1, pp. 361–386, Jan. 2017.

[65] R. E. Melchers, *Structural reliability : analysis and prediction*, 2nd ed. John Wiley, 1999, ISBN: 0471987719.

[66] Y. Dai and C. Yang, "Methods and advances in the study of aeroelasticity with uncertainties," *Chinese J. Aeronaut.*, vol. 27, no. 3, pp. 461–474, 2014.

[67] K. J. Badcock, S. Timme, S. Marques, H. Khodaparast, M. Prandina, J. E. Mottershead, A. Swift, A. Da Ronch, and M. A. Woodgate, "Transonic aeroelastic simulation for instability searches and uncertainty analysis," *Prog. Aerosp. Sci.*, vol. 47, no. 5, pp. 392–423, 2011.

[68] P. Beran and B. Stanford, "Uncertainty Quantification in Aeroelasticity," in *Lect. Notes Comput. Sci. Eng.* Vol. 92, 2013, pp. 59–103, ISBN: 9783319008844. DOI: 10.1007/978-3-319-00885-1_2.

[69] G. Alefeld and G. Mayer, "Interval analysis: Theory and applications," *J. Comput. Appl. Math.*, vol. 121, no. 1, pp. 421–464, 2000.

[70] S. S. Rao and L. Berke, "Analysis of uncertain structural systems using interval analysis," *AIAA J.*, vol. 35, no. 4, pp. 727–735, May 1997.

[71] Y. Zheng and Z. Qiu, "Non-probabilistic stability reliability analysis of composite laminated panels in supersonic flow with uncertain-but-bounded parameters," in *2018 AIAA Non-Deterministic Approaches Conf.*, Kissimmee, Florida, 2018.

[72] Y. Zheng and Z. Qiu, "An efficient method for flutter stability analysis of aeroelastic systems considering uncertainties in aerodynamic and structural parameters," *Mech. Syst. Signal Process.*, vol. 126, pp. 407–426, 2019.

[73] X. Chen, Z. Qiu, X. Wang, Y. Li, and R. Wang, "Uncertain reduced-order modeling for unsteady aerodynamics with interval parameters and its application on robust flutter boundary prediction," *Aerosp. Sci. Technol.*, vol. 71, pp. 214–230, 2017.

[74] S. Marques, K. J. Badcock, H. H. Khodaparast, and J. E. Mottershead, "How structural model variability influences transonic aeroelastic stability," *J. Aircr.*, vol. 49, no. 5, pp. 1189–1199, 2012.

[75] R. L. Muhanna and R. L. Mullen, "Uncertainty in Mechanics Problems—Interval–Based Approach," *J. Eng. Mech.*, vol. 127, no. 6, pp. 557–566, Jun. 2001.

[76] W. Krämer, "Generalized Intervals and the Dependency Problem," *Pamm*, vol. 6, no. 1, pp. 683–684, 2006.

[77] M. Rezaei, S. A. Fazelzadeh, A. Mazidi, M. I. Friswell, and H. H. Khodaparast, "Fuzzy uncertainty analysis and reliability assessment of aeroelastic aircraft wings," *Aeronaut. J.*, vol. 124, no. 1275, pp. 786–811, May 2020.

[78] A. Iannelli, A. Marcos, R. Bombardieri, and R. Cavallaro, "Linear Fractional Transformation co-modeling of high-order aeroelastic systems for robust flutter analysis," *Eur. J. Control*, vol. 54, pp. 49–63, Jul. 2020.

[79] N. Wiener, "The Homogeneous Chaos," *Am. J. Math.*, vol. 60, no. 4, pp. 897–936, Jan. 1938.

[80] R. G. Ghanem and P. D. Spanos, *Stochastic Finite Elements: A Spectral Approach*, Revised Ed. Mineola, New York: Dover Publications Inc, 2012.

[81] M. Rosenblatt, "Remarks on a Multivariate Transformation," *Ann. Math. Stat.*, vol. 23, no. 3, pp. 470–472, 1952.

[82] P. Kumar, B. Sanderse, K. Boorsma, and M. Caboni, "Global sensitivity analysis of model uncertainty in aeroelastic wind turbine models," *J. Phys. Conf. Ser.*, vol. 1618, no. 4, 2020.

[83] I. Sobol, "Global sensitivity indices for nonlinear mathematical models and their Monte Carlo estimates," *Math. Comput. Simul.*, vol. 55, no. 1-3, pp. 271–280, 2001.

[84] A. Saltelli, P. Annoni, I. Azzini, F. Campolongo, M. Ratto, and S. Tarantola, "Variance based sensitivity analysis of model output. Design and estimator for the total sensitivity index," *Comput. Phys. Commun.*, vol. 181, no. 2, pp. 259–270, 2010.

[85] A. Suryawanshi and D. Ghosh, "Reliability based optimization in aeroelastic stability problems using polynomial chaos based metamodels," *Struct. Multidiscip. Optim.*, vol. 53, no. 5, pp. 1069–1080, 2016.

[86] M. S. Eldred, "Recent advances in non-intrusive polynomial chaos and stochastic collocation methods for uncertainty analysis and design," in *AIAA ASME ASCE AHS ASC Struct. Struct. Dyn. Mater. Conf.*, Palm Springs, California: American Institute of Aeronautics and Astronautics Inc., 2009.

[87] A. Chateauneuf, "Principles of reliability-based design optimization," in *Struct. Des. Optim. Considering Uncertainties*, London: Taylor & Francis, 2008, pp. 3–30, ISBN: 9780203938522. DOI: 10.1201/b10995-3.

[88] M. F. Othman, G. H. Silva, P. H. Cabral, A. P. Prado, A. Pirrera, and J. E. Cooper, "A robust and reliability-based aeroelastic tailoring framework for composite aircraft wings," *Compos. Struct.*, vol. 208, pp. 101–113, 2019.

[89] C. Scarth and J. E. Cooper, "Reliability-based aeroelastic design of composite plate wings using a stability margin," *Struct. Multidiscip. Optim.*, vol. 57, no. 4, pp. 1695–1709, 2018.

[90] C. Scarth, P. N. Sartor, J. E. Cooper, P. M. Weaver, and G. H. Silva, "Robust and reliability-based aeroelastic design of composite plate wings," *AIAA J.*, vol. 55, no. 10, pp. 3539–3552, 2017.

[91] B. Stanford and P. Beran, "Minimum-mass panels under probabilistic aeroelastic flutter constraints," *Finite Elem. Anal. Des.*, vol. 70-71, pp. 15–26, 2013.

[92] S. Missoum, C. Dribusch, and P. Beran, "Reliability-based design optimization of nonlinear aeroelasticity problems," *J. Aircr.*, vol. 47, no. 3, pp. 992–998, 2010.

[93] S.-K. Choi, R. V. Grandhi, and R. A. Canfield, *Reliability-based Structural Design*. London: Springer, 2007.

[94] M. Allen and K. Maute, "Reliability-based design optimization of aeroelastic structures," *Struct. Multidiscip. Optim.*, vol. 27, no. 4, pp. 228–242, 2004.

[95] A. Manan and J. Cooper, "Design of composite wings including uncertainties: A probabilistic approach," *J. Aircr.*, vol. 46, no. 2, pp. 601–607, May 2009.

[96] D. J. Ewins, *Modal Testing: Theory, Practice and Application*, 2nd ed. Baldock, Hertfordshire, England: Research Studies Press, 2000.

[97] B. Peeters, H. Van Der Auweraer, P. Guillaume, and J. Leuridan, "The PolyMAX frequency-domain method: A new standard for modal parameter estimation?" *Shock Vib.*, vol. 11, no. 3-4, pp. 395–409, 2004.

[98] J. He, "Structural modification," *Philos. Trans. Math. Phys. Eng. Sci.*, vol. 359, no. 1778, pp. 187–204, 2001.

[99] J. E. Mottershead and Y. M. Ram, "Inverse eigenvalue problems in vibration absorption: Passive modification and active control," *Mech. Syst. Signal Process.*, vol. 20, no. 1, pp. 5–44, 2006.

[100] W. Duncan, "The admittance method for obtaining the natural frequencies of systems," *London, Edinburgh, Dublin Philos. Mag. J. Sci.*, vol. 32, no. 214, pp. 401–409, 1941.

[101] Carter, "The Vibration of Airserew Blades with particular reference to their Response to Harmonic Torque Impulses in the Drive," Reports and Memoranda of the Aeronautical Research Committee 1758, Tech. Rep., 1936.

[102] J. T. Weissenburger, "Effect of local modifications on the vibration characteristics of linear systems," *J. Appl. Mech. Trans. ASME*, vol. 35, no. 2, pp. 327–322, 1964.

[103] R. J. Pomazal and V. W. Snyder, "Local modifications of damped linear systems," *AIAA J.*, vol. 9, no. 11, pp. 2216–2221, May 1971.

[104] S. H. Tsai, H. Ouyang, and J. Y. Chang, "Inverse structural modifications of a geared rotor-bearing system for frequency assignment using measured receptances," *Mech. Syst. Signal Process.*, vol. 110, pp. 59–72, 2018.

[105] J. E. Mottershead, M. Ghandchi Tehrani, D. Stancioiu, S. James, and H. Shahverdi, "Structural modification of a helicopter tailcone," *J. Sound Vib.*, vol. 298, no. 1-2, pp. 366–384, Nov. 2006.

[106] O. Zarraga, I. Ulacia, J. M. Abete, and H. Ouyang, "Receptance based structural modification in a simple brake-clutch model for squeal noise suppression," *Mech. Syst. Signal Process.*, vol. 90, pp. 222–233, 2017.

[107] M. G. Tehrani, "Passive Modification and Active Vibration Control by The Receptance Method," Ph.D. dissertation, University of Liverpool, 2007.

[108] J. E. Mottershead, M. G. Tehrani, and Y. M. Ram, "Eigenvalue Assignment Problems in Vibration Using Measured Receptances: Passive Modification and Active Control," in *CISM Int. Cent. Mech. Sci. Courses Lect.* Vol. 529, Springer International Publishing, 2011, pp. 179–202.

[109] F. Casciati, J. Rodellar, and U. Yildirim, "Active and semi-active control of structures-theory and applications: A review of recent advances," *J. Intell. Mater. Syst. Struct.*, vol. 23, no. 11, pp. 1181–1195, 2012.

[110] Y. M. Ram and J. E. Mottershead, "The receptance method in active vibration control," *AIAA J.*, vol. 45, no. 3, pp. 562–567, 2007.

[111] Y. Ram and J. Mottershead, "The Receptance Method in Active Vibration Control," in *47th AIAA/ASME/ASCE/AHS/ASC Struct. Struct. Dyn. Mater. Conf.*, Newport, Rhode Island, 2006.

[112] J. Sherman and W. Morrison, "Adjustment of an inverse matrix corresponding to a change in one element of a given matrix," *Ann. Math. Stat.*, vol. 21, no. 1, pp. 124–127, 1950.

[113] M. Ghandchi Tehrani, J. E. Mottershead, A. T. Shenton, and Y. M. Ram, "Robust pole placement in structures by the method of receptances," *Mech. Syst. Signal Process.*, vol. 25, no. 1, pp. 112–122, 2011.

[114] Y. M. Ram and J. E. Mottershead, "Multiple-input active vibration control by partial pole placement using the method of receptances," *Mech. Syst. Signal Process.*, vol. 40, no. 2, pp. 727–735, 2013.

[115] G. P. Liu and R. J. Patton, *Eigenstructure Assignment for Control System Design*, 1st ed. Chichester: John Wiley & Sons Ltd, 1998.

[116] J. E. Mottershead, M. G. Tehrani, S. James, and Y. M. Ram, "Active vibration suppression by pole-zero placement using measured receptances," *J. Sound Vib.*, vol. 311, no. 3-5, pp. 1391–1408, 2008.

[117] M. Ghandchi Tehrani, R. N. Elliott, and J. E. Mottershead, "Partial pole placement in structures by the method of receptances: Theory and experiments," *J. Sound Vib.*, vol. 329, no. 24, pp. 5017–5035, 2010.

[118] M. Ghandchi Tehrani, L. Wilmshurst, and S. J. Elliott, "Receptance method for active vibration control of a nonlinear system," *J. Sound Vib.*, vol. 332, no. 19, pp. 4440–4449, 2013.

[119] C. Zhen, S. Jiffri, D. Li, J. Xiang, and J. E. Mottershead, "Feedback linearisation of nonlinear vibration problems: A new formulation by the method of receptances," *Mech. Syst. Signal Process.*, vol. 98, pp. 1056–1068, 2018.

[120] D. Lisitano, S. Jiffri, E. Bonisoli, and J. E. Mottershead, "Experimental feedback linearisation of a non-smooth nonlinear system by the method of receptances," *Math. Mech. Solids*, vol. 24, no. 2, pp. 465–482, Feb. 2019.

[121] K. V. Singh, "Active control with the method of receptances: Recent progresses and its application in active aeroelastic control," *Springer Proc. Math. Stat.*, vol. 308, pp. 159–182, Jul. 2020.

[122] K. Vikram Singh, L. A. McDonough, J. Mottershead, J. Cooper, K. V. Singh, L. A. McDonough, J. Mottershead, and J. Cooper, "Active Aeroelastic Control Using the Receptance Method," in *Proc. ASME 2010 Int. Mech. Eng. Congr. Expo.*, Vancouver, British Columbia, Canada, 2010, pp. 137–146.

[123] X. Wei, J. E. Mottershead, and Y. M. Ram, "Partial pole placement by feedback control with inaccessible degrees of freedom," *Mech. Syst. Signal Process.*, vol. 70-71, pp. 334–344, Mar. 2016.

[124] K. V. K. Singh, C. Black, and R. Kolonay, "Active aeroelastic output feedback control with partial measurements by the method of receptances," *Aerosp. Sci. Technol.*, vol. 86, pp. 47–63, Mar. 2019.

[125] M. Xia and S. Li, "A combined approach for active vibration control of fluid-loaded structures using the receptance method," *Arch. Appl. Mech.*, vol. 88, no. 10, pp. 1683–1694, Oct. 2018.

[126] K. V. Singh, R. N. Brown, and R. Kolonay, "Receptance-based active aeroelastic control with embedded control surfaces having actuator dynamics," *J. Aircr.*, vol. 53, no. 3, pp. 830–845, 2016.

[127] K. V. Singh, L. A. McDonough, R. Kolonay, and J. E. Cooper, "Receptance-based active aeroelastic control using multiple control surfaces," *J. Aircr.*, vol. 51, no. 1, pp. 335–341, 2014.

[128] B. Mokrani, F. Palazzo, J. E. Mottershead, and S. Fichera, "Multiple-input multiple-output experimental aeroelastic control using a receptance-based method," *AIAA J.*, vol. 57, no. 7, pp. 3066–3077, 2019.

[129] E. Papatheou, X. Wei, S. Jiffri, M. Prandina, M. Ghandchi Tehrani, S. Bode, K. Vikram Singh, J. E. Mottershead, and J. E. Cooper, "Flutter control using vibration test data: Theory, rig design and preliminary results," in *Int. Conf. Noise Vib. Eng. 2012, ISMA 2012, USD 2012 Int. Conf. Uncertain. Struct. Dyn.*, Leuven, Belgium, 2012, pp. 3047–3060.

[130] S. Fichera, S. Jiffri, and J. E. Mottershead, "Design and wind tunnel test of a MODular aeroelastic FLEXible wing (MODFLEX)," in *Proc. Int. Conf. Noise Vib. Eng. ISMA 2016*, 2016.

[131] J. E. Mottershead, M. G. Tehrani, and Y. M. Ram, "Assignment of eigenvalue sensitivities from receptance measurements," *Mech. Syst. Signal Process.*, vol. 23, no. 6, pp. 1931–1939, 2009.

[132] M. G. Tehrani, J. E. Mottershead, and Y. M. Ram, "Eigenvalue sensitivity assignment by the receptance method," in *2008 Proc. 9th Bienn. Conf. Eng. Syst. Des. Anal.*, vol. 2, Haifa, Israel, 2009, pp. 695–700.

[133] M. Lu and Z. J. Bai, "A modified optimization method for robust partial quadratic eigenvalue assignment using receptances and system matrices," *Appl. Numer. Math.*, vol. 159, pp. 73–92, Jan. 2021.

[134] Z. J. Bai, M. Lu, and Q. Y. Wan, "Minimum norm partial quadratic eigenvalue assignment for vibrating structures using receptances and system matrices," *Mech. Syst. Signal Process.*, vol. 112, no. 4, pp. 265–279, 2018.

[135] Y. Liang, H. Ouyang, and H. Yamaura, "Robust pole assignment for friction induced vibration based on receptance method," in *Proc. ASME Des. Eng. Tech. Conf.*, vol. 8, Boston, Massachusetts, USA, 2015. DOI: 10.1115/DETC201547177.

[136] Y. Liang, H. Yamaura, and H. Ouyang, "Active assignment of eigenvalues and eigensensitivities for robust stabilization of friction-induced vibration," *Mech. Syst. Signal Process.*, vol. 90, pp. 254–267, 2017.

[137] S. Fichera, T. A. Guimarães, S. Jiffri, D. A. Rade, and J. E. Mottershead, "Design of a receptance-based active aeroelastic controller in the presence of parametric uncertainties," in *31st Congr. Int. Counc. Aeronaut. Sci. ICAS 2018*, Belo Horizonte, Brazil, 2018.

[138] G. Platanitis and T. W. Strganac, "Control of a Nonlinear Wing Section Using Leading- and Trailing-Edge Surfaces," *J. Guid. Control. Dyn.*, vol. 27, no. 1, pp. 52–58, 2004.

[139] K. W. Lee and S. N. Singh, "Adaptive control of multi-input aeroelastic system with constrained inputs," *J. Guid. Control. Dyn.*, vol. 38, no. 12, pp. 2337–2350, 2015.

[140] C. Martinelli, "Design , Validation and Control of an Aeroelastic Two DOF System," Masters thesis, Politecnico di Torino, 2019.

[141] B. Mokrani, A. Batou, S. Fichera, L. Adamson, D. Alaluf, and J. E. Mottershead, "The minimum norm multi-input multi-output receptance method for partial pole placement," *Mech. Syst. Signal Process.*, vol. 129, pp. 437–448, 2019.

[142] R. Storn and K. Price, "Differential Evolution – A Simple and Efficient Heuristic for Global Optimization over Continuous Spaces," *J. Glob. Optim.*, vol. 11, pp. 341–359, 1997.

[143] G. Di Pillo, S. Lucidi, and F. Rinaldi, "An approach to constrained global optimization based on exact penalty functions," *J. Glob. Optim.*, vol. 54, no. 2, pp. 251–260, 2012.

[144] J. Ding and A. Zhou, "Eigenvalues of rank-one updated matrices with some applications," *Appl. Math. Lett.*, vol. 20, no. 12, pp. 1223–1226, 2007.

[145] G. H. Golub and C. F. Van Loan, *Matrix Computations*, 4th ed. Baltimore, Maryland: The John Hopkins University Press, 2013.

[146] M. Buehren, *Differential Evolution*, 2008. [Online]. Available: https://uk.mathworks.com/matlabcentral/fileexchange/18593-differential-evolution.

Appendix A

Differential Evolution

Here, the Differential Evolution optimisation algorithm by Storn and Price [142] is described. This algorithm is used throughout the thesis in both the numerical and experimental examples. The first section describes the general principles of the method and how the algorithm is formulated. The second section briefly outlines the implementation that is used and the settings that are chosen in the optimisation problems presented in this thesis.

A.1 General Principles

The differential evolution (DE) algorithm by Storn and Price is a global optimisation technique that is based on the principle of stochastic optimisation. By contrast with conventional techniques, DE does not rely on analytic or computational gradients; instead, it is a heuristic method that does not require mathematical insights or structures found in the objective function. For this reason, DE is appropriate for optimisation problems where the objective function is non-convex or contains a potentially large number of locally minima solutions.

The general idea of the method is as follows. Consider a generic objective function $f : \mathbb{R}^n \rightarrow \mathbb{R}$. It is desired to find a vector $\mathbf{x}^*$ for which

$$f(\mathbf{x}^*) \leq f(\mathbf{y}), \quad \forall \mathbf{y} \in \mathbb{R}^n, \mathbf{y} \neq \mathbf{x}^*. \tag{A.1}$$

To do this, a set of NP candidate vectors are first selected as random points in the parameter space. Each candidate vector is expressed as $\mathbf{x}_{i,G}, i = 1, 2, NP$, where G is the current iteration of the optimisation.

At each iteration, for each candidate vector a corresponding mutant vector is generated according to

$$\boldsymbol{\nu}_{i,G+1} = \mathbf{x}_{r_1,G} + F(\mathbf{x}_{r_2,G} - \mathbf{x}_{r_3,G}), \tag{A.2}$$

where r_1, r_2, r_3 are unique, randomly selected indices from the set of NP candidate vectors[1]; and $F \in [0, 2]$ is named the amplification factor. To increase diversity, a corresponding crossover vector is then formed as

$$\mathbf{u}_{i,G+1} = \left[u_{1i,G+1}, u_{2i,G+1}, \ldots, u_{3i,G+1}\right]^T. \tag{A.3}$$

For each element $u_{ji,G+1}$, a value r_j is chosen randomly from a uniform distribution of $[0, 1]$.

[1] Note that r_1, r_2 and r_3 cannot correspond to the index of the candidate vector.

If $r_j < CR$, where $CR \in [0, 1]$ is a chosen, fixed value, then $u_{ji,G+1} = \nu_{ji,G+1}$. Otherwise, $u_{ji,G+1} = x_{ji,G}$.

Once the crossover vector has been formed for each candidate vector, they are all tested against the objective function. If $f(\mathbf{u}_{i,G+1}) \leq f(\mathbf{x}_{i,G})$, then $\mathbf{x}_{i,G+1} = \mathbf{u}_{i,G+1}$. Otherwise, $\mathbf{x}_{i,G+1} = \mathbf{x}_{i,G}$ and the candidate vector does not change.

This process is then repeated for each iteration until some stopping condition has been reached. This can either be a maximum number of iterations or a given percentage difference between the objective function over a specified number of iterations. Regardless, however, the optimum vector $\mathbf{x}^*$ is taken as the best performing candidate vector at the final iteration.

The differential evolution algorithm has been shown to give a good performance across a range of different test cases [142]. However, it is worth stressing again that the method itself does not guarantee that the global minimum is found. Further details on the specifics of the method may be found in the original paper by Storn and Price [142]. This also includes pseudocode, pictorial demonstrations, and benchmark tests.

A.2 Implementation

In the examples that are presented in this thesis, the implementation by Markus Buehren was used [146]. This version of the DE method is implemented in MATLAB and uses the following parameters:

$$F = 0.8, \tag{A.4}$$

$$CR = 0.7, \tag{A.5}$$

$$NP = 10D, \tag{A.6}$$

where D is the number of parameters in the optimisation. These parameters are generic accepted values for the DE method and worked sufficiently well in all applications tested.

The implementation by Markus Buehren also includes by default modifiable upper and lower bound intervals for the optimisation parameters. These were used for example in the upper and lower bounds of the optimum poles. However, for other constraints it was necessary to formulate them as a penalty to the objective function. For example, for a constraint of the form

$$g(\mathbf{x}) < 0, \tag{A.7}$$

the objective function was modified to

$$\hat{f}(\mathbf{x}) = f(\mathbf{x}) + c\left(\max(0, g(\mathbf{x}))\right), \tag{A.8}$$

where c is a parameter that is chosen appropriately to scale the penalty.

Throughout this thesis, the stopping condition was done manually. For each optimisation, the optimum candidate vector and its corresponding objective function value was displayed to the screen at each iteration. Once sufficient convergence was observed (approximately less than 0.1% variation between iterations), the optimisation was stopped. Another useful test of convergence was that in some optimisations the newly generated candidate vectors did not change from the previous iteration and thus there was no meaningful mutations. One could have used a formal stopping condition in the optimisation code. However, it was determined that noise from experimental data or from PC expansion fitting (see Chapter 7) sometimes

stopped the optimisation prematurely and thus led to a sub-optimal performance.

This page is intentionally left blank.

Appendix B

Single-Input, Leading-Edge Control

The single-input case study from optimisation two was repeated but using the leading-edge control surface instead of the trailing-edge control surface. Table B.1 shows the results of the control iteration method with the same parameters as in the original case study.

Table B.1: Single-input, leading-edge scheduling with a frequency separation metric.

Iteration	v_{it} (m/s)	v_{lim} (m/s)	v^* (m/s)
Open-loop	0	11.0	11.3
1	11.0	11.0	11.4
2	11.0	11.0	11.4
3	11.0	11.0	11.4

As shown, the leading-edge has essentially no impact on the system and barely modifies the flutter speed.